

Radiative Corrections in Relic Density Calculations

Dissertation

vorgelegt von

Francesco Dighera

Betreuer: Prof. Dr. Martin Beneke

Lehrstuhl für Theoretische Elementarteilchenphysik T31
Fakultät für Physik der Technischen Universität München





Lehrstuhl für Theoretische Elementarteilchenphysik T31
Fakultät für Physik der Technischen Universität München

Radiative Corrections in Relic Density Calculations

Francesco Dighera

Vollständiger Abdruck der von der Fakultät für Physik der Technischen Universität München zur Erlangung der akademischen Grades eines

Doktors der Naturwissenschaften

genehmigten Dissertation.

Vorsitzender: Prof. Dr. L. Fabbietti

Prüfer der Dissertation: 1. Prof. Dr. M. Beneke

2. Prof. Dr. B. Garbrecht

Die Dissertation wurde am 12.05.2016 bei der Technischen Universität München eingereicht und durch die Fakultät für Physik am 11.07.2016 angenommen.

Abstract

The experimental determination of the dark matter abundance in the Universe has reached the percent level accuracy, demanding the same precision from theoretical calculations. To improve the accuracy of the prediction within the thermal production mechanism (followed by the so-called “freeze-out”), the dark matter annihilation cross section has to be computed beyond the leading order in perturbation theory. In the first part of this thesis we address this problem establishing a consistent framework for relic density at next-to-leading order, based on the closed time-path approach to quantum field theory at finite temperature. In many relevant scenarios the non-perturbative effect known as Sommerfeld enhancement is the leading radiative correction and its impact on the relic density can be very large. We study this effect in the general Minimal Supersymmetric Standard Model in the second part of this thesis, and in particular we present a detailed phenomenological analysis on the relic density of TeV-scale wino-like neutralino dark matter.

Zusammenfassung

Die experimentelle Bestimmung der Menge an dunkler Materie im Universum hat mittlerweile eine Genauigkeit im Subprozentbereich erreicht, was eine vergleichbare Präzision theoretischer Rechnungen erforderlich macht. Um die Genauigkeit der Vorhersage im Rahmen des thermischen Produktionsmechanismus (gefolgt vom sogenannten “freeze-out”) zu verbessern, muss der Wirkungsquerschnitt der Vernichtung dunkler Materie jenseits der führenden Ordnung Störungstheorie berechnet werden. Im ersten Teil dieser Arbeit wird dieses Problem durch die Einführung eines konsistenten Formalismus zur Bestimmung der Reliktdichte in nächstführender Ordnung angegangen. Dieser Formalismus beruht auf der “Closed Time-Path”-Formulierung von Quantenfeldtheorien bei endlichen Temperaturen. In vielen relevanten Szenarien ist die führende Strahlungskorrektur durch den als Sommerfeldverstärkung bekannten nichtperturbativen Effekt gegeben. Dieser kann einen sehr großen Einfluss auf die Reliktdichte haben. Im zweiten Teil dieser Arbeit wird dieser Effekt im allgemeinen Minimalen Supersymmetrischen Standardmodell untersucht. Insbesondere wird eine detaillierte phänomenologische Analyse der Reliktdichte von Dunkler Materie aus winoartigen Neutralinos an der TeV-Skala präsentiert.

Contents

| | |
|--|-----------|
| Introduction | 1 |
| 1 Dark matter relic density in the freeze-out scenario | 7 |
| 1.1 Standard Cosmology | 7 |
| 1.2 The freeze-out scenario | 9 |
| 1.3 The cold dark matter case: WIMP miracle | 11 |
| 1.4 The Boltzmann equation | 13 |
| 2 The Boltzmann equation from QFT | 21 |
| 2.1 The closed time-path formalism | 22 |
| 2.1.1 Introduction | 22 |
| 2.1.2 The equilibrium propagators | 24 |
| 2.1.3 The Kadanoff-Baym equation | 27 |
| 2.2 Derivation of the Boltzmann equation | 29 |
| 2.2.1 The gradient expansion | 29 |
| 2.2.2 On-shell reduction of the Kadanoff-Baym equation | 31 |
| 2.3 The collision term at leading order | 33 |
| 2.3.1 The model | 33 |
| 2.3.2 The collision term at LO | 35 |
| 2.4 Boltzmann equation beyond the leading order | 39 |
| 2.4.1 Naïve approach and arising questions | 40 |
| 2.4.2 NLO collision term at finite temperature | 42 |
| 2.5 The collision term at next-to-leading order | 43 |
| 2.5.1 Calculation of an example diagram | 44 |
| 2.5.2 Calculation with scattering methods | 47 |
| 2.5.3 The results | 54 |
| 3 Effective theory approach to thermal corrections | 65 |
| 3.1 The Heavy Particle Effective Theory | 65 |

| | | |
|----------|---|------------|
| 3.1.1 | The HPET Lagrangian up to $\mathcal{O}(1/M)$ | 66 |
| 3.1.2 | The reparametrization invariance | 69 |
| 3.1.3 | Calculation of the matrix elements | 70 |
| 3.2 | The charged particle decay in HPET | 72 |
| 3.3 | Thermal corrections to $\langle\sigma_{\text{ann}}v\rangle$ within HPET | 75 |
| 3.3.1 | First step: integrate out the heavy scalar at the amplitude level | 76 |
| 3.3.2 | Second step: cross section | 81 |
| 4 | Relic density of neutralino dark matter in the MSSM | 93 |
| 4.1 | Introduction and motivation | 94 |
| 4.2 | The R -conserving phenomenological-MSSM | 95 |
| 4.2.1 | The neutralino and chargino sector | 99 |
| 4.3 | The Sommerfeld enhancement | 103 |
| 4.3.1 | The Sommerfeld enhancement in quantum mechanics | 104 |
| 4.3.2 | The Sommerfeld enhancement in quantum field theory | 109 |
| 4.3.3 | EFT treatment, co-annihilations and higher orders | 115 |
| 4.3.4 | The neutralino/sfermion co-annihilation in the pMSSM | 125 |
| 4.4 | The procedure in our code | 130 |
| 4.4.1 | General framework and limitations | 130 |
| 4.4.2 | Generation of a parameter card from the parameters | 132 |
| 4.4.3 | Calculation of mass splittings and running couplings | 132 |
| 4.4.4 | Calculation of the annihilation matrices | 134 |
| 4.4.5 | Calculation of the Sommerfeld factors | 135 |
| 4.4.6 | Thermal average and solution of the Boltzmann equation | 137 |
| 4.5 | Results of our analysis for wino-like dark matter | 138 |
| 4.5.1 | Scan strategy and constraints | 139 |
| 4.5.2 | Results | 144 |
| | Conclusions | 163 |
| A | Matching of the decay width at NLO in the HPET | 165 |
| A.1 | Operator expansion in HPET | 165 |
| A.2 | Next-to-leading order matching | 166 |
| B | Wilson coefficients for neutralino/sfermion co-annihilation | 169 |
| B.1 | Decomposition into coupling and kinematics factors | 169 |
| B.2 | Notation for the kinematic factors in the electronic supplement | 172 |
| C | Improved non-relativistic expansion of s-channel propagators | 179 |

Introduction

One of the most compelling among the open questions in physics concerns the nature of dark matter (DM), a component of our Universe whose existence has been established by observations at astrophysical and cosmological scales.

The first evidence for the existence of some “missing mass” has been discovered in the 1930’s by Zwicky, studying the velocity dispersion of galaxies in the Coma Cluster [1, 2]. The amount of ordinary matter in a cluster, mainly consisting of intergalactic gas, can be estimated by telescopic measurements and within Newtonian Gravitation it determines the predicted motion of the galaxies. What Zwicky observed is that a lot more mass than the estimated one had to be present in the cluster in order to reproduce the measured velocity dispersion. More evidences were found by Rubin in the 1970’s, applying the same argument on a smaller scale to the rotational velocities of stars in disk galaxies [3–6]. More recently those evidences have been confirmed by several weak [7] and strong [8] gravitational lensing measurements, in particular the observation of the Bullet Cluster in 2004, which provided the first “direct empirical proof of the existence of DM” [9]. The Bullet Cluster is a system of two galaxy clusters observed shortly (on cosmological scales) after their collision, see Fig. 1. While the ordinary matter (hot gas observed in X-rays) is concentrated at the center of the system as a result of the interaction among the particles, the total mass (inferred by weak lensing) is distributed around two centers moving apart from each other. This shows that most of the matter constituting the clusters is unseen and at most weakly self-interacting. All those evidences are of gravitational origin and, within General Relativity, they suggest the existence in the Universe of an additional component described by the equation of state of matter, which has been named “dark matter”.

The currently most accurate determination of the abundance of DM in the Universe is somewhat indirect, coming from global fits of the parameters in the standard cosmological model (Λ CDM) to a variety of observations. Combining the measurements of the cosmic microwave background (CMB) power spectrum with high resolution CMB data from the Atacama Cosmology Telescope (ACT) and the South Pole Telescope (SPT), and data from four different galaxy redshift surveys on the baryon acoustic oscillation (BAO), the *Planck* collaboration obtained [10]

$$\Omega_{\text{DM}}h^2 = 0.1188(10) , \tag{1}$$

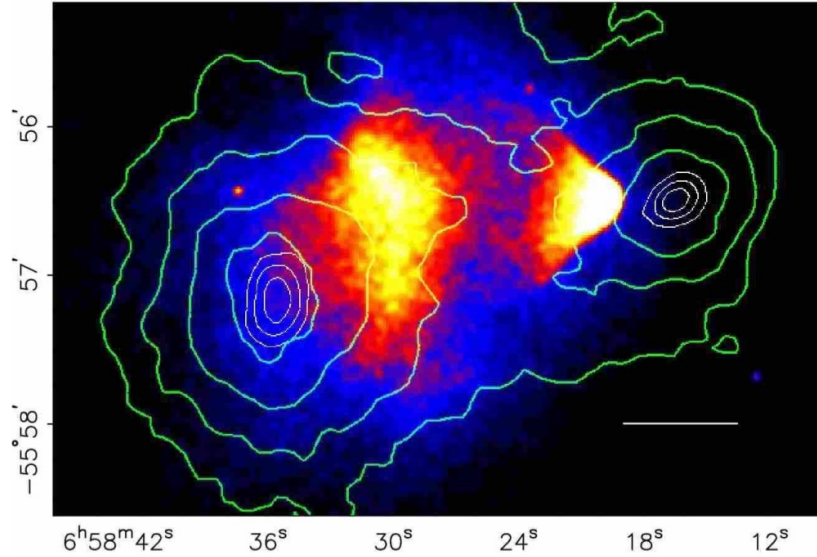


Figure 1: The Chandra X-ray image of the hot intergalactic gas in the Bullet Cluster, from [9]. The overlaid green contours tracking the total mass distribution are the weak lensing κ reconstruction with the outer contour level at $\kappa = 0.16$ and increasing in steps of 0.07. The white bar indicates 200 kpc at the distance of the cluster.

where $h = 0.6780(77)$ is the Hubble constant in units of 100 km/s Mpc , giving the present expansion rate of the Universe. The DM, being five times more abundant than ordinary baryonic matter [10]

$$\Omega_{\text{b}} h^2 = 0.02230(14) , \quad (2)$$

is the dominant component of all the structures ranging from galaxies (spheroidal “dark halo”) to groups, clusters and superclusters (filaments, walls and voids).

The search for DM has been a growing interest for many years now, and a lot of effort has been devoted to it both on the experimental and observational side, with direct and indirect detection experiments and searches at the particle colliders, and on the theory and phenomenology side, involving cosmology, astrophysics and particle physics. For a recent review on the searching strategies and the most studied theoretical frameworks see e.g. [11].

Since so far only its gravitational effects have been measured, it might be possible to explain the observations without introducing a matter component, but through a modification of the law of gravity itself. Attempts in this direction have been done, such as the “Modified Newtonian Dynamics” (MOND) [12], and its covariant version, the “Tensor-Vector-Scalar” (TeVeS) [13], but at present they are not able to reproduce the observations, in particular the Bullet Cluster, without the introduction of some DM component [14].

Within the known elementary particles of the Standard Model (SM) only neutrinos, being stable and electrically neutral, contribute to DM. They cannot however account for the observed abundance Ω_{DM} , since they are not “cold”.¹ Interesting candidates for DM might still arise within the SM, such as the “Primordial Black Holes” (PBH) [15], or more exotic “Macroscopic DM” [16], but they are severely constrained.

The by far most studied class of models is the particle DM, consisting in the introduction of one or more new particle species beyond the Standard Model (BSM). The experimental observations only constrain a few properties of an hypothetical particle DM, leaving many possibilities open for models of BSM physics. The first obvious requirement, that simply follows from the existence of a DM component at present time, is that it has to be stable or with a lifetime larger than the age of the Universe. Secondly, as the name suggests, the main property of DM is to be dark, meaning that it has not been observed to interact with light. This implies that the electromagnetic coupling of a DM particle must be very small, unless its mass is very large [17]. Possible interactions or self-interactions within a “dark sector” (a set of additional BSM particle species, weakly or not at all interacting with the SM species) are partially constrained. The extended shape of the dark halos requires the bulk of DM to be dissipationless, even though a certain 5-10% fraction could be dissipative and even form a “Dark Disc” [18]. The upper limit on self-interaction comes from the Bullet Cluster but it is still very large $\sigma_{\text{self}}/m \sim 2 \times 10^{-24} \text{ cm}^2/\text{GeV}$. The mass of the main DM component is in general only constrained within 80 orders of magnitude, an upper bound of $2 \times 10^{48} \text{ GeV}$ coming from unsuccessful searches for “Massive Astrophysical Compact Halo Objects” (MACHOS) [19], and a lower one less well determined, but at least as low as 10^{-31} GeV , the mass of the “Fuzzy DM” candidate [20]. Beside satisfying those properties, a good candidate for DM must be provided with a production mechanism, able to account for the observed abundance. Different mechanisms have been explored, both within the standard cosmology picture, and introducing ad-hoc cosmological modifications. The latter possibility is largely unconstrained, since we have no experimental observations on the period of the thermal history of the Universe preceding $T \sim 4 \text{ MeV}$, the lowest possible reheating temperature [21]. For a recent and comprehensive review on DM production mechanisms see [22].

In this thesis we will focus on the “freeze-out” scenario, in which DM is thermally produced in the early Universe [23–25]. This scenario, applicable to a large class of particle DM models, is by far the most studied, and arguably the most natural, among the DM production mechanisms. According to this paradigm the observed amount of DM is the relic density of one or more new particle species that were produced in the early Universe, when the large interaction rates were keeping them in thermal equilibrium with the background plasma of SM particles. As a result

¹The classification of DM into hot, warm and cold refers to how relativistic it is when galactic size perturbations enter into the horizon, around $T \sim \text{keV}$. Hot dark matter (HDM) is relativistic, cold dark matter (CDM) is non-relativistic and warm dark matter (WDM) is becoming non-relativistic at this moment. In the ΛCDM cosmological model the bulk of DM must be cold (or possibly warm) in order to reproduce the correct formation of galactic structures.

of the expansion of the Universe the interaction rates decrease and ultimately the annihilation of the new particles “freezes-out”, leading to their decoupling from the background plasma. In the subsequent period and until the present day, the amount of DM particles per comoving volume remains approximately constant. Quantitative results in this framework are obtained by describing the early Universe as a plasma in kinetic theory, such that the relic abundance Ω_{DM} is determined by the present value of the number density n_χ of the DM species, obtained by solving a Boltzmann equation. This framework is rather general and the details of the considered particle model enter the main formula for the calculation of n_χ through the cross section (times velocity) $\sigma_{\text{ann}}v$ for the process responsible of DM annihilation into SM particles. The standard approach is semi-classical, since it combines the usual Boltzmann equation with cross sections computed in quantum field theory (QFT) [23–25].

The uncertainty on the experimental value (1) is already at the percent level, such that an accurate theoretical prediction of Ω_{DM} can be useful to provide strong constraints on BSM scenarios. In the freeze-out framework, the bottleneck in precision when computing Ω_{DM} is presently given by the cross section $\sigma_{\text{ann}}v$, which is usually computed at the leading order (LO) in perturbation theory. In this thesis we studied the problem of radiative corrections to $\sigma_{\text{ann}}v$ in the freeze-out scenario, focusing in particular on two issues, one more formal and one on the phenomenology side.

The formal aspect that we studied concerns the consistent and general framework for including radiative corrections in relic density calculations. In the past few years the standard tools for particle physics calculations, based on the “in-out formalism” for the scattering of particles in vacuum (zero-temperature) have been applied to the DM context to consider radiative corrections to the LO cross section [26–33]. A naïve generalization of the standard semi-classical approach obtained by including next-to-leading order (NLO) corrections to $\sigma_{\text{ann}}v$ is however conceptually problematic, since it ignores the finite-temperature infrared divergences from soft and collinear radiation and virtual effects. In [34] we addressed this problem and introduced a framework to extend consistently the semi-classical approach to higher order in perturbation theory. Within the closed time-path (CTP) approach to non-equilibrium QFT the Boltzmann equation can be derived from first principles under suitable assumptions. Compared to the naïve approach based on zero-temperature calculations, a new class of corrections is found, resulting from the soft interactions of the annihilating DM particles with the background plasma. As we discuss in [35], these corrections are most easily computed within an effective theory approach that closely resembles the heavy quark effective theory (HQET) used to address non-perturbative corrections in QCD.

On the phenomenology side we focused on the minimal supersymmetric extension of the standard model (R -conserving MSSM) [36], in which the lightest supersymmetric particle (LSP) is stable and electrically neutral, thus being a natural candidate for thermally produced DM. In a wide and phenomenologically rich and interesting portion of the MSSM parameter space, the annihilation cross section receives large radiative corrections from a non-perturbative effect called Sommerfeld enhancement [37–43]. Based on the suitable effective field theory framework

developed in [44–46], we wrote a computer program to compute the Sommerfeld enhanced relic abundance of neutralino DM in the general MSSM, and used it as a first application to explore in detail the parameter space in heavy wino-like scenarios [47]. The results of our analysis in the general MSSM exhibit a richer phenomenology compared to previous studies limited to simplified scenarios. We identify interesting regions in the parameters, and in particular in the neutralino mass, in which models reproduce the abundance (1) and at the same time have strong signatures for indirect detection experiments in the near future.

The thesis is organised as follows. We start in Chapter 1 with a short description of the freeze-out framework in the standard cosmological background. No new results are presented here, but several concepts that will be important in the rest of the work are defined, and many useful references are given. The standard results are rederived in Chapter 2 within a non-equilibrium QFT approach, which is then used to obtain a consistent extension of the relic density calculations to NLO in perturbation theory, as introduced for the first time in our paper [34]. The main features of this formalism are investigated within a realistic “MSSM inspired” toy model for DM, by explicit calculation of the leading correction to $\sigma_{\text{ann}}v$ from the interaction with the background SM plasma. In Chapter 3 we show that soft thermal corrections can in general be computed most easily within an heavy particle effective field theory approach (HPET), which also provides physical interpretation for certain contributions [35]. We show explicitly how to reproduce within this framework the results for $\sigma_{\text{ann}}v$ from the previous Chapter, and we further consider the decay rate of a charged particle in a photon bath. The phenomenological analysis of the heavy wino-like DM in the MSSM that we presented in [47] is the topic of Chapter 4. Additionally, we provide here a pedagogical review of the effective field theory approach to the calculation of Sommerfeld enhanced annihilation rates. As an illustrative example we consider the case of neutralino/sfermion co-annihilation, for which we collect the complete results in the Appendix B.

Chapter 1

Dark matter relic density in the freeze-out scenario

In this Chapter we review the basic ingredients for the calculation of the present day abundance of dark matter Ω_{DM} in the cold dark matter (CDM) freeze-out scenario, the most widely studied and arguably most natural of the DM production mechanisms.

In the first Section we briefly review the standard cosmological model that describes the early Universe, in which DM was produced. We then describe qualitatively the mechanism of thermal freeze-out in Sec. 1.2 and show with simple arguments and order-of-magnitude estimates why it is considered a natural candidate for DM production in Sec. 1.3. We conclude in Sec. 1.4 with the standard calculation of Ω_{DM} , which is based on the solution of a semi-classical Boltzmann equation.

For the presentation contained in this Chapter we mainly follow the original paper from Gondolo and Gelmini [25]. A more exhaustive treatment of basic topics can be found in the books from Kolb and Turner [23] and Dodelson [24]. The interested reader may also find useful the recent reviews [22, 48, 49], from which we took many comments and observations.

1.1 Standard Cosmology

In the fundamental picture of the Big Bang scenario, the Universe is described as a system expanding adiabatically from a hot and dense initial state existing around 10^{10} years ago. At early times all the standard model (SM) particles, and possibly some still undiscovered ones, were forming a thermal plasma, in which all the processes allowed by the fundamental particle theory were happening at high rates, keeping all the species in both chemical and kinetic equilibrium.

The most stringent constraints to the Big Bang theory are currently provided by the nucleosynthesis (BBN), the fusion of protons and neutrons into light elements (D, ^3He , ^4He and

${}^7\text{Li}$). Occurring around 200s after the Big Bang, at $T \sim 0.8\text{ MeV}$, the BBN is the earliest episode in thermal history of the Universe of which we have trace.¹ The calculation within the standard models of cosmology and elementary particles reproduces with very good accuracy the observed primordial abundances of the light elements,² thus providing strong constraints on the subsequent history of the Universe. Concerning the period preceding the BBN, the only constraint on possible new physics is the reheating temperature, namely the highest temperature in the radiation dominated period, being larger than 4 MeV [21]. This constraint requires that any additional particle beyond the SM, that was in thermal equilibrium with the photon background, must have been non-relativistic at the time of BBN. This sets a lower bound of $\sim 1.3\text{ MeV}$ on the mass of such particles.

Under the assumptions of homogeneity and isotropy, the Universe is described by the Friedmann-Robertson-Walker (FRW) metric³

$$ds^2 = dt^2 - a^2(t) \left[\frac{dr^2}{1 - kr^2} + r^2 d\Omega^2 \right], \quad (1.1)$$

where k is a constant describing the spatial curvature that can assume the values $k = -1, 0, 1$, corresponding to open (hyperbolic), flat (Euclidean) and closed (spherical) geometry, respectively. The dynamics is encoded in the scale factor $a(t)$, obtained by solving the Friedmann equation

$$\left(\frac{\dot{a}}{a} \right)^2 + \frac{k}{a^2} = \frac{8\pi G_N}{3} \rho, \quad (1.2)$$

where the dot denotes a time derivative, $G_N = 6.70837(80) \times 10^{-39} \text{ GeV}^{-2}$ is the Newton's constant [51] and ρ the total average energy density. The expansion is encoded in the Hubble rate

$$H(t) \equiv \frac{\dot{a}(t)}{a(t)}, \quad (1.3)$$

whose present value⁴ is $H_0 = 100 h \text{ km/s}_{\text{Mpc}}$, with $h = 0.6780(77)$ [52]. The Universe proves to be flat to a very good approximation [52], so we will set $k = 0$ in the following. The present day total energy density is then close to the critical value [51]

$$\rho_0 \simeq \rho_{\text{crit}} \equiv \frac{3H_0^2}{8\pi G_N} = 1.05375(13) \times 10^{-5} h^2 \frac{\text{GeV}}{\text{cm}^3}. \quad (1.4)$$

The Friedmann equation (1.2) is one component of the Einstein equation for the FRW metric (1.1) and it has to be accompanied by the equation of state, specifying the physical properties

¹The standard time unit for the history of the Universe is the temperature T of the photons.

²There is indeed a discrepancy between the observation and prediction of the ${}^7\text{Li}$ abundance, known as the ‘‘lithium problem’’, see [50].

³We adopt natural units, $c = \hbar = k_B = 1$.

⁴Following the standard convention we denote with a subscript ‘‘0’’ the present value of time dependent quantities. Recall that by definition $a_0 = 1$.

of the matter and energy content of the Universe. Non-relativistic matter, radiation and dark energy (cosmological constant) contribute differently to ρ , leading to different solutions for the scale factor $a(t)$. In general we can write

$$\rho = \frac{\pi^2}{30} g_{\text{eff}}(T) T^4, \quad (1.5)$$

where g_{eff} counts the effective number of relativistic degrees of freedom for the energy density and is described in detail in [25]. The Hubble rate is then given by

$$H = \sqrt{\frac{\pi^2}{90} g_{\text{eff}}(T)} \frac{T^2}{M_P}, \quad (1.6)$$

where $M_P \equiv 1/\sqrt{8\pi G_N}$ is the Planck mass.

In the following we will be interested in the radiation dominated epoch ($T \gtrsim 1$ eV), in which case the equation of state for the energy density reads

$$\rho_{\text{rad}} = \rho_{\text{crit}} a^{-4}, \quad (1.7)$$

from which we can write, under the approximation $\rho \simeq \rho_{\text{rad}}$,

$$a(T) \simeq \sqrt{\frac{H_0}{H(T)}} = \left(\frac{g_{\text{eff}}(T_0)}{g_{\text{eff}}(T)} \right)^{\frac{1}{4}} \frac{T_0}{T}. \quad (1.8)$$

The above equation gives the parametrization of the scale factor in terms of the temperature T , and will be useful in the following to study the evolution of the DM density during the Universe expansion.

1.2 The freeze-out scenario

As already mentioned, the early Universe can be described as a hot and dense state, in which all the existing particle species are efficiently kept in thermal equilibrium by large interaction rates.⁵ As long as the temperature and pressure of the plasma are not too large, this state can be approximately described within a semi-classical formulation of kinetic theory. In this Section we will follow this standard approach to describe the main features of the freeze-out scenario and to show how it provides a natural mechanism for dark matter production. Later on in Chapter 2 we will study the validity of the obtained results by rederiving them from first principles, following a consistent procedure in quantum field theory at finite temperature.

In kinetic theory each particle species is described by its distribution function $f(p, x)$, which gives the number of particles in a given phase-space region around momentum p and position

⁵The interaction rate for a certain process is inversely proportional to the average time between two successive interactions.

x. Note that, even though we do not write it explicitly, the distribution function depends in general also on the internal (spin) degrees of freedom of the corresponding particle. In the homogeneous and isotropic FRW Universe the distribution functions can only depend on the energy $\omega \equiv \sqrt{m^2 + \vec{p}^2}$ and on time. In the following we will only be interested in the number density, defined by integrating the distribution function over the momentum and summing over the spin

$$n(t) = \int dn(t) \equiv \int \frac{d^3\vec{p}}{(2\pi)^3} \sum_{\text{spin}} f(\omega, t) . \quad (1.9)$$

The transport equation that governs the distribution functions for a closed subset of interacting species is a set of coupled Boltzmann equations, in which the collision term encodes all the possible interactions. We will study the integrated Boltzmann equation for the number density in Sec. 1.4, while now we limit ourselves to a qualitative description of the expected solution.

As the universe expands and cools down, all the particle number densities must decrease by dilution, and so do the reaction rates for any process, being proportional to the number densities of the interacting species. When the corresponding rate $\Gamma_{i \rightarrow f}$ drops below the expansion rate H , the given reaction $i \rightarrow f$ essentially stops occurring. Eventually all the reactions that involve creation or destruction of a given particle species must drop below H . From this time on that particle is no longer kept in chemical equilibrium with the background plasma, and its number density $n(t)$ is only affected by the dilution due to the Universe expansion: it “freezes-out”.

It is useful to define the yield of a certain species $Y(t)$, as its number density divided by the entropy density of the Universe

$$Y(t) \equiv \frac{n(t)}{s(t)} , \quad (1.10)$$

where in analogy with (1.5), we write the entropy density by introducing an effective number of relativistic degrees of freedom h_{eff}

$$s = \frac{2\pi^2}{45} h_{\text{eff}}(T) T^3 . \quad (1.11)$$

As long as each species contributing to the total energy and entropy is in equilibrium and can be considered as an ideal gas, there is no entropy production and the entropy density is conserved in a comoving volume⁶

$$s(t) = s_0 a^{-3}(t) , \quad (1.12)$$

with $s_0 = 2777.5 \text{ cm}^{-3}$ the entropy density today.⁷ In an iso-entropic Universe the yield has the meaning of a comoving number density, and after the freeze-out it remains constant. The

⁶An example of known situation in which the entropy density is not conserved is the QCD quark-hadron phase transition, occurred at $T \sim 150 - 400 \text{ MeV}$.

⁷The numerical value is obtained from (1.11) with the CMB temperature $T_0 = 2.7255 \text{ K} = 2.34865 \times 10^{-13} \text{ GeV}$ [51] and $h_{\text{eff}}(T_0) = 3.91$, corresponding to photons and three species of neutrinos.

thermal decoupling scenario provides a natural explanation for the observed DM density in terms of the relic abundance of a frozen-out species χ

$$\begin{aligned}\Omega_{\text{DM}} &\equiv \frac{\rho_\chi(t_0)}{\rho_{\text{crit}}} \\ &= \frac{m_\chi n_\chi(t_0)}{\rho_{\text{crit}}} \\ &= \frac{m_\chi}{\rho_{\text{crit}}} Y_\chi(t_0) s_0 .\end{aligned}\tag{1.13}$$

The temperature at which the freeze-out occurs, as well as the equation to determine $Y_\chi(t_0)$, depends on the DM particle mass and on its interactions. We will discuss this in detail in Sec. 1.4. The number-changing interaction that freezes-out can be the decay or, for stable particles, the annihilation. The freeze-out may occur when the DM is still in the relativistic regime, or when it is already in the non-relativistic one. Those two scenarios are called hot (HDM) and cold dark matter (CDM) respectively. The intermediate (warm) situation has also been considered (WDM). A description of many of the most studied DM candidates, also not relying on the thermal production mechanism described here, can be found in [48] and references therein.

1.3 The cold dark matter case: WIMP miracle

The most widely studied realisation of the freeze-out scenario, and the one that we will consider here, is the CDM one. Before studying in detail the semi-classical Boltzmann equation for this scenario in the next Section, we review here the principal properties, mainly following [49]. In order to capture the main features without too many technical complications, we will rely here on order-of-magnitude estimates only, leaving the precise formulation to the next Section.

Consider a neutral and stable particle χ that can undergo a certain annihilation process $\chi\bar{\chi} \rightarrow X$. Assume that the chemical potential vanishes, and therefore the particle χ and its antiparticle $\bar{\chi}$ have the same number density $n_\chi = n_{\bar{\chi}}$. The annihilation rate is given by

$$\Gamma_{\text{ann}} = n_\chi \sigma_{\text{ann}} ,\tag{1.14}$$

where σ_{ann} is the corresponding cross section.

As discussed in the previous Section, before the freeze-out the DM particle is in thermal equilibrium with the photon background and the other SM particles coupled to it. In thermal equilibrium the solution to the integrated Boltzmann equation for the number density of a non-relativistic species is approximately given by the Maxwell-Boltzmann distribution

$$n^{\text{eq}} \simeq g \left(\frac{mT}{2\pi} \right)^{\frac{3}{2}} e^{-\frac{m}{T}} ,\tag{1.15}$$

where g denotes the number of internal (spin) degrees of freedom of the considered particle, and we assumed that the system is “unpolarized” with respect to the internal degrees of freedom.

The time at which the annihilation freezes-out can be approximately estimated by requiring $\Gamma_{\text{ann}} \sim H$. Introducing $x \equiv m_\chi/T$ and neglecting $\mathcal{O}(1)$ prefactors⁸ we get

$$\begin{aligned} \Gamma_{\text{ann}}(T_{\text{f.o.}}) &\sim H(T_{\text{f.o.}}) \\ n_\chi(T_{\text{f.o.}}) &\sim \frac{T_{\text{f.o.}}^2}{M_p \sigma_{\text{ann}}} \\ \sqrt{x_{\text{f.o.}}} e^{-x_{\text{f.o.}}} &\sim \frac{1}{m_\chi M_p \sigma_{\text{ann}}} \end{aligned} \quad (1.16)$$

where the subscript “f.o.” denotes quantities evaluated at the freeze-out time. We note that, if the interaction of the relic is at the weak scale $\sigma_{\text{ann}} \sim G_F^2 m_\chi^2$ and $m_\chi \sim 100$ GeV, then the right hand side (r.h.s) of the above equation is around 10^{-15} . Moreover for r.h.s. in the range $\{10^{-10}, 10^{-20}\}$ one gets for $x_{\text{f.o.}}$ the range $\{20, 50\}$. In consistency with our assumptions we obtain that the freeze-out occurs when χ is in the non-relativistic regime: for the typical value $x_{\text{f.o.}} \sim 20$ the relative velocity of the two annihilating particles is $v_{\text{f.o.}} \sim 0.3$. Moreover we note that for any relevant value of m_χ , the freeze-out always occurs in the radiation dominated epoch.

Under the assumption of entropy conservation $Y(t_0) = Y_{\text{f.o.}}$ and we can write (1.13) as

$$\begin{aligned} \Omega_{\text{DM}} &= \frac{m_\chi}{\rho_{\text{crit}}} n_\chi(t_{\text{f.o.}}) \frac{s_0}{s_{\text{f.o.}}} \\ &\sim \frac{m_\chi}{\rho_{\text{crit}}} n_\chi(t_{\text{f.o.}}) \frac{T_0^3}{T_{\text{f.o.}}^3} \end{aligned} \quad (1.17)$$

where in the second line we used entropy conservation (1.12), the scale factor in radiation domination epoch (1.8), and we dropped the factor $\left(\frac{g_{\text{eff}}(T_0)}{g_{\text{eff}}(T_{\text{f.o.}})}\right)^{\frac{3}{4}} \sim \mathcal{O}(1)$. Replace now the second line of (1.16) to get

$$\begin{aligned} \Omega_{\text{DM}} &\sim \left(\frac{T_0^3}{\rho_{\text{crit}} M_p}\right) \frac{x_{\text{f.o.}}}{\sigma_{\text{ann}}} \\ \left(\frac{\Omega_{\text{DM}}}{0.2}\right) &\sim \frac{x_{\text{f.o.}}}{20} \left(\frac{10^{-8} \text{ GeV}^{-2}}{\sigma_{\text{ann}}}\right) \end{aligned} \quad (1.18)$$

where in the second line we replaced the numerical values. The result (1.18) is named “WIMP miracle”: a weakly interacting massive particle is a natural candidate for DM since it has the correct observed relic density.

⁸Note that we can safely drop $\sqrt{g_{\text{eff}}(T)}$ in the expression (1.6) for the Hubble rate since it varies approximately in the range $\{1, 0.2\}$ for $T \sim \{10^{-2}, 10^5\}$ MeV, see [25].

We conclude this Section with a comment on the nature of the miracle. Even though the relation $\sigma_{\text{ew}} \simeq G_F^2 T_{\text{f.o.}}^2 \simeq 10^{-8} \text{ GeV}^{-2}$ indicates the electroweak scale as a “natural” place for the miracle to occur, thermal freeze-out giving the observed relic abundance has indeed a broader range of validity. An approximate upper limit for m_χ in the CDM picture can be estimated by considering the unitarity limit in the partial wave expansion [53]. Assuming that only the lowest partial wave contributes, unitarity implies that the cross section can be written as

$$\sigma_{\text{ann}} \sim \frac{g^4}{m_\chi^2}, \quad (1.19)$$

where g is a coupling constant and perturbativity requires $g^2 \lesssim \sqrt{4\pi}$. Inserting this condition in (1.18) and requiring $\Omega_{\text{DM}} \lesssim 0.2$ one gets the upper bound $m_\chi \lesssim 120 \text{ TeV}$. An approximate lower limit can instead be estimated simply by replacing the electroweak cross section $\sigma_{\text{ann}} \sim G_F^2 m_\chi^2$ in (1.18). The result $m_\chi \gtrsim 10 \text{ GeV}$ is the Lee-Weinberg limit [54]. Note that in most of the proposed models the annihilation cross section depends on the DM mass in a more complicated way than the simple ones assumed above, therefore the above limits have to be taken just as eyeballing values.

1.4 The Boltzmann equation

In the previous Section we described the general features of the freeze-out framework by introducing approximate expressions and order-of-magnitude estimates. In this Section we will work out the detailed calculation of the present day comoving number density $Y_\chi(t_0)$ for a single WIMP species χ , by following the usual semi-classical approach of solving the Boltzmann equation [25].

The distribution function f of a certain species is governed in kinetic theory by the Boltzmann equation

$$L[f] = C[f], \quad (1.20)$$

where L is the Liouville operator, giving the net rate of change in time of f , and C is the collision operator, representing the number of particles per phase-space volume that are lost or gained per unit time under collision with other particles. Note that, whenever different species interact among each other, the collision term connects the corresponding Boltzmann equations in a coupled set.

The meaning of the Liouville operator is more explicit in its non-relativistic form

$$L_{\text{NR}} = \frac{\partial}{\partial t} + \frac{d\vec{x}}{dt} \cdot \frac{\partial}{\partial \vec{x}} + \frac{d\vec{v}}{dt} \cdot \frac{\partial}{\partial \vec{v}}. \quad (1.21)$$

The covariant form is given by

$$L = p^\mu \frac{\partial}{\partial x^\mu} - \Gamma^\mu_{\nu\rho} p^\nu p^\rho \frac{\partial}{\partial p^\mu}$$

$$= \omega \frac{\partial}{\partial t} - H |\vec{p}|^2 \frac{\partial}{\partial \omega}, \quad (1.22)$$

where $\Gamma^\mu_{\nu\rho}$ is the Christoffel symbol of the background metric and the second line holds in the homogeneous and isotropic FRW Universe (1.1). Since we are interested in number densities, rather than distribution functions, we define the integrated Liouville operator

$$\begin{aligned} L[n] &\equiv \int \frac{d^3\vec{p}}{(2\pi)^3} \sum_{\text{spin}} \frac{L[f]}{\omega} \\ &= \frac{dn}{dt} + 3H n \\ &= s \frac{dY}{dt}, \end{aligned} \quad (1.23)$$

where the second term in the second line, obtained via integration by parts, represents the dilution due to the expansion of the Universe and we can absorb it in the definition of the yield (1.10) under the assumption of no entropy production (1.12). It is customary to parametrize the time with $x \equiv m/T$ and write

$$\begin{aligned} L[n] &= s \frac{dY}{dx} \frac{dx}{ds} \frac{ds}{da} \frac{da}{dt} \\ &= s \frac{dY}{dx} \frac{dx}{ds} \left(-3\frac{s}{a}\right) (aH) \\ &= s^2 \left(-3H \frac{dx}{ds}\right) \frac{dY}{dx}, \end{aligned} \quad (1.24)$$

where in the second line we used again the entropy conservation (1.12) and the term in brackets in the last line can be computed from (1.6) and (1.11)

$$-\frac{1}{3H} \frac{ds}{dx} = \left(\frac{45}{\pi} G_N\right)^{-\frac{1}{2}} \sqrt{g_*} \frac{m}{x^2}, \quad (1.25)$$

where to parametrize the content of the Universe we use the degrees of freedom parameter g_* introduced in [25]

$$\sqrt{g_*} = \frac{h_{\text{eff}}}{\sqrt{g_{\text{eff}}}} \left(1 + \frac{1}{3} \frac{T}{h_{\text{eff}}} \frac{dh_{\text{eff}}}{dT}\right). \quad (1.26)$$

The r.h.s. of the Boltzmann equation (1.20), integrated over the momenta and summed over the spin is

$$C[n] \equiv \int \frac{d^3\vec{p}}{(2\pi)^3} \sum_{\text{spin}} \frac{C[f]}{\omega}. \quad (1.27)$$

The form of the collision term depends on the relevant processes among the particles present in the plasma. We consider the evolution of the number density of a stable particle species χ ,

that interacts with SM particles via $2 \rightarrow 2$ processes only. The integration over the momentum in (1.27) cancels the contributions from processes that do not modify the number of χ , in particular scattering processes $\chi i \rightarrow \chi j$. Because χ is stable, the only relevant processes are pair annihilations of the form $\chi\bar{\chi} \rightarrow ij$, which contribution reads

$$C[n_\chi] = \int d\Pi_{\chi\bar{\chi}(ij)} \sum_{\text{spin}} \left[|\mathcal{M}_{ij \rightarrow \chi\bar{\chi}}|^2 f_i f_j (1 \pm f_\chi)(1 \pm f_{\bar{\chi}}) - |\mathcal{M}_{\chi\bar{\chi} \rightarrow ij}|^2 f_\chi f_{\bar{\chi}} (1 \pm f_i)(1 \pm f_j) \right], \quad (1.28)$$

where the integration measure is

$$d\Pi_{\chi\bar{\chi}(ij)} \equiv d\Pi_\chi d\Pi_{\bar{\chi}} d\Pi_i d\Pi_j (2\pi)^4 \delta^{(4)}(p_\chi + p_{\bar{\chi}} - p_i - p_j), \quad (1.29)$$

$$d\Pi_X = \frac{d^3\vec{p}_X}{(2\pi)^3 2\omega_X},$$

$|\mathcal{M}_{i \rightarrow f}|^2$ denotes the matrix element squared for the process $i \rightarrow f$, and the sign $+$ ($-$) applies to bosons (fermions) and represents the Bose enhancement (Pauli blocking). Note that in (1.28) the distribution functions of all the involved species ($\chi, \bar{\chi}, i, j$) appear, such that the four corresponding Boltzmann equations form a coupled set.

In order to proceed we consider the following assumptions:

1. CP invariance, resulting in $|\mathcal{M}_{\chi\bar{\chi} \rightarrow ij}|^2 = |\mathcal{M}_{ij \rightarrow \chi\bar{\chi}}|^2 \equiv |\mathcal{M}|^2$;
2. $\omega \gg \mu$, where μ is the chemical potential. This is true for almost all the species at almost all times, and it implies that there is no χ - $\bar{\chi}$ asymmetry, such that $f_{\bar{\chi}} = f_\chi$;⁹
3. $\omega \gg T$, valid since all the energies are at the m_χ scale due to the $2 \rightarrow 2$ kinematics and around the freeze-out $m_\chi \sim 20 T$;
4. the annihilation products i, j are in thermal equilibrium $f_{i,j} = f_{i,j}^{\text{eq}}$, such that in the cosmic comoving frame their distributions are described either by the Bose-Einstein or by the Fermi-Dirac statistics¹⁰

$$f^{\text{eq}}(\omega, t) = \begin{cases} \frac{1}{e^{\frac{\omega-\mu}{T}} - 1} \equiv f_B(\omega) & \text{for bosons ,} \\ \frac{1}{e^{\frac{\omega-\mu}{T}} + 1} \equiv f_F(\omega) & \text{for fermions .} \end{cases} \quad (1.30)$$

⁹We note that the opposite assumption $f_{\bar{\chi}} \neq f_\chi$ is also consistent and is the main ingredient of asymmetric dark matter models (ADM), in which the DM density is due to an asymmetry which is linked to the baryon-antibaryon one. See [55] for a review.

¹⁰Note that, even though we do not write explicitly $f_{B,F}(\omega, t)$, in the considered scenario the equilibrium distributions do have a time dependence through the temperature T .

This is justified since they usually have stronger interactions compared to those with χ , and we can then decouple the Boltzmann equations for $f_{i,j}$ by neglecting f_χ in the collision term. Under the assumptions 2 and 3 the quantum statistical factor ± 1 can be neglected and both the Bose-Einstein and the Fermi-Dirac distributions are well approximated by the Maxwell-Boltzmann one, and are therefore exponentially suppressed

$$f^{\text{eq}}(\omega, t) \simeq e^{-\frac{\omega}{T}} \ll 1 . \quad (1.31)$$

5. χ remains in kinetic equilibrium even after the occurrence of the chemical decoupling. This happens because the kinetic equilibrium is maintained by scattering processes as $\chi i \rightarrow \chi j$, whose rate Γ_{sca} is proportional to the number density of the SM particle i and the scattering cross section σ_{sca} . Typically around the freeze-out $m_i \ll T$ and therefore the particle i is in the relativistic regime and n_i is not exponentially suppressed.¹¹ The annihilation rate Γ_{ann} is instead proportional to the exponentially suppressed density n_χ and to the cross section σ_{ann} . Since they are related by crossing symmetry, the cross sections satisfy $\sigma_{\text{sca}} \sim \sigma_{\text{ann}}$. The different distribution functions leads therefore to $\Gamma_{\text{ann}} \ll \Gamma_{\text{sca}}$, implying that the kinetic decoupling occurs at much lower temperatures than the chemical one. The distributions in kinetic equilibrium are proportional to those in thermal equilibrium, with a proportionality factor independent of momentum, such that we can write

$$f_\chi(\omega, t) = \frac{n_\chi(t)}{n_\chi^{\text{eq}}(t)} f_\chi^{\text{eq}}(\omega, t) . \quad (1.32)$$

This in particular implies that f_χ is also exponentially suppressed;

6. the plasma is “unpolarized” with respect to the internal degrees of freedom, such that the distribution functions are independent on them.

Under the above listed assumptions, and making use of the energy conservation to write

$$f_i f_j = e^{-\frac{\omega_i + \omega_j}{T}} = e^{-\frac{\omega_\chi + \omega_{\bar{\chi}}}{T}} = f_\chi^{\text{eq}} f_{\bar{\chi}}^{\text{eq}} , \quad (1.33)$$

the integrated collision term (1.28) simplifies to

$$C[n_\chi] = \langle \sigma_{\text{ann}} v \rangle (n_\chi^{\text{eq}2} - n_\chi^2) , \quad (1.34)$$

where we introduced the invariant, spin-averaged total annihilation cross section $\sigma_{\text{ann}} \equiv \sigma_{\chi\bar{\chi} \rightarrow ij}$, defined according to

$$\sigma_{ab \rightarrow ij} \equiv \frac{1}{v_{ab}} \frac{1}{4\omega_a \omega_b} \int d\Pi_i d\Pi_j (2\pi)^4 \delta^{(4)}(p_a + p_b - p_i - p_j) |\overline{\mathcal{M}}_{ab \rightarrow ij}|^2 , \quad (1.35)$$

¹¹The characteristic energy scale for scattering process is given by the temperature since the kinematic does not set it to m_χ as for the annihilation and production.

with

$$|\overline{\mathcal{M}}_{ab \rightarrow ij}|^2 \equiv \frac{1}{g_a g_b} \sum_{\text{spin}} |\mathcal{M}_{ab \rightarrow ij}|^2, \quad (1.36)$$

the Møller velocity $v \equiv v_{\chi\bar{\chi}}$, where

$$v_{ab} \equiv \frac{\sqrt{(p_a \cdot p_b)^2 - m_a^2 m_b^2}}{\omega_a \omega_b}, \quad (1.37)$$

and the thermal average

$$\langle \sigma_{\text{ann}} v \rangle \equiv \frac{\int dn_{\chi}^{\text{eq}} dn_{\bar{\chi}}^{\text{eq}} \sigma_{\text{ann}} v}{\int dn_{\chi}^{\text{eq}} dn_{\bar{\chi}}^{\text{eq}}}. \quad (1.38)$$

Before writing down the final form of the Boltzmann equation we make a few observations on the collision term:

- we considered here a single annihilation process $\chi\bar{\chi} \rightarrow ij$. The derivation can be straightforwardly applied to the more general case of several $2 \rightarrow 2$ annihilation channels and the result is simply given by the same expression (1.34) with the identification

$$\sigma_{\text{ann}} \equiv \sum_{i,j} \sigma_{\chi\bar{\chi} \rightarrow ij}, \quad (1.39)$$

with $\sigma_{\chi\bar{\chi} \rightarrow ij}$ defined as in (1.35);

- both σ_{ann} and $v n_{\chi}^2$ are Lorentz invariant quantities;
- in any frame where the two particles a and b move collinearly, the Møller velocity v_{ab} is equal to the relative velocity $v_{\text{rel}} \equiv |\vec{v}_a - \vec{v}_b|$, where $\vec{v}_a \equiv \vec{p}_a/\omega_a$, ecc.;
- the approach we followed is semi-classical, in the sense that the annihilation cross section computed within quantum field theory enters in the usual Boltzmann equation of classical kinetic theory;
- so far we considered a single DM particle species χ annihilating into SM particles. In most of the new physics models, however, there are many more new particles that can interact with each other and be close in mass. If more species χ_a exists, such that $m_a - m_1$ is much smaller than the temperature $T_{\text{f.o.}}$ at which the lightest particle in the set χ_1 freezes-out, then the number densities n_a are not strongly Boltzmann suppressed and the freeze-out processes of the various species are inter-connected. If all the species χ_a are stable or eventually decay in χ_1 , then the DM abundance is obtained by considering the Boltzmann equation for the total number density $n_{\chi} \equiv \sum_{a=1}^N n_a$. In this case the calculation of the

collision term has to be modified by introducing an “effective” cross section, that includes the appropriately Boltzmann-weighted contribution from the co-annihilating particles, as described in [56]

$$\langle \sigma_{\text{ann}} v \rangle \longrightarrow \langle \sigma_{\text{eff}} v \rangle \equiv \sum_{a,b=1}^N \langle \sigma_{ab} v_{ab} \rangle \frac{n_a^{\text{eq}} n_b^{\text{eq}}}{n^{\text{eq}^2}}, \quad (1.40)$$

where the Møller velocity v_{ab} was defined in (1.37) and $\sigma_{ab} \equiv \sum_{i,j} \sigma_{ab \rightarrow ij}$ is the total cross section for the pair-annihilation of the two-particle state ab .¹² The introduction of co-annihilations can either enlarge or reduce the effective cross section, depending on the strength of the interaction of the co-annihilating particles and on their degrees of freedom, see [49] and references therein for a more detailed discussion and some examples;

- the thermally-averaged effective cross section can be written in terms of a single integral, suitable for numerical integration [56]

$$\langle \sigma_{\text{eff}} v \rangle = \frac{\sum_{a,b=1}^N g_a g_b \int_{(m_a+m_b)^2}^{\infty} ds \sigma_{ab} \frac{(p_a \cdot p_b)^2 - m_a^2 m_b^2}{2\sqrt{s}} K_1\left(\frac{\sqrt{s}}{T}\right)}{T \left(\sum_{a=1}^N g_a m_a^2 K_2\left(\frac{m_a}{T}\right) \right)^2}, \quad (1.41)$$

where s is the center-of-mass energy squared and K_n is the modified Bessel function of the 2nd kind, of order n . The numerator is in the form of a convolution of the cross section and a temperature-dependent thermal kernel. Note that heavy co-annihilation channels are suppressed by the Boltzmann weight $e^{m_i+m_j-2m_1}$, which arises from the asymptotic expansion of the Bessel function $K_1(\sqrt{s}/T)$ for large $\sqrt{s}/T > 2m_1/T \gg 1$.

The final form of the semi-classical integrated Boltzmann equation for the comoving number density of pair annihilating DM is finally obtained combining the Liouville term (1.24) with the collision term (1.34)

$$\frac{dY_\chi}{dx} = \left(\frac{45}{\pi} G_N \right)^{-\frac{1}{2}} \sqrt{g_*} \frac{m_\chi}{x^2} \langle \sigma_{\text{eff}} v \rangle (Y_\chi^{\text{eq}^2} - Y_\chi^2). \quad (1.42)$$

The above equation, in which both g_* and $\langle \sigma_{\text{eff}} v \rangle$ depend on x , is in the form of a Riccati equation and must be solved numerically. The integration should range from $x = 0$ to $x = x_0 = m_\chi/T_0$ to obtain the present day abundance (1.13), however it is in practice sufficient to start from $x = 1$, since for smaller x the deviation of Y_χ^2 from its equilibrium value is negligibly small. The use of the Maxwell-Boltzmann distributions to approximate the particle statistics is then justified and amounts to a correction of less than 1%. The boundary condition is then

$$Y_\chi(1) = Y_\chi^{\text{eq}}(1) = \frac{45 g_\chi}{4\pi^4} \frac{x^2 K_2(x)}{h_{\text{eff}}\left(\frac{m_\chi}{x}\right)} \Big|_{x=1}. \quad (1.43)$$

¹²Note that the definition $\langle \sigma_{\text{eff}} v \rangle$ for the r.h.s. of (1.40) is an abuse of notation, since it does not correspond to the thermal average (1.38) of the product σ_{eff} times v . In fact σ_{eff} is not defined at all.

The numerical result from the state-of-the-art calculation [57] of the degrees of freedom parameter $\sqrt{g_*}$ is tabulated and public available (see e.g. [58, 59]). Analytic approximate expressions are also present in the literature [25]. The thermally averaged cross section times velocity for pair annihilations is model dependent and must be computed in quantum field theory.

In this Chapter we reviewed the standard freeze-out scenario for CDM, in which the observed abundance Ω_{DM} (1.13) is given by the thermal relic $Y_\chi(t_0)$ of a stable particle χ , that can be obtained by solving the semi-classical Boltzmann equation (1.42). It is important to keep in mind that the temperature range that is relevant for the integration of the Boltzmann equation (1.42) corresponds in large measure to a time period preceding the BBN, an epoch on which we have no experimental observations. The assumptions that in Sec. 1.4 we introduced and justified in the standard cosmology, may not hold in other cosmological models. Many of the possible non-standard cosmologies that have been proposed in relation with their effect on the DM abundance are reviewed in [22]. Moreover we recall that, even in the standard cosmology, non-thermal production mechanisms may be at work, such as the one in the asymmetric dark matter model (ADM), in which an initial asymmetry $f_\chi \neq f_{\bar{\chi}}$ leads to DM production in a way analogous to the standard baryogenesis.

Chapter 2

The Boltzmann equation from QFT

In the previous Chapter we introduced within a semi-classical approach the Boltzmann equation for annihilating DM, which can be written for the number density as

$$\frac{dn_\chi}{dt} + 3Hn_\chi = C[n_\chi] , \quad (2.1)$$

with collision term given, under the assumption of CP conservation, by

$$\begin{aligned} C[n_\chi] &= \int d\Pi_{\chi\bar{\chi}(ij)} \sum_{\text{spin}} \left[|\mathcal{M}_{ij \rightarrow \chi\bar{\chi}}|^2 \left(f_i f_j (1 \pm f_\chi)(1 \pm f_{\bar{\chi}}) - f_\chi f_{\bar{\chi}} (1 \pm f_i)(1 \pm f_j) \right) \right] \\ &= \langle \sigma_{\text{ann}} v \rangle (n_\chi^{\text{eq}2} - n_\chi^2) , \end{aligned} \quad (2.2)$$

where the integration measure is

$$\begin{aligned} d\Pi_{\chi\bar{\chi}(ij)} &\equiv d\Pi_\chi d\Pi_{\bar{\chi}} d\Pi_i d\Pi_j (2\pi)^4 \delta^{(4)}(p_\chi + p_{\bar{\chi}} - p_i - p_j) , \\ d\Pi_X &= \frac{d^3\vec{p}_X}{(2\pi)^3 2\omega_X} . \end{aligned} \quad (2.3)$$

In this Chapter we present the derivation of the Boltzmann equation (2.1) from first principles within the closed time-path (CTP) approach to non-equilibrium quantum field theory (QFT). This provides a consistent framework to study systematically the perturbative expansion of the collision term beyond the leading order (LO).

In the first Section we briefly introduce the CTP framework, mainly following [60]. We then derive the Boltzmann equation within this framework in Sec. 2.2, and show the equivalence of this result with (2.1) in Sec. 2.3, by explicit computation of the CTP collision term at LO in a realistic DM model. In Sec. 2.4 we argue that in the semi-classical approach the perturbative expansion of $\sigma_{\text{ann}} v$ in (2.2) is not well defined beyond the LO. We conclude in Sec. 2.5 with the presentation of the consistent treatment of the collision term at NLO, firstly introduced in our paper [34].

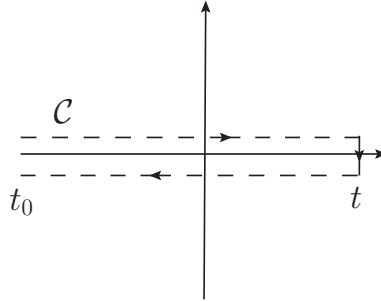


Figure 2.1: The contour \mathcal{C} in the complex time plane. The upper (lower) branch, running forward (backward) in time is called \mathcal{C}_+ (\mathcal{C}_-). The imaginary part of the time variable on the branches \mathcal{C}_\pm is small, such that the vertical segments of the contour can be neglected [64].

2.1 The closed time-path formalism

In this Section we review the derivation within the CTP formalism of the Kadanoff-Baym equation, that encodes the quantum dynamics and will be the starting point for the derivation of the Boltzmann equation in Sec. 2.2. In order to make the physical description more manifest, we also derive here the expressions for the propagators at thermal equilibrium, thus justifying the CTP Feynman rules that we will need in the explicit calculations of Secs. 2.3 and 2.5. Since the DM particle in the model that we will consider in Sec. 2.3 is a fermion, we only present in this Section the equations for the Green function S of a fermionic field ψ . The treatment for the case of a scalar field is analogous, and explicit expressions can be found e.g. in [60].

2.1.1 Introduction

The scattering of elementary particles is described by the “in-out formalism” of QFT, in which the system is assumed to be in a definite “in” state at $t \rightarrow -\infty$ and the interest is on the definite “out” state at $t \rightarrow +\infty$. When the considered system is a plasma of interacting particles, in general out of equilibrium, the “in-out formalism” is however not appropriate, since the interest is on time evolution of expectation values of physical quantities given the initial conditions at some finite time $t = t_0$. In other words, the physical information of the system is contained in ensemble averages of the relevant observables. A theoretical framework for such problems is provided by the Schwinger-Keldysh or closed time-path formalism [61–63], in which the time is defined on a closed path \mathcal{C} on the complex plane that runs from t_0 to t on an upper branch \mathcal{C}_+ (small positive imaginary part) and back on a lower branch \mathcal{C}_- (small negative imaginary part), see Fig. 2.1. The Green functions are defined as in the “in-out formalism” but with the chronological time ordering operator \mathcal{T} replaced by the time ordering $\mathcal{T}_{\mathcal{C}}$ along the contour \mathcal{C} , and the vacuum state $|0\rangle$ replaced by a certain ensemble $|\Omega\rangle$ that describes the physical state

of the system at the time t_0 . For a Dirac fermion field ψ the propagator reads¹

$$iS_{\alpha\beta}(x, y) \equiv \langle \Omega | \mathcal{T}_{\mathcal{C}} \{ \psi_{\alpha}(x) \bar{\psi}_{\beta}(y) \} | \Omega \rangle , \quad (2.4)$$

where we wrote explicitly the fermion indices α, β . The way in which this formalism reproduces the appropriate ensemble average will become more transparent in the following Section, where the case of thermal equilibrium is studied.

In order to perform calculations it is more practical to write quantities in terms of a real time variable. This is done by splitting the contour \mathcal{C} into its two branches \mathcal{C}_{\pm} such as

$$\begin{aligned} \int_{\mathcal{C}} d^4x &\longrightarrow \sum_a \int_{t_0}^t dx^0 \int_{-\infty}^{+\infty} d^3\vec{x} , \\ \delta_{\mathcal{C}}^4(x-y) &\longrightarrow a \delta_{ab} \delta^4(x-y) , \\ iS(x, y) &\longrightarrow iS^{ab}(x, y) , \end{aligned} \quad (2.5)$$

where the labels $a, b = \pm$ denote the branch on which the time argument lies, and additional factors a appear since the lower branch runs backwards in time. The four real-time propagators read

$$\begin{aligned} iS_{\alpha\beta}^{-+}(x, y) &\equiv iS_{\alpha\beta}^{>}(x, y) \equiv \langle \Omega | \psi_{\alpha}(x) \bar{\psi}_{\beta}(y) | \Omega \rangle , \\ iS_{\alpha\beta}^{+-}(x, y) &\equiv iS_{\alpha\beta}^{<}(x, y) \equiv -\langle \Omega | \bar{\psi}_{\beta}(y) \psi_{\alpha}(x) | \Omega \rangle , \\ iS_{\alpha\beta}^{++}(x, y) &\equiv iS_{\alpha\beta}^t(x, y) \equiv \langle \Omega | \mathcal{T} \{ \psi_{\alpha}(x) \bar{\psi}_{\beta}(y) \} | \Omega \rangle , \\ iS_{\alpha\beta}^{--}(x, y) &\equiv iS_{\alpha\beta}^{\bar{t}}(x, y) \equiv \langle \Omega | \bar{\mathcal{T}} \{ \psi_{\alpha}(x) \bar{\psi}_{\beta}(y) \} | \Omega \rangle , \end{aligned} \quad (2.6)$$

where $\mathcal{T} (\bar{\mathcal{T}})$ denotes chronological (anti-chronological) time ordering in real time and the minus sign in $S^{<}$ is due to anticommutation of fermion fields. Note that only two of the four real-time Green functions are independent, since they satisfy the constraint relations

$$S^t(x, y) = \Theta(x^0 - y^0) S^{>}(x, y) + \Theta(y^0 - x^0) S^{<}(x, y) , \quad (2.7)$$

$$S^{\bar{t}}(x, y) = \Theta(x^0 - y^0) S^{<}(x, y) + \Theta(y^0 - x^0) S^{>}(x, y) . \quad (2.8)$$

In order to describe the physical behaviour of the system it is convenient to introduce the retarded and advanced Green functions

$$\begin{aligned} S^r &\equiv S^t - S^{<} , \\ S^a &\equiv S^t - S^{>} , \end{aligned} \quad (2.9)$$

and their hermitian and anti-hermitian parts

$$S^h \equiv \frac{1}{2} (S^a + S^r) , \quad (2.10)$$

¹Recall that the propagator is “ i ” times the Green function.

$$S^A \equiv \frac{1}{2i} (S^a - S^r) = \frac{i}{2} (S^> - S^<) . \quad (2.11)$$

Note that from the definition (2.6) it follows

$$\left(\gamma^0 i S^{\lessgtr}(x, y) \right)^\dagger = \gamma^0 i S^{\lessgtr}(y, x) , \quad (2.12)$$

such that it is actually the combination $\gamma^0 S^h$ that is hermitian. The Green functions S^{\lessgtr} are called Wightman functions and encode the kinetic (statistical) properties of the system, while the anti-hermitian Green function S^A describes the spectral properties and is therefore called spectral function. We will see this explicitly in the next Section.

The Green function is determined by solving the equation of motion derived from the Lagrangian. Let's start from the free Dirac Lagrangian

$$\mathcal{L}_0 = \bar{\psi} (i\cancel{\partial} - m) \psi , \quad (2.13)$$

and the corresponding tree-level action

$$I_0[\psi] = \int_{\mathcal{C}} d^4x \mathcal{L}_0 , \quad (2.14)$$

from which we obtain, by variation with respect to $\bar{\psi}$, the Dirac equation for the field ψ

$$(i\cancel{\partial} - m) \psi = 0 . \quad (2.15)$$

From this equation it follows the corresponding one for the Green function

$$(i\cancel{\partial}_x - m) iS_0(x, y) = i \delta_{\mathcal{C}}^4(x - y) , \quad (2.16)$$

that in real-time components reads

$$(i\cancel{\partial}_x - m) iS_0^{\lessgtr}(x, y) = 0 , \quad (2.17)$$

$$(i\cancel{\partial}_x - m) iS_0^{t,\bar{t}}(x, y) = \pm i \delta^4(x - y) . \quad (2.18)$$

2.1.2 The equilibrium propagators

In order to better understand how the closed time-path approach describes statistical ensembles, we now compute explicitly the real-time Green functions at equilibrium. The first observation is that at equilibrium the system must be homogeneous, such that the Green functions can only depend on the relative coordinate $r \equiv x - y$. We can then define the Fourier space Green function $S_{\text{eq}}(p)$ as

$$iS_{\text{eq}}(x - y) = \int \frac{d^4p}{(2\pi)^4} e^{-ip \cdot (x-y)} iS_{\text{eq}}(p) , \quad (2.19)$$

such that the equations of motion (2.17, 2.18) become

$$(\not{p} - m) iS_{\text{eq}}^{\lessgtr}(p) = 0 , \quad (2.20)$$

$$(\not{p} - m) iS_{\text{eq}}^{t,\bar{t}}(p) = \pm i . \quad (2.21)$$

Multiplying by $(\not{p} + m)$ we can write the following parametrization

$$iS_{\text{eq}}^{\lessgtr}(p) = (2\pi) \delta(p^2 - m^2) G^{\lessgtr}(p) , \quad (2.22)$$

$$iS_{\text{eq}}^{t,\bar{t}}(p) = \pm \frac{i(\not{p} + m)}{p^2 - m^2} + (2\pi) \delta(p^2 - m^2) (\not{p} + m) g^{t,\bar{t}}(p) , \quad (2.23)$$

where $g^{t,\bar{t}}(p)$ are two scalar functions and $G^{\lessgtr}(p)$ are matrices in the spinor space. Note that the parametrization functions $G^{\lessgtr}(p)$ and $g^{t,\bar{t}}(p)$ are not fixed by the equations of motion. The constraint (2.7) in Fourier space reads

$$S_{\text{eq}}^t(p) + S_{\text{eq}}^{\bar{t}}(p) = S_{\text{eq}}^<(p) + S_{\text{eq}}^>(p) , \quad (2.24)$$

and leads to

$$(\not{p} + m) \left(g^t(p) + g^{\bar{t}}(p) \right) = G^<(p) + G^>(p) . \quad (2.25)$$

At equilibrium an additional constraint on the Green function is provided by the Kubo-Martin-Schwinger (KMS) relation [65, 66], a general periodicity property of the thermal correlation function of two time-dependent (Heisenberg) operators

$$\langle \Omega | A(t) B(t') | \Omega \rangle = \langle \Omega | B(t') A(t + i\beta) | \Omega \rangle , \quad (2.26)$$

where β is the inverse of the equilibrium temperature. Applied to the fermion field operators $A B = \psi \bar{\psi}$ and written in momentum space it reads

$$S_{\text{eq}}^>(p) = -e^{\beta p^0} S_{\text{eq}}^<(p) . \quad (2.27)$$

Combining the KMS relation with the constraint (2.25) we can fix the spinor structure of the parametrizing functions $G^{\lessgtr} \equiv (\not{p} + m) g^{\lessgtr}$, since

$$\begin{aligned} (\not{p} + m) \left(g^t(p) + g^{\bar{t}}(p) \right) &= \left(1 - e^{\beta p^0} \right) G^<(p) \\ g^t(p) + g^{\bar{t}}(p) &= \left(1 - e^{\beta p^0} \right) g^<(p) . \end{aligned} \quad (2.28)$$

Additionally, the real-time Green functions must satisfy the spectral sum rule²

$$\int \frac{dp^0}{\pi} \gamma^0 \frac{i}{2} (S_{\text{eq}}^>(p) - S_{\text{eq}}^<(p)) = \mathbb{1}$$

²This constraint follows simply from the equal time anticommutation relation of the spinor field and is valid in general, not just at equilibrium.

$$\int dp^0 \gamma^0 \left(1 + e^{\beta p^0}\right) \delta(p^2 - m^2) (\not{p} + m) g^>(p) = -\mathbb{1} , \quad (2.29)$$

whose solution is

$$g^<(p) = -\varepsilon(p^0) \frac{1}{1 + e^{\beta p^0}} , \quad (2.30)$$

where $\varepsilon(p^0)$ denotes the sign function

$$\varepsilon(p^0) \equiv \Theta(p^0) - \Theta(-p^0) . \quad (2.31)$$

Inserting the above solution into (2.28) we get

$$g^t(p) + g^{\bar{t}}(p) = -\varepsilon(p^0) \frac{1 - e^{\beta p^0}}{1 + e^{\beta p^0}} . \quad (2.32)$$

Taking the second constraint equation (2.8) and substituting in it (2.22) and the solution for $g^>(p)$ that we just found, we get

$$g^t(p) = g^{\bar{t}}(p) . \quad (2.33)$$

Combining the results derived above we can write the equilibrium real-time propagators in momentum space as

$$\begin{aligned} iS_{\text{eq}}^>(p) &= -2\pi (\not{p} + m) \delta(p^2 - m^2) [-\Theta(p^0) (1 - f_F(\omega)) + \Theta(-p^0) f_F(\omega)] , \\ iS_{\text{eq}}^<(p) &= -2\pi (\not{p} + m) \delta(p^2 - m^2) [\Theta(p^0) f_F(\omega) - \Theta(-p^0) (1 - f_F(\omega))] , \\ iS_{\text{eq}}^t(p) &= \frac{i (\not{p} + m)}{p^2 - m^2 + i\eta} - 2\pi (\not{p} + m) \delta(p^2 - m^2) f_F(\omega) , \\ iS_{\text{eq}}^{\bar{t}}(p) &= -\frac{i (\not{p} + m)}{p^2 - m^2 - i\eta} - 2\pi (\not{p} + m) \delta(p^2 - m^2) f_F(\omega) , \end{aligned} \quad (2.34)$$

where we introduced the Fermi-Dirac distribution function with vanishing chemical potential

$$f_F(\omega) \equiv \frac{1}{e^{\beta\omega} + 1} , \quad \omega \equiv \sqrt{m^2 + \vec{p}^2} , \quad (2.35)$$

and we recovered the standard pole prescription by making use of

$$\frac{i}{p^2 - m^2 + i\eta} = \mathcal{P} \left(\frac{i}{p^2 - m^2} \right) + \pi \delta(p^2 - m^2) , \quad (2.36)$$

where \mathcal{P} denotes the principal part and $\eta \rightarrow 0^+$. For the spectral function (2.11) we get

$$S_{\text{eq}}^A(p) = \pi (\not{p} + m) \delta(p^2 - m^2) \varepsilon(p^0) . \quad (2.37)$$

Note that the statistical information is contained in the distribution function $f_F(\omega)$ and is not present in S_{eq}^A . On the other hand, the δ -function in (2.37) restricts the spectrum of the excitations to the mass shell

$$p^0 = \pm \sqrt{m^2 + \vec{p}^2} , \quad (2.38)$$

thus containing the spectral properties of the system, as anticipated with the choice of the name. We also note that, as expected, at zero temperature the distribution function vanish and the time-ordered propagator reduces to the usual Feynman one

$$iS^t(p)|_{T=0} = \frac{i(\not{p} + m)}{p^2 - m^2 + i\eta} . \quad (2.39)$$

A similar procedure can be applied to the propagator $i\Delta(x, y) \equiv \langle \Omega | T_{\mathcal{C}} \phi(x) \phi^\dagger(y) | \Omega \rangle$ of a bosonic field ϕ , in which case the result is [64]

$$\begin{aligned} i\Delta_{\text{eq}}^>(p) &= 2\pi \delta(p^2 - m^2) [\Theta(p^0) (1 + f_B(\omega)) + \Theta(-p^0) f_B(\omega)] , \\ i\Delta_{\text{eq}}^<(p) &= 2\pi \delta(p^2 - m^2) [\Theta(p^0) f_B(\omega) + \Theta(-p^0) (1 + f_B(\omega))] , \\ i\Delta_{\text{eq}}^t(p) &= \frac{i}{p^2 - m^2 + i\eta} + 2\pi \delta(p^2 - m^2) f_B(\omega) , \\ i\Delta_{\text{eq}}^{\bar{t}}(p) &= -\frac{i}{p^2 - m^2 - i\eta} + 2\pi \delta(p^2 - m^2) f_B(\omega) , \end{aligned} \quad (2.40)$$

where the statistical factor is given by the Bose-Einstein distribution with vanishing chemical potential

$$f_B(\omega) \equiv \frac{1}{e^{\beta\omega} - 1} , \quad \omega \equiv \sqrt{m^2 + \vec{p}^2} . \quad (2.41)$$

For a vector boson in the Feynman gauge the propagator is

$$iD_{\text{eq}}^{\mu\nu}(p) = -g^{\mu\nu} i\Delta_{\text{eq}}(p) . \quad (2.42)$$

The equilibrium propagators derived in this section will be useful in the following when the perturbative calculation of the collision term in the CTP formalism will be considered.

2.1.3 The Kadanoff-Baym equation

In this Section we study how the equation of motion (2.16) changes when the interaction terms in the Lagrangian are considered explicitly

$$\mathcal{L} = \mathcal{L}_0 + \mathcal{L}_{\text{int}} . \quad (2.43)$$

We follow the approach based on the two-particle-irreducible (2PI) effective action [67, 68]

$$\Gamma[S] = -i \text{Tr} [S_0^{-1} S] - i \text{Tr} [\ln S^{-1}] + \Gamma_2[S] , \quad (2.44)$$

where the trace denotes both space-time integration and summation over spinor indices. The first term is the classical (tree-level) action (2.14), the second corresponds to the one-loop vacuum diagram and the third to the sum over all the 2PI vacuum diagrams. In this framework the equation of motion in absence of sources is the Schwinger-Dyson equation, obtained by extremizing the 2PI effective action

$$\begin{aligned}
0 &= \frac{\delta\Gamma[S]}{\delta S(z,x)} \\
0 &= -iS_0^{-1}(x,z) + iS^{-1}(x,z) + \frac{\delta\Gamma_2[S]}{\delta S(z,x)} \\
(i\cancel{\partial}_x - m) iS(x,y) &= i\delta_C^4(x-y) + \int d^4z \Sigma(x,z) iS(z,y) ,
\end{aligned} \tag{2.45}$$

where in the third line we multiplied from the right by $S(z,y)$, integrated over z , used the tree-level equation of motion (2.16) and introduced the 1PI self-energy

$$\Sigma(x,y) \equiv -i \frac{\delta\Gamma_2[S]}{\delta S(y,x)} . \tag{2.46}$$

The Schwinger-Dyson equation (2.45) is the fundamental quantum dynamical equation corresponding to the Lagrangian (2.43) and its complexity is contained in the self-energy (2.46), which is a complicated functional of the Green function.

In terms of the real-time Green functions the Schwinger-Dyson equation reads

$$(i\cancel{\partial}_x - m) S^{ab}(x,y) = ia \delta^{ab} \delta^4(x-y) + \sum_c c \int d^4z \Sigma^{ac}(x,z) S^{cb}(z,y) , \tag{2.47}$$

where the real-time self-energies are defined by

$$\Sigma^{ab}(x,y) \equiv -i a b \frac{\delta\Gamma_2[S]}{\delta S^{ba}(y,x)} . \tag{2.48}$$

We now split the Schwinger-Dyson equation (2.47) into the following two equations

$$(i\cancel{\partial}_x - m) S^{r,a}(x,y) - \int d^4z \Sigma^{r,a}(x,z) S^{r,a}(z,y) = \delta^4(x-y) , \tag{2.49}$$

$$(i\cancel{\partial}_x - m) S^{\bar{s}}(x,y) - \int d^4z \Sigma^r(x,z) S^{\bar{s}}(z,y) = \int d^4z \Sigma^{\bar{s}}(x,z) S^a(z,y) , \tag{2.50}$$

the reason for it being to make the physical meaning more manifest: the retarded and advanced propagators describe mostly the spectral properties of the system, as seen in the free case

in (2.37), while the Wightman functions encode the statistical, or kinetic ones. The kinetic equation (2.50) can be written in the form of the Kadanoff-Baym equation [69]

$$(i\partial_x - m) S^{\lessgtr}(x, y) - \int d^4z \left(\Sigma^h(x, z) S^{\lessgtr}(z, y) + \Sigma^{\lessgtr}(x, z) S^h(z, y) \right) = \mathcal{C}[S] , \quad (2.51)$$

where the collision term is defined as

$$\mathcal{C}[S] \equiv \frac{1}{2} \int d^4z \left(\Sigma^>(x, z) S^<(z, y) - \Sigma^<(x, z) S^>(z, y) \right) , \quad (2.52)$$

and the hermitian self-energy Σ^h is defined analogously to S^h in (2.10). It is important to stress that the Kadanoff-Baym equation follows from first principles and encodes the full quantum dynamics of the system, thus being valid in general to describe out-of-equilibrium situations. In the form (2.51, 2.52) and with the self-energies defined in (2.48), the Kadanoff-Baym equation is an exact functional equation for the Green function. Due to the presence of memory integrals, it is in general too complicated to be solved, even numerically. It is the argument of the next Section to see how and under which assumptions the Kadanoff-Baym equation (2.51) can be brought into the simpler form of the Boltzmann equation.

2.2 Derivation of the Boltzmann equation

In the previous Section we have seen that the dynamics of an out-of-equilibrium quantum system is described within the CTP formalism by the Kadanoff-Baym equation (2.51), a complicated functional equation for the Green function of the considered quantum field.

In this Section we describe the procedure and the assumptions that are needed to simplify the Kadanoff-Baym equation and write it in the form of a Boltzmann equation for the phase-space distribution of the considered species. The procedure is divided in two steps, the gradient expansion and the on-shell reduction.

2.2.1 The gradient expansion

The first step is to separate the internal fluctuations of the system, that occur at the microscopic scale of particle interactions, from the behaviour at macroscopic scales, which in general out-of-equilibrium situations is related to some non-trivial background effect. We shall assume that the system is close to chemical and kinetic equilibrium, namely that the variations of the background are slow compared to the characteristic time scale of the internal fluctuations. Under this assumption it is in general justified to neglect memory effects, and extend the contour \mathcal{C} from $t_0 \rightarrow -\infty$ to $t \rightarrow +\infty$. This allows us to perform the “gradient expansion”, consisting in a perturbative expansion of the Kadanoff-Baym equation in the small energy scale of background variations. Define the relative and the average coordinates as

$$r \equiv x - y , \quad X \equiv \frac{x + y}{2} , \quad (2.53)$$

and write the Green function in Wigner representation (Fourier transform with respect to the relative coordinate)

$$S(p, X) \equiv \int d^4r e^{ip \cdot r} S\left(X + \frac{r}{2}, X - \frac{r}{2}\right). \quad (2.54)$$

The coordinate p represents the momentum of plasma excitations (the microscopic fluctuations), while the coordinate X describes the macroscopic background variations. As we have already seen in Sec. 2.1.2, at equilibrium the system is homogeneous and the Green function does not depend on the average coordinate X . Close to equilibrium we can assume the variations depending on X , to be small compared to the momentum scale of plasma excitations, namely

$$\nabla S \ll p S, \quad (2.55)$$

where we denote $\nabla \equiv \partial/\partial X$. The above relation is the condition for the gradient expansion, consisting in neglecting higher powers of ∇/p .

As we will discuss in Sec. 2.3, in the context of relic density calculation an expansion to leading order in the gradients is enough to capture all the relevant physics processes. The Kadanoff-Baym equation (2.51) written in Wigner space and expanded to first order in the gradients reads

$$\left(\not{p} + \frac{i}{2}\not{\nabla} - m\right) S^{\lessgtr} - \Sigma^h S^{\lessgtr} - \Sigma^{\lessgtr} S^h + \frac{i}{2}\{\Sigma^h, S^{\lessgtr}\} + \frac{i}{2}\{\Sigma^{\lessgtr}, S^h\} + \mathcal{O}(\nabla^2) = \mathcal{C}, \quad (2.56)$$

where the curly brackets denote an analogue of the Poisson brackets with respect to the coordinates X and p

$$\{A, B\} \equiv \frac{\partial A}{\partial p_\mu} \frac{\partial B}{\partial X^\mu} - \frac{\partial A}{\partial X_\mu} \frac{\partial B}{\partial p^\mu}. \quad (2.57)$$

The expanded collision term in Wigner space reads

$$\mathcal{C} = \frac{1}{2}(\Sigma^> S^< - \Sigma^< S^>) - \frac{i}{4}(\{\Sigma^>, S^<\} - \{\Sigma^<, S^>\}) + \mathcal{O}(\nabla^2). \quad (2.58)$$

Separating the hermitian and anti-hermitian parts leads to constraint and kinetic equations, that we need at the zeroth and first order in the gradients, respectively. We obtain

$$2p^0 \gamma^0 i S^{\lessgtr} - \{\vec{p} \cdot \vec{\gamma} \gamma^0 + m \gamma^0 + \Sigma^h \gamma^0, \gamma^0 i S^{\lessgtr}\} - \{i \Sigma^{\lessgtr} \gamma^0, \gamma^0 S^h\} = i\mathcal{C} - i\mathcal{C}^\dagger, \quad (2.59)$$

$$i \partial_t \gamma^0 i S^{\lessgtr} - [\vec{p} \cdot \vec{\gamma} \gamma^0 + m \gamma^0 + \Sigma^h \gamma^0, \gamma^0 i S^{\lessgtr}] - [i \Sigma^{\lessgtr} \gamma^0, \gamma^0 S^h] = i\mathcal{C} + i\mathcal{C}^\dagger, \quad (2.60)$$

where $\{\cdot, \cdot\}$ and $[\cdot, \cdot]$ denote here the anti-commutator and commutator, respectively. The constraint equation (2.59) to zeroth order in perturbation theory, i.e. neglecting all the self-energy terms, takes the simple form

$$\{(\not{p} - m) \gamma^0, i \gamma^0 S^{\lessgtr}\} = 0. \quad (2.61)$$

It describes the spectral properties of the quasi-particles and in particular puts constraints on the structure of the Green function. Inserting the most general parameterization of the spinor matrix structure compatible with spatial isotropy,

$$iS^{\lessgtr} = m \left(h_s^{\lessgtr} + h_p^{\lessgtr} \gamma^5 \right) + h_{v0}^{\lessgtr} p^0 \gamma^0 - h_{v3}^{\lessgtr} \vec{p} \cdot \vec{\gamma} + h_{a0}^{\lessgtr} p^0 \gamma^0 \gamma^5 - h_{a3}^{\lessgtr} \vec{p} \cdot \vec{\gamma} \gamma^5 + h_t^{\lessgtr} [\gamma^0, \vec{p} \cdot \vec{\gamma}] , \quad (2.62)$$

the constraint equation (2.61) leads to the conditions

$$h_s^{\lessgtr} = h_{v0}^{\lessgtr} = h_{v3}^{\lessgtr} \equiv h^{\lessgtr} , \quad h_p^{\lessgtr} = h_{a0}^{\lessgtr} = h_{a3}^{\lessgtr} = h_t^{\lessgtr} = 0 . \quad (2.63)$$

Hence the Green function must be of the form

$$iS^{\lessgtr} = (\not{p} + m) h^{\lessgtr} . \quad (2.64)$$

2.2.2 On-shell reduction of the Kadanoff-Baym equation

The second step of the derivation of the Boltzmann equation is the “on-shell reduction”, based on the assumption that the spectral function of the system is the same as for free particles, given in (2.37)

$$S^A = S_{\text{eq}}^A$$

$$\frac{i}{2} (S^> - S^<) = \pi (\not{p} + m) \delta(p^2 - m^2) \varepsilon(p^0) . \quad (2.65)$$

We note that imposing the condition (2.55) for the gradient expansion is equivalent to assume that the characteristic length of background fluctuations is much larger than the De Broglie wavelength of the particles in the plasma. At zeroth order in the gradients, at which we are working, this argument is enough to justify the quasi-particle approximation (2.65) (see [67]). More delicate is the case of extending the treatment to first order in the gradients, which is beyond the scope of this work. An accurate analysis in the context of electroweak baryogenesis can be found in [60].

Under the quasi-particle assumption (2.65) the general solution (2.64) of the constraint equation (2.61) can also be written in the form of the Kadanoff-Baym ansatz

$$iS^> = -2 S_{\text{eq}}^A \left[-\Theta(p^0)(1 - f_\psi(\vec{p})) - \Theta(-p^0)f_{\bar{\psi}}(-\vec{p}) \right] , \quad (2.66)$$

$$iS^< = -2 S_{\text{eq}}^A \left[\Theta(p^0)f_\psi(\vec{p}) + \Theta(-p^0)(1 - f_{\bar{\psi}}(-\vec{p})) \right] , \quad (2.67)$$

where we traded the two parametrizing functions h^{\lessgtr} for $f_\psi, f_{\bar{\psi}}$. By comparing the above form of the Wightman functions with the equilibrium one given in (2.34) we can interpret the functions $f_\psi, f_{\bar{\psi}}$ as the phase-space distributions of the particle ψ and its anti-particle $\bar{\psi}$ respectively. The

real-time propagators in Wigner space can then be written under the considered assumptions as

$$\begin{aligned}
iS^>(p) &= -2\pi (\not{p} + m) \delta(p^2 - m^2) [-\Theta(p^0)(1 - f_\psi(\vec{p})) + \Theta(-p^0)f_{\bar{\psi}}(-\vec{p})] , \\
iS^<(p) &= -2\pi (\not{p} + m) \delta(p^2 - m^2) [\Theta(p^0)f_\psi(\vec{p}) - \Theta(-p^0)(1 - f_{\bar{\psi}}(-\vec{p}))] , \\
iS^t(p) &= \frac{i(\not{p} + m)}{p^2 - m^2 + i\eta} - 2\pi (\not{p} + m) \delta(p^2 - m^2) [\Theta(p^0)f_\psi(\vec{p}) - \Theta(-p^0)f_{\bar{\psi}}(-\vec{p})] , \\
iS^{\bar{t}}(p) &= -\frac{i(\not{p} + m)}{p^2 - m^2 - i\eta} - 2\pi (\not{p} + m) \delta(p^2 - m^2) [\Theta(p^0)f_\psi(\vec{p}) - \Theta(-p^0)f_{\bar{\psi}}(-\vec{p})] . \quad (2.68)
\end{aligned}$$

The Boltzmann equation now follows from combining the kinetic equation (2.60) at first order of the gradient expansion with the solution (2.66-2.67) of the zeroth-order constraint equation in the quasi-particle approximation. We first note that the term $[\vec{p} \cdot \vec{\gamma} \gamma^0 + m \gamma^0, \gamma^0 iS^{\lessgtr}]$ vanishes with the above ansatz for S^{\lessgtr} . Next we examine the terms containing commutators with self-energies. We assume that the deviation from thermal equilibrium is sufficiently small that the self-energies can be computed with the propagators (2.68). Note that in general \mathcal{L}_{int} contains interactions of ψ with other particles species, whose propagators enter then the self-energies calculation. This means that the Kadanoff-Baym equation (2.56) has to be coupled to similar equations for the other interacting species. We will assume in the following that any species other than ψ is in thermal equilibrium, such that the corresponding equations decouple and the propagators can be written as in (2.34, 2.40, 2.42). Then at one-loop we can use parametrizations

$$\Sigma^h = \alpha p^0 \gamma^0 - \beta \vec{p} \cdot \vec{\gamma} + \sigma m , \quad \Sigma^{\lessgtr} = a^{\lessgtr} p^0 \gamma^0 - b^{\lessgtr} \vec{p} \cdot \vec{\gamma} + c^{\lessgtr} m , \quad (2.69)$$

where α , β , σ , a^{\lessgtr} , b^{\lessgtr} and c^{\lessgtr} are scalar functions of the momentum. With this ansatz one can check that both $[i\Sigma^{\lessgtr} \gamma^0, \gamma^0 S^h]$ and $[\Sigma^h \gamma^0, \gamma^0 iS^{\lessgtr}]$ are proportional to $\vec{p} \cdot \vec{\gamma}$ and for this reason, after taking the trace over spinor indices, will not contribute to the Boltzmann equation. Finally, multiplying (2.60) by $2\Theta(p^0)$, taking the trace over all the spinor indices, integrating over p^0 and \vec{p} , and replacing the time derivative by the covariant one, as appropriate in the FRW background

$$\partial_t \rightarrow \partial_t - H \vec{p} \cdot \frac{\partial}{\partial \vec{p}} , \quad (2.70)$$

we obtain, after using (2.64) with (2.68),

$$\frac{dn}{dt} + 3Hn = C_{\text{CTP}}[n] , \quad (2.71)$$

with the collision term on the right-hand side given by

$$C_{\text{CTP}}[n] \equiv - \int \frac{d^4 p}{(2\pi)^4} \Theta(p^0) \frac{1}{2} \text{Tr} [\mathcal{C} + \mathcal{C}^\dagger] . \quad (2.72)$$

We conclude that the integrated Boltzmann equation (2.71), together with the above expression for the collision term, is the consistent limit of the complete Kadanoff-Baym equation when the gradient expansion and the on-shell reduction are justified.

2.3 The collision term at leading order

In the previous Section we derived the Boltzmann equation (2.71) from first principles in QFT within the CTP approach, and we obtained the form (2.72) for the collision term. We now want to show that in the DM freeze-out scenario, where the collision term is determined by $2 \rightarrow 2$ annihilation processes computed at the LO in perturbation theory, this result reproduces the one from the semi-classical approach of Chapter 1. In practice we have to show that the collision term (2.72) is equivalent to (2.2), namely that it holds

$$C_{\text{CTP}} \stackrel{!}{=} \int d\Pi_{\chi\bar{\chi}(ij)} \sum_{\text{spin}} \left[|\mathcal{M}_{\chi\bar{\chi} \rightarrow ij}|^2 \left(f_i f_j (1 \pm f_\chi)(1 \pm f_{\bar{\chi}}) - f_\chi f_{\bar{\chi}} (1 \pm f_i)(1 \pm f_j) \right) \right]. \quad (2.73)$$

In this Section we show that this is indeed the case, by explicit computation of the CTP collision term in a realistic model of fermionic DM. In Sec. 2.3.1 we introduce the DM model and comment on the validity of the assumptions under which (2.71) was derived, then we compute the collision term in Sec. 2.3.2.

2.3.1 The model

We consider the extension of the Standard Model by an $SU(2) \times U(1)$ singlet Majorana fermion and a scalar doublet $\phi = (\phi^+, \phi^0)^T$. The relevant terms in the Lagrangian read

$$\mathcal{L} = -\frac{1}{4} F^{\mu\nu} F_{\mu\nu} + \bar{f} (i\not{D} - m_f) f + \frac{1}{2} \bar{\chi} (i\not{D} - m_\chi) \chi + (D_\mu \phi)^\dagger (D^\mu \phi) - m_\phi^2 \phi^\dagger \phi + \mathcal{L}_{\text{int}}, \quad (2.74)$$

$$\mathcal{L}_{\text{int}} = \lambda \bar{\chi} P_L f^- \phi^+ + \text{h.c.}, \quad (2.75)$$

where $P_L = \frac{1-\gamma_5}{2}$ is the left-handed chiral projector and the SM fermions form a left-handed doublet $f = (f^0, f^-)^T$. In this model the only interaction involving the DM particle χ is the Yukawa interaction with the “sfermion” ϕ and SM (light) fermion doublet f , of which we include only the charged component. The neutral component would affect the inclusive tree level cross section through the $\lambda \bar{\chi} P_L f^0 \phi^0$ interaction, which allows $\chi\bar{\chi} \rightarrow f^0 \bar{f}^0$, however this process receives no radiative corrections since it contains only electrically neutral particles. The scenario we have in mind, realized in the minimal supersymmetric standard model (MSSM) if the dark matter is the bino, is an electroweak or TeV-scale DM particle, and a scalar (sfermion) with mass $m_\phi > m_\chi \approx \mathcal{O}(0.1-1 \text{ TeV})$. In this situation the freeze-out occurs after the electroweak phase transition. In the covariant derivative we therefore keep only the electromagnetic term.

Before moving on to the calculation of the CTP collision term (2.72) we briefly comment here on the validity of the assumptions under which the result (2.72) has been derived. The first step of the derivation is based upon the assumption that the system is close to equilibrium. As we have seen in Chapter 1, in the freeze-out scenario the characteristic scale of background variations is the Hubble expansion rate H , and the DM particle χ is driven out-of-equilibrium when $\Gamma_{\text{ann}} \sim H$, corresponding to $T \sim m_\chi/20$. Making use of (1.6) we can estimate the gradients to be of the order

$$\nabla \sim H \sim \frac{T^2}{M_P} . \quad (2.76)$$

On the other hand, the typical energy scale of microscopic interactions is given by the temperature T of the plasma

$$p \sim T . \quad (2.77)$$

From the estimates in the two equations above we conclude that the condition (2.55) for the gradient expansion is valid before and around the freeze-out

$$\frac{\nabla}{p} \sim \frac{m_\chi}{M_P} \ll 1 . \quad (2.78)$$

As we argued in the previous Section, the on-shell reduction that we perform as the second step of the derivation is justified at this order in the gradient expansion. In writing the parametrization (2.62) we assumed spatial isotropy, which is a property of the FRW cosmology. Finally, we assumed that the species other than χ are in equilibrium to write (2.69). This assumption was necessary also for the derivation of the semi-classical equation (2.1), and is therefore consistent.

A final comment concerns the Majorana nature of the DM particle χ in the considered model. The difference with respect to the Dirac fermion ψ is the self-conjugacy property

$$\chi = \chi^c \equiv C \bar{\chi}^T , \quad (2.79)$$

where C is the charge-conjugation matrix. The above relation leads to different possible contractions for the two fields entering the definition of the propagator

$$iS_{\alpha\beta}(x, y) \equiv \langle \Omega | \mathcal{T}_C \{ \chi_\alpha(x) \bar{\chi}_\beta(y) \} | \Omega \rangle , \quad (2.80)$$

and the anticommutation property of fermionic operators results in different relative signs among the various contractions. A consistent way to derive Feynman rules for Majorana fields at zero-temperature is presented in [70]. In order to write down the amplitude of a given Feynman diagram, one has to start by fixing an arbitrary orientation (*fermion flow*) for each fermionic chain.³ The contribution to the diagram from a fermion chain can be then computed by writing down the Dirac matrices starting from an external leg (or from an

³In the following we will denote the fermion flow with additional arrows close to each fermionic propagator.

arbitrary one for a closed loop) and proceeding opposite to the chosen fermion flow through the chain. Whenever the fermion flow is antiparallel to the charge flow (denoted by the arrow *on* fermionic propagators) the propagator $iS^{ab}(p)$ has to be replaced with the charge-conjugate one

$$S'^{ab}(p) \equiv C \left(S^{ab}(p) \right)^T C^{-1}, \quad (2.81)$$

where the transpose is with respect to the spinor indices only. Additionally the Majorana condition implies the identification of particles and anti-particles, resulting in $f_{\bar{\chi}} = f_{\chi}$.

2.3.2 The collision term at LO

As we have seen in Sec. 2.2, the fermion collision term in the CTP formalism to zeroth order in gradient expansion is given by (2.58)

$$\mathcal{C}_{\chi} = \frac{1}{2} (\Sigma^{>} S^{<} - \Sigma^{<} S^{>}) . \quad (2.82)$$

The self-energies Σ^{\lessgtr} can be computed in perturbation theory by drawing the corresponding diagrams and calculating them with the CTP cutting rules [64]. According to these rules, formulated in real-time, for each interaction term in the Lagrangian one has to consider two types of vertices, denoted by ‘+’ and ‘-’. The type ‘+’ vertex factor is derived from the Lagrangian in the usual ($T = 0$) way, while the corresponding type ‘-’ is simply its complex conjugate. In a Feynman diagram the real-time propagator $iS^{ab}(p)$ is used to connect a vertex of type a and one of type b with momentum p flowing from b to a . In the real-time self-energies Σ^{ab} , the types of the vertices connected to the external legs are thus fixed to be a and b , while one has to sum over both types of internal vertices (see below for an explicit example).

In the scenario that we consider here we have to use for the DM particle χ the propagators in (2.68), with distribution functions depending only on the energy ω_{χ} . For any other particle species we can instead use the equilibrium propagators (2.34, 2.40, 2.42). Note that the thermal part of the scalar propagator is exponentially suppressed, since $m_{\phi} > m_{\chi} \gg T_{\text{f.o.}}$. For the particle ϕ we therefore retain the $T = 0$ part only of diagonal propagators.

The two terms $\Sigma^{<}$ and $\Sigma^{>}$ account for all possible processes, which include annihilation, production and scattering processes for χ , as well as absorption processes characteristic of the finite-temperature plasma. In the kinetic equation for the particle number density, the contributions from particle-number preserving scattering processes $\chi f \rightarrow \chi f$ cancel out after summing over the two terms on the right-hand side of (2.82), taking the trace and performing the integral over the particle four-momentum in (2.72). These terms will therefore be omitted right away.

We start from the calculation at leading order in the coupling (loop) expansion to show the correspondence between the self-energy diagrams and annihilation processes. The one-loop self energy, shown in Fig. 2.2, describes $1 \leftrightarrow 2$ processes, which are not relevant for the relic-density computation, because they are kinematically forbidden or exponentially suppressed.

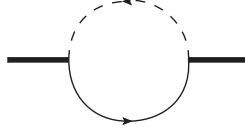


Figure 2.2: The DM self-energy at one loop. The same diagram topology with reversed charge flow arrows is not shown.

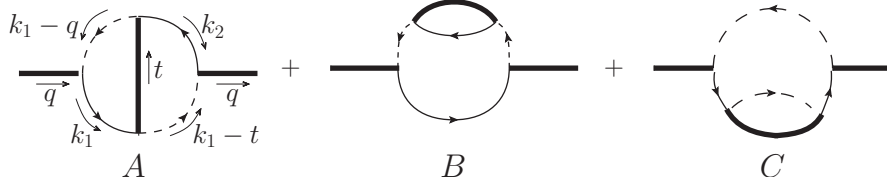


Figure 2.3: The DM self-energy at two loops. Momenta flow along the arrows next to each line. The chosen convention for the fermion flow is also specified by those arrows. The same diagram topologies with reversed charge flow arrows are not shown for simplicity. In the following they are taken into account and denoted by a superscript *rev*.

Therefore, the LO annihilation process $\chi\bar{\chi} \leftrightarrow f\bar{f}$ must be encoded in the two-loop self-energy diagrams of Fig. 2.3. Let us consider the contribution to $\Sigma^>(q)$ from diagram *A* in Fig. 2.3. Since $\Sigma^> = \Sigma^{-+}$, the left vertex is of the type ‘+’ and the right one of type ‘-’, while one has to sum over both types of internal vertices. We thus get for $i\Sigma_A^>$ the sum of the four diagrams in Fig. 2.4, where uncircled and circled vertices denote type ‘+’ and type ‘-’ vertices, respectively. Fixing the fermion flow and assigning the momenta as in Fig. 2.3, the whole expression appearing in the collision term reads

$$i\Sigma_A^>(q) iS^<(q) = \sum_{a,b=\pm} -a b \lambda^4 \int \frac{d^4 t}{(2\pi)^4} \frac{d^4 k_1}{(2\pi)^4} \frac{d^4 k_2}{(2\pi)^4} (2\pi)^4 \delta^{(4)}(q+t-k_1-k_2) \\ \times i\Delta^{+a}(k_1-q) i\Delta^{-b}(k_1-t) P_R iS_f^{a-}(-k_2) P_L iS^{ab}(t) P_L iS_f^{b+}(k_1) P_R iS^{+-}(q) . \quad (2.83)$$

Dropping the exponentially suppressed thermal part of the scalar propagators implies that only the ‘++’ and ‘--’ components of Δ^{ab} are non-vanishing, so the endpoints of a scalar (dashed) line must either both be circled or not. The only diagram in Fig. 2.4 that is left is A_{III} . Taking the trace over the spinor indices, which accounts for the polarization sum in the number density equation, the previous equation simplifies to

$$\text{Tr} [\Sigma_{A_{\text{III}}}^>(q) S^<(q)] = -\lambda^4 \int \frac{d^4 t}{(2\pi)^4} \frac{d^4 k_1}{(2\pi)^4} \frac{d^4 k_2}{(2\pi)^4} (2\pi)^4 \delta^{(4)}(q+t-k_1-k_2)$$

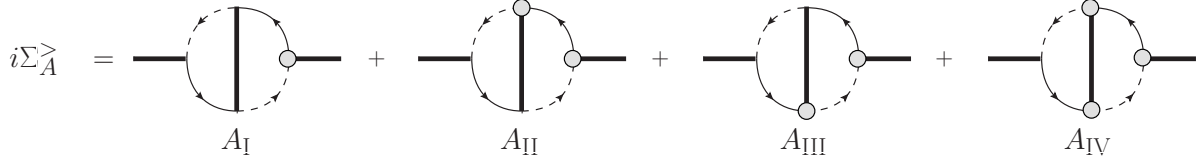


Figure 2.4: $i\Sigma_A^>$ as given by the CTP Feynman rules. Uncircled and circled vertices denote type ‘+’ and type ‘-’ vertices, respectively.

$$\times \underbrace{i\Delta^{++}(k_1-q) i\Delta^{--}(k_1-t)}_{\equiv \mathcal{S}} \underbrace{\text{Tr} \left[P_R iS_f'^{+-}(-k_2) P_L iS^{+-}(t) P_L iS_f^{-+}(k_1) P_R iS^{+-}(q) \right]}_{\equiv \mathcal{F}}. \quad (2.84)$$

Since in the scalar part \mathcal{S} we need only the $T = 0$ part of the propagators, we have

$$\mathcal{S} = \frac{i}{(k_1 - q)^2 - m_\phi^2 + i\eta} \frac{-i}{(k_1 - t)^2 - m_\phi^2 - i\eta}. \quad (2.85)$$

In the fermion part \mathcal{F} both the $T = 0$ and the thermal parts contribute, in principle. However, the expression involves only the purely thermal off-diagonal CTP propagator, leaving

$$\begin{aligned} \mathcal{F} &= \text{Tr} \left[P_R (\not{k}_2 + m_f) P_L (\not{t} + m_\chi) P_L (\not{k}_1 + m_f) P_R (\not{q} + m_\chi) \right] \\ &\times (2\pi)^4 \delta(q^2 - m_\chi^2) \delta(t^2 - m_\chi^2) \delta(k_1^2 - m_f^2) \delta(k_2^2 - m_f^2) \\ &\times [\Theta(-k_2^0) f_F(\omega_{\bar{f}}) - \Theta(k_2^0) (1 - f_F(\omega_{\bar{f}}))] [\Theta(t^0) f_\chi(\omega_{\bar{\chi}}) - \Theta(-t^0) (1 - f_\chi(\omega_{\bar{\chi}}))] \\ &\times [-\Theta(k_1^0) (1 - f_F(\omega_f)) + \Theta(-k_1^0) f_F(\omega_f)] [\Theta(q^0) f_\chi(\omega_\chi) - \Theta(-q^0) (1 - f_\chi(\omega_\chi))], \quad (2.86) \end{aligned}$$

where we defined

$$\begin{aligned} \omega_\chi &\equiv \sqrt{m_\chi^2 + \vec{q}^2}, & \omega_{\bar{\chi}} &\equiv \sqrt{m_\chi^2 + \vec{t}^2}, \\ \omega_f &\equiv \sqrt{m_f^2 + \vec{k}_1^2}, & \omega_{\bar{f}} &\equiv \sqrt{m_f^2 + \vec{k}_2^2}. \end{aligned} \quad (2.87)$$

The last two lines of (2.86) lead to 16 distinct terms describing different processes in the thermal plasma. Half of them vanish after multiplying by $\Theta(q^0)$ as needed for (2.72). Out of the remaining 8 terms, 5 are kinematically forbidden since they refer to $4 \leftrightarrow 0$ and $1 \leftrightarrow 3$ processes as $\chi \rightarrow \chi f \bar{f}$. One is left with two terms corresponding to scatterings ($\chi f \rightarrow \chi f$ and $\chi \bar{f} \rightarrow \chi \bar{f}$), which do not contribute to the number-changing processes and cancel out after including the $\Sigma^{<S>}$ contribution, and one term describing the annihilation process $\chi \bar{\chi} \rightarrow f \bar{f}$. Only this last term contributes to the integrated collision term. Finally, renaming the momenta according to

$$p_\chi \equiv q, \quad p_{\bar{\chi}} \equiv t, \quad p_f \equiv k_1, \quad p_{\bar{f}} \equiv k_2, \quad (2.88)$$

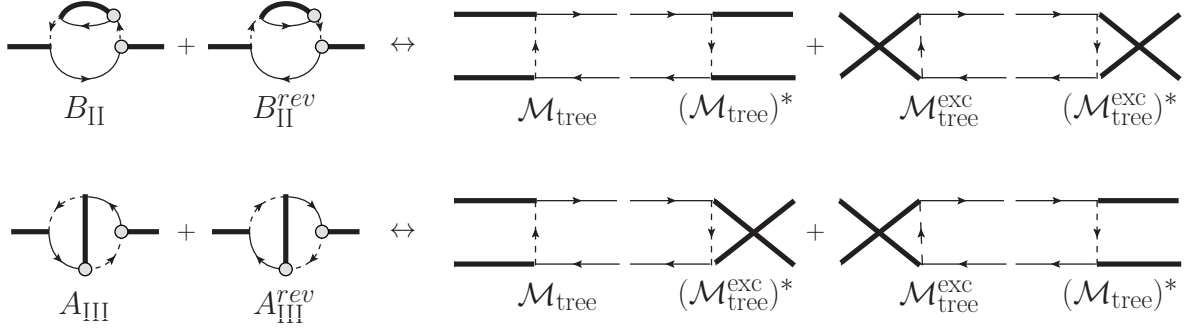


Figure 2.5: Tree-level annihilation diagrams for a Majorana fermion and their matching with the two-loop self-energies. For simplicity we omit the imaginary unit from the labels, such that for a diagram labeled by \mathcal{M} , the associated amplitude is given by $i\mathcal{M}$. Note the correspondence between reversing the charge flow arrows and crossing the external legs.

we get

$$\begin{aligned} \text{Tr} [\Sigma_{A_{\text{III}}}^>(p_\chi) S^<(p_\chi)] &= \frac{1}{2\omega_\chi} (2\pi) \delta(p_\chi^0 - \omega_\chi) \int d\Pi_{\bar{\chi}} d\Pi_f d\Pi_{\bar{f}} (2\pi)^4 \delta^{(4)}(p_\chi + p_{\bar{\chi}} - p_f - p_{\bar{f}}) \\ &\quad \times \sum_{\text{spin}} \left[|\mathcal{M}_{A_{\text{III}}}|^2 f_\chi(\omega_\chi) f_\chi(\omega_{\bar{\chi}}) (1 - f_F(\omega_f)) (1 - f_F(\omega_{\bar{f}})) \right], \quad (2.89) \end{aligned}$$

where we note that all the momenta are on-shell. Adding the hermitian conjugate and integrating this expression with $-d^4p_\chi/(2\pi)^4 \frac{1}{2}\Theta(p_\chi^0)$, as appropriate to the collision term for the χ number density (2.72), and accounting for the factor 1/2 in (2.82), the structure of the result is now manifestly as in (2.2), with a zero-temperature squared matrix element multiplied by the statistical factors corresponding to the process $\chi\bar{\chi} \rightarrow f\bar{f}$. The matrix element squared can indeed be recognized as the interference term between the two tree-level diagrams for the annihilation process as shown in Fig. 2.5 according to the definition $\mathcal{M}_{\chi\bar{\chi} \rightarrow f\bar{f}} = \mathcal{M}_{\text{tree}} + \mathcal{M}_{\text{tree}}^{\text{exc}}$. Specifically

$$|\mathcal{M}_{A_{\text{III}}}|^2 = -\lambda^4 \mathcal{S} \text{Tr} [\dots] = \mathcal{M}_{\text{tree}} (\mathcal{M}_{\text{tree}}^{\text{exc}})^*, \quad (2.90)$$

where the trace refers to the first line of (2.86). The same procedure applied to the diagram B in Fig. 2.3 and to the corresponding diagrams with reversed charge flow arrows leads to the identifications

$$\begin{aligned} |\mathcal{M}_{B_{\text{II}}}|^2 &= |\mathcal{M}_{\text{tree}}|^2, \\ |\mathcal{M}_{A_{\text{III}}^{\text{rev}}}|^2 &= \mathcal{M}_{\text{tree}}^{\text{exc}} (\mathcal{M}_{\text{tree}})^*, \\ |\mathcal{M}_{B_{\text{II}}^{\text{rev}}}|^2 &= |\mathcal{M}_{\text{tree}}^{\text{exc}}|^2. \end{aligned} \quad (2.91)$$

Diagram C of Fig. 2.3 does not contribute, since as discussed above we can ignore any contribution with an off-diagonal scalar CTP propagator. Thus we finally obtain

$$\int \frac{d^4 p}{(2\pi)^4} \Theta(p^0) \frac{1}{4} \text{Tr} \left[\Sigma^> S^< + (\Sigma^> S^<)^\dagger \right] = \int d\Pi_{\chi\bar{\chi}(f\bar{f})} \sum_{\text{spin}} \left[|\mathcal{M}_{\chi\bar{\chi} \rightarrow f\bar{f}}|^2 f_\chi f_{\bar{\chi}} (1-f_f) (1-f_{\bar{f}}) \right]. \quad (2.92)$$

The calculation of $\Sigma^< S^>$ is analogous and reproduces the first term in (2.73), which corresponds to the production process $f\bar{f} \rightarrow \chi\bar{\chi}$. We therefore conclude that – as anticipated – at LO in the CTP formalism, that is, inserting the DM self-energy at two loops into (2.82) and (2.72) for the integrated collision term, leads to the standard Boltzmann equation (2.1). At LO in the coupling expansion the integrated collision term is, provided the tree level $2 \rightarrow 2$ processes are $\chi\bar{\chi} \leftrightarrow f\bar{f}$, as in (2.2).

Note that the above described procedure can be applied straightforwardly to the case of a Dirac fermion, the only difference being that, as no clashing arrows are allowed, the diagram of type A and B^{rev} are not present.

2.4 Boltzmann equation beyond the leading order

In the previous Section we showed by explicit calculation that the collision term of the transport equation in the CTP approach (2.72) at LO in the coupling (loop) expansion is equivalent to the one of the semi-classical Boltzmann equation (2.2). In this Section we address the problem of extending the calculation of the annihilation cross section $\sigma_{\text{ann}} v$ to the next-to-leading order (NLO) in perturbation theory.

In recent years there has been an increasing interest in higher-order corrections to scattering and annihilation processes involving DM particles. The main phenomenological importance of such corrections is related to the modification of the annihilation spectra relevant for the indirect searches. Quite generally, the increasing precision of dark matter observations will require more accurate computations of the scattering and annihilation processes, in some cases at full next-to-leading order (NLO) in the coupling constant. In particular, it has also been noted recently that corrections to the annihilation rate can affect non-negligibly the relic density computation [26–33, 71]. With this in mind the first numerical codes including the higher-order corrections are being developed, SloopS [72–74] and DM@NLO [75, 76]. What is usually done is to compute $\sigma_{\text{ann}} v$ in (2.2) by including the virtual and real radiation corrections to the two-particle processes $\chi\bar{\chi} \rightarrow ij$ using standard quantum field theory methods *at zero temperature*.

In Sec. 2.4.1 we show that this procedure raises a number of questions on its conceptual validity. We then describe how the formalism presented in the previous Section provides the answers to those questions in Sec. 2.4.2. The main result is that the systematic approach provides a justification for the NLO expansion of the collision term in the conventional form (2.2) of the freeze-out equation, provided that the annihilation cross section $\sigma_{\text{ann}} v$ is replaced by an

effective cross section, containing finite temperature corrections. This result was obtained for the first time in our paper [34]. The explicit calculation of the leading thermal correction in the model of Sec. 2.3.1 will be addressed later on, in the next Section.

2.4.1 Naïve approach and arising questions

In this Section we present the naïve approach adopted so far in the literature and raise some questions on its validity. The annihilation cross section times velocity entering (2.2) is defined at LO as (1.35, 1.38)

$$\langle \sigma_{\text{ann}}^{\text{LO}} v \rangle = \frac{1}{n_{\chi}^{\text{eq}2}} \int d\Pi_{\chi\bar{\chi}(ij)} \sum_{\text{spin}} f_{\chi}^{\text{eq}} f_{\bar{\chi}}^{\text{eq}} |\mathcal{M}_{\chi\bar{\chi} \rightarrow ij}^{\text{LO}}|^2 . \quad (2.93)$$

The standard NLO correction at zero temperature, considering for definiteness an electromagnetic radiation, is

$$\langle \sigma_{\text{ann}}^{\text{NLO}} v \rangle \equiv \frac{1}{n_{\chi}^{\text{eq}2}} \int d\Pi_{\chi\bar{\chi}(ij)} \sum_{\text{spin}} f_{\chi}^{\text{eq}} f_{\bar{\chi}}^{\text{eq}} \left[|\mathcal{M}_{\chi\bar{\chi} \rightarrow ij}^{\text{NLO}}|^2 + d\Pi_{(\gamma)} |\mathcal{M}_{\chi\bar{\chi} \rightarrow ij\gamma}|^2 \right] , \quad (2.94)$$

with the interpretation $d\Pi_{\chi\bar{\chi}(ij)} d\Pi_{(\gamma)} = d\Pi_{\chi\bar{\chi}(ij\gamma)}$. The first term is the one-loop virtual correction and the second one the real emission. It is well known that each of these two terms is separately divergent, but their sum is finite: the Bloch-Nordsieck cancellations and Kinoshita-Lee-Nauenberg (KLN) theorem [77–79] ensure that physical observables are free of infrared divergences, as they involve summation over initial and final degenerate states, in the sense of inclusiveness or experimental resolution in energy and angles. The naïve approach consists in writing the Boltzmann equation (2.1) with

$$\langle \sigma_{\text{ann}} v \rangle \longrightarrow \langle \sigma_{\text{ann}}^{\text{LO}} v \rangle + \langle \sigma_{\text{ann}}^{\text{NLO}} v \rangle . \quad (2.95)$$

By looking at the expression (2.94) of $\langle \sigma_{\text{ann}}^{\text{NLO}} v \rangle$ a natural question arises:

- I. Why should the time evolution of n_{χ} be described by inclusive two-particle cross sections

$$\sigma_{\text{ann}} \longrightarrow \sum_X \sigma_{\chi\bar{\chi} \rightarrow X} , \quad (2.96)$$

and a Boltzmann equation of the form applicable to $2 \rightarrow 2$ reactions? The real radiation amplitude involves three-particle final states, typically containing an additional photon or gluon, which are themselves abundant in the plasma. Moreover, absorption processes exist in the plasma, but are neglected in the above computation.

Additional questions arise when trying to justify the identification (2.95) within the semi-classical approach. One would in fact expect the above identification to follow from a collision term of the form of (2.2)

$$\begin{aligned}
C^{\text{NLO}}[n_\chi] = \int d\Pi_{\chi\bar{\chi}(ij)} \sum_{\text{spin}} & \left[|\mathcal{M}_{\chi\bar{\chi}\rightarrow ij}^{\text{NLO}}|^2 (f_i f_j - f_\chi f_{\bar{\chi}}) \right. \\
& + d\Pi_{(\gamma)} |\mathcal{M}_{\chi\bar{\chi}\rightarrow ij\gamma}|^2 (f_i f_j f_\gamma - f_\chi f_{\bar{\chi}}(1+f_\gamma)) \\
& \left. + d\Pi_\gamma |\mathcal{M}_{\chi\bar{\chi}\gamma\rightarrow ij}|^2 (f_i f_j(1+f_\gamma) - f_\chi f_{\bar{\chi}} f_\gamma) \right], \quad (2.97)
\end{aligned}$$

where again we used $1 \pm f \approx 1$ except for the photon distribution function. The collision term (2.97) contains both annihilation and production contributions, which are however symmetric and can be described by the same thermally averaged cross section, as long as the theory is CP invariant and the DM particles are in kinetic equilibrium. It can be most easily seen by making use of the detailed balance relation for the photon distribution function

$$f_\gamma = e^{-\frac{\omega_\gamma}{T}} (1 + f_\gamma), \quad (2.98)$$

and the Maxwell approximation for the remaining ones and the energy conservation. Then the result is

$$C^{\text{NLO}}[n_\chi] = \langle \sigma_{\text{ann}}^{\text{NLO}} v \rangle (n_\chi^{\text{eq}2} - n_\chi^2), \quad (2.99)$$

with

$$\begin{aligned}
\langle \sigma_{\text{ann}}^{\text{NLO}} v \rangle \equiv \frac{1}{n_\chi^{\text{eq}2}} \int d\Pi_{\chi\bar{\chi}(ij)} \sum_{\text{spin}} f_\chi^{\text{eq}} f_{\bar{\chi}}^{\text{eq}} & \left[|\mathcal{M}_{\chi\bar{\chi}\rightarrow ij}^{\text{NLO}}|^2 \right. \\
& \left. + d\Pi_{(\gamma)} |\mathcal{M}_{\chi\bar{\chi}\rightarrow ij\gamma}|^2 (1+f_\gamma) + d\Pi_\gamma |\mathcal{M}_{\chi\bar{\chi}\gamma\rightarrow ij}|^2 f_\gamma \right]. \quad (2.100)
\end{aligned}$$

In order to get the zero-temperature form (2.94) from the above expression the photon distribution has to be neglected. This step is however not justified, since there are relevant regions of photon phase space $d\Pi_\gamma$, where the photon energy is small, in which case $f_\gamma \sim \omega_\gamma^{-1}$ is arbitrarily large. However, if one simply keeps f_γ in the expression for the collision term, the virtual one-loop and real terms, $|\mathcal{M}_{\chi\bar{\chi}\rightarrow ij}^{\text{NLO}}|^2$ and $\int d\Pi_\gamma |\mathcal{M}_{\chi\bar{\chi}\gamma\rightarrow ij}|^2$, respectively, are multiplied by different factors, and the standard IR cancellation no longer occurs. Moreover, since $f_\gamma \sim \omega_\gamma^{-1}$, an additional IR divergence is generated, which is more severe than the zero-temperature, logarithmic divergences. The following questions then arise:

- II. How do the soft and collinear infrared (IR) divergences cancel at finite temperature?
- III. Assuming IR finiteness can be shown, what are the leading finite-temperature effects on the annihilation cross sections and the relic density?

The problems of the approach presented above do actually lead to an ever more fundamental question:

- IV. Does the transport equation itself receive quantum corrections when it is derived from general principles of non-equilibrium quantum field theory (QFT) to NLO accuracy?

In the following we will address the above questions. In the next Section we will comment on questions I. and IV., thus providing an alternative formula to (2.94). The questions II. and III. are then studied in Sec. 2.5, by explicit calculation of the CTP collision term at NLO in the model of Sec. 2.3.1.

2.4.2 NLO collision term at finite temperature

As we have seen in Sec. 2.2, the derivation of the Boltzmann equation is based upon a gradient expansion. The question IV. of the previous Section can then be reformulated in those terms: “is it consistent to retain further terms in the coupling (loop) expansion but only the leading one in the gradients?” In order to answer to this question we have to compare the parameters governing the two expansions. The estimate for the gradients in the freeze-out scenario is given in (2.78), while the perturbative expansion is governed by the coupling factor α . The relevant condition then reads

$$\frac{\nabla}{p} \sim \frac{m_\chi}{M_P} \ll \alpha \ll 1 . \quad (2.101)$$

For DM masses well below the Planck scale and small couplings, the perturbative expansion is therefore justified and the second term is much more important than higher order gradient terms. This discussion justifies the calculation at NLO of the CTP collision term (2.72). We will do this explicitly in our toy model in Sec. 2.5, but we now want to predict the structure of the result. For definiteness we consider again the correction to the process $\chi\bar{\chi} \rightarrow ij$ from an additional electroweak radiation.

We start from the IR-divergent expression (2.100) introduced in the previous Section. First of all it is important to realize that the photons in the plasma contribute not only to the $2 \rightarrow 3$ emission and $3 \rightarrow 2$ absorption processes, but also to the virtual, one-loop two-body amplitude. Indeed, it has been shown in the special cases of muon decay [80] and the right-handed neutrino production rate [81–85] relevant to leptogenesis, that when finite-temperature Feynman rules are used in the computation of the decay or production rate, the additional IR divergence cancels. In particular, leptogenesis also involves a non-equilibrium situation. The proof of the cancellation of all divergences in the general case does not seem to exist, though some partial results can be found in [86–89]. Let us therefore add and make explicit the finite-temperature correction to the virtual correction by replacing

$$|\mathcal{M}_{\chi\bar{\chi} \rightarrow ij}^{\text{NLO}}|^2 \rightarrow |\mathcal{M}_{\chi\bar{\chi} \rightarrow ij}^{\text{NLO } T=0}|^2 + |\mathcal{M}_{\chi\bar{\chi} \rightarrow ij}^{\text{NLO } T \neq 0}|^2 , \quad (2.102)$$

and likewise for the inverse process.⁴ Since the SM particles may have masses smaller or of order of $T_{\text{f.o.}}$, we also abandon the assumption that $f_{i,j}$ are exponentially small in the $2 \rightarrow 3$ and $3 \rightarrow 2$ processes, where particles i, j do not necessarily have energies of order m_χ . We can then extend and reorganize the thermally averaged cross section up to NLO into the expression

$$\begin{aligned} \langle \sigma_{\text{CTP}} v \rangle &= \frac{1}{n_\chi^{\text{eq}2}} \int d\Pi_{\chi\bar{\chi}ij} \sum_{\text{spin}} f_\chi^{\text{eq}} f_{\bar{\chi}}^{\text{eq}} \left\{ \left(|\mathcal{M}_{\chi\bar{\chi} \rightarrow ij}^{\text{LO}}|^2 + |\mathcal{M}_{\chi\bar{\chi} \rightarrow ij}^{\text{NLO } T=0}|^2 + d\Pi_\gamma |\mathcal{M}_{\chi\bar{\chi} \rightarrow ij\gamma}|^2 \right) \right. \\ &+ |\mathcal{M}_{\chi\bar{\chi} \rightarrow ij}^{\text{NLO } T \neq 0}|^2 + d\Pi_\gamma \left[f_\gamma (|\mathcal{M}_{\chi\bar{\chi} \rightarrow ij\gamma}|^2 + |\mathcal{M}_{\chi\bar{\chi}\gamma \rightarrow ij}|^2) \right. \\ &\left. \left. + f_i (|\mathcal{M}_{\chi\bar{\chi}i \rightarrow j\gamma}|^2 \pm |\mathcal{M}_{\chi\bar{\chi} \rightarrow ij\gamma}|^2) + f_j (|\mathcal{M}_{\chi\bar{\chi}j \rightarrow i\gamma}|^2 \pm |\mathcal{M}_{\chi\bar{\chi} \rightarrow ij\gamma}|^2) \right] \right\}, \quad (2.103) \end{aligned}$$

where for simplicity we do not distinguish any more $d\Pi_{\chi\bar{\chi}(ij\gamma)}$ from $d\Pi_{\chi\bar{\chi}i(j\gamma)}$, with the interpretation $d\Pi_{\mathbf{i}\mathbf{f}} |\mathcal{M}_{\mathbf{i} \rightarrow \mathbf{f}}|^2 = d\Pi_{\mathbf{i}(\mathbf{f})} |\mathcal{M}_{\mathbf{i} \rightarrow \mathbf{f}}|^2$. Note that we have neglected terms with more than three distribution functions, as they are necessarily exponentially suppressed relative to those given, since the kinematics of $2 \leftrightarrow 3$ processes allows only one particle to be soft. The NLO collision term also includes the processes $\chi\bar{\chi}j \leftrightarrow i\gamma$, and $\chi\bar{\chi}i \leftrightarrow j\gamma$, which appear first at this order. In the effective cross section there are both T -independent and T -dependent IR divergences. The former are present in the first line on the right-hand side of (2.103). However, the expressions in the brackets are IR finite by the standard $T = 0$ KLN cancellations, and we will not discuss them further. Our main interest is in the remaining two lines which contain the finite-temperature correction to the one-loop virtual amplitude and emission and absorption processes multiplied by additional phase-space distribution functions. In the next Section we will demonstrate by explicit calculation that the CTP collision term (2.72) up to NLO in the couplings can indeed be written as

$$C_{\text{CTP}} = \langle \sigma_{\text{CTP}} v \rangle (n_\chi^{\text{eq}2} - n_\chi^2), \quad (2.104)$$

where the CTP annihilation cross section is given, as in (2.103), by the sum of the standard $T = 0$ cross section up to NLO and an additional *thermal* NLO correction

$$\sigma_{\text{CTP}} = \sigma_{\text{ann}}^{\text{LO}} + \sigma_{\text{ann}}^{\text{NLO } T=0} + \sigma_{\text{ann}}^{\text{NLO } T \neq 0}. \quad (2.105)$$

We will also prove that the finite-temperature correction is IR finite.

2.5 The collision term at next-to-leading order

In the previous Section we concluded that the CTP collision term (2.72) for DM in the freeze-out scenario can consistently be computed at the NLO in the coupling expansion. In this

⁴Note that for the standard WIMP annihilation scenarios, there are no finite-temperature corrections to the tree-level amplitudes of $2 \rightarrow 2$ and $2 \rightarrow 3$ or $3 \rightarrow 2$ processes, because at tree level annihilation occurs through t -channel exchange of a particle with mass larger than m_χ , or through highly virtual s -channel particles.

Section we perform this calculation explicitly within the model described in Sec. 2.3.1, for which we found at the LO the result (2.73). As we are primarily interested in the infrared divergence cancellation at finite temperature and the leading finite-temperature correction, we drop the terms that can be associated with the $T = 0$ NLO correction.⁵ Our aim is therefore to show that

$$\begin{aligned}
C_{\text{CTP}}^{\text{NLO } T \neq 0} = & \int d\Pi_{\chi\bar{\chi}ij} \sum_{\text{spin}} (f_{\chi}^{\text{eq}} f_{\bar{\chi}}^{\text{eq}} - f_{\chi} f_{\bar{\chi}}) \left\{ |\mathcal{M}_{\chi\bar{\chi} \rightarrow ij}^{\text{NLO } T \neq 0}|^2 \right. \\
& + d\Pi_{\gamma} \left[f_{\gamma} (|\mathcal{M}_{\chi\bar{\chi} \rightarrow ij\gamma}|^2 + |\mathcal{M}_{\chi\bar{\chi}\gamma \rightarrow ij}|^2) \right. \\
& \left. \left. + f_i (|\mathcal{M}_{\chi\bar{\chi}i \rightarrow j\gamma}|^2 \pm |\mathcal{M}_{\chi\bar{\chi} \rightarrow ij\gamma}|^2) + f_j (|\mathcal{M}_{\chi\bar{\chi}j \rightarrow i\gamma}|^2 \pm |\mathcal{M}_{\chi\bar{\chi} \rightarrow ij\gamma}|^2) \right] \right\}, \quad (2.106)
\end{aligned}$$

and that this is IR finite. In Sec. 2.5.1 we list the three-loops CTP self-energies that enter the calculation and we show explicitly on an example diagram how they reproduce (2.106). We then describe the method of computing the finite-temperature cross sections entering (2.106) in Sec. 2.5.2, emphasizing the differences with respect to the $T = 0$ case. The results and the discussion are finally presented in Sec. 2.5.3. The main result, obtained for the first time in our paper [34], is the demonstration of the IR finiteness of relic density computations at NLO. The leading thermal correction is found to be suppressed by four powers of the temperature T^4/m_{χ}^4 , with respect to the standard $T = 0$ radiative correction.

2.5.1 Calculation of an example diagram

The Feynman diagrams that we have to compute are the three-loop DM self-energies obtained by adding a photon line in all possible ways to the diagrams A and B in Fig. 2.3. Diagrams leading to s-channel photon exchange via a loop-induced $\chi\bar{\chi}\gamma$ coupling of DM to the photon do not contribute to the *thermal* correction. At NLO there are 24 three-loop self-energy diagrams contributing to $\Sigma^>$ of a Majorana fermion. They are given in Tables 2.1 and 2.2, together with the corresponding processes that they describe after associating the terms in the CTP sums with squared matrix elements. Since the thermal part of the propagators always contains the on-shell delta function $\delta(p^2 - m^2)$ we refer to these contributions as “cuts” of the self-energy diagrams.

As an example we consider in this Section the self-energy diagram in Fig. 2.6, which corresponds to the diagram in the 10th line of Table 2.2. Following the rules described in Sec. 2.3, we obtain $2^4 = 16$ different terms from the CTP sum over circled and uncircled vertices. Most of them, however, do not contribute as they involve the exponentially suppressed thermal part

⁵The finite part of the $T = 0$ correction is indeed parametrically larger than the finite- T correction. Its computation is already well understood and could be straightforwardly included in the formalism presented here.

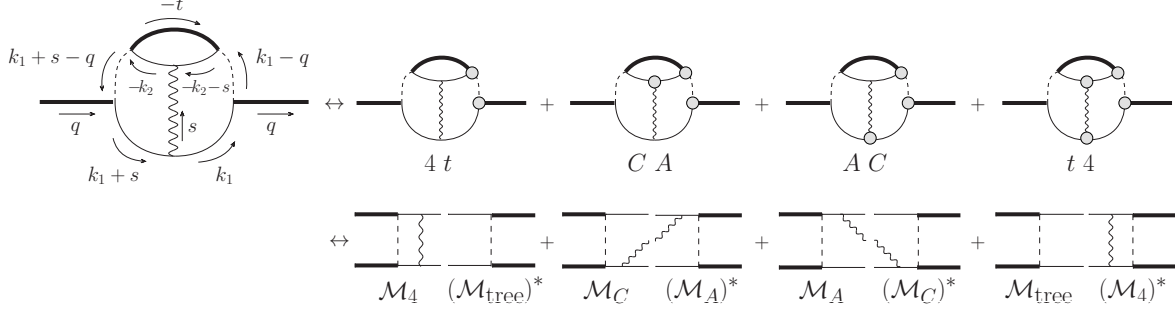


Figure 2.6: An example three-loop self-energy contribution to $i\Sigma^>$ decomposed into a sum over “cuts” and the interpretation of the cuts as scattering processes. For simplicity we omit the imaginary unit from the labels, such that for a diagram labeled by \mathcal{M} , the associated amplitude is given by $i\mathcal{M}$. $i\Sigma^>$ is obtained by taking the sum over all possible diagrams in which the vertex attached to the external line on the left (right) is of type ‘+’ (‘-’). The correspondence between reversing the charge flow arrows and crossing the external fermion legs is the same as displayed in Fig. 2.5. For simplicity, from this Figure on, we will denote with a single diagram with no arrows the sum of the two diagrams with and without reversed arrows.

of the scalar propagator. As shown in Fig. 2.6, the remaining four can be associated with virtual and real photon NLO corrections. To confirm this interpretation, we consider the second cut of the diagram in Fig. 2.6, labelled CA , and show that it corresponds to the interference term of the two real photon emission amplitudes from the different final state legs multiplied by the associated Bose enhancement factors. Proceeding as in Sec. 2.3.2 we obtain for this contribution the expression

$$\begin{aligned}
\text{Tr} [i\Sigma_{CA}^>(q) iS^<(q)] &= -\lambda^4 e^2 \int \frac{d^4 t}{(2\pi)^4} \frac{d^4 k_1}{(2\pi)^4} \frac{d^4 k_2}{(2\pi)^4} \frac{d^4 s}{(2\pi)^4} (2\pi)^4 \delta^{(4)}(q+t-k_1-k_2-s) \\
&\times \underbrace{i\Delta^{++}(k_1+s-q) i\Delta^{--}(k_1-q)}_{\equiv \mathcal{S}} \underbrace{\text{Tr}\{P_R iS^{-+}(-t) P_L iS^{+-}(-k_2) \gamma^\mu iS^{--}(-k_2-s)\}}_{\equiv \mathcal{F}_1} \\
&\times \underbrace{iD_{\mu\nu}^{++}(s)}_{\equiv \mathcal{V}} \underbrace{\text{Tr}\{P_L iS^{+-}(k_1) \gamma^\nu iS^{++}(k_1+s) P_R iS^{+-}(q)\}}_{\equiv \mathcal{F}_2} . \tag{2.107}
\end{aligned}$$

In the scalar part \mathcal{S} it is again sufficient to keep only the $T=0$ part of the propagators, while the photon propagator \mathcal{V} contains only the thermal part. Omitting for brevity the traces over the numerator Dirac matrices we get

$$\mathcal{V} = -g_{\mu\nu} 2\pi \delta(s^2) [\Theta(s^0) (1+f_B(\omega_\gamma)) + \Theta(-s^0) f_B(\omega_\gamma)] , \tag{2.108}$$

$$\begin{aligned}
\mathcal{F}_1 &\propto 2\pi\delta(t^2 - m_\chi^2) [-\Theta(-t^0)(1 - f_\chi(\omega_{\bar{\chi}})) + \Theta(t^0)f_\chi(\omega_{\bar{\chi}})] \\
&\quad \times 2\pi\delta(k_2^2 - m_f^2) [\Theta(-k_2^0)f_F(\omega_{\bar{f}}) - \Theta(k_2^0)(1 - f_F(\omega_{\bar{f}}))] \\
&\quad \times \left[\frac{-i}{(k_2 + s)^2 - m_f^2 - i\eta} - 2\pi\delta((k_2 + s)^2 - m_f^2) \right. \\
&\quad \left. \times [\Theta(-k_2^0 - s^0)f_F(|k_2^0 + s^0|) + \Theta(k_2^0 + s^0)f_F(|k_2^0 + s^0|)] \right], \quad (2.109)
\end{aligned}$$

$$\begin{aligned}
\mathcal{F}_2 &\propto 2\pi\delta(k_1^2 - m_f^2) [-\Theta(k_1^0)(1 - f_F(\omega_f)) + \Theta(-k_1^0)f_F(\omega_f)] \\
&\quad \times \left[\frac{i}{(k_1 + s)^2 - m_f^2 + i\eta} - 2\pi\delta((k_1 + s)^2 - m_f^2) \right. \\
&\quad \left. \times [\Theta(k_1^0 + s^0)f_F(|k_1^0 + s^0|) + \Theta(-k_1^0 - s^0)f_F(|k_1^0 + s^0|)] \right] \\
&\quad \times (2\pi)\delta(q^2 - m_\chi^2) [\Theta(q^0)f_\chi(\omega_\chi) - \Theta(-q^0)(1 - f_\chi(\omega_\chi))], \quad (2.110)
\end{aligned}$$

where we use the definitions in (2.87) and additionally $\omega_\gamma \equiv |\vec{s}|$. From the above expressions we see that the contributions from the thermal parts of the $S^{++}(k_1 + s)$ and $S^{--}(-k_2 - s)$ are vanishing, since the combination of δ -functions multiplying those terms has no support. We are then left with 32 terms, from which again half vanishes after multiplying by $\Theta(q^0)$. Out of the remaining terms, 8 describe emission and 8 absorption of a photon attached to the tree-level diagram. Among those terms there are 6 that correspond to processes which are kinematically forbidden and from the remaining ones 6 describe scatterings and 4 annihilation. Only annihilation terms eventually contribute to the Boltzmann equation for the χ particle number, hence (2.107) simplifies to

$$\begin{aligned}
\text{Tr} [\Sigma_{CA}^>(p_\chi) S^<(p_\chi)] &= \frac{1}{2\omega_\chi} (2\pi)\delta(p_\chi^0 - \omega_\chi) \int d\Pi_{\bar{\chi}} d\Pi_f d\Pi_{\bar{f}} d\Pi_\gamma \sum_{\text{spin}} f_\chi(\omega_\chi) f_\chi(\omega_{\bar{\chi}}) \\
&\quad \times \left[\delta^{(4)}(p_\chi + p_{\bar{\chi}} - p_f - p_{\bar{f}} - p_\gamma) |\mathcal{M}_{CA}(p_f, p_{\bar{f}}, p_\gamma)|^2 (1 - f_F(\omega_f)) (1 - f_F(\omega_{\bar{f}})) (1 + f_B(\omega_\gamma)) \right. \\
&\quad - \delta^{(4)}(p_\chi + p_{\bar{\chi}} - p_f - p_{\bar{f}} + p_\gamma) |\mathcal{M}_{CA}(p_f, p_{\bar{f}}, -p_\gamma)|^2 f_B(\omega_\gamma) (1 - f_F(\omega_f)) (1 - f_F(\omega_{\bar{f}})) \\
&\quad - \delta^{(4)}(p_\chi + p_{\bar{\chi}} - p_f + p_{\bar{f}} - p_\gamma) |\mathcal{M}_{CA}(p_f, -p_{\bar{f}}, p_\gamma)|^2 f_F(\omega_{\bar{f}}) (1 - f_F(\omega_f)) (1 + f_B(\omega_\gamma)) \\
&\quad \left. - \delta^{(4)}(p_\chi + p_{\bar{\chi}} + p_f - p_{\bar{f}} - p_\gamma) |\mathcal{M}_{CA}(-p_f, p_{\bar{f}}, p_\gamma)|^2 f_F(\omega_f) (1 - f_F(\omega_{\bar{f}})) (1 + f_B(\omega_\gamma)) \right], \quad (2.111)
\end{aligned}$$

where we renamed the momenta as in (2.88) and we defined $p_\gamma \equiv s$. The factors $\sum_{\text{spin}} |\mathcal{M}_{CA}|^2$ collect the traces contained in the definition of \mathcal{F}_1 and \mathcal{F}_2 , coupling constants, as well as the non-thermal propagator denominators. The first one (the second line of (2.111)) can be

identified with the interference of zero-temperature emission amplitude, namely

$$|\mathcal{M}_{CA}(p_f, p_{\bar{f}}, p_\gamma)|^2 = \mathcal{M}_C (\mathcal{M}_A)^* . \quad (2.112)$$

By crossing symmetry one can identify the remaining ones with the amplitudes for absorption processes:

$$\begin{aligned} |\mathcal{M}_{CA}(p_f, p_{\bar{f}}, -p_\gamma)|^2 &= |\mathcal{M}_{CA}^{X\bar{X}\gamma \rightarrow f\bar{f}}(p_f, p_{\bar{f}}, p_\gamma)|^2 , \\ -|\mathcal{M}_{CA}(-p_f, p_{\bar{f}}, p_\gamma)|^2 &= |\mathcal{M}_{CA}^{X\bar{X}\bar{f} \rightarrow \bar{f}\gamma}(p_f, p_{\bar{f}}, p_\gamma)|^2 , \\ -|\mathcal{M}_{CA}(p_f, -p_{\bar{f}}, p_\gamma)|^2 &= |\mathcal{M}_{CA}^{X\bar{X}f \rightarrow f\gamma}(p_f, p_{\bar{f}}, p_\gamma)|^2 , \end{aligned} \quad (2.113)$$

where the minus sign comes from interchanging the fermions between initial and final states.

As for the LO result (2.89), we now have to add the hermitian conjugate, integrate with $-d^4p_x/(2\pi)^4 \frac{1}{2} \Theta(p_x^0)$, multiply by the factor 1/2 in (2.82) and repeat the same calculation for $\Sigma^<S^>$. The example shows that the surviving terms from the three-loop CTP self-energy correspond precisely to the collision term in the form of (2.106), once terms with more than three distribution functions are neglected. In the following Section we discuss the computation of the IR divergent and leading IR finite thermal correction, separately for the real and virtual cuts.

2.5.2 Calculation with scattering methods

In the previous Sections we have seen that the CTP collision term at NLO in the coupling expansion can be written as in (2.106), namely in terms of an effective cross section (2.104), which is the sum of various integrated scattering matrix elements computed with finite-temperature Feynman rules (2.103). We now turn to the explicit calculation of those squared matrix elements. As shown in Tables 2.1 and 2.2, from the annihilation amplitude point of view the diagrams that we have to compute can be arranged into three classes: *i*) processes corresponding to thermal emission and absorption, *ii*) thermal internal virtual corrections and *iii*) thermal corrections to mass and wave-function renormalization on the external legs. We use this classification for organizing the discussion of the computation in this Section, even though it is somewhat artificial from the self-energy diagram point of view. The reason is that we want to show a clear connection between the usual way of doing calculations and the quantities appearing in the collision term as derived from CTP formalism. When showing the results for IR divergence cancellation and leading thermal correction in Sec. 2.5.3, we revert to the more natural classification based on different self-energy diagrams.

As we will see in the following, each thermal NLO term in (2.106) can be written as

$$\int_{\omega_{\min}}^{\omega_{\max}} d\omega f_{B,F}(\omega) S(\omega) , \quad (2.114)$$

where ω is the energy of the thermal particle measured in the rest frame of the plasma. The lower extreme ω_{\min} is equal to the mass of the thermal particle while the upper one ω_{\max} is determined by the phase-space δ -function contained in the integration measure. For virtual corrections to the $2 \rightarrow 2$ process and for the $3 \rightarrow 2$ (absorption) processes $\omega_{\max} = \infty$, while for the $2 \rightarrow 3$ (emission) processes there is a kinematic limit $\omega_{\max} \sim \mathcal{O}(m_\chi)$. In the freeze-out framework, we are interested at temperatures around $T_{\text{f.o.}} \sim m_\chi/20$, such that the equilibrium distributions $f_{B,F}(\omega)$ are exponentially suppressed for $\omega \sim m_\chi$. The upper limit in (2.114) is therefore not relevant and may be safely extended to infinity. In the case of thermal fermion contributions $\omega_{\min} = m_f$ and the integral (2.114) can only be solved numerically. However, such contributions are either exponentially suppressed (if $m_f \gtrsim T$) or effectively as in the massless case (if $m_f \ll gT$). In particular, in the temperature range which we are interested in, the light SM fermions can be treated as massless.⁶ In the following, for thermal fermions we will present the analytic expressions in the $m_f = 0$ limit. The methods of calculation are however applicable in general for finite m_f .

At this point we can perform an expansion of $S(\omega)$ retaining terms up to linear order in ω/m_χ , and the final integral over ω can be expressed in terms of

$$T^{n+1}J_n \equiv \int_0^\infty d\omega f_B(\omega) \omega^n = \begin{cases} \text{divergent} & n \leq 0, \\ \mathcal{O}(T^{n+1}) & n > 0, \end{cases} \quad (2.115)$$

for thermal photon, and

$$T^{n+1}I_n \equiv \int_0^\infty d\omega f_F(\omega) \omega^n = \begin{cases} \text{divergent} & n \leq -1, \\ \mathcal{O}(T^{n+1}) & n > -1, \end{cases} \quad (2.116)$$

for thermal fermion. The divergence for $n = 0$ in (2.115) follows from the Bose enhancement $f_B(\omega) \sim \omega^{-1}$ of soft photons and implies a stronger divergence than at zero temperature, where the soft IR divergence is only logarithmic. There is no such enhancement for fermions, hence the only divergence that is encountered in this case comes from the terms proportional to ω^{-1} . Of particular relevance will be the integrals

$$J_1 = 2I_1 = \frac{\pi^2}{6}, \quad J_3 = \frac{8}{7}I_3 = \frac{\pi^4}{15}, \quad (2.117)$$

to which the corrections of order $\mathcal{O}(T^2)$ and $\mathcal{O}(T^4)$ are proportional.

Thermal emission and absorption

The computation of the emission and absorption processes at finite temperature follows the same procedure as is well known from the $T = 0$ case, simply because at NLO all the contributions from the thermal part of internal propagators are either exponentially suppressed or

⁶The top quark on the other hand is too heavy to be present in the plasma, unless the DM particle mass is significantly above 1 TeV.

kinematically forbidden at this order, as explained for the example diagram in Sec. 2.5.1. The only difference comes from the fact that the external particles can be thermal, in which case the corresponding external leg is multiplied by the phase-space distribution function. From (2.106), that we justified in Sec. 2.5.1, the thermal emission and absorption contributions to the annihilation process are given by

$$C_{\text{CTP}}^{\text{real } T \neq 0} = \int d\Pi_{\chi\bar{\chi}f\bar{f}\gamma} \sum_{\text{spin}} (f_{\chi}^{\text{eq}} f_{\bar{\chi}}^{\text{eq}} - f_{\chi} f_{\bar{\chi}}) \left[f_{\gamma} (|\mathcal{M}_{\chi\bar{\chi} \rightarrow f\bar{f}\gamma}|^2 + |\mathcal{M}_{\chi\bar{\chi}\gamma \rightarrow f\bar{f}}|^2) \right. \\ \left. + f_{\bar{f}} (|\mathcal{M}_{\chi\bar{\chi}\bar{f} \rightarrow \bar{f}\gamma}|^2 - |\mathcal{M}_{\chi\bar{\chi} \rightarrow f\bar{f}\gamma}|^2) + f_f (|\mathcal{M}_{\chi\bar{\chi}f \rightarrow f\gamma}|^2 - |\mathcal{M}_{\chi\bar{\chi} \rightarrow f\bar{f}\gamma}|^2) \right]. \quad (2.118)$$

Let us focus first on photon emission and absorption, given in the first line. During the freeze-out photons are in equilibrium, and therefore emission and absorption of hard photons with energies ω of order of $m_{\chi} \gg T \sim T_{\text{f.o.}}$ are exponentially suppressed by the distribution function f_{γ} . The scattering matrix elements can therefore be evaluated in an expansion in $\omega \sim T_{\text{f.o.}} \ll m_{\chi}$, that is, in the soft-photon regime. In particular, the leading IR divergence could be obtained from the amplitudes in the eikonal approximation. However, since we are interested also in the leading finite thermal correction, we compute the full amplitude. After performing the integration over all phase-space variables except the energy ω of the emitted or absorbed particle, we are left with an expression of the form (2.114)

$$\int d\Pi_{f\bar{f}\gamma} f_{\gamma} |\mathcal{M}_{\chi\bar{\chi} \rightarrow f\bar{f}\gamma}|^2 = \int_0^{\omega_{\text{max}}} d\omega f_B(\omega) S_{\chi\bar{\chi} \rightarrow f\bar{f}\gamma}(\omega). \quad (2.119)$$

The amplitude for the annihilation process $\chi(p_1)\bar{\chi}(p_2) \rightarrow f(k_1)\bar{f}(k_2)\gamma(q)$ can be written as⁷

$$i\mathcal{M}_{\text{em}} \equiv i\mathcal{M}_{\chi\bar{\chi} \rightarrow f\bar{f}\gamma} = i g \lambda^2 [(\mathcal{M}_A - \mathcal{M}_A^{\text{exc}}) + (\mathcal{M}_B - \mathcal{M}_B^{\text{exc}}) + (\mathcal{M}_C - \mathcal{M}_C^{\text{exc}})], \quad (2.120)$$

where the letters A, B, C refer to the amplitudes as given in Table 2.1, and the three terms are

$$\mathcal{M}_A - \mathcal{M}_A^{\text{exc}} = \frac{\bar{u}(k_1)\not{\epsilon}^*(q)(\not{k}_1 + \not{q} + m_f)P_R u(p_1) \bar{v}(p_2)P_L v(k_2)}{[(k_1 + q)^2 - m_f^2][(p_2 - k_2)^2 - m_{\phi}^2]} - (p_1 \leftrightarrow p_2), \quad (2.121)$$

$$\mathcal{M}_B - \mathcal{M}_B^{\text{exc}} = (p_2 - p_1 + k_1 - k_2) \cdot \epsilon^*(q) \frac{\bar{u}(k_1)P_R u(p_1) \bar{v}(p_2)P_L v(k_2)}{[(p_1 - k_1)^2 - m_{\phi}^2][(p_2 - k_2)^2 - m_{\phi}^2]} - (p_1 \leftrightarrow p_2), \quad (2.122)$$

$$\mathcal{M}_C - \mathcal{M}_C^{\text{exc}} = \frac{\bar{u}(k_1)P_R u(p_1) \bar{v}(p_2)P_L(-\not{k}_2 - \not{q} + m_f)\not{\epsilon}^*(q)v(k_2)}{[(k_2 + q)^2 - m_f^2][(p_1 - k_1)^2 - m_{\phi}^2]} - (p_1 \leftrightarrow p_2). \quad (2.123)$$

For the absorption process, due to the crossing symmetry, the amplitude squared summed over polarizations can be obtained from the emission process by changing the sign of the four momentum of the particle emitted and absorbed from the thermal bath, as in (2.113).

⁷For the amplitudes we follow the notation of [90].

Although the emission and absorption contributions have different phase-space integration limits, we have already seen that this is irrelevant up to exponentially small terms in m_χ/T . Thus, when the emission contribution is expanded in the form

$$S_{\chi\bar{\chi}\rightarrow f\bar{f}\gamma}(\omega) = \sum_{n=-1}^{\infty} S^{(n)}\omega^n, \quad (2.124)$$

the crossing symmetry (2.113) implies

$$S_{\chi\bar{\chi}\gamma\rightarrow f\bar{f}}(\omega) = \sum_{n=-1}^{\infty} (-1)^{n+1} S^{(n)}\omega^n, \quad (2.125)$$

for the corresponding absorption process. Since (2.118) always involves the sum of emission and absorption, even terms in the expansion in ω cancel. Eqs. (2.115), (2.116) then imply that the leading finite-temperature correction is at least of order $\tau^2 \equiv T^2/m_\chi^2$.

The contributions to the function $S(\omega)$ from thermal photon emission and absorption, though divergent, can be computed without regularization in four dimensions. As we will show later, in fact, the cancellation of the linear IR divergence (proportional to J_{-1}) against the thermal virtual correction, can be shown algebraically before integration over the photon energy ω . The integration over the remaining phase-space variables that was already done to arrive at the function $S(\omega)$ is finite, since the non-vanishing fermion mass plays the role of the regulator for collinear divergences. This is no longer the case when the thermal fermion emission and absorption processes are considered, since the integral over photon energy contained in $S(\omega)$ has to be regularized. In this case we perform the phase-space integration in dimensional regularization with $D = 4 - 2\eta$ and $\eta < 0$.

Thermal virtual corrections

Thermal virtual corrections arise from terms in the CTP sum, to which the thermal parts of the diagonal ‘++’ or ‘--’ photon and fermion propagators contribute. As the scalar is at least as heavy as the DM particle it has a negligible thermal contribution and we do not consider the corresponding amplitudes. We only need to include the terms when one of the virtual particles is thermal. When two are thermal this gives the imaginary part, which does not contribute to the real part of the interference with the tree diagram, while when three are thermal at least one of them has to have momentum of order m_χ and is therefore exponentially suppressed by the phase-space distribution function.

We denote the relevant amplitudes by \mathcal{M}_i with $i = 1, \dots, 5$, and the contribution from the thermal part of the photon (SM fermion) propagator by \mathcal{M}_i^γ (\mathcal{M}_i^f). The corresponding diagrams are displayed in Table 2.1. The general form of every virtual contribution is

$$i\mathcal{M}_i^{\gamma,f} = \int \frac{d^4q}{(2\pi)^4} F_i^{\gamma,f}(q^0, \vec{q}) 2\pi\delta(q^2 - m_{\gamma,f}^2) f_{B,F}(|q^0|), \quad (2.126)$$

where $m_\gamma = 0$ and for thermal photons

$$F_1^\gamma = -ig^2\lambda^2 \frac{\bar{u}(k_1)(2\not{p}_1 - 2\not{k}_1 + \not{q})(\not{k}_1 - \not{q} + m_f)P_R u(p_1)\bar{v}(p_2)P_L v(k_2)}{[(k_1 - q)^2 - m_f^2][(p_1 - k_1 + q)^2 - m_\phi^2][(p_1 - k_1)^2 - m_\phi^2]} - (p_1 \leftrightarrow p_2), \quad (2.127)$$

$$F_2^\gamma = F_1^\gamma, \quad (2.128)$$

$$F_3^\gamma = \frac{ig^2\lambda^2}{2} \frac{(2p_1 - 2k_1 - q)^2 \bar{u}(k_1)P_R u(p_1)\bar{v}(p_2)P_L v(k_2)}{[(p_1 - k_1)^2 - m_\phi^2]^2[(p_1 - k_1 - q)^2 - m_\phi^2]} - (p_1 \leftrightarrow p_2), \quad (2.129)$$

$$F_4^\gamma = ig^2\lambda^2 \frac{\bar{u}(k_1)\gamma^\mu(\not{k}_1 + \not{q} + m_f)P_R u(p_1)\bar{v}(p_2)P_L(-\not{k}_2 + \not{q} + m_f)\gamma_\mu v(k_2)}{[(k_1 + q)^2 - m_f^2][(p_1 - k_1 - q)^2 - m_\phi^2][(k_2 - q)^2 - m_f^2]} - (p_1 \leftrightarrow p_2), \quad (2.130)$$

$$F_5^\gamma = -4ig^2\lambda^2 \frac{\bar{u}(k_1)P_R u(p_1)\bar{v}(p_2)P_L v(k_2)}{[(p_1 - k_1)^2 - m_\phi^2]^2} - (p_1 \leftrightarrow p_2), \quad (2.131)$$

while for thermal fermions,

$$F_1^f = ig^2\lambda^2 \frac{\bar{u}(k_1)(2\not{p}_1 - \not{k}_1 - \not{q})(\not{q} + m_f)P_R u(p_1)\bar{v}(p_2)P_L v(k_2)}{(q - k_1)^2[(p_1 - q)^2 - m_\phi^2][(p_1 - k_1)^2 - m_\phi^2]} - (p_1 \leftrightarrow p_2), \quad (2.132)$$

$$F_2^f = F_1^f, \quad (2.133)$$

$$F_4^f = -ig^2\lambda^2 \frac{\bar{u}(k_1)\gamma^\mu(\not{q} + m_f)P_R u(p_1)\bar{v}(p_2)P_L(\not{q} - \not{k}_1 - \not{k}_2 + m_f)\gamma_\mu v(k_2)}{[(q - k_1 - k_2)^2 - m_f^2][(p_1 - q)^2 - m_\phi^2](q - k_1)^2} - (p_1 \leftrightarrow p_2). \quad (2.134)$$

Note that $F_3^f = F_5^f = 0$, since there are no internal fermion lines in these diagrams, and that F_4^f has to be counted twice, since any one of the two fermion lines in the loop can be thermal.

Given these expressions we first perform the integral over q^0 , which leads to

$$\mathcal{M}_i^{\gamma,f} = \int \frac{d^3\vec{q}}{(2\pi)^3 2\omega} \left[F_i^{\gamma,f}(\omega, \vec{q}) + F_i^{\gamma,f}(-\omega, \vec{q}) \right] f_{B,F}(\omega), \quad (2.135)$$

with

$$\omega \equiv \begin{cases} |\vec{q}| & \text{for photons,} \\ \sqrt{\vec{q}^2 + m_f^2} & \text{for fermions.} \end{cases} \quad (2.136)$$

Changing the integration variable $\vec{q} \rightarrow -\vec{q}$ in the second integral gives $F_i^{\gamma,f}(q) + F_i^{\gamma,f}(-q)$ in the bracket. Then we compute the interference of the resulting expression with the tree-level amplitude and perform the integration over the two-body phase space together with the angles of \vec{q} . We are left with an integral over the ω in the form of (2.114), which can be computed in expansion in T/m_χ by expanding the integrand in ω . The result involves the same integrals J_n, I_n as was the case for the emission and absorption terms.

Thermal corrections to external legs

The remaining part of the virtual correction can be interpreted as a thermal correction to the mass and wave-function renormalization of the external SM fermion lines. Due to the universality of the renormalization factor, we can follow the standard procedure (see e.g. [80,91]) of computing the one-loop corrected thermal propagator

$$iS_F^T(p) = \frac{i}{\not{p} - m_f - \text{Re } \Sigma^T} . \quad (2.137)$$

When the result for the self-energy at one loop is written as

$$\Sigma^T(p) = \not{p}c_B - 2m_f(c_B + c_F) + (\not{K}_B + \not{K}_F) , \quad (2.138)$$

with quantities $c_{B,F}$, $K_{B,F}^\mu$ to be defined shortly, the propagator is expressed as

$$iS_F^T(p) = i \frac{\not{p}(1 - c_B) + m_f[1 - 2(c_B + c_F)] - (\not{K}_B + \not{K}_F)}{p^2(1 - 2c_B) - m_f^2[1 - 4(c_B + c_F)] - 2p \cdot (K_B + K_F) + \mathcal{O}(\alpha^2)} . \quad (2.139)$$

The subscript B refers to the contribution when the photon propagator in the one-loop self-energy diagram is thermal and the SM fermion propagator is not. Vice-versa for the quantities with subscript F . Then

$$c_B = 2g^2 \int \frac{d^4q}{(2\pi)^3} \frac{\delta(q^2) f_B(|q^0|)}{(p+q)^2 - m_f^2} , \quad K_B^\mu = 2g^2 \int \frac{d^4q}{(2\pi)^3} q^\mu \frac{\delta(q^2) f_B(|q^0|)}{(p+q)^2 - m_f^2} , \quad (2.140)$$

for the thermal photon contribution, and

$$c_F = -2g^2 \int \frac{d^4q}{(2\pi)^3} \frac{\delta(q^2 - m_f^2) f_F(|q^0|)}{(p+q)^2} , \quad K_F^\mu = 2g^2 \int \frac{d^4q}{(2\pi)^3} q^\mu \frac{\delta(q^2 - m_f^2) f_F(|q^0|)}{(p+q)^2} , \quad (2.141)$$

for thermal fermions. The wave-function renormalization factor is derived from the expansion of the propagator around the particle pole. Let $\hat{p}^\mu = (\hat{p}^0, \vec{p})$ with $\hat{p}^0 = (m_f^2 + \vec{p}^2)^{1/2}$ be the on-shell limit of the external momentum p , and let \hat{f} denote the value $f(\hat{p})$ of a function $f(p^0, \vec{p})$. Then one finds that c_B vanishes on-shell by antisymmetry of the integrand under $q \rightarrow -q$, i.e. $\hat{c}_B = 0$, so that its expansion around the on-shell value reads

$$c_B = (p^2 - m_f^2) \hat{c}'_B + \mathcal{O}((p^2 - m_f^2)^2) , \quad \text{with} \quad \hat{c}'_B = -\frac{\alpha}{\pi} \frac{J_{-1}}{m_f^2} , \quad (2.142)$$

and J_{-1} the divergent integral defined in (2.115). The explicit calculation of the integral defining c_F in (2.141) shows that the thermal fermion contribution \hat{c}_F is only vanishing in the $m_f = 0$ limit, so that in general

$$c_F = \hat{c}_F + (p^2 - m_f^2) \hat{c}'_F + \mathcal{O}((p^2 - m_f^2)^2) . \quad (2.143)$$

The coefficients \hat{c}_F and \hat{c}'_F can be obtained in general by solving the integrals numerically. In the massless case they simplify to

$$\hat{c}_F|_{m_f=0} = 0, \quad \hat{c}'_F|_{m_f=0} = \frac{4\alpha}{3\pi|\vec{p}|^2} I_{-1}, \quad (2.144)$$

with I_{-1} defined in (2.116). The vector contribution from the photon \hat{K}_B^μ in the on-shell limit reads

$$\hat{K}_B^\mu = \frac{\alpha}{\pi} J_1 \frac{T^2}{|\vec{p}|} \left(L_p, \frac{\vec{p}}{|\vec{p}|} \left[\frac{\hat{p}^0}{|\vec{p}|} L_p - 2 \right] \right), \quad \text{with} \quad L_p = \log \frac{\hat{p}^0 + |\vec{p}|}{\hat{p}^0 - |\vec{p}|}, \quad (2.145)$$

and J_1 given by (2.117). The fermion contribution \hat{K}_F^μ in the massless limit is divergent on-shell. We use dimensional regularization ($D = 4 - 2\eta$ and the $\overline{\text{MS}}$ scheme), which gives

$$\hat{K}_F^\mu|_{m_f=0} = \frac{\alpha}{\pi} I_1^D \frac{T^2}{|\vec{p}|} \left(\mathcal{I}(\eta), \frac{\vec{p}}{|\vec{p}|} \left[\frac{\hat{p}^0}{|\vec{p}|} \mathcal{I}(\eta) - 2 \right] \right), \quad \text{with} \quad \mathcal{I}(\eta) = \frac{\sqrt{\pi} e^{\eta\gamma_E}}{(-\eta)\Gamma(\frac{1}{2} - \eta)}, \quad (2.146)$$

where

$$T^2 I_1^D = \mu^{2\eta} \int_0^\infty d\omega \omega^{1-2\eta} f_F(\omega), \quad (2.147)$$

is the D -dimensional generalization of (2.116). The quantities $2p \cdot K_B$, $2p \cdot K_F$ appearing in the denominator of (2.139) can be related to c_B , c_F by

$$2p \cdot K_B = \delta m_B^2 - (p^2 - m_f^2) c_B, \quad 2p \cdot K_F = \delta m_F^2 + (p^2 + m_f^2) c_F, \quad (2.148)$$

as follows immediately from the defining expressions (2.140), (2.141). Here

$$\begin{aligned} \delta m_B^2 &= \frac{4\alpha}{\pi} J_1 = \frac{2\pi}{3} \alpha T^2, \\ \delta m_F^2 &= \frac{4\alpha}{\pi} \int_{m_f}^\infty d\omega \sqrt{\omega^2 - m_f^2} f_F(\omega) \xrightarrow{m_f=0} \frac{4\alpha}{\pi} I_1 = \frac{\pi}{3} \alpha T^2, \end{aligned} \quad (2.149)$$

contribute to the thermal corrections to the fermion mass. Expanding the fermion propagator (2.139) around the corrected mass-shell, we obtain, up to non-singular terms,

$$iS_F^T(p) = i (1 - 2m_f^2(\hat{c}'_B + \hat{c}'_F) + \hat{c}_F) \frac{\not{p} + m_f(1 - 2\hat{c}_F) - \hat{K}_B - \hat{K}_F}{p^2 - m_f^2 - \delta m_B^2 - \delta m_F^2 + 2m_f^2\hat{c}_F} + \mathcal{O}(\alpha^2). \quad (2.150)$$

In the massless case $m_f = 0$, this simplifies to

$$iS_F^T(p) = i \left(1 + \frac{2\alpha}{\pi} J_{-1} \right) \frac{\not{p} - \hat{K}_B - \hat{K}_F}{p^2 - \delta m_B^2 - \delta m_F^2} + \mathcal{O}(\alpha^2). \quad (2.151)$$

In summary, the thermal plasma affects the external SM fermion lines, and therefore the annihilation cross section computation, in three ways:

1. Modification of the spinor orthogonality relations

$$\sum_s u(p, s) \bar{u}(p, s) = \not{p} + m_f(1 - 2\hat{c}_F) - \hat{\not{K}}_B - \hat{\not{K}}_F . \quad (2.152)$$

This contribution to the annihilation cross section $\sigma_{\text{CTP}} v$ is simply obtained by computing the tree-level diagrams with the modified relation (2.152) and taking the $\mathcal{O}(\alpha)$ term. We note from (2.145) and (2.146) that this contribution is finite for thermal photon, while it contains a $1/\eta$ pole for thermal fermion in the massless limit. This pole cancels when adding the corresponding real correction “cut”.

2. Temperature-dependent wave-function renormalization

$$Z_2^T = 1 - 2m_f^2(\hat{c}'_B + \hat{c}'_F) + \hat{c}_F \xrightarrow{m_f=0} 1 + \frac{2\alpha}{\pi} J_{-1} . \quad (2.153)$$

The contribution is simply the $\mathcal{O}(\alpha)$ term in $[(Z_2^T)^2 - 1](\sigma_{\text{ann}}^{\text{LO}} v)$. We note that this contribution is divergent only for the thermal photon case, and it vanishes for the thermal fermion in the massless limit.

3. Shift of the fermion pole mass by the thermal contributions

$$\Delta m_f^2 \equiv \delta m_B^2 + \delta m_F^2 - 2m_f^2 \hat{c}_F + \mathcal{O}(\alpha^2) , \quad (2.154)$$

which leads to a change in the phase-space integration. This results in a contribution to cross section that can be written as

$$\begin{aligned} \Delta \sigma_{ph} &= [\sigma_{\text{ann}}^{\text{LO}} v](m_f^2 + \Delta m_f^2) - [\sigma_{\text{ann}}^{\text{LO}} v](m_f^2) \\ &\simeq \frac{d[\sigma_{\text{ann}}^{\text{LO}} v]}{dm_f^2} \Delta m_f^2 + \mathcal{O}((\Delta m_f^2)^2) , \end{aligned} \quad (2.155)$$

This contribution is finite for both thermal photon and fermion. In the massless limit this is ensured by the fact that $\sigma_{\text{ann}}^{\text{LO}} v$ is analytic in m_f^2 .

2.5.3 The results

In the previous Section we described how to write each thermal NLO contribution to the collision term in the form of an integral over the energy ω of the particle from the plasma that is involved in the annihilation. Scattering processes depend further on the masses m_χ , m_f , m_ϕ , and the DM energy E_χ , which in the following we parametrize with dimensionless variables

$$\epsilon \equiv \frac{m_f}{2m_\chi} , \quad \xi \equiv \frac{m_\phi}{m_\chi} , \quad e_\chi \equiv \frac{E_\chi}{m_\chi} . \quad (2.156)$$

Freeze-out occurs when the DM particles are non-relativistic, so that we can expand the S functions entering (2.114) for $e_\chi \simeq 1$. We performed the calculation for the first two terms of this expansion, which correspond to the S - and P -wave terms, respectively, keeping the full dependence on the scalar and SM fermion mass parameters ξ and ϵ

$$s \sigma_{\text{ann}}^{\text{NLO } T \neq 0} v = a + b v_{\text{CM}}^2, \quad (2.157)$$

where in the center-of-mass frame $s = 4E_\chi^2$ is the total energy and v_{CM} the velocity of one DM particle ($E_\chi = m_\chi \sqrt{1 + v_{\text{CM}}^2}$). For future reference we report here the corresponding tree-level result

$$s \sigma_{\text{ann}}^{\text{LO}} v = a_{\text{tree}} + b_{\text{tree}} v_{\text{CM}}^2, \quad (2.158)$$

with

$$a_{\text{tree}} = \frac{\lambda^4}{2\pi} \epsilon^2 \frac{\sqrt{1 - 4\epsilon^2}}{(1 + \xi^2 - 4\epsilon^2)^2}, \quad (2.159)$$

$$b_{\text{tree}} = \frac{\lambda^4}{3\pi} \frac{1 + \xi^4 - \epsilon^2 (9 + 8\xi^2 + 5\xi^4) + \epsilon^4 (31 + 46\xi^2 + 7\xi^4) - 8\epsilon^6 (9 + 7\xi^2) + 112\epsilon^8}{\sqrt{1 - 4\epsilon^2} (1 + \xi^2 - 4\epsilon^2)^4}. \quad (2.160)$$

In the first term the overall ϵ^2 factor implies the well-known helicity suppression of S -wave annihilation of a Majorana fermion into SM fermions.

Going to arbitrary higher orders in the non-relativistic expansion is possible if needed, while S cannot be found in a closed form without relying in any expansion. In order to check that our conclusions do not rely on the non-relativistic expansion, we also computed the result with keeping the full dependence on e_χ , performing in this case an expansion for large scalar mediator mass $\xi \gg 1$, up to the order $\mathcal{O}(\xi^{-10})$. The first two terms for the tree-level read

$$s \sigma_{\text{ann}}^{\text{LO}} v = \frac{\lambda^4 \sqrt{e_\chi^2 - 4\epsilon^2}}{6\pi e_\chi} \left[\frac{1}{\xi^4} \left(2e_\chi^2 (e_\chi^2 - 1) - \epsilon^2 (2e_\chi^2 - 5) \right) \right. \\ \left. + \frac{1}{\xi^6} \left(-4e_\chi^2 (3e_\chi^4 - 4e_\chi^2 + 1) + 2\epsilon^2 (20e_\chi^4 - 28e_\chi^2 + 5) - 8\epsilon^4 (2e_\chi^2 - 5) \right) \right] + \mathcal{O}(\xi^{-8}). \quad (2.161)$$

The heavy scalar expansion may be physically motivated, since often (but not necessarily) the scalar particle in the DM model is significantly heavier than the DM particle itself. Going to high order in $1/\xi$ is motivated by the observation that one needs to retain terms up to $\mathcal{O}(\xi^{-8})$ to see the lifting of helicity suppression of the non-thermal NLO contribution [90].

In the following we present and discuss the obtained results. We start with the study of IR divergence cancellation. For simplicity we will show explicitly the expressions for the leading S -wave result of IR divergent terms from thermal photon. This allows us to make some

important observations and we explicitly checked their validity in the other cases listed above. We then compute the leading thermal correction, which will turn out to be of order $\mathcal{O}(\tau^4)$. We consider separately the corrections from thermal photon and fermions, and again we show explicitly the expressions for S -wave. All computations were done in Feynman gauge.

Cancellation of IR divergences

The NLO amplitudes entering (2.106) can have singular terms of the order $\mathcal{O}(\omega^{-1})$ at small ω , which at $T = 0$ lead to the usual logarithmic soft divergence. At finite temperature, the enhancement of the Bose distribution function $f_B(\omega)$ for small energies results in linear and logarithmic divergences, encoded in the singular integrals J_{-1} and J_0 , respectively. As already pointed out, the latter actually cancels out. In the real contributions this happens when both the emission and absorption of thermal photons are included, due to the different sign of these contributions for even orders in ω . A similar cancellation occurs in the thermal loop contributions, as can be seen in (2.135). The results for the remaining part proportional to J_{-1} are given separately for all self-energy diagrams in Table 2.3

$$a = \frac{\alpha}{\pi\epsilon^2} a_{\text{tree}} F_{-1} J_{-1} + \text{finite} , \quad (2.162)$$

where we factor out⁸ the tree-level S -wave annihilation cross section (2.159).

As we can see from Table 2.3, the cancellation of divergences between virtual and real corrections to an inclusive process occurs separately within each self-energy diagram after summing over all possible cuts. While this is well known at zero-temperature, where in fact it holds more generally for off-shell self-energy diagrams, this is an important result since there is no general theorem that ensured it at finite temperature. Moreover this ensures that the collision term in the Boltzmann equation is IR finite, since it is directly built out of the self-energies Σ^{\lessgtr} . The logarithm present in the last row is defined in Table 2.6 and contains a collinear divergence $L \xrightarrow{\epsilon \rightarrow 0} \log \epsilon$ in the limit of small SM fermion mass. This collinear divergence also cancels in the sum. The tree annihilation cross section is helicity-suppressed, $a_{\text{tree}} \propto \epsilon^2$. The appearance of terms in Table 2.3 and Tables 2.4 and 2.5 below, which are not $\mathcal{O}(\epsilon^2)$ for small ϵ , implies that individual terms are not helicity-suppressed.

Finite correction from thermal photon

Once the divergent J_{-1} and J_0 contributions are cancelled, the remaining finite correction is at least of $\mathcal{O}(\tau^2)$, proportional to the integral J_1 . Again, we first show the diagram-by-diagram results for the S -wave contributions, which can be found in Tables 2.4 and 2.5 for the diagrams of type A and B , respectively

⁸The divergence can be factorized from the tree cross section, because it comes from the soft region. The same structure of the divergence was found for the hard photon scattering in the thermal plasma [89].

$$a = c_{\tau^2} \frac{1}{2\epsilon^2} a_{\text{tree}} F_1 + \mathcal{O}(\tau^4) , \quad (2.163)$$

where

$$c_{\tau^2} \equiv \frac{\pi}{3} \alpha \tau^2 . \quad (2.164)$$

We see that the separate contributions are significantly more complex than was the case for the divergent parts. The first simplification occurs when summing over the different cuts of a given self-energy diagram. At this stage all the logarithms L cancel, which is a sign of cancellation of the collinear divergence on a diagram-by-diagram basis. An even more remarkable cancellation occurs upon adding separately all diagrams of type A and B , respectively, such that the sum for each table vanishes.

Beyond the S -wave case displayed explicitly in the tables, we computed the thermal correction to the P -wave cross section; further without the partial wave expansion in the limit $\xi \gg 1$, up to the order $\mathcal{O}(\tau^2 \xi^{-10})$, retaining full dependence on e_χ and ϵ . In all cases we find that the thermal correction vanishes at $\mathcal{O}(\tau^2)$. The exact cancellation of the $\mathcal{O}(\tau^2)$ correction is certainly not accidental, and it has also been observed in the neutral Higgs decay to two fermions [92]. An example of a process in which the correction starts at this order is the charged particle decay [80], in which the thermal correction to the total width was found to be related to its tree-level expression by the simple factor $-c_{\tau^2}$. These results suggest that the structure of the leading thermal correction could be determined by first principles. This aspect is investigated Chapter 3.

The leading correction is then of $\mathcal{O}(\tau^4)$. The total result is rather lengthy (and not very illuminating), even in the S -wave limit. It is interesting to note that the helicity suppression of the S -wave cross section is lifted at this order. In fact in the limit of massless SM fermions the correction is

$$\Delta a_{\tau^4}^{\epsilon=0} = \frac{2\pi^2 \lambda^4 \alpha \tau^4}{45} \frac{1}{(1 + \xi^2)^4} = \frac{4\pi}{45} \alpha \tau^4 \frac{1}{(1 + \xi^2)^2} \frac{a_{\text{tree}}}{\epsilon^2} \Big|_{\epsilon=0} . \quad (2.165)$$

We note that in this limit, as for the the NLO $T = 0$ radiative correction, there is an additional ξ^{-4} suppression. This is easy to understand, since it is the hard photon emission from internal Bremsstrahlung from the scalar mediator that lifts the helicity suppression. In fact for finite fermion mass or beyond the S -wave limit $e_\chi = 1$, the correction starts already at $\mathcal{O}(\xi^{-4})$

$$s \sigma_{\text{ann} \nu} |_{\tau^4} = \frac{\pi^2 \lambda^4 \alpha \tau^4}{135 e_\chi^3 (e_\chi^2 - 4\epsilon^2)^{5/2} \xi^4} \left(-2e_\chi^6 (e_\chi^2 - 1) + \epsilon^2 e_\chi^4 (22e_\chi^2 - 25) \right. \\ \left. - \epsilon^4 e_\chi^2 (80e_\chi^2 - 101) + 3\epsilon^6 (38e_\chi^2 - 47) \right) + \mathcal{O}(\xi^{-6}) . \quad (2.166)$$

The thermal correction in (2.165) can be larger than the tree-level S -wave cross section a_{tree} when ϵ is very small (e.g., for SM leptons). Nevertheless, it is always parametrically smaller than the zero-temperature $\mathcal{O}(\alpha)$ NLO correction, which has no τ^4 suppression.

Finite correction from thermal fermions

Like photons, the light SM fermions are very abundant in the plasma around freeze-out and also contribute to the finite-temperature correction, see (2.106). The method of computation of these contributions follows the same steps as for thermal photons, and has been described in Sec. 2.5.2. However, the results differ considerably between these two cases. This is, because at zero temperature soft fermion radiation does not cause IR divergences. Furthermore, the Fermi-Dirac distribution is finite in the soft limit, hence the degree of divergence is not changed at finite temperature. As a consequence the thermal fermion contributions have no IR divergences from soft fermions. However, for massless fermions there is a divergence from hard-collinear photons, which has the same origin as the corresponding $T = 0$ divergence. When working in the massless limit, we use dimensional regularization to regulate this divergence. The poles in $1/\eta$ cancel in the sum over all cuts for a given CTP self-energy diagram.

As discussed in Sec. 2.5.2, for thermal fermions we present the analytic results for $\epsilon = 0$. Once again the total correction vanishes at order $\mathcal{O}(\tau^2)$. In contrast to the thermal photon case, however, here each self-energy diagram vanishes separately, due to an exact cancellation between real and virtual corrections. At the order $\mathcal{O}(\tau^4)$ the correction from thermal massless fermions in the S -wave limit is

$$\Delta a_{\tau^4, \text{ thermal fermions}}^{\epsilon=0} = \frac{7\pi^2 \lambda^4 \alpha \tau^4}{180} \frac{3\xi^4 + 4\xi^2 + 5}{(\xi^4 - 1)^3}, \quad (2.167)$$

while the leading term in the heavy-scalar limit is

$$s \sigma_{\text{ann}v}|_{\tau^4, \text{ thermal fermions}}^{\epsilon=0} = \frac{7\pi^2 \lambda^4 \alpha \tau^4 (e_\chi^2 - 1)}{135 e_\chi^2 \xi^4}. \quad (2.168)$$

Comparing the above results with (2.165) and (2.166) we note that the thermal correction from thermal massless fermions is parametrically of the same order as the one from thermal photons, namely of $\mathcal{O}(\xi^{-8})$ in the S -wave limit (for $\epsilon = 0$) but already starting at $\mathcal{O}(\xi^{-4})$ beyond this limit.

| CTP diagram | Real | Virtual |
|-------------|--|--|
| | \mathcal{M}_A $(\mathcal{M}_A^{\text{exc}})^*$ | $\mathcal{M}_{k_1^T}$ $(\mathcal{M}_{\text{tree}}^{\text{exc}})^*$ + <i>e.c.</i> |
| | \mathcal{M}_C $(\mathcal{M}_C^{\text{exc}})^*$ | $\mathcal{M}_{k_2^T}$ $(\mathcal{M}_{\text{tree}}^{\text{exc}})^*$ + <i>e.c.</i> |
| | \mathcal{M}_B $(\mathcal{M}_B^{\text{exc}})^*$ | $\mathcal{M}_{k_1^T}$ $(\mathcal{M}_{\text{tree}}^{\text{exc}})^*$ |
| | \mathcal{M}_A $(\mathcal{M}_B^{\text{exc}})^*$ | $\mathcal{M}_{\text{tree}}$ $(\mathcal{M}_1^{\text{exc}})^*$ |
| | \mathcal{M}_B $(\mathcal{M}_A^{\text{exc}})^*$ | \mathcal{M}_1 $(\mathcal{M}_{\text{tree}}^{\text{exc}})^*$ |
| | \mathcal{M}_C $(\mathcal{M}_B^{\text{exc}})^*$ | $\mathcal{M}_{\text{tree}}$ $(\mathcal{M}_2^{\text{exc}})^*$ |
| | \mathcal{M}_B $(\mathcal{M}_C^{\text{exc}})^*$ | \mathcal{M}_2 $(\mathcal{M}_{\text{tree}}^{\text{exc}})^*$ |
| | \mathcal{M}_3 $(\mathcal{M}_{\text{tree}}^{\text{exc}})^*$ | \mathcal{M}_3 $(\mathcal{M}_{\text{tree}}^{\text{exc}})^*$ |
| | $\mathcal{M}_{\text{tree}}$ $(\mathcal{M}_3^{\text{exc}})^*$ | $\mathcal{M}_{\text{tree}}$ $(\mathcal{M}_3^{\text{exc}})^*$ |
| | \mathcal{M}_A $(\mathcal{M}_C^{\text{exc}})^*$ + <i>e.c.</i> | \mathcal{M}_4 $(\mathcal{M}_{\text{tree}}^{\text{exc}})^*$ + <i>e.c.</i> |
| | \mathcal{M}_5 $(\mathcal{M}_{\text{tree}}^{\text{exc}})^*$ | \mathcal{M}_5 $(\mathcal{M}_{\text{tree}}^{\text{exc}})^*$ |
| | $\mathcal{M}_{\text{tree}}$ $(\mathcal{M}_5^{\text{exc}})^*$ | $\mathcal{M}_{\text{tree}}$ $(\mathcal{M}_5^{\text{exc}})^*$ |

Table 2.1: The self-energy diagrams of type *A* and the correspondence to the diagrams leading to real emission and absorption, virtual corrections and the correction to the external SM fermion legs. For simplicity we omit the imaginary unit from the labels, such that for a diagram labeled by \mathcal{M} , the associated amplitude is given by $i\mathcal{M}$. The *e.c.* stands for exchanging the DM fermion legs in both parts of the amplitude and complex conjugation.

| CTP diagram | Real | Virtual |
|-------------|---|---|
| | | |
| | \mathcal{M}_A $(\mathcal{M}_A)^*$ | $\mathcal{M}_{k_1^T}$ $(\mathcal{M}_{\text{tree}})^*$ + <i>c.c.</i> |
| | | |
| | \mathcal{M}_C $(\mathcal{M}_C)^*$ | $\mathcal{M}_{k_2^T}$ $(\mathcal{M}_{\text{tree}})^*$ + <i>c.c.</i> |
| | | |
| | \mathcal{M}_B $(\mathcal{M}_B)^*$ | |
| | | |
| | \mathcal{M}_A $(\mathcal{M}_B)^*$ | $\mathcal{M}_{\text{tree}}$ $(\mathcal{M}_1)^*$ |
| | | |
| | \mathcal{M}_B $(\mathcal{M}_A)^*$ | \mathcal{M}_1 $(\mathcal{M}_{\text{tree}})^*$ |
| | | |
| | \mathcal{M}_C $(\mathcal{M}_B)^*$ | $\mathcal{M}_{\text{tree}}$ $(\mathcal{M}_2)^*$ |
| | | |
| | \mathcal{M}_B $(\mathcal{M}_C)^*$ | \mathcal{M}_2 $(\mathcal{M}_{\text{tree}})^*$ |
| | | |
| | | \mathcal{M}_3 $(\mathcal{M}_{\text{tree}})^*$ |
| | | |
| | | $\mathcal{M}_{\text{tree}}$ $(\mathcal{M}_3)^*$ |
| | | |
| | \mathcal{M}_A $(\mathcal{M}_C)^*$ + <i>c.c.</i> | \mathcal{M}_4 $(\mathcal{M}_{\text{tree}})^*$ + <i>c.c.</i> |
| | | |
| | | \mathcal{M}_5 $(\mathcal{M}_{\text{tree}})^*$ |
| | | |
| | | $\mathcal{M}_{\text{tree}}$ $(\mathcal{M}_5)^*$ |

Table 2.2: The self-energy diagrams of type *B* and the correspondence to the diagrams leading to real emission and absorption, virtual corrections and the correction to the external SM fermion legs. For simplicity we omit the imaginary unit from the labels, such that for a diagram labeled by \mathcal{M} , the associated amplitude is given by $i\mathcal{M}$. The *c.c.* stands for complex conjugation.

| The divergent part F_{-1} | | | | | |
|-----------------------------|---|--|--------|--|---|
| Type A | Real | Virtual | Type B | Real | Virtual |
| | $1 - 2\epsilon^2$ | $-1 + 2\epsilon^2$ | | -1 | 1 |
| | $1 - 2\epsilon^2$ | $-1 + 2\epsilon^2$ | | -1 | 1 |
| | 0 | | | 0 | |
| | 0 | 0 | | 0 | 0 |
| | 0 | 0 | | 0 | 0 |
| | 0 | 0 | | 0 | 0 |
| | 0 | 0 | | 0 | 0 |
| | 0 | 0 | | 0 | 0 |
| | $\frac{2(1-2\epsilon^2)^2}{\sqrt{1-4\epsilon^2}} L$ | $-\frac{2(1-2\epsilon^2)^2}{\sqrt{1-4\epsilon^2}} L$ | | $-\frac{2(1-2\epsilon^2)}{\sqrt{1-4\epsilon^2}} L$ | $\frac{2(1-2\epsilon^2)}{\sqrt{1-4\epsilon^2}} L$ |
| | | 0 | | | 0 |
| | | 0 | | | 0 |

Table 2.3: Coefficients F_{-1} of the divergent integral J_{-1} omitting the overall factor $\alpha/\pi\epsilon^2 \times a_{\text{tree}}$, as defined in (2.162). Here “Real” includes both emission and absorption, while “Virtual” comprises vertex and external leg corrections. An empty space means that the corresponding contribution does not exist, while 0 implies that the diagram exists, but is finite. L denotes the logarithm as defined in Table 2.6.

| The finite part J_1 | | |
|-----------------------|---|--|
| Type A | Real | Virtual |
| | $\frac{2(1-\xi^2)}{D^2 D_\xi^2} + \frac{(1-2\epsilon^2)p_1(\epsilon, \xi)}{2D^2 D_\xi^2} + \frac{1}{2\sqrt{D}}L$ | $\frac{(1-2\epsilon^2)(\xi^2-3D)}{2DD_\xi} - \frac{1}{2\sqrt{D}}L$ |
| | — " — | — " — |
| | $-\frac{4(1-2\epsilon^2)D}{D_\xi^2}$ | |
| | $-\frac{2(1-2\epsilon^2)\xi^2}{D_\xi^2} - \frac{f_1(\epsilon, \xi)}{\sqrt{DD_\xi^2}}L$ | $\frac{2(1-2\epsilon^2)(D-\xi^2)}{D_\xi^2} + \frac{f_1(\epsilon, \xi)}{\sqrt{DD_\xi^2}}L$ |
| | — " — | — " — |
| | — " — | — " — |
| | — " — | — " — |
| | | $-\frac{4(1-2\epsilon^2)D}{D_\xi^2}$ |
| | | — " — |
| | $\frac{2(1-2\epsilon^2)p_2(\epsilon, \xi) + (1-\xi^2)^2}{D^2 D_\xi^2} + \frac{4f_2(\epsilon, \xi)}{\sqrt{DD_\xi^2}}L$ | $\frac{16\epsilon^2(2-3\epsilon^2) - (3-\xi^2)^2}{D_\xi^2} - \frac{4f_2(\epsilon, \xi)}{\sqrt{DD_\xi^2}}L$ |
| | | $\frac{4(1-2\epsilon^2)}{D_\xi}$ |
| | | — " — |
| Total: | 0 | |

Table 2.4: Coefficients F_1 of the finite $\mathcal{O}(\tau^2)$ correction for the type A diagrams, as defined in (2.163). D , D_ξ and polynomials p_i and f_i are defined in Table 2.6.

| The finite part F_1 | | |
|-----------------------|---|--|
| Type B | Real | Virtual |
| | $\epsilon^2 \left(1 - \frac{12}{D_\xi^2} + \frac{4}{DD_\xi} + \frac{2\epsilon^2}{D^2} \right) - \frac{1}{2\sqrt{D}} L$ | $\frac{2}{D_\xi} - \frac{1}{2D} + \frac{1}{2\sqrt{D}} L$ |
| | — ” — | — ” — |
| | $\frac{4D}{D_\xi^2}$ | |
| | $\frac{2\xi^2}{D_\xi^2} + \frac{f_3(\epsilon, \xi)}{\sqrt{DD_\xi^2}} L$ | $\frac{2(\xi^2 - D)}{D_\xi^2} - \frac{f_3(\epsilon, \xi)}{\sqrt{DD_\xi^2}} L$ |
| | — ” — | — ” — |
| | — ” — | — ” — |
| | — ” — | — ” — |
| | | $\frac{4D}{D_\xi^2}$ |
| | | — ” — |
| | $\frac{2(1-2\epsilon^2)p_3(\epsilon, \xi) - 4(1-\xi^2)^2}{D^2 D_\xi^2} - \frac{2f_4(\epsilon, \xi)}{\sqrt{DD_\xi^2}} L$ | $\frac{(3-\xi^2)^2 - 8\epsilon^2(1-2\epsilon^2 + \xi^2)}{D_\xi^2} + \frac{2f_4(\epsilon, \xi)}{\sqrt{DD_\xi^2}} L$ |
| | | $-\frac{4}{D_\xi}$ |
| | | — ” — |
| Total: | 0 | |

Table 2.5: Coefficients F_1 of the finite $\mathcal{O}(\tau^2)$ correction for the type B diagrams, as defined in (2.163). D , D_ξ and polynomials p_i and f_i are defined in Table 2.6.

$$D = 1 - 4\epsilon^2$$

$$D_\xi = 1 - 4\epsilon^2 + \xi^2$$

$$L = \log \frac{1-2\epsilon^2-\sqrt{1-4\epsilon^2}}{2\epsilon^2}$$

$$f_1(\epsilon, \xi) = (1 - \epsilon^2)(D - \xi^2) + 2\epsilon^2\xi^2$$

$$f_2(\epsilon, \xi) = (1 - \epsilon^2)(D - \xi^2) + 2\epsilon^2$$

$$f_3(\epsilon, \xi) = D(1 + 2\epsilon^2) - (1 - 2\epsilon^2)\xi^2$$

$$f_4(\epsilon, \xi) = (2 + D_\xi^2\epsilon^2 - 2\xi^2)$$

$$p_1(\epsilon, \xi) = -3 + \xi^4(1 - 4\epsilon^2 - 4\epsilon^4) + \xi^2(6 - 24\epsilon^2 + 120\epsilon^4 + 32\epsilon^6) - 12\epsilon^2 - 20\epsilon^4 - 32\epsilon^6 - 64\epsilon^8$$

$$p_2(\epsilon, \xi) = 3 + \xi^4(-1 + 2\epsilon^4) + \xi^2(2 - 4\epsilon^2 + 20\epsilon^4 - 16\epsilon^6) - 36\epsilon^2 + 114\epsilon^4 - 144\epsilon^6 + 32\epsilon^8$$

$$p_3(\epsilon, \xi) = -2 + \xi^4(2 + 5\epsilon^2 + 8\epsilon^4) + \xi^2(-6 + 2\epsilon^2 - 24\epsilon^4 - 64\epsilon^6) + 37\epsilon^2 - 64\epsilon^4 + 16\epsilon^6 + 128\epsilon^8$$

Table 2.6: The definitions used in the results Tables 2.3, 2.4 and 2.5.

Chapter 3

Effective theory approach to thermal corrections

In the previous Chapter we explicitly computed in an example model the leading temperature-dependent correction to the (thermally averaged) annihilation cross section times velocity, relevant for the determination of the dark matter relic density. The calculation was performed with the standard techniques of scattering matrix computation, as in our paper [34].

In this Chapter we will show how the hierarchy $m_\chi \gg T$ among the relevant energy scales allows to perform the same calculation within an effective field theory framework. In addition to a considerable simplification of the calculations, this approach has the further advantage of providing a physical interpretation for certain contributions [35].

We open this Chapter with a brief review of the necessary concepts on the heavy particle effective theory (HPET) in Sec. 3.1. As a first application of this framework in the context of thermal corrections we compute in Sec. 3.2 the decay width of a heavy charged particle. We finally consider the dark matter annihilation in Sec. 3.3, where we reproduce the results of the previous Chapter.

3.1 The Heavy Particle Effective Theory

A practical description of systems characterized by two (or more) well separated energy scales can be provided by making use of effective field theories. The basic idea is to remove from the Lagrangian of the full theory those degrees of freedom that are not relevant at the energy scale under study. This can be done in two steps: *i*) identify and integrate out the degrees of freedom heavier than a cutoff scale M , thus generating nonlocal terms, and *ii*) perform an operator product expansion (OPE) of those terms into a series of local operators. This procedure results in a consistent disentanglement of the long-distance (soft) physics, which determines the structure of the local operators, from the short-distance (hard) modes, whose

effect is encoded into “effective couplings” multiplying each operator.

Those effective couplings are called Wilson coefficients and, as they are insensitive to the soft modes, have the important property of being process-independent. At tree-level the Wilson coefficients can simply be obtained by expanding the full theory in the relevant regime. The situation is more involved when radiative corrections are considered, since one has to take into account the contributions to the loop from the momentum region that has been integrated out. In this case the coefficients have to be determined by matching the EFT and full theory results for suitable benchmark processes at the desired perturbative order. As long as the characteristic energy Λ of the considered processes is smaller than M , the EFT provides an approximate description of the full theory. The degree of approximation depends on the inclusion in the OPE of local operators of increasing dimension, which are suppressed by additional powers of the small ratio Λ/M .

EFTs have been successfully applied to a variety of problems, and a recent pedagogical introduction can be found e.g. in [93, 94]. In the following we review the EFT approach to the soft interactions of a heavy particle, and its application in the context of low temperature thermal background.

3.1.1 The HPET Lagrangian up to $\mathcal{O}(1/M)$

We are interested here in the interaction of heavy particles with the soft photons of a low temperature thermal background. For an effective description of this problem we consider its analogy with mesons containing a heavy quark (c , b), for which $m_c, m_b \gg \Lambda_{\text{QCD}}$. Since the characteristic scale of the interactions involved in the binding of a heavy and a light quark to a meson is Λ_{QCD} , the heavy quark in the meson is always very close to on-shell. The low-energy modes of the heavy quark resulting from the soft interactions with the light quarks and gluons in the hadron can be described within the heavy quark effective theory (HQET), first discovered in [95, 96] and then formulated as an effective field theory in [97, 98]. In this Section we introduce the Lagrangian of the heavy particle effective theory (HPET), corresponding to the case of a Dirac fermion ψ of mass M with QED interactions. The Majorana case can be treated similarly, and has been described in [99, 100].

The first step for separating the energy scales consists in parametrizing the momentum of the heavy fermion as

$$p^\mu = Mv^\mu + k^\mu, \quad (3.1)$$

where v is a timelike 4-velocity with $v^2 = 1$ and $v^0 > 0$, and k describes the fluctuations due to interactions with the other particles in the system, and by assumption its components are much smaller than M . The above parametrization is valid in a given reference frame and exploits the fact that the heavy particle remains approximately on-shell due to the soft scale of the interactions. In particular, in the case of HQET v can be chosen to be the four-velocity of the hadron. Similarly, in the case of interest here it is consistent to set v to the velocity of the thermal plasma. It is important to note that we are introducing here some redundancy, as

the single momentum p is replaced by two momenta v and k . We postpone the discussion of some important consequences of this redundancy in the next Section, and for now we consider v as a fixed parameter of the effective theory and treat k as the kinematic momentum. In the full theory, the relativistic field ψ is described by the Dirac Lagrangian

$$\mathcal{L}_{\text{Dirac}} = \bar{\psi} (i\mathcal{D} - M) \psi , \quad (3.2)$$

with QED covariant derivative

$$D_\mu \psi = (\partial_\mu - ieA_\mu) \psi . \quad (3.3)$$

Since we are interested in describing small fluctuations of the heavy particle around the momentum Mv^μ , we use the velocity v to define a splitting of the field ψ into an ‘‘upper’’ component h_v and a ‘‘lower’’ one H_v [101]

$$h_v(x) \equiv e^{iMv \cdot x} \frac{1 + \not{v}}{2} \psi(x), \quad H_v(x) \equiv e^{iMv \cdot x} \frac{1 - \not{v}}{2} \psi(x), \quad (3.4)$$

such that

$$\psi(x) = e^{-iMv \cdot x} (h_v(x) + H_v(x)) . \quad (3.5)$$

The component fields satisfy the constraints

$$\not{v} h_v = h_v , \quad \not{v} H_v = -H_v , \quad (3.6)$$

from which the following relations can be derived

$$\bar{h}_v \gamma^\mu h_v = v^\mu \bar{h}_v h_v , \quad \bar{H}_v \gamma^\mu H_v = -v^\mu \bar{H}_v H_v , \quad \bar{h}_v H_v = \bar{H}_v h_v = 0 . \quad (3.7)$$

In terms of the component fields the Dirac Lagrangian assumes the form

$$\mathcal{L}_v = \bar{h}_v v \cdot iD h_v + \bar{H}_v i\mathcal{D}_\perp h_v + \bar{h}_v i\mathcal{D}_\perp H_v - \bar{H}_v (2M + v \cdot iD) H_v , \quad (3.8)$$

where the transverse part of any four-vector q is defined as

$$q_\perp^\mu \equiv g_\perp^{\mu\nu} q_\nu \equiv (g^{\mu\nu} - v^\mu v^\nu) q_\nu . \quad (3.9)$$

The equations of motion for the component fields read

$$v \cdot iD h_v = -i\mathcal{D}_\perp H_v , \quad (3.10)$$

$$(2M + v \cdot iD) H_v = i\mathcal{D}_\perp h_v . \quad (3.11)$$

The small fluctuations of ψ around the momentum Mv^μ are described by the massless field h_v , once the heavy field H_v is consistently integrated out [101]. This is equivalent to replacing H_v with the solution of its equation of motion (3.11)

$$H_v = \frac{i\mathcal{D}_\perp}{2M + v \cdot iD} h_v = \frac{i\mathcal{D}_\perp}{2M} h_v + \mathcal{O}\left(\frac{1}{M^2}\right) . \quad (3.12)$$

$$\begin{aligned} \begin{array}{c} \xrightarrow{k} \\ \xrightarrow{k} \end{array} &= \frac{1+\phi}{2} \frac{i}{k \cdot v + i\eta} & \begin{array}{c} \mu \\ \text{wavy} \\ \xrightarrow{\quad} \\ \xrightarrow{\quad} \end{array} &= iev^\mu \end{aligned}$$

Figure 3.1: The HPET Feynman rules at leading order in $1/M$.

$$\begin{aligned} \begin{array}{c} \xrightarrow{k} \\ \xrightarrow{k} \end{array} \blacksquare &= \frac{i}{2M} k_\perp^2 & \begin{array}{c} \mu \\ \text{wavy} \\ \begin{array}{c} \xrightarrow{k} \\ \xrightarrow{k'} \end{array} \blacksquare \end{array} &= \frac{ie}{2M} (k + k')_\perp^\mu & \begin{array}{c} \mu \quad \nu \\ \text{wavy} \quad \text{wavy} \\ \xrightarrow{\quad} \blacksquare \end{array} &= \frac{ie^2}{2M} g_\perp^{\mu\nu} \end{aligned}$$

Figure 3.2: The Feynman rules for the interaction vertices encoded in the kinetic operator \mathcal{O}_k .

The *tree-level* HPET Lagrangian to arbitrary order in $1/M$ is obtained by expanding (3.12) and inserting it into (3.8)

$$\mathcal{L}_{v \text{ tree}} = \bar{h}_v v \cdot iD h_v + \frac{1}{2M} \mathcal{O}_k + \frac{1}{2M} \mathcal{O}_m + \mathcal{O}\left(\frac{1}{M^2}\right), \quad (3.13)$$

where the kinetic energy and the magnetic moment operators are defined as

$$\mathcal{O}_k \equiv \bar{h}_v (iD_\perp)^2 h_v, \quad (3.14)$$

$$\mathcal{O}_m \equiv \frac{1}{2} e \bar{h}_v F_{\mu\nu} \sigma^{\mu\nu} h_v, \quad (3.15)$$

where $ieF_{\mu\nu} \equiv [iD_\mu, iD_\nu]$ is the photon field-strength tensor and $\sigma^{\mu\nu} \equiv \frac{i}{2} [\gamma^\mu, \gamma^\nu]$. The equation of motion for the HPET field h_v is

$$v \cdot iD h_v = -\frac{1}{2M} \left((iD_\perp)^2 + \frac{1}{2} e F_{\mu\nu} \sigma^{\mu\nu} \right) h_v + \mathcal{O}\left(\frac{1}{M^2}\right), \quad (3.16)$$

and the Feynman rules are displayed in Figs. 3.1, 3.2 and 3.3. By means of (3.5) and (3.12) we obtain the expansion of the fermion field in the full theory in terms of the effective field

$$\psi(x) = e^{-iMv \cdot x} \left(1 + \frac{i\mathcal{D}_\perp}{2M} \right) h_v(x) + \mathcal{O}\left(\frac{1}{M^3}\right). \quad (3.17)$$

Beyond the tree level, higher dimensional operators receive perturbative corrections that are encoded into Wilson coefficients, to be determined by matching with appropriate scattering processes in the full theory. In particular, the coefficients multiplying the kinetic and magnetic

$$\text{Diagram} = \frac{ie}{4M} C_m [\not{\not{a}}, \gamma^\mu]$$

Figure 3.3: The Feynman rule for the interaction vertex encoded in the magnetic operator \mathcal{O}_m .

moment operators can be matched by computing the scattering amplitude of an on-shell fermion in an external electromagnetic field in HPET with the same amplitude in full QED, expanded up to linear terms in $1/M$. The result is [94]

$$C_k = F_1(0) , \quad C_m = 1 + F_2(0) , \quad (3.18)$$

where $F_{1,2}(q^2)$ are the charge and magnetic moment form factors parametrizing the electron-photon interaction. It is well known that $F_1(0) = 1$ to all orders as a consequence of Ward identity, or current conservation, and that the anomalous magnetic moment $F_2(0) = \mathcal{O}(\alpha)$ is finite. Therefore C_m does not need to be renormalized and we can set it to one when working at leading order in $\alpha \equiv e^2/4\pi$.

To conclude the description of the effective theory we fix the normalization of the states such that

$$\langle \psi(p, s); \Omega_T | \psi(p', s'); \Omega_T \rangle = v^0 (2\pi)^3 \delta^3(\vec{p} - \vec{p}') \delta_{s, s'} , \quad (3.19)$$

where v is the velocity of the thermal bath.

3.1.2 The reparametrization invariance

The field h_v that we introduced in the previous Section depends explicitly on the 4-velocity vector v that we chose to parametrize the heavy particle momentum p in (3.1). The effective theory provides an approximate description of the system if the heavy particle residual momentum k and the momenta k_i of all the photons involved in the interactions are small

$$k \ll M , \quad k_i \ll M . \quad (3.20)$$

This condition does not fix v uniquely since any choice $v' = v + \delta v$, with $\delta v \sim k/M$, must result in an equivalent effective theory. The Lagrangian of the HPET must therefore be invariant under the transformation

$$(v, k) \leftrightarrow (v + \delta v, k - M\delta v) , \quad (3.21)$$

where δv is an arbitrary four-vector which satisfies

$$(v + \delta v)^2 = 1 . \quad (3.22)$$

The above requirement (3.21) is called reparametrization invariance [102], and solves the redundancy arising from the introduction of two vectors v and k in place of the single one p .

As important consequences, reparametrization invariance *i)* reduces the number of independent operators and *ii)* implies fixed relations (to all orders in perturbation theory) among Wilson coefficients of terms of different orders in the $1/M$ expansion. The variation of the HPET Lagrangian (3.13) under the transformation in (3.21) is

$$\delta\mathcal{L}_v = (1 - C_k) \left(\bar{h}_v \delta v \cdot iD h_v + M \bar{h}_v v \cdot \delta v h_v \right), \quad (3.23)$$

where we used $(\delta v)^2 = -2v \cdot \delta v$, according to (3.22). The requirement of reparametrization invariance fixes therefore the coefficient of the kinetic operator to $C_k = 1$. As we have already seen, this result agrees with the one from the matching calculation, as a consequence of current conservation.

In terms of matrix elements, this constraint results in a fixed ratio of the coefficients for the kinetic operator and

$$\mathcal{O}_1 \equiv \bar{h}_v h_v. \quad (3.24)$$

The proportionality factor can be obtained by expanding the corresponding operator to the required order in $1/M$ by means of (3.17). In the following we will be interested in the decay width of the heavy particle, in which case the relevant operator is

$$\bar{\psi}\psi = \mathcal{O}_1 + \frac{1}{4M^2} (\mathcal{O}_k + \mathcal{O}_m) + \mathcal{O}\left(\frac{1}{M^3}\right). \quad (3.25)$$

Note that we found here for the magnetic operator the same coefficient as for the kinetic one. It is however important to mention once again that this relation is only valid at the tree-level (see (3.18)), as the magnetic operator, not being related to the kinetic term by reparametrization invariance, is not protected from radiative corrections.

3.1.3 Calculation of the matrix elements

Before considering specific processes, we present in this Section the calculation of the matrix elements of the the effective theory operators $\mathcal{O}_{1,k,m}$ between full theory states

$$M_i \equiv \frac{1}{2} \sum_{\text{spin}} \langle \psi; \Omega_T | \mathcal{O}_i | \psi; \Omega_T \rangle. \quad (3.26)$$

We start by considering the matrix element of the electromagnetic current. Since the only four-vector on which it can depend is the plasma velocity v , it can be parametrized as

$$\langle \psi; \Omega_T | \bar{\psi} \gamma^\mu \psi | \psi; \Omega_T \rangle = v^\mu A. \quad (3.27)$$

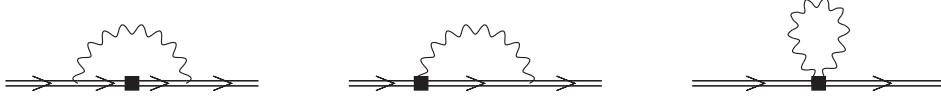


Figure 3.4: The HPET diagrams corresponding to $M_{k,2}$, $M_{k,3}$ and $M_{k,4}$, respectively.

The parameter A can be obtained by taking the zero component, which corresponds to the matrix element of the electromagnetic charge $Q = \int d^3\vec{x} \psi^\dagger(x)\psi(x)$

$$v^0 A = \frac{1}{V} \langle \psi; \Omega_T | Q | \psi; \Omega_T \rangle = v^0 \quad \Rightarrow \quad A = 1 , \quad (3.28)$$

where V denotes the volume and we used the normalization condition (3.19). Note that the above result holds to all order in $1/M$. The constraints that current conservation poses on the effective theory can be obtained by expanding the current in terms of HPET operators by means of (3.17), thus obtaining

$$\langle \psi; \Omega_T | \bar{\psi} \gamma^\mu \psi | \psi; \Omega_T \rangle = v^\mu \left[M_1 - \frac{1}{4M^2} (M_k + M_m) \right] + \mathcal{O} \left(\frac{1}{M^3} \right) . \quad (3.29)$$

The comparison with (3.27) leads to

$$M_1 = 1 + \frac{1}{4M^2} (M_k + M_m) + \mathcal{O} \left(\frac{1}{M^3} \right) . \quad (3.30)$$

According to the Feynman rules for the kinetic operator given in Fig. 3.2, its matrix element is given by the three diagrams depicted in Fig. 3.4,

$$M_k = M_{k,2} + 2 M_{k,3} + M_{k,4} + \mathcal{O}(\tau^3) , \quad (3.31)$$

where the thermal photon propagator is (see Sec. 2.1)

$$\begin{aligned} \langle \Omega_T | \mathcal{T} \{ A_\mu(x) A_\nu(y) \} | \Omega_T \rangle &= iD_{\mu\nu}^{++}(x, y) \\ &= \int \frac{d^4k}{(2\pi)^4} e^{-ik \cdot (x-y)} iD_{\mu\nu}^{++}(k) . \end{aligned} \quad (3.32)$$

Using the normalization of the spinors $\bar{u}_v^r u_v^s = \delta^{rs}$, which is consistent with (3.19), we get

$$M_{k,2} = -i 2M \int \frac{d^4k}{(2\pi)^4} iD_{\mu\nu}^{++}(k) (ie)^2 v^\mu v^\nu \frac{ik_\perp^2}{2M} \left(\frac{i}{v \cdot k} \right)^2 , \quad (3.33)$$

$$M_{k,3} = -i 2M \int \frac{d^4k}{(2\pi)^4} iD_{\mu\nu}^{++}(k) (ie)^2 v^\mu \frac{k_\perp^\nu}{2M} \frac{i}{v \cdot k} , \quad (3.34)$$

$$M_{k,4} = -i 2M \int \frac{d^4 k}{(2\pi)^4} iD_{\mu\nu}^{++}(k) (ie)^2 \frac{-ig_{\perp}^{\mu\nu}}{2M} . \quad (3.35)$$

Since we are interested in the temperature-dependent correction, we retain only the thermal part of the equilibrium photon propagator (2.42)

$$iD_{\mu\nu}^{++}(k) \rightarrow -g_{\mu\nu} 2\pi \delta(k^2) f_B(\omega) , \quad (3.36)$$

where $f_B(\omega) = \frac{1}{e^{\omega/T} - 1}$ (with $\omega \equiv |\vec{k}|$), is the Bose-Einstein distribution with vanishing chemical potential. Performing the integration as in (2.115) we obtain

$$\begin{aligned} M_{k,2} &= \frac{\pi}{3} \alpha T^2 , \\ M_{k,3} &= 0 , \\ M_{k,4} &= -3 \frac{\pi}{3} \alpha T^2 , \end{aligned} \quad (3.37)$$

so that

$$M_k = -2M^2 c_{\tau^2} , \quad (3.38)$$

where we parametrize the temperature dependence through the dimensionless quantity

$$c_{\tau^2} \equiv \frac{\pi}{3} \alpha \tau^2 , \quad \tau \equiv \frac{T}{M} \ll 1 . \quad (3.39)$$

Finally, the matrix element of the magnetic operator vanish since it is proportional to

$$M_m \propto \text{Tr} [M(1 + \not{\psi})\sigma^{\mu\nu}] = 0 . \quad (3.40)$$

In the next Section we will see how the matrix elements computed here can be used to determine the leading thermal corrections to the decay rate of a charged fermion in a photon bath.

3.2 The charged particle decay in HPET

In this Section we consider the decay $\psi \rightarrow \phi \chi$ of a heavy charged fermion ψ into a light charged fermion χ and a neutral massless scalar ϕ , via the interaction

$$\mathcal{L} \supset \lambda \bar{\psi} P_L \chi \phi + \text{h.c.} , \quad (3.41)$$

where $P_L = \frac{1-\gamma_5}{2}$ is the left-handed chiral projector. We are interested in the leading thermal correction to the spin-averaged total decay width in presence of an unpolarized thermal bath of photons at temperature T , much smaller than $M \equiv m_\psi$. If the decaying particle is approximately at rest in the reference frame of the photon bath, the system can be consistently described by the HPET introduced in the previous Section, and the expansion of the decay

width in terms of the HPET operators $\mathcal{O}_{1,k,m}$ given in (3.24), (3.14) and (3.15) corresponds to an expansion up to $\mathcal{O}(\tau^2)$. This model has been previously considered in [80], where the explicit calculation of the relevant next-to-leading order Feynman diagrams lead to the result

$$\Gamma_T = \Gamma_0 (1 - c_{\tau^2}) + \mathcal{O}(\tau^4) , \quad (3.42)$$

where $\Gamma_0 \equiv M \frac{\lambda^2}{32\pi} \left(1 - \frac{m_\chi^4}{M^4}\right)$ is the tree-level decay width. In the following we reproduce and interpret the above result within the HPET approach.

The decay products are light particles with hard momenta, that cannot appear in the effective theory and must therefore be integrated out. For this reason we make use of the optical theorem and express the decay width in terms of the discontinuity on the physical cut of the forward scattering amplitude

$$\Gamma_T \equiv 2 \operatorname{Im} \left\{ \frac{1}{2} \sum_{\text{spin}} \langle \psi; \Omega_T | \mathcal{O}(p) | \psi; \Omega_T \rangle \right\} , \quad (3.43)$$

where we denoted with $\mathcal{O}(p)$ the time-ordered product of two currents

$$\mathcal{O}(p) \equiv -i \int d^4x e^{-ip \cdot x} \mathcal{T}\{J(0) J^\dagger(x)\} , \quad (3.44)$$

$$J(x) \equiv \lambda \phi(x) \bar{\psi}(x) P_L \chi(x) . \quad (3.45)$$

The decay width can be written in terms of the local operators of the effective theory by performing an OPE of the current product in (3.44)

$$\mathcal{O}(p) = \sum_{i=1,k,m} C_i(p) \mathcal{O}_i . \quad (3.46)$$

Introducing for the imaginary part of the coefficients the following definition

$$\widehat{C}_i \equiv 2 \operatorname{Im} \{C_i\} , \quad (3.47)$$

we obtain

$$\begin{aligned} \Gamma_T &= \sum_{i=1,k,m} \widehat{C}_i M_i \\ &= \widehat{C}_1 \left(1 + \frac{M_k}{4M^2}\right) + \widehat{C}_k M_k + \mathcal{O}(\tau^4) \\ &= \widehat{C}_1 \left(1 + \frac{M_k}{2M^2}\right) + \mathcal{O}(\tau^4) \end{aligned} \quad (3.48)$$

$$= \widehat{C}_1 (1 - c_{\tau^2}) + \mathcal{O}(\tau^4) , \quad (3.49)$$

where in the second line we used (3.30) and (3.40), in the third one we made use of reparametrization invariance to set (see (3.25))

$$\widehat{C}_k = \frac{1}{4M^2} \widehat{C}_1 , \quad (3.50)$$

and in the last one we used (3.38).

At leading order the only relevant operator is \mathcal{O}_1 and therefore the zero-temperature decay width is simply given by its coefficient, $\Gamma_0 = \widehat{C}_1$. In agreement with the result (3.42) from [80], we found here that the leading thermal correction in this model is simply proportional to Γ_0 , with coefficient equal to $-c_{\tau^2}$. The same result could also be obtained with a direct OPE method, without the transition to the effective theory, as the one applied to semileptonic B-decays in [103].

As explained in [104] the HPET approach provides a physical interpretation for the correction from the kinetic energy operator: the particle ψ in thermal equilibrium with the photon bath has an effective (thermal) mass that differs from M and an effective four-velocity that differs from the one of the plasma. It is worth mentioning that within the HPET approach, due to the constraint provided by reparametrization invariance, the result can be obtained without the calculation of any next-to-leading order diagram. Moreover, the HPET result (3.49) automatically applies to the three-body muon decay as well, since the different short-distance structure only enters the coefficient \widehat{C}_1 and does not affect the calculation of the matrix elements. This result also agrees with [80]. In the following Section we complete the calculation of the thermal width by computing the leading order Wilson coefficient \widehat{C}_1 . Additionally, in Appendix A we cross-check the reparametrization invariance relation (3.50) by explicitly computing the coefficient \widehat{C}_k .

Leading order matching

The matching condition for the leading order coefficient \widehat{C}_1 is

$$\widehat{C}_1 M_1 = 2 \operatorname{Im} \left\{ \frac{1}{2} \sum_{\text{spin}} \langle \psi; \Omega_T | \mathcal{O}(p) | \psi; \Omega_T \rangle \right\}_{p=Mv} , \quad (3.51)$$

where the full theory matrix element on the r.h.s. is given by the diagram in Fig. 3.5 and has to be expanded to zeroth power of the residual momentum k , namely for $p = Mv$. We get

$$\widehat{C}_1 = \lambda^2 2 \operatorname{Im} \left\{ -i \int \frac{d^d q}{(2\pi)^d} \frac{1}{(q-p)^2} \frac{1}{q^2 - m_\chi^2} \frac{1}{2} \sum_{\text{spin}} \bar{u}(p) P_R (\not{q} + m_\chi) P_L u(p) \right\} . \quad (3.52)$$

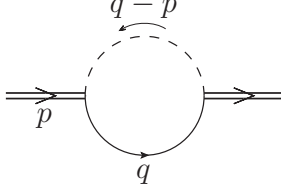


Figure 3.5: Diagram contributing to the OPE of $\mathcal{O}(p)$ at leading order.

Due to the sum over polarizations the operator $\bar{\psi}\gamma^\mu\gamma_5\psi$ does not contribute and the only relevant operator is $\bar{\psi}\gamma^\mu\psi$, whose matrix element is fixed by current conservation (3.27). Introducing Feynman parametrization, shifting the loop momentum as $l^\mu \equiv q^\mu - xp^\mu$, and defining

$$\Delta \equiv (1-x)(m_\chi^2 - xM^2), \quad (3.53)$$

we obtain

$$\begin{aligned} \widehat{C}_1 &= \lambda^2 M \operatorname{Im} \left\{ -i \int_0^1 dx x \int \frac{d^d l}{(2\pi)^d} \frac{1}{(l^2 - \Delta)^2} \right\} \\ &= \frac{\lambda^2}{16\pi^2} M \operatorname{Im} \left\{ \int_0^1 dx x \log \frac{4\pi}{\Delta} \right\} \\ &= \frac{\lambda^2}{32\pi} M \left(1 - \frac{m_\chi^4}{M^4} \right), \end{aligned} \quad (3.54)$$

where in the second line we took the $d \rightarrow 4$ limit and kept only the term with non-vanishing imaginary part. As expected, the above result agrees with the the leading order decay width in (3.42).

3.3 Thermal corrections to $\langle \sigma_{\text{ann}} v \rangle$ within HPET

In this Section we analyze within the HPET approach the pair-annihilation process $\chi\bar{\chi} \rightarrow f\bar{f}$ that we studied in Chapter 2. For simplicity we will refer here to the case of χ being a Dirac fermion, which corresponds to retaining only the type- B diagrams of Chapter 2, but the methods that we present can be straightforwardly applied to the case in which χ is a Majorana fermion as well. The annihilating fermions χ and $\bar{\chi}$ are neutral and therefore do not interact directly with the soft particles in the plasma. Because of this, their momenta can be simply parametrized as

$$p_i = m_\chi v_i, \quad i = 1, 2, \quad (3.55)$$

where $v_i^2 = 1$ and there is no need for introducing residual momenta. In other words, the momenta p_i are fixed parameters in the effective theory and can be used as labels instead of v_i for conveniency. We will adopt this convention in the following.

In this Section we will show how to obtain within the HPET approach the following results from the calculations of Chapter 2

- tree-level (zero-temperature) cross section, first two terms in the heavy-scalar expansion

$$s \sigma_{\text{ann}}^{\text{LO}} v |_{\text{Dirac}} = \frac{\lambda^4 \sqrt{e_\chi^2 - 4\epsilon^2}}{24\pi e_\chi} \left[\frac{1}{\xi^4} \left(e_\chi^2 (4e_\chi^2 - 1) - 4\epsilon^2 (e_\chi^2 - 1) \right) \right. \\ \left. + \frac{1}{\xi^6} \left(-2e_\chi^2 (12e_\chi^4 - 10e_\chi^2 + 1) + 8\epsilon^2 (10e_\chi^4 - 8e_\chi^2 + 1) - 32\epsilon^4 (e_\chi^2 - 1) \right) \right] + \mathcal{O}(\xi^{-8}) ; \quad (3.56)$$

- separate contributions of $\mathcal{O}(\tau^2)$ from thermal photons, as in Table 2.5 but for the first two terms in the heavy-scalar expansion, retaining the full energy dependence;
- total correction of $\mathcal{O}(\tau^4)$ from thermal photons at order $\mathcal{O}(\xi^{-4})$;

$$s \sigma_{\text{ann}} v |_{\tau^4, \text{Dirac}} = \frac{\pi^2 \lambda^4 \alpha \tau^4}{540 e_\chi^3 (e_\chi^2 - 4\epsilon^2)^{5/2} \xi^4} \left(-e_\chi^6 (4e_\chi^2 - 1) + 2\epsilon^2 e_\chi^4 (22e_\chi^2 - 7) \right. \\ \left. - \epsilon^4 e_\chi^2 (160e_\chi^2 - 61) + 4\epsilon^6 (57e_\chi^2 - 21) \right) + \mathcal{O}(\xi^{-6}) . \quad (3.57)$$

- separate contributions of $\mathcal{O}(\tau^2)$ from thermal fermions in the massless limit ($\epsilon = 0$);
- total correction of $\mathcal{O}(\tau^4)$ from thermal fermions at order $\mathcal{O}(\xi^{-4})$;

$$s \sigma_{\text{ann}} v |_{\tau^4, \text{Dirac, thermal fermions}}^{\epsilon=0} = \frac{7\pi^2 \lambda^4 \alpha \tau^4 (4e_\chi^2 - 1)}{1080 e_\chi^2 \xi^4} + \mathcal{O}(\xi^{-6}) . \quad (3.58)$$

The procedure that we follow is divided in two steps. We start by integrating out the heavy scalar, thus generating local four-particle annihilation vertices which can be combined in a “total current”. The cross section is then obtained as the matrix element of a time-ordered product of two total currents.

3.3.1 First step: integrate out the heavy scalar at the amplitude level

Consider the tree-level annihilation amplitude for the process $\chi\bar{\chi} \rightarrow f\bar{f}$, depicted in Fig. 3.6

$$\mathcal{M}_{\text{tree}} = \langle f\bar{f} | \mathcal{O}_{\text{ann}}^{(0)} | \chi\bar{\chi} \rangle , \quad (3.59)$$

where¹

$$\mathcal{O}_{\text{ann}}^{(0)} = (-i\lambda^2) \frac{1}{t - m_\phi^2} \bar{f}_1 P_R \chi_1 \bar{\chi}_2 P_L f_2 . \quad (3.60)$$

¹In the following we adopt the short-hand notation $\chi_i \equiv \chi(p_i)$, $f_i \equiv f(k_i)$.

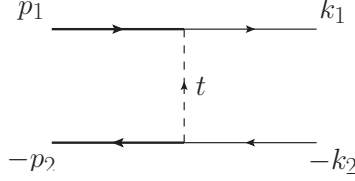


Figure 3.6: The tree-level annihilation diagram $i\mathcal{M}_{\text{tree}}$.

Under the assumption that the scalar ϕ is heavy, we can integrate it out by expanding the corresponding propagator

$$\frac{1}{t - m_\phi^2} = -\frac{1}{m_\phi^2} \left(1 + \frac{t}{m_\phi^2} + \mathcal{O}(m_\phi^{-4}) \right), \quad (3.61)$$

where the t -channel momentum squared can be written as

$$t = m_\chi^2 + m_f^2 - p_1 \cdot k_1 - p_2 \cdot k_2. \quad (3.62)$$

Up to terms that are suppressed by higher powers of $1/m_\phi^2$, $\mathcal{O}_{\text{ann}}^{(0)}$ can then be written in terms of the following *local* four-fermion operators

$$\begin{aligned} \mathcal{O}_{\text{ann}}^{(0)} = & \frac{i\lambda}{m_\phi^2} \left\{ \left(1 + \frac{m_\chi^2 + m_f^2}{m_\phi^2} \right) \bar{f}_1 P_R \chi_1 \bar{\chi}_2 P_L f_2 \right. \\ & \left. + \frac{1}{m_\phi^2} [(iD_\alpha \bar{f}_1) P_R (i\partial^\alpha \chi_1) \bar{\chi}_2 P_L f_2 + \bar{f}_1 P_R \chi_1 (i\partial_\alpha \bar{\chi}_2) P_L (iD^\alpha f_2)] + \mathcal{O}(m_\phi^{-4}) \right\}. \end{aligned} \quad (3.63)$$

Note that, as required by gauge invariance, charged fermions momenta are associated to covariant derivatives, rather than ordinary ones. By means of the Fierz identity

$$[P_R]_{ij} [P_L]_{kl} = \frac{1}{2} [P_R \gamma^\mu]_{il} [P_L \gamma_\mu]_{kj}, \quad (3.64)$$

we obtain

$$\mathcal{O}_{\text{ann}}^{(0)} = \frac{i\lambda^2}{2m_\phi^2} \left[\left(1 + \frac{m_\chi^2 + m_f^2}{m_\phi^2} \right) J_0^\mu + \frac{1}{m_\phi^2} J_1^\mu + \mathcal{O}(m_\phi^{-4}) \right] \bar{\chi}_2 P_L \gamma_\mu \chi_1, \quad (3.65)$$

where we introduced the current operators

$$J_0^\mu \equiv \bar{f}_1 P_R \gamma^\mu f_2, \quad (3.66)$$

$$J_1^\mu \equiv p_1^\alpha (iD_\alpha \bar{f}_1) P_R \gamma^\mu f_2 + p_2^\alpha \bar{f}_1 P_R \gamma^\mu (iD_\alpha f_2), \quad (3.67)$$

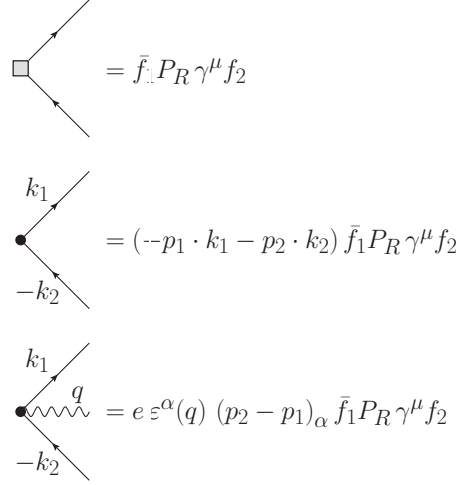


Figure 3.7: The diagrammatic rules for the current operators J_0^μ (first line) and J_1^μ (second and third lines).

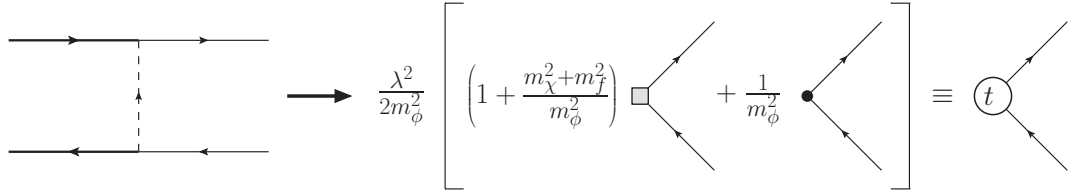


Figure 3.8: Matching of the tree-level annihilation diagram $i\mathcal{M}_{\text{tree}}$. We omit here $\bar{\chi}_2 P_L \gamma_\mu \chi_1$ (see (3.65)), as it does not enter the definition of the currents.

which can be represented diagrammatically as in Fig. 3.7. The result of the matching for the zero-photon amplitude is summarized in Fig. 3.8.

The same procedure can be followed to integrate out the heavy scalar from the one-photon amplitude

$$\mathcal{M}_1 = \langle f \bar{f} \gamma | \mathcal{O}_{\text{ann}}^{(1)} | \chi \bar{\chi} \rangle, \quad (3.68)$$

in which case $\mathcal{O}_{\text{ann}}^{(1)}$ can be written as the sum of:

- i*) the current J_0^μ in time-ordered product with the Lagrangian $\bar{f} f \gamma$ vertex term ($\mathcal{L}_{\bar{f} f \gamma}$);
- ii*) the non-photon term from J_1^μ in time-ordered product with $\mathcal{L}_{\bar{f} f \gamma}$;
- iii*) the one-photon term from J_1^μ (local operator);

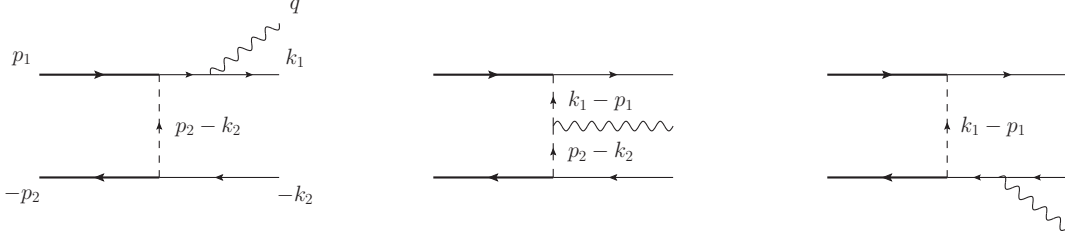


Figure 3.9: The three diagrams contributing to the one-photon amplitude $i\mathcal{M}_1$.

iv) other one-photon local operators that do not appear in $\mathcal{O}_{\text{ann}}^{(0)}$, because they do not have a zero-photon term.

The computation of the full theory amplitude is only required to match the coefficients of terms in *iv)*, as the remaining ones are fixed by gauge invariance. The amplitude is given by the three diagrams depicted in Fig. 3.9 and the corresponding operator is

$$\begin{aligned} \mathcal{O}_{\text{ann}}^{(1)} = (ie\lambda^2) \varepsilon_\alpha(q) & \left[\frac{1}{(p_2 - k_2)^2 - m_\phi^2} \bar{f}_1 \gamma^\alpha \frac{\not{k}_1 + \not{q} + m_f}{(k_1 + q)^2 - m_f^2} P_R \chi_1 \bar{\chi}_2 P_L f_2 \right. \\ & + \frac{1}{(p_2 - k_2)^2 - m_\phi^2} \frac{1}{(k_1 - p_1)^2 - m_\phi^2} (-p_1 + p_2 + k_1 - k_2)^\alpha \bar{f}_1 P_R \chi_1 \bar{\chi}_2 P_L f_2 \\ & \left. + \frac{1}{(k_1 - p_1)^2 - m_\phi^2} \bar{f}_1 P_R \chi_1 \bar{\chi}_2 P_L \frac{-\not{k}_2 - \not{q} + m_f}{(k_2 + q)^2 - m_f^2} \gamma^\alpha f_2 \right]. \end{aligned} \quad (3.69)$$

Perform the expansion as in (3.61) and write the t -channel momentum squared as

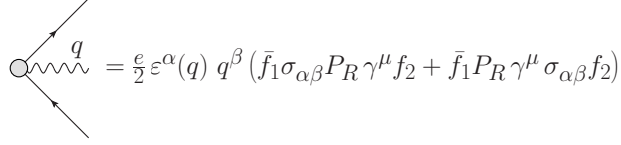
$$\begin{aligned} (p_2 - k_2)^2 &= Y_A + \frac{1}{2} \left[(k_1 + q)^2 - m_f^2 \right] && \text{in the first diagram,} \\ (k_1 - p_1)^2 &= Y_C + \frac{1}{2} \left[(k_2 + q)^2 - m_f^2 \right] && \text{in the third diagram,} \end{aligned} \quad (3.70)$$

where

$$\begin{aligned} Y_A &\equiv m_\chi^2 + m_f^2 - p_1 \cdot (k_1 + q) - p_2 \cdot k_2, \\ Y_C &\equiv m_\chi^2 + m_f^2 - p_1 \cdot k_1 - p_2 \cdot (k_2 + q). \end{aligned} \quad (3.71)$$

At the required order, in the second diagram each scalar propagator can be replaced by the leading term $-1/m_\phi^2$. Performing also the Fierz transformation (3.64) we get

$$\mathcal{O}_{\text{ann}}^{(1)} = -\frac{ie\lambda^2}{2m_\phi^2} \varepsilon_\alpha(q) \left[\left(1 + \frac{Y_A}{m_\phi^2} \right) \bar{f}_1 \gamma^\alpha \frac{\not{k}_1 + \not{q} + m_f}{(k_1 + q)^2 - m_f^2} P_R \gamma^\mu f_2 + \frac{1}{2m_\phi^2} \bar{f}_1 \gamma^\alpha (\not{k}_1 + \not{q} + m_f) P_R \gamma^\mu f_2 \right]$$



$$\text{Diagram} = \frac{e}{2} \varepsilon^\alpha(q) q^\beta (\bar{f}_1 \sigma_{\alpha\beta} P_R \gamma^\mu f_2 + \bar{f}_1 P_R \gamma^\mu \sigma_{\alpha\beta} f_2)$$

Figure 3.10: The diagrammatic rule for the current operator J_m^μ .

$$\begin{aligned}
& + \frac{1}{m_\phi^2} (p_1 - p_2 - k_1 + k_2)^\alpha \bar{f}_1 P_R \gamma^\mu f_2 \\
& + \left(1 + \frac{Y_C}{m_\phi^2} \right) \bar{f}_1 P_R \gamma^\mu \frac{-\not{k}_2 - \not{q} + m_f}{(k_2 + q)^2 - m_f^2} \gamma^\alpha f_2 + \frac{1}{2m_\phi^2} \bar{f}_1 P_R \gamma^\mu (-\not{k}_2 - \not{q} + m_f) \gamma^\alpha f_2 \left] \bar{\chi}_2 P_L \gamma_\mu \chi_1 .
\end{aligned} \tag{3.72}$$

In the first terms of both the first and the third line we recognize the contributions *i*) and *ii*), namely the time-ordered product of $\mathcal{L}_{\bar{f}f\gamma}$ with J_0^μ and the non-photon term from J_1^μ . Note in particular that the relative coefficient between the contributions from the two current is the same as in the zero-photon amplitude (3.65), as expected. The second diagram, together with the remaining terms from the other two diagrams, contributes to local one-photon operators. By means of the equations of motion we can simplify the second terms of both the first and the third line of (3.69) as

$$\begin{aligned}
\bar{f}_1 \gamma^\alpha (\not{k}_1 + \not{q} + m_f) &= 2k_1^\alpha \bar{f}_1 - \bar{f}_1 i \sigma^{\alpha\beta} q_\beta , \\
(-\not{k}_2 - \not{q} + m_f) \gamma^\alpha f_2 &= -2k_2^\alpha f_2 - i \sigma^{\alpha\beta} q_\beta f_2 ,
\end{aligned} \tag{3.73}$$

where $\sigma^{\alpha\beta} \equiv \frac{i}{2} [\gamma^\alpha, \gamma^\beta]$ and we dropped terms $\propto q^\alpha$, as they vanish by Ward identity when contracted with $\varepsilon_\alpha(q)$. By summing the first term in each line of the above equation with the contribution from the second diagram, we reproduce the one-photon term from the current J_1^μ , see *iii*). Finally, the second term in each line of (3.73) corresponds to contributions of type *iv*), coming from the additional current

$$J_m^\mu \equiv -\frac{e}{4} F_{\alpha\beta} \left(\bar{f}_1 \sigma^{\alpha\beta} P_R \gamma^\mu f_2 + \bar{f}_1 P_R \gamma^\mu \sigma^{\alpha\beta} f_2 \right) , \tag{3.74}$$

which can be represented diagrammatically as in Fig. 3.10. We note that, while the structure of the above current is determined by gauge and Lorentz invariance, the coefficient with which it enters $\mathcal{O}_{\text{ann}}^{(1)}$ can only be obtained by performing the matching calculation described here. In particular, the arbitrary prefactor $-1/4$ has been chosen in the definition above such that the coefficient is the same as the one of J_1^μ . The result of the matching for the one-photon amplitude is summarized in Fig. 3.11 in terms of the three one-photon vertices defined in Fig. 3.12.

The calculation of the two-photon amplitude $\mathcal{M}_2 = \langle f \bar{f} \gamma \gamma | \mathcal{O}_{\text{ann}}^{(2)} | \chi \bar{\chi} \rangle$ can be performed in the same way and leads to the results displayed in Fig. 3.13. Note that the local two-

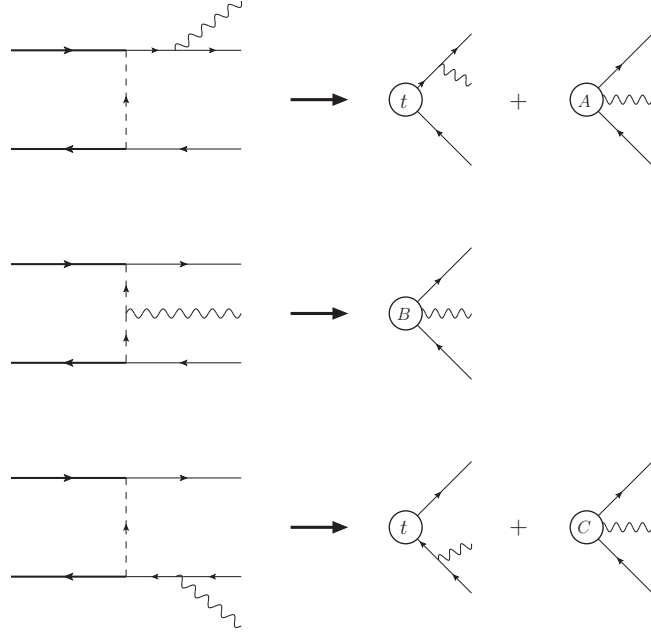


Figure 3.11: Matching of the one-photon annihilation diagrams contributing to $i\mathcal{M}_1$.

photon vertex, defined in Fig. 3.14, cancels out in the gauge-invariant sum of the diagrams. This is consistent with the fact that there is no two-photon local operator contributing at the required order. Because of this, the matching of the two-photon amplitude is only needed for the diagram-by-diagram comparison with the results from Chapter 2, that we will present in the following.

3.3.2 Second step: cross section

The annihilation cross section can be expressed, by means of the optical theorem, in terms of the following forward scattering matrix element

$$\begin{aligned}
 s \sigma_{\text{ann}v} &= 2 \text{Im} \left\{ \frac{1}{4} \sum_{\text{spin}} \langle \chi \bar{\chi}; \Omega_T | \mathcal{O}^{\mu\nu}(p) (\bar{\chi}_2 P_L \gamma_\mu \chi_1 \bar{\chi}_1 \gamma_\nu P_R \chi_2) | \chi \bar{\chi}; \Omega_T \rangle \right\}, \\
 &= 2 \text{Im} \left\{ \langle \Omega_T | \mathcal{O}^{\mu\nu}(p) | \Omega_T \rangle \right\} \text{tr} \chi_{\mu\nu}, \tag{3.75}
 \end{aligned}$$

where in the second line we defined

$$\text{tr} \chi^{\mu\nu} \equiv \frac{1}{4} \sum_{\text{spin}} \langle \chi \bar{\chi} | \bar{\chi}_2 P_L \gamma^\mu \chi_1 \bar{\chi}_1 \gamma^\nu P_R \chi_2 | \chi \bar{\chi} \rangle$$

$$\begin{aligned}
\text{A} &= \frac{\lambda^2}{2m_\phi^4} e \varepsilon^\alpha(q) \bar{f}_1 [(-k_1)_\alpha + \frac{i}{2} \sigma_{\alpha\beta} q^\beta] P_R \gamma^\mu f_2 \\
\text{B} &= \frac{\lambda^2}{2m_\phi^4} e \varepsilon^\alpha(q) (-p_1 + p_2 + k_1 - k_2)_\alpha \bar{f}_1 P_R \gamma^\mu f_2 \\
\text{C} &= \frac{\lambda^2}{2m_\phi^4} e \varepsilon^\alpha(q) \bar{f}_1 P_R \gamma^\mu [(k_2)_\alpha + \frac{i}{2} \sigma_{\alpha\beta} q^\beta] f_2
\end{aligned}$$

$$\text{A} + \text{B} + \text{C} = \frac{\lambda^2}{2m_\phi^4} \left[\text{Diagram 1} + \text{Diagram 2} \right] \equiv \text{t}$$

Figure 3.12: The diagrammatic rules for the vertices used in the one-photon matching in Fig. 3.11.

$$= \frac{1}{4} \text{Tr} \left\{ (\not{p}_2 - m_\chi) P_L \gamma^\mu (\not{p}_1 + m_\chi) \gamma^\nu P_R \right\} . \quad (3.76)$$

The state $|\chi\bar{\chi}; \Omega_T\rangle$ represents the annihilating pair in the thermal photon background, $p \equiv p_1 + p_2$ is the total incoming momentum and $s \equiv p^2$ the center-of-mass energy squared. The operator $\mathcal{O}^{\mu\nu}(p)$ is the time-ordered product of two “total” currents

$$\mathcal{O}^{\mu\nu}(p) \equiv -i \int d^4x e^{-ip \cdot x} \mathcal{T} \left\{ J_t^\mu(0) J_t^{\nu\dagger}(x) \right\} , \quad (3.77)$$

defined as

$$J_t^\mu \equiv \frac{\lambda^2}{2m_\phi^2} \left[\left(1 + \frac{m_\chi^2 + m_f^2}{m_\phi^2} \right) J_0^\mu + \frac{1}{m_\phi^2} J_1^\mu + \frac{1}{m_\phi^2} J_m^\mu \right] + \mathcal{O}(m_\phi^{-6}) , \quad (3.78)$$

and corresponding to the diagrammatic rules depicted in Figs. 3.8 and 3.12.

At the leading order the matrix element in (3.75) is given by the diagram depicted in Fig. 3.15, which reads

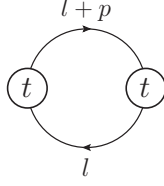


Figure 3.15: The diagram ${}_{tt}D_{11}$, giving the leading order contribution to the matrix element $i\langle\Omega_T|\mathcal{O}^{\mu\nu}(p)|\Omega_T\rangle\text{tr}\chi_{\mu\nu}$.

The numerator is

$$N(l) \equiv \frac{\lambda^4}{4m_\phi^4} \left[1 + 2\frac{m_\chi^2 + m_f^2}{m_\phi^2} - 2\frac{m_\chi}{m_\phi^2} (v_1 \cdot (l+p) - v_2 \cdot l) \right] \text{Tr} \left\{ (l + \not{p}) \gamma^\mu \not{l} \gamma^\nu P_L \right\} \text{tr}\chi_{\mu\nu} . \quad (3.81)$$

Performing the loop integration and computing the imaginary part we obtain (3.56).

As we are interested in the leading correction to the cross section from the interaction with soft photons and fermions from the thermal background, we perform the OPE of the current product $\mathcal{O}^{\mu\nu}(p)$

$$\mathcal{O}^{\mu\nu}(p) = \sum_i C_i^{\mu\nu}(p) \mathcal{O}_i , \quad (3.82)$$

and retain only scalar contractions of the following operators

$$\mathcal{O}_1 \equiv \mathbb{1} , \quad F^{\alpha\beta}(0)F^{\gamma\delta}(0) , \quad \bar{f}(0)\Gamma f(0) , \quad \bar{f}(0)\Gamma iD^\alpha f(0) , \quad (3.83)$$

where both the photon and the fermion fields are those of the HPET, thus describing soft particles only, and Γ is a 4×4 matrix in spinor space. The operators above are the only ones that contribute to the cross section up to $\mathcal{O}(\tau^4)$. Adopting the following definitions

$$\widehat{C}_i \equiv 2\text{Im} \{C_i^{\mu\nu}(p)\} \text{tr}\chi_{\mu\nu} , \quad (3.84)$$

$$M_i \equiv \langle\Omega_T|\mathcal{O}_i|\Omega_T\rangle , \quad (3.85)$$

we get

$$s\sigma_{\text{ann}}v = \sum_i \widehat{C}_i M_i . \quad (3.86)$$

As we did for the decay, we first compute the thermal matrix elements M_i and then we move on to the matching calculation required to get the coefficients \widehat{C}_i .

Calculation of the matrix elements

We start by considering the matrix element in the thermal vacuum of the second operator in (3.83)

$$M_A^{\alpha\beta\gamma\delta} \equiv \langle\Omega_T|F^{\alpha\beta}(0)F^{\gamma\delta}(0)|\Omega_T\rangle . \quad (3.87)$$

Since the only four-vector on which it can depend is the plasma velocity v , and due to the antisymmetry property of the field strength tensor, we can write the following parametrization

$$\begin{aligned} M_A^{\alpha\beta\gamma\delta} = & \frac{c_1}{2} \left(g^{\alpha\gamma} g^{\beta\delta} - g^{\alpha\delta} g^{\beta\gamma} \right) + \frac{c_2}{4} \left(v^\alpha \left(v^\gamma g^{\beta\delta} - v^\delta g^{\beta\gamma} \right) + v^\beta \left(v^\delta g^{\alpha\gamma} - v^\gamma g^{\alpha\delta} \right) \right) \\ & + c_3 \varepsilon^{\alpha\beta\gamma\delta} + \frac{c_4}{2} \left(v^\alpha v_\rho \varepsilon^{\rho\beta\gamma\delta} - v^\beta v_\rho \varepsilon^{\rho\alpha\gamma\delta} \right) . \end{aligned} \quad (3.88)$$

In order to determine the values of the parameters we consider the following contractions

$$\langle \Omega_T | F_{\mu\nu} F^{\mu\nu} | \Omega_T \rangle = 6 c_1 + \frac{3}{2} c_2 , \quad (3.89)$$

$$\langle \Omega_T | v_\mu v^\nu F_{\alpha\nu} F^{\alpha\mu} | \Omega_T \rangle = \frac{3}{2} c_1 + \frac{3}{4} c_2 , \quad (3.90)$$

$$\langle \Omega_T | F_{\mu\nu} \varepsilon^{\mu\nu\alpha\beta} F_{\alpha\beta} | \Omega_T \rangle = -24 c_3 - 6 c_4 , \quad (3.91)$$

$$\langle \Omega_T | v_\mu v^\nu F_{\alpha\nu} \varepsilon^{\alpha\mu\rho\sigma} F_{\rho\sigma} | \Omega_T \rangle = -6 c_3 - 3 c_4 . \quad (3.92)$$

By using the definition of the thermal photon propagator (3.32) and (3.36) we can write

$$\begin{aligned} \langle \Omega_T | \mathcal{T} \left\{ F^{\alpha\beta}(x) F^{\gamma\delta}(y) \right\} | \Omega_T \rangle = & \int \frac{d^4 k}{(2\pi)^4} e^{ik(x-y)} (-2\pi) \delta(k^2) f_B(\omega) \\ & \times \left(k^\alpha k^\gamma g^{\beta\delta} - k^\alpha k^\delta g^{\beta\gamma} - k^\beta k^\gamma g^{\alpha\delta} + k^\beta k^\delta g^{\alpha\gamma} \right) , \end{aligned} \quad (3.93)$$

where ω is the photon energy in the frame of the plasma. Evaluating this expression at $x = y = 0$ and contracting it as in (3.89 - 3.92), we obtain integrals of the form of (2.115). Inserting the result (2.117) for J_3 we immediately get, in agreement with [100] (see also [105])

$$\langle \Omega_T | F_{\mu\nu} F^{\mu\nu} | \Omega_T \rangle = 0 , \quad (3.94)$$

$$\langle \Omega_T | v_\mu v^\nu F_{\alpha\nu} F^{\alpha\mu} | \Omega_T \rangle = -\frac{\pi^2}{15} T^4 , \quad (3.95)$$

$$\langle \Omega_T | F_{\mu\nu} \varepsilon^{\mu\nu\alpha\beta} F_{\alpha\beta} | \Omega_T \rangle = 0 , \quad (3.96)$$

$$\langle \Omega_T | v_\mu v^\nu F_{\alpha\nu} \varepsilon^{\alpha\mu\rho\sigma} F_{\rho\sigma} | \Omega_T \rangle = 0 , \quad (3.97)$$

from which we obtain the parameters

$$c_1 = -\frac{1}{4} c_2 = \frac{2\pi^2}{45} T^4 , \quad c_3 = c_4 = 0 . \quad (3.98)$$

We conclude that the thermal photons contribute at the order $\mathcal{O}(\tau^4)$ via the following four scalar operators

$$\mathcal{O}_{A1} \equiv (v_1^\mu v_2^\nu F_{\mu\nu})^2 , \quad \mathcal{O}_{An} \equiv v_i^\mu v_j^\nu F_{\alpha\mu} F_{\nu}^\alpha \quad \text{for } n \equiv i + j = 2, 3, 4 , \quad (3.99)$$

and the corresponding condensates are

$$M_{A1} = \frac{\pi^2}{45} T^4 (1 - (v_1 \cdot v_2)^2 - 2(v \cdot v_1)^2 - 2(v \cdot v_2)^2 + 4v \cdot v_1 v \cdot v_2 v_1 \cdot v_2) , \quad (3.100)$$

$$M_{An} = \frac{\pi^2}{45} T^4 (v_i \cdot v_j - 4v \cdot v_i v \cdot v_j) \quad \text{for } n \equiv i + j = 2, 3, 4 . \quad (3.101)$$

The matrix elements in the thermal vacuum of the last two operators in (3.83) can be computed along the same line by using the definition of the thermal fermion propagator (see (2.6) and (2.19))

$$\begin{aligned} \langle \Omega_T | \mathcal{T} \{ f(x) \bar{f}(y) \} | \Omega_T \rangle &= iS^{++}(x, y) \\ &= \int \frac{d^4 k}{(2\pi)^4} e^{-ik \cdot (x-y)} iS^{++}(k) , \end{aligned} \quad (3.102)$$

and retaining the thermal part only (2.34)

$$iS^{++}(k) \rightarrow -2\pi (\not{k} + m_f) \delta(k^2 - m_f^2) f_F(\omega) . \quad (3.103)$$

Decomposing the generic matrix Γ on the basis $\{\mathbb{1}, \gamma_5, \gamma^\mu, \gamma^\mu \gamma_5, \sigma^{\mu\nu}\}$ we find that the only non-vanishing matrix elements are

$$\langle \Omega_T | \bar{f}(0) f(0) | \Omega_T \rangle = -4m_f \int \frac{d^4 k}{(2\pi)^3} \delta(k^2 - m_f^2) f_F(\omega) , \quad (3.104)$$

which corresponds to a fermion condensate correction of $\mathcal{O}(\epsilon\tau^2)$, and

$$M_f^{\mu\alpha} \equiv \langle \Omega_T | \bar{f}(0) \gamma^\mu iD^\alpha f(0) | \Omega_T \rangle = 4 \int \frac{d^4 k}{(2\pi)^3} k^\mu k^\alpha \delta(k^2 - m_f^2) f_F(\omega) , \quad (3.105)$$

which can be parametrized as

$$M_f^{\mu\alpha} = d_1 g^{\mu\alpha} + d_2 v^\mu v^\alpha . \quad (3.106)$$

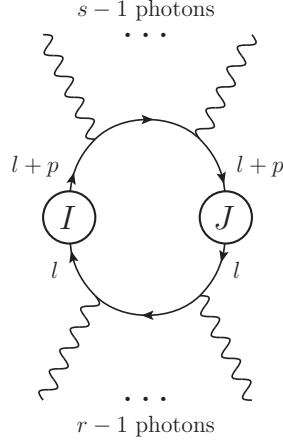
For $m_f = 0$ we can use the integral in (2.116) and the result (2.117) for I_3 to compute the contractions of $M_f^{\mu\alpha}$ with $g_{\mu\alpha}$ and $v_\mu v_\alpha$ and obtain

$$4d_1 + d_2 = 0 , \quad (3.107)$$

$$d_1 + d_2 = \frac{7\pi^2}{60} T^4 , \quad (3.108)$$

from which it follows

$$d_1 = -\frac{1}{4} d_2 = -\frac{7\pi^2}{180} T^4 . \quad (3.109)$$

Figure 3.16: Generic diagram IJD_{rs} .

We conclude that the contributions to $\mathcal{O}(\tau^4)$ from thermal fermions are due to the following three operators

$$\mathcal{O}_{fn} \equiv \bar{f}(0) \psi_i v_j \cdot iD f(0) \quad \text{for } n \equiv i + j = 2, 3, 4, \quad (3.110)$$

which condensates are

$$M_{fn} = -\frac{7\pi^2}{180} T^4 (v_i \cdot v_j - 4v \cdot v_i v \cdot v_j) \quad \text{for } n \equiv i + j = 2, 3, 4. \quad (3.111)$$

As expected by power-counting, both the photon and the fermion condensate contribute at the same order $\mathcal{O}(\tau^4)$

$$\begin{aligned} s \sigma_{\text{ann}} v &= \hat{C}_1 + \left(\frac{\pi^2}{45} m_\chi^4 \tau^4 \right) \left[\hat{C}_{A1} (1 - (v_1 \cdot v_2)^2 - 2(v \cdot v_1)^2 - 2(v \cdot v_2)^2 + 4v \cdot v_1 v \cdot v_2 v_1 \cdot v_2) \right. \\ &\quad \left. + \sum_{n=2,3,4} \left(\hat{C}_{An} - \frac{7}{4} \hat{C}_{fn} \right) (v_i \cdot v_j - 4v \cdot v_i v \cdot v_j) \right] + \mathcal{O}(\tau^6). \end{aligned} \quad (3.112)$$

Diagrams calculation

Before moving on to the matching calculation, we define here the notation for the relevant diagrams. Consider the generic diagram IJD_{rs} depicted in Fig. 3.16, where the labels I, J denote vertex factors and $r-1$ ($s-1$) the number of photons attached to the lower (upper) loop leg. In the limit in which all the photon momenta vanish, the denominator can be written in terms of Feynman parameters as

$$d_{rs}^{-1} = [(l^2 - m_f^2)^r ((l+p)^2 - m_f^2)^s]^{-1}$$

$$\begin{aligned}
&= \int_0^1 dx \frac{\Gamma(r+s)}{\Gamma(r)\Gamma(s)} x^{r-1} (1-x)^{s-1} [x(l^2 - m_f^2) + (1-x)((l+p)^2 - m_f^2)]^{-r-s} \\
&= \int_0^1 dx \frac{\Gamma(r+s)}{\Gamma(r)\Gamma(s)} x^{r-1} (1-x)^{s-1} [q^2 - \Delta]^{-r-s} , \tag{3.113}
\end{aligned}$$

where in the last line we defined the shifted loop momentum and Δ as in (3.80). We can therefore write

$$\begin{aligned}
{}_{IJ}D_{rs} &= \int \frac{d^d l}{(2\pi)^d} \frac{{}_{IJ}N_{rs}(l)}{d_{rs}} \\
&= \sum_m \int_0^1 dx \frac{\Gamma(r+s)}{\Gamma(r)\Gamma(s)} x^{r-1} (1-x)^{s-1} {}_{IJ}C_{rs}^{(m)} I_{m(r+s)} , \tag{3.114}
\end{aligned}$$

where ${}_{IJ}C_{rs}^{(m)}$ is the coefficient of q^m in the numerator after the loop momentum shift and we defined

$$\begin{aligned}
I_{mn} &\equiv \int \frac{d^d q}{(2\pi)^d} \frac{q^m}{(q^2 - \Delta)^n} \\
&= \frac{i}{(4\pi)^{d/2}} (-1)^{n+\frac{m}{2}} \Delta^{\frac{m}{2}-n+\frac{d}{2}} \frac{\Gamma(\frac{m+d}{2}) \Gamma(n - \frac{m}{2} - \frac{d}{2})}{\Gamma(\frac{d}{2}) \Gamma(n)} . \tag{3.115}
\end{aligned}$$

The above expression holds for even values of m , while the integral vanishes for odd values.

Matching at order $\mathcal{O}(\tau^2)$, thermal photons

Within the OPE approach of this Chapter, the fact that the correction vanishes at order $\mathcal{O}(\tau^2)$ follows from the absence of gauge invariant operators that could contribute at this order. As a proof of concept, we can anyway perform a diagram-by-diagram comparison with the results from Chapter 2.

Any $\mathcal{O}(\tau^2)$ thermal-photon contribution to $s\sigma_{v_{\text{rel}}}$ can be computed by considering a two-photon diagram of the type displayed in Fig. 3.16, closing the photon line and retaining the thermal part only of the equilibrium propagator (3.36)

$${}_{IJ}\bar{D}_{rs} \equiv 2 \text{Im} \{ -i {}_{IJ}D_{rs}|_{\text{thermal photon}} \} . \tag{3.116}$$

The separate diagram-by-diagram comparison with the results from Chapter 2 is made possible by the matching of the two-photon amplitude, summarized in Fig. 3.13. If we denote with $s\sigma_{v_{\text{rel}}}|_{\text{line } n}$ the contribution to the cross section from the diagram in the n^{th} line of Table 2.2, the identifications read

$$s\sigma_{\text{ann}v}|_{\text{line } 1} = \left[{}_{tt}\bar{D}_{13} + ({}_{At}\bar{D}_{12} + {}_{tA}\bar{D}_{12}) - \frac{1}{2} ({}_{dt}\bar{D}_{11} + {}_{td}\bar{D}_{11}) \right] , \tag{3.117}$$

$$s \sigma_{\text{ann}} v|_{\text{line 2}} = \left[{}_{tt}\overline{D}_{31} + ({}_{Ct}\overline{D}_{21} + {}_{tC}\overline{D}_{21}) - \frac{1}{2} ({}_{dt}\overline{D}_{11} + {}_{td}\overline{D}_{11}) \right], \quad (3.118)$$

$$s \sigma_{\text{ann}} v|_{\text{line 3}} = \mathcal{O}(\xi^{-8}), \quad (3.119)$$

$$s \sigma_{\text{ann}} v|_{\text{line 4}} = {}_{tB}\overline{D}_{12}, \quad (3.120)$$

$$s \sigma_{\text{ann}} v|_{\text{line 5}} = {}_{Bt}\overline{D}_{12}, \quad (3.121)$$

$$s \sigma_{\text{ann}} v|_{\text{line 6}} = {}_{tB}\overline{D}_{21}, \quad (3.122)$$

$$s \sigma_{\text{ann}} v|_{\text{line 7}} = {}_{Bt}\overline{D}_{21}, \quad (3.123)$$

$$s \sigma_{\text{ann}} v|_{\text{line 8}} = \mathcal{O}(\xi^{-8}), \quad (3.124)$$

$$s \sigma_{\text{ann}} v|_{\text{line 9}} = \mathcal{O}(\xi^{-8}), \quad (3.125)$$

$$s \sigma_{\text{ann}} v|_{\text{line 10}} = [{}_{tt}\overline{D}_{22} + ({}_{At}\overline{D}_{21} + {}_{tA}\overline{D}_{21}) + ({}_{Ct}\overline{D}_{12} + {}_{tC}\overline{D}_{12})], \quad (3.126)$$

$$s \sigma_{\text{ann}} v|_{\text{line 11}} = {}_{dt}\overline{D}_{11}, \quad (3.127)$$

$$s \sigma_{\text{ann}} v|_{\text{line 12}} = {}_{td}\overline{D}_{11}. \quad (3.128)$$

We performed the computation of the diagrams on the r.h.s. as described above and checked that we correctly reproduce the partial results for $s \sigma v_{\text{rel}}$ to order $\mathcal{O}(\xi^{-6})$, retaining the full energy dependence (no partial wave expansion).

Matching at order $\mathcal{O}(\tau^4)$, thermal photons

The matching condition for the photon operators is obtained by taking the one-photon matrix element

$$\begin{aligned} \sum_{n=1,\dots,4} \widehat{C}_{An} \langle \gamma | \mathcal{O}_{An} | \gamma \rangle &= 2 \text{Im} \{ \langle \gamma | \mathcal{O}^{\mu\nu}(p) | \gamma \rangle \} \text{tr} \chi_{\mu\nu} \\ &= 2 \text{Im} \left\{ -i {}_{tt}E_{13} - i {}_{tt}E_{22} - i {}_{tt}E_{31} \right\}_{\text{order } k^2} + \mathcal{O}(m_\phi^{-6}), \end{aligned} \quad (3.129)$$

where in the second line we used ${}_{tt}E_{rs}$ to denote the diagram as in Fig. 3.16 but with finite photon momentum k

$${}_{tt}E_{rs} = \int \frac{d^d l}{(2\pi)^d} \frac{\overline{M}_{rs}(l, k)}{D_{rs}(k)}. \quad (3.130)$$

We expand up to second order in k . The numerator can be written as

$$\overline{M}_{rs}(l, k) = \overline{M}_{rs}(l) + k_\alpha \overline{M}_{rs}^\alpha(l) + k_\alpha k_\beta \overline{M}_{rs}^{\alpha\beta}(l) + \mathcal{O}(k^3). \quad (3.131)$$

Expanding also the denominator we get

$${}_{tt}E_{13}|_{\text{order } k^2} = k_\alpha k_\beta \int \frac{d^d l}{(2\pi)^d} \frac{2(l+p)^\alpha \overline{M}_{13}^\beta(l)}{d_{14}} + \frac{4(l+p)^\alpha (l+p)^\beta \overline{M}_{13}(l)}{d_{15}}, \quad (3.132)$$

and similar expressions for the remaining two diagrams. The integrals are now independent on the photon momentum and can be performed as described in the previous Section. The results are

$$\widehat{C}_{A1} \propto -6\epsilon^2 e_\chi^4 + 42\epsilon^4 e_\chi^2 - 72\epsilon^6, \quad (3.133)$$

$$\widehat{C}_{A2} = \widehat{C}_{A4} \propto 2e_\chi^8 - 5\epsilon^2 e_\chi^4 (4e_\chi^2 - 1) + \epsilon^4 e_\chi^2 (66e_\chi^2 - 35) - 12\epsilon^6 (7e_\chi^2 - 5), \quad (3.134)$$

$$\widehat{C}_{A3} \propto -10\epsilon^2 e_\chi^4 (2e_\chi^2 - 1) + 70\epsilon^4 e_\chi^2 (2e_\chi^2 - 1) - 24\epsilon^6 (11e_\chi^2 - 5), \quad (3.135)$$

where the proportionality factor reads $\frac{\alpha\lambda^4}{48e_\chi^5 \xi^4 (e_\chi^2 - 4\epsilon^2)^{5/2}}$. The $\mathcal{O}(\tau^4)$ contribution to the cross section from thermal photons can then be computed as

$$\begin{aligned} s \sigma_{\text{ann}} v|_{\tau^4, \text{Dirac}} &= \left(\frac{\pi^2}{45} m_\chi^4 \tau^4 \right) \left[\widehat{C}_{A1} \left(1 - (v_1 \cdot v_2)^2 - 2(v \cdot v_1)^2 - 2(v \cdot v_2)^2 + 4v \cdot v_1 v \cdot v_2 v_1 \cdot v_2 \right) \right. \\ &\quad \left. + \sum_{n=2,3,4} \widehat{C}_{An} (v_i \cdot v_j - 4v \cdot v_i v \cdot v_j) \right] \\ &= \left(\frac{\pi^2}{45} m_\chi^4 \tau^4 \right) \left[\widehat{C}_{A1} (4e_\chi^2 (e_\chi^2 - 1)) - (\widehat{C}_{A2} + \widehat{C}_{A4}) (4e_\chi^2 - 1) - \widehat{C}_{A3} (2e_\chi^2 + 1) \right], \end{aligned} \quad (3.136)$$

where in the second line we assumed that the center-of-mass frame of the annihilation coincides with the rest frame of the thermal background, such that $p = \sqrt{s} v$ and

$$v \cdot v_1 = v \cdot v_2 = e_\chi, \quad v_1 \cdot v_2 = 2e_\chi^2 - 1. \quad (3.137)$$

Inserting (3.133 - 3.135) into (3.136) we correctly reproduce the expected result (3.57).

Matching at order $\mathcal{O}(\tau^4)$, thermal fermions

The matching condition for the fermion operators is obtained by taking the one-fermion matrix element

$$\begin{aligned} \sum_{n=2,3,4} \widehat{C}_{fn}(p) \langle f | \mathcal{O}_{fn} | f \rangle &= 2 \text{Im} \{ \langle f | \mathcal{O}^{\mu\nu}(p) | f \rangle \} \text{tr} \chi_{\mu\nu} \\ &= 2 \text{Im} \left\{ \left(-iE_{[1]} - iE_{[1]}^{rev} \right) + \left(-iE_{[2]} - iE_{[2]}^{rev} \right) \right. \\ &\quad \left. + \left(-iE_{[3]} - iE_{[3C]} - iE_{[3]}^{rev} - iE_{[3C]}^{rev} \right) \right\}_{\text{order } k^2} + \mathcal{O}(m_\phi^{-6}), \end{aligned} \quad (3.138)$$

where the diagrams in the last two lines are depicted in Fig. 3.17. The calculation is analogous

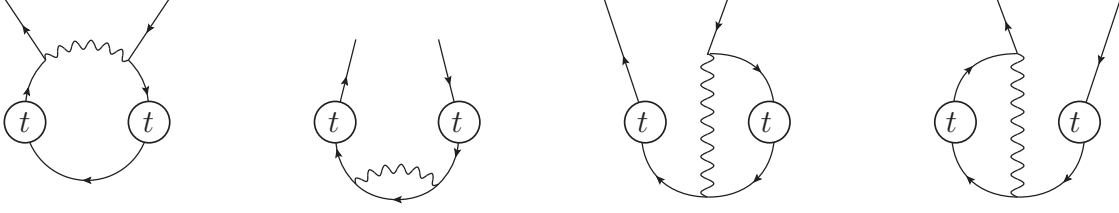


Figure 3.17: The diagrams $E_{[1]}$, $E_{[2]}$, $E_{[3]}$ and $E_{[3C]}$. The same diagrams with reversed charge flow are denoted by a superscript *rev*.

to the one in the previous paragraph and the results are

$$\widehat{C}_{f2} = \widehat{C}_{f4} = \frac{\alpha\lambda^4}{12e_\chi^2\xi^4}, \quad (3.139)$$

$$\widehat{C}_{f3} = 0. \quad (3.140)$$

The $\mathcal{O}(\tau^4)$ contribution to the cross section from thermal fermions can then be computed as

$$s\sigma_{\text{ann}v}|_{\tau^4, \text{Dirac, thermal fermions}} = \left(-\frac{7\pi^2}{180}m_\chi^4\tau^4\right) \sum_{n=2,3,4} \widehat{C}_{fn} (v_i \cdot v_j - 4v \cdot v_i v \cdot v_j). \quad (3.141)$$

As in the thermal photon case, setting $p = \sqrt{s}v$ we correctly reproduce the expected result (3.58).

Chapter 4

Relic density of neutralino dark matter in the MSSM

Among the proposed models for physics beyond the Standard Model (BSM), one of the most promising and therefore studied ones is its minimal supersymmetric extension, the MSSM. On top of the theoretical issues that it addresses (hierarchy problem, gauge coupling unification), an important feature of this model is that it provides a natural candidate for a DM particle, the lightest neutralino, that can account for the whole measured abundance Ω_{DM} over a large region of the parameter space. Moreover, this model can be constrained by complementary experimental searches, such as DM direct and indirect detection and collider searches. In this Chapter we concentrate on the relic density of TeV-scale neutralinos, a wide scenario that covers many viable and phenomenologically interesting regions of the MSSM parameter space.

We open this Chapter with an introduction, in order to provide the motivation for our study. We then briefly introduce the phenomenological MSSM (pMSSM) in Sec. 4.2, mainly focusing on the properties of the neutralino-chargino sector that will be relevant in the following. In Sec. 4.3 we consider the non-perturbative effect called Sommerfeld enhancement and we argue that, in the scenario we are interested in, it leads to potentially large corrections to the relic density. We start with a review of the procedure to consistently treat this effect in an effective field theory formalism, first developed in [44–46]. As an illustrative example we present the full results within this formalism for the case of neutralino co-annihilation with a sfermion. In Sec. 4.4 we then describe how we implemented into an automated code the formalism to compute the Sommerfeld-enhanced relic density for a generic point of the pMSSM parameter space. We conclude in Sec. 4.5 by presenting the analysis of wino-like scenarios that we performed, and discussing the obtained results [47].

4.1 Introduction and motivation

In Chapter 1 we described the cold dark matter (CDM) freeze-out scenario, the most widely studied and arguably most natural among the DM production mechanisms. In this scenario the present day abundance of DM is the relic density of a particle species that was thermally produced in the early Universe and that subsequently decoupled from the thermal plasma. The relic abundance is determined by the co-annihilation cross sections of DM particles around the freeze-out, occurring at $T_{\text{f.o.}} \sim m_\chi/20$, when co-annihilating particles were in the non-relativistic regime. As we have seen, a particle species with weak interaction strength and mass around the electroweak or TeV scale (WIMP) yields to the correct order of magnitude for the relic density in the freeze-out scenario, thus being a natural candidate for CDM.

In this Chapter we will focus on an important example of WIMPs, the neutralinos in the minimal supersymmetric extension of the Standard Model (MSSM) with R -parity conservation. In the past few years the study of neutralino DM has become an increasing interest on both the experimental and the phenomenological side, due to the possibility for complementary searches in direct and indirect detection, and at colliders. Within this context, scenarios with DM masses below 1 TeV are becoming somewhat constrained, see e.g. [106–109] for recent analyses. Scenarios with heavier DM interpolate to minimal models, as the supersymmetric particles form approximate electroweak multiplets (except for degeneracies). In particular, when the lightest neutralino is the partner of the $SU(2)_L$ gauge bosons and all the other supersymmetric particles are decoupled to very high masses (“pure-wino” limit), the obtained scenario corresponds to the well-studied minimal triplet model, in which the SM is extended by adding a fermionic $SU(2)_L$ triplet. Similarly, the “pure-Higgsino” limit of the MSSM corresponds to the addition to the SM of two fermionic $SU(2)_L$ doublets.

Compared to TeV-scale neutralinos, the gauge and Higgs bosons are light, such that their exchange between two non-relativistic neutralinos generates long-range Yukawa potentials. As it is well known from non-relativistic quantum mechanics, the presence of a long-range interaction affects the rate of short-distance processes such as pair-annihilation via the non-perturbative effect known as Sommerfeld enhancement [37]. In the context of dark matter, this effect was first studied by Hisano et al. [38, 39] for the present day annihilation cross section into two photons, relevant for indirect detection, in the pure-wino and pure-Higgsino limits. Mainly motivated by the anomalous positron excess measured by PAMELA, the study of the enhancement due to the exchange of a new light particle as a mechanism to boost the DM annihilation rates was subsequently considered [110]. Since then an increasing literature on the topic appeared [40–43, 111–116]. The Sommerfeld effect may lead to a very large modification of the total annihilation cross section, up to several orders of magnitude. Such a large enhancement of the cross section results in an $\mathcal{O}(1)$ reduction of the relic abundance, compared to the perturbative calculation. Even though such a dramatic effect is only found in peculiar scenarios, for a TeV-scale dominantly wino neutralino (“wino-like”) the enhancement is *generically* large,

and cannot be neglected in any reliable calculation.¹

Having this in mind we developed a code, based on the theoretical framework described in [44–46], that computes the Sommerfeld-enhanced relic density of a generic MSSM point. Within this framework mixed states and multiple co-annihilation channels are properly treated and off-diagonal contributions to the cross section are included, thus extending and generalizing the analyses present in the literature [41–43].

The code allowed us to perform a detailed study of so far unexplored wino-like scenarios [47], which depart from the pure-wino limit due to the mixing with the Higgsino and bino states, as well as the interactions with sfermions, and result in a rich phenomenology. This is particularly relevant in light of the recent strong constraints on the pure-wino scenario from cosmic ray observations [116, 118, 119].

4.2 The R -conserving phenomenological-MSSM

In this Section we briefly introduce the minimally supersymmetric standard model (MSSM), focusing on the properties that are needed to understand the study of the wino-like DM relic density in the following. For an introductory and complete review see e.g. [36], from which we base the presentation in this Section.

Originally introduced to address the “hierarchy problem” [120], a symmetry relating fermions to bosons and vice-versa is now a main ingredient of various among the most studied BSM models. Such a symmetry, whose generators are fermionic operators, is called *supersymmetry* (SUSY). The single-particle states of a theory whose Lagrangian is invariant under SUSY transformations, fall into irreducible representations of the SUSY algebra, called supermultiplets. Each supermultiplet contains both fermion and boson states, which are called superpartners of each other. The minimal supersymmetric extension of the Standard Model (MSSM) is obtained by embedding each SM particle into either a chiral or a gauge supermultiplet. The MSSM spectrum contains therefore all the SM particles and the corresponding superpartners, called *sparticles*. Compared to the corresponding particle, each sparticle has the same set of $SU(3)_C \times SU(2)_L \times U(1)_Y$ quantum numbers but spin differing by $1/2$ unit, as collected in Tables 4.1 and 4.2.

On top of the kinetic and gauge terms for the superfields listed in the tables, the renormalizable MSSM Lagrangian may contain any term that is gauge and SUSY invariant. The sum of those terms constitute the *superpotential*. In the most general superpotential, terms that violate either the baryon number (B) or the lepton number (L) are allowed. Those terms are problematic, since they need to be strongly suppressed in order for the proton to be as stable as experimentally observed (lifetime larger than 10^{32} years). On the other hand, B and

¹The residual theoretical error on the relic density from neglecting other type of enhanced corrections (Sudakov logarithms, potential QCD effects for quark and gluon final states), as well as ordinary, non-enhanced corrections, is estimated to be of $\mathcal{O}(5\%)$ [117].

| Names | | spin 0 | spin 1/2 | $SU(3)_C, SU(2)_L, U(1)_Y$ |
|---|-----------|-----------------------------|---------------------------------|--|
| squarks, quarks ($\times 3$ families) | Q | $(\tilde{u}_L \tilde{d}_L)$ | $(u_L d_L)$ | $(\mathbf{3}, \mathbf{2}, \frac{1}{6})$ |
| | \bar{u} | \tilde{u}_R^* | u_R^\dagger | $(\bar{\mathbf{3}}, \mathbf{1}, -\frac{2}{3})$ |
| | \bar{d} | \tilde{d}_R^* | d_R^\dagger | $(\bar{\mathbf{3}}, \mathbf{1}, \frac{1}{3})$ |
| sleptons, leptons ($\times 3$ families) | L | $(\tilde{\nu} \tilde{e}_L)$ | (νe_L) | $(\mathbf{1}, \mathbf{2}, -\frac{1}{2})$ |
| | \bar{e} | \tilde{e}_R^* | e_R^\dagger | $(\mathbf{1}, \mathbf{1}, 1)$ |
| Higgs, Higgsinos | H_u | $(H_u^+ H_u^0)$ | $(\tilde{H}_u^+ \tilde{H}_u^0)$ | $(\mathbf{1}, \mathbf{2}, +\frac{1}{2})$ |
| | H_d | $(H_d^0 H_d^-)$ | $(\tilde{H}_d^0 \tilde{H}_d^-)$ | $(\mathbf{1}, \mathbf{2}, -\frac{1}{2})$ |

Table 4.1: Chiral supermultiplets in the MSSM. The spin-0 fields are complex scalars while the spin- $\frac{1}{2}$ fields are left-handed two-component Weyl fermions.

| Names | spin 1/2 | spin 1 | $SU(3)_C, SU(2)_L, U(1)_Y$ |
|-----------------|-----------------------------|-------------|-------------------------------|
| gluino, gluon | \tilde{g} | g | $(\mathbf{8}, \mathbf{1}, 0)$ |
| winos, W bosons | $\tilde{W}^\pm \tilde{W}^0$ | $W^\pm W^0$ | $(\mathbf{1}, \mathbf{3}, 0)$ |
| bino, B boson | \tilde{B}^0 | B^0 | $(\mathbf{1}, \mathbf{1}, 0)$ |

Table 4.2: Gauge supermultiplets in the MSSM.

L cannot simply be postulated as exact symmetries of the theory, since they are known to be violated by non-perturbative electroweak effects [121]. The common way out to this problem is to postulate an additional symmetry called “ R -parity”, a multiplicative conserved quantum number defined for each particle as

$$P_R = (-1)^{3(B-L)+2s}, \quad (4.1)$$

where $B = 1/3$ ($-1/3$) for each particle in Q (\bar{u}, \bar{d}), $B = 0$ for any other particle, $L = 1$ (-1) for each particle in L (\bar{e}), $L = 0$ for any other particle, and s is the spin of the particle. This symmetry has the effect of forbidding both B and L violating terms in the renormalizable superpotential, while not preventing their violation in non-perturbative effects. In the above formulation, the R -parity does not commute with supersymmetry, since different particles in the same supermultiplet have different values of P_R . Indeed it is easy to see that each SM and Higgs particle has $P_R = +1$, while all the sparticles have $P_R = -1$. Each interaction vertex obtained from an R -parity conserving superpotential must therefore contain an even

number of sparticles. This leads to an important property of R -parity conserving realizations of the MSSM, namely the stability of the lightest supersymmetric particle (LSP). The R -conserving MSSM provides therefore naturally a candidate for dark matter whenever the LSP is electrically neutral, since any other SUSY particle will eventually decay into it. We consider here the R -parity conserving MSSM, for which the most general superpotential reads

$$W = \bar{u}\mathbf{y}_u QH_u - \bar{d}\mathbf{y}_d QH_d - \bar{e}\mathbf{y}_e LH_d + \mu H_u H_d \quad , \quad (4.2)$$

where the dimensionless Yukawa couplings \mathbf{y}_u , \mathbf{y}_d and \mathbf{y}_e are 3×3 complex matrices in family space, and the complex parameter μ is the SUSY version of the SM Higgs mass parameter. When the electroweak symmetry is spontaneously broken, the Yukawa couplings must reproduce the current masses and CKM mixing angles of the ordinary quarks and leptons.

If SUSY was not broken, all the particles in the same supermultiplet would have the same mass, and some sparticle would have been already discovered. In order to be phenomenologically viable, supersymmetry must therefore be broken at a certain scale $\Lambda_{\text{soft}} \gtrsim \text{TeV}$. Many models of symmetry breaking have been proposed, and each one leads to different properties of the low-energy spectrum. From a phenomenological point of view and without loss of generality it is useful to write an *effective* MSSM Lagrangian defined at the electroweak scale and containing extra SUSY-breaking terms. Those terms must be gauge invariant and “soft”, meaning that the SUSY-breaking couplings must be of positive mass dimension with characteristic scale Λ_{soft} . The most general expression for the soft Lagrangian reads

$$\begin{aligned} \mathcal{L}_{\text{soft}} = & -\frac{1}{2} \left(M_3 \tilde{g}\tilde{g} + M_2 \tilde{W}\tilde{W} + M_1 \tilde{B}\tilde{B} + \text{c.c.} \right) \\ & - \left(\tilde{u} \mathbf{a}_u \tilde{Q} H_u - \tilde{d} \mathbf{a}_d \tilde{Q} H_d - \tilde{e} \mathbf{a}_e \tilde{L} H_d + \text{c.c.} \right) \\ & - \tilde{Q}^\dagger \mathbf{m}_Q^2 \tilde{Q} - \tilde{L}^\dagger \mathbf{m}_L^2 \tilde{L} - \tilde{u} \mathbf{m}_u^2 \tilde{u}^\dagger - \tilde{d} \mathbf{m}_d^2 \tilde{d}^\dagger - \tilde{e} \mathbf{m}_e^2 \tilde{e}^\dagger \\ & - m_{H_u}^2 H_u^* H_u - m_{H_d}^2 H_d^* H_d - (b H_u H_d + \text{c.c.}) \quad , \end{aligned} \quad (4.3)$$

where the introduced free parameters are:

- $M_{1,2,3}$ gaugino soft masses;
- $\mathbf{a}_{u,d,e}$ trilinear couplings (3×3 matrices in family space);
- $\mathbf{m}_{Q,L,\bar{u},\bar{d},\bar{e}}^2$ sfermion soft masses (3×3 hermitian matrices in family space);
- $m_{H_{u,d}}^2, b$ Higgsino soft masses.

The new parameters listed above are in general complex, with the only exception of $m_{H_{u,d}}^2$, that must be real. After all the possible redefinitions for the phases and flavor basis of the quark and lepton supermultiplets are taken into account, one is left with 105 masses, phases

and mixing angles, in addition to the 19 free parameters in the SM [122]. The pMSSM is therefore an effective theory defined at the electroweak scale by the Lagrangian

$$\mathcal{L}_{\text{pMSSM}} = \mathcal{L}_{\text{kin+gauge}} + W + \mathcal{L}_{\text{soft}} . \quad (4.4)$$

The physical low-energy spectrum is obtained by diagonalizing the mass matrices arising as a result of the electroweak symmetry breaking (EWSB), $SU(2)_L \times U(1)_Y \rightarrow U(1)_{\text{EM}}$.

Since it will be important for our study, in the remaining of this Section we describe the parametrization of the Higgs sector, and in the following one we study the mixing of the Higgsinos with the electroweak gauginos. For a detailed description of the EWSB mechanism in the MSSM we refer the reader to the review [36]. The main difference with the standard Higgs mechanism in the SM is that in the MSSM there are two Higgs doublets, and the neutral components of both of them acquire a vacuum expectation value (VEV)

$$v_u \equiv \langle H_u^0 \rangle , \quad v_d \equiv \langle H_d^0 \rangle . \quad (4.5)$$

Via a redefinition of the phases of H_u and H_d , and a $U(1)_Y$ gauge transformation, one can set both the VEVs to be real and positive, and the mass parameter b to be real, without loss of generality. The two VEVs are usually written in terms of the parameters v and $\tan \beta$, defined as

$$v^2 \equiv v_u^2 + v_d^2 , \quad \tan \beta \equiv \frac{v_u}{v_d} . \quad (4.6)$$

As in the SM, the parameter v can be related to the known mass of the Z boson and the electroweak gauge couplings

$$v^2 = \frac{2m_Z^2}{g_1^2 + g_2^2} \simeq (174 \text{ GeV})^2 , \quad (4.7)$$

while $\tan \beta$ is a free parameter. The Higgs sector can be conveniently parametrized by introducing the real parameter

$$M_A^2 \equiv m_{H_u}^2 + m_{H_d}^2 + 2|\mu|^2 , \quad (4.8)$$

and replacing the parameters m_{H_u}, m_{H_d} and b with M_A, v and $\tan \beta$ by means of the conditions for the minimum of the scalar potential, that at tree-level read

$$\begin{aligned} \sin 2\beta &= \frac{2b}{M_A^2} , \\ m_Z^2 &= \frac{|m_{H_d}^2 - m_{H_u}^2|}{\cos 2\beta} - M_A^2 . \end{aligned} \quad (4.9)$$

As a side remark, we note that the relation (4.9) highlights the so called “ μ problem”, namely the necessity of a certain fine tuning between the SUSY-respecting μ parameter (entering the definition of M_A^2) and the soft parameters, since the characteristic scale of μ is in general

expected to be larger than Λ_{soft} . Possible extensions of the MSSM at very high energies in order to include a mechanism that relates the value of μ with the soft scale Λ_{soft} can be found in the literature, see e.g. [123]. In the following we will consider μ to be at the scale Λ_{soft} .

For phenomenological studies it is useful to reduce the number of free parameters by introducing simplifying assumptions on the SUSY-breaking terms. For our study we will consider the following CP -conserving and minimal flavour violating relations

$$\begin{aligned}
M_{1,2,3} &\in \mathbb{R} ; \\
\mathbf{a}_{\mathbf{u},\mathbf{d},\mathbf{e}} &= \begin{pmatrix} A_{u,d,e} & 0 & 0 \\ 0 & A_{c,s,\mu} & 0 \\ 0 & 0 & A_{t,b,\tau} \end{pmatrix}, \quad \text{with } A_i \in \mathbb{R} ; \\
\mathbf{m}_{\mathbf{Q},\mathbf{L},\mathbf{\bar{u}},\mathbf{\bar{d}},\mathbf{\bar{e}}}^2 &= \begin{pmatrix} M_{Q_1,L_1,\bar{u}_1,\bar{d}_1,\bar{e}_1}^2 & 0 & 0 \\ 0 & M_{Q_2,L_2,\bar{u}_2,\bar{d}_2,\bar{e}_2}^2 & 0 \\ 0 & 0 & M_{Q_3,L_3,\bar{u}_3,\bar{d}_3,\bar{e}_3}^2 \end{pmatrix}, \quad \text{with } M_i \in \mathbb{R} .
\end{aligned} \tag{4.10}$$

Under the above assumptions the only source of CP violation is in the CKM matrix of the SM. The above conditions are usually referred to as “soft SUSY-breaking universality”, and are often considered in order to avoid large flavour- and CP -violating effects, that are in general strongly constrained by experiments. In addition to the constraints in (4.10), it is often assumed that the first two generations of squarks and sleptons with the same quantum numbers are mass degenerate, and their trilinear couplings are negligible. In this case one is left with 19 free parameters.

4.2.1 The neutralino and chargino sector

Since it is of particular relevance for our subsequent discussion, in this Section we describe the properties of the neutralinos (charginos), the mass eigenstates corresponding to the neutral (charged) components of the Higgsinos and electroweak gauginos.

Neutralinos Because of the EWSB, the neutral components of the Higgsinos ($\tilde{H}_u^0, \tilde{H}_d^0$) and of the electroweak gauginos (\tilde{B}^0, \tilde{W}^0) mix with each other. The mass term for this set of particles contained in the Lagrangian can be written in matrix form

$$\mathcal{L}_{\chi^0 \text{ mass}} = -\frac{1}{2} \psi_0^T \mathbf{M}_0 \psi_0 + \text{c.c.} , \tag{4.11}$$

with the introduction of

$$\psi_0^T \equiv \left(\tilde{B} \quad \tilde{W} \quad \tilde{H}_d^0 \quad \tilde{H}_u^0 \right) , \tag{4.12}$$

and the tree-level mass matrix

$$\mathbf{M}_0 \equiv \begin{pmatrix} M_1 & 0 & -m_Z c_\beta s_W & m_Z s_\beta s_W \\ 0 & M_2 & m_Z c_\beta c_W & -m_Z s_\beta c_W \\ -m_Z c_\beta s_W & m_Z c_\beta c_W & 0 & -\mu \\ m_Z s_\beta s_W & -m_Z s_\beta c_W & -\mu & 0 \end{pmatrix}, \quad (4.13)$$

where we adopt the shorthand notation $c_\beta \equiv \cos \beta$, $s_\beta \equiv \sin \beta$, $c_W \equiv \cos \theta_W$, $s_W \equiv \sin \theta_W$, and θ_W is the Weinberg angle. The mass matrix above is symmetric and can therefore be diagonalized by a single unitary² matrix \mathbf{Z}

$$\mathbf{Z}^* \mathbf{M}_0 \mathbf{Z}^{-1} = \begin{pmatrix} M_{\chi_1^0} & 0 & 0 & 0 \\ 0 & M_{\chi_2^0} & 0 & 0 \\ 0 & 0 & M_{\chi_3^0} & 0 \\ 0 & 0 & 0 & M_{\chi_4^0} \end{pmatrix}. \quad (4.14)$$

The eigenvalues in (4.14) are real but can be of either sign, such that the physical (positive) neutralino masses $m_{\chi_i^0}$ are related to them by

$$M_{\chi_i^0} = \eta_i m_{\chi_i^0}, \quad (4.15)$$

where the signs $\eta_i = \pm 1$ determine the CP -eigenvalues of the physical neutralino fields.³ By definition the neutralinos are numbered according to their mass, with χ_1^0 being the lightest, and are obtained as

$$\begin{pmatrix} \chi_1^0 & \chi_2^0 & \chi_3^0 & \chi_4^0 \end{pmatrix} \equiv (\mathbf{Z} \psi_0)^T. \quad (4.16)$$

The composition of the i^{th} neutralino χ_i^0 is usually expressed in terms of its bino-, wino- and Higgsino-fraction, defined as $|Z_{i1}|^2$, $|Z_{i2}|^2$ and $|Z_{i3}|^2 + |Z_{i4}|^2$, respectively.

Charginos The charged components of the Higgsinos (\tilde{H}_u^+ , \tilde{H}_d^-) and of the wino (\tilde{W}^\pm) also mix with each other, thus leading to the charginos

$$\mathcal{L}_{\chi^\pm \text{ mass}} = -\frac{1}{2} \psi_\pm^T \mathbf{M}_\pm \psi_\pm + \text{c.c.}, \quad (4.17)$$

²We consider here the generic case in which the parameters M_1 , M_2 and μ are complex. If they are real, then the matrix \mathbf{Z} is real and orthogonal.

³A suitable redefinition of the fields to incorporate the CP -eigenvalues into the mixing matrix is possible and equivalent to define the physical masses $m_{\chi_i^0}$ as the square roots of the eigenvalues of the hermitian square $\mathbf{M}_0^\dagger \mathbf{M}_0$. This convention will be adopted in the following, when we describe the effective field theory in the non-relativistic regime.

where

$$\psi_{\pm}^T \equiv \left(\widetilde{W}^+ \quad \widetilde{H}_u^+ \quad \widetilde{W}^- \quad \widetilde{H}_d^- \right), \quad (4.18)$$

and the mass matrix in 2×2 block form

$$\mathbf{M}_{\pm} \equiv \begin{pmatrix} \mathbf{0} & \mathbf{X}^T \\ \mathbf{X} & \mathbf{0} \end{pmatrix}, \quad (4.19)$$

with

$$\mathbf{X} = \begin{pmatrix} M_2 & \sqrt{2} s_{\beta} m_W \\ \sqrt{2} c_{\beta} m_W & \mu \end{pmatrix}. \quad (4.20)$$

The matrix \mathbf{X} is not symmetric and can be diagonalized with the introduction of two unitary matrices

$$\mathbf{U}^* \mathbf{X} \mathbf{V}^{-1} = \begin{pmatrix} m_{\chi_1^{\pm}} & 0 \\ 0 & m_{\chi_2^{\pm}} \end{pmatrix}, \quad (4.21)$$

from which the charginos are obtained as

$$\begin{pmatrix} \chi_1^+ \\ \chi_2^+ \end{pmatrix} \equiv \mathbf{V} \begin{pmatrix} \widetilde{W}^+ \\ \widetilde{H}_u^+ \end{pmatrix}, \quad \begin{pmatrix} \chi_1^- \\ \chi_2^- \end{pmatrix} \equiv \mathbf{U} \begin{pmatrix} \widetilde{W}^- \\ \widetilde{H}_d^- \end{pmatrix}. \quad (4.22)$$

The chargino masses $m_{\chi_{1,2}^{\pm}}$ are the square roots of the (doubly degenerate) eigenvalues of the hermitian square $\mathbf{M}_{\pm}^{\dagger} \mathbf{M}_{\pm}$.

Mass splittings The general analytic solution for the mixing matrices and the masses in the neutralino/chargino sector have been obtained in [124]. While the full results are rather complicated, simpler approximate solutions can be found for models with parameters M_1 , M_2 and μ at the TeV scale. In particular, if the splittings are also much larger than the electroweak scale

$$\begin{aligned} ||M_{1,2}| \pm |\mu||^2 &\gg m_W^2, \\ ||M_1| \pm |M_2||^2 &\gg m_W^2, \end{aligned} \quad (4.23)$$

then the effect of the EWSB can be seen as a small perturbation. The eigenvalue problem can be solved perturbatively and at the leading order one obtains a wino-, a bino-, and two Higgsino-like neutralinos, of masses respectively $|M_1|$, $|M_2|$ and $|\mu|$. The two charginos are a wino- and a Higgsino-like, of masses respectively $|M_2|$ and $|\mu|$. Higher order corrections, determining in particular the splitting of the charginos with the corresponding neutralinos,

are suppressed by powers of $(m_W/\text{TeV})^2$. If at least two of the neutralino mass parameters are close to each other (their splitting being smaller than the electroweak scale), the effect of the mixing may become large. We consider here two cases, the wino-Higgsino and the wino-bino mixing, both under the assumption that the mass parameters are real. We adopt a convention where the wino mass parameter M_2 is positive, which can be done without loss of generality by appropriate field reparametrization.

For $|M_1| \gg |\mu| \gtrsim M_2$ the heaviest neutralino χ_4^0 is almost purely bino and its mass is much larger than those of the remaining three neutralinos, whose bino fraction is negligible (*bino decoupling region*). In this scenario the masses of the three light neutralinos and of the charginos are nearly degenerate. The wino-Higgsino mixing is moderate for $\delta\mu \equiv |\mu| - M_2 \gg m_W$, in which case the splitting $\delta m_{\chi_1^\pm} \equiv m_{\chi_1^\pm} - m_{\chi_1^0}$ can be approximately written as

$$\delta m_{\chi_1^\pm} \simeq \frac{1}{2} \frac{m_W^4 M_2 (c_\beta^2 - s_\beta^2)^2}{(\mu^2 - M_2^2)^2}. \quad (4.24)$$

In the opposite regime $\delta\mu \ll m_W$ the mixing is maximal and the mass splitting is

$$\delta m_{\chi_1^\pm} \simeq \frac{m_Z^2}{8M_2} \left(c_W^2 (1 \mp s_{2\beta}) \left(1 - \frac{\delta\mu}{\sqrt{2}(s_\beta \pm c_\beta)m_W} \right) + 2s_W^2 (1 \pm s_{2\beta}) \frac{M_2}{M_1} \right), \quad (4.25)$$

where the upper (lower) sign corresponds to whether μ is positive (negative), and we defined $s_{2\beta} \equiv \sin 2\beta$. We have kept the leading sub-leading correction for large $|M_1|$, but dropped terms of order $m_Z^2 \delta\mu / M_2 |M_1|$.

Similarly, for $|\mu| \gg |M_1| \gtrsim M_2$ there are two heavy almost pure Higgsinos, while the two light and nearly degenerate $\chi_{1,2}^0$ have negligible Higgsino fraction (*Higgsino decoupling region*). For negative values of M_1 the wino-bino mixing is suppressed and the tree-level mass difference of the chargino with the wino is negligible.⁴ On the other hand, for positive M_1 the mixing can be moderate or large, depending on the value of $\delta M_1 \equiv M_1 - M_2$. In particular, for $s_{2\beta} m_Z^2 \ll 2|\mu| \delta M_1$ the mixing is moderate and governed by the parameter

$$\theta_b = \frac{s_{2\beta} s_{2W} m_Z^2}{2\mu \delta M_1}, \quad (4.26)$$

where $s_{2W} \equiv \sin 2\theta_W$. Note that the presence of μ in the denominator of θ_b reflects the fact that the bino only mixes with the wino via the off-diagonal terms in the Higgsino block of the neutralino mass matrix. Because of this, in order that the wino-like neutralino contains a substantial bino component, the M_1 and M_2 parameters should be highly degenerate.⁵ The

⁴As in the pure-wino limit, the mass difference in this case is dominated by the radiative induced splitting. We will comment more on this in Sec. 4.4.3.

⁵Another possibility is of course to consider lower values of $|\mu|$. In this case however the Higgsinos are no longer decoupled and all the neutralinos mix with each other. Because of the larger couplings compared to the bino component, the resulting scenario closely resemble the above discussed wino-Higgsino one.

splitting of the lightest chargino in this case is approximately given by

$$\delta m_{\chi_1^\pm} \simeq \theta_b^2 \delta M_1 \left(1 + \frac{2M_2}{s_{2\beta} \mu} \right) . \quad (4.27)$$

In the opposite situation $s_{2\beta} m_Z^2 \gg 2|\mu| \delta M_1$ the mixing is large and the mass splitting can be written as

$$\delta m_{\tilde{\chi}_1^+} \simeq \begin{cases} -c_W^2 \delta M_1 - c_W^2 \frac{m_Z^2}{\mu} \left(s_{2\beta} + \frac{M_2}{\mu} \right), & \text{if } \mu < 0 \text{ and } s_{2\beta} |\mu| > M_2 , \\ -s_W^2 \delta M_1 + s_W^2 \frac{m_Z^2}{\mu} \left(s_{2\beta} + \frac{M_2}{\mu} \right), & \text{otherwise .} \end{cases} \quad (4.28)$$

We note that, in both the cases of moderate and large wino-bino mixing, there is a clear decrease in $m_{\chi_1^+}$ as δM_1 increases. Apart from this, one finds that the mass splitting decreases (when μ is positive) as $\tan \beta$ or μ increases. Moreover, under the assumptions where (4.27) and the first line of (4.28) hold, for the same value of $|\mu|$ the mass splitting is always smaller for $\mu > 0$, than for $\mu < 0$.

Because of the different interactions with SM particles of Higgsinos and electroweak gauginos, the composition and mass hierarchy of the neutralinos and charginos plays a key role in determining the DM properties in the pMSSM. Moreover, as we will see in the next Section, the size of the Sommerfeld enhancement is particularly sensitive to the mass splitting between the lightest chargino and neutralino, as it influences the location of the resonance. The formulae introduced in this Section will therefore prove useful to interpret the results of the analysis presented in Sec. 4.5.

4.3 The Sommerfeld enhancement

In this Section we present the Sommerfeld enhancement, an effect consisting in the modification of the rate for a short-range process in presence of a long-range potential. As we will see, this effect leads to generically large corrections to the annihilation rate of heavy neutralinos at freeze-out, thus affecting in a relevant way the calculation of DM relic density in this scenario.

We start in Sec. 4.3.1 by introducing the Sommerfeld enhancement in the context of non-relativistic quantum mechanics, and by solving the Schrödinger equation that describes its effect. In Sec. 4.3.2 we investigate how the Sommerfeld enhancement arises in quantum field theory, by explicit calculation of the relevant Feynman diagrams in the non-relativistic limit in a simple QFT model. When moving on from the simple model to the full neutralino/chargino co-annihilation in the pMSSM, a number of generalizations are needed. A schematic description of the required formalism, originally introduced in [44–46], is provided in Sec. 4.3.3. We conclude in Sec. 4.3.4 with the application of the presented formalism to the neutralino/sfermion co-annihilation in the pMSSM. The full results from the procedure described in this last Section are collected in Appendix B and can be used to further generalize the framework introduced in [44–46].

4.3.1 The Sommerfeld enhancement in quantum mechanics

The Sommerfeld enhancement is an elementary effect in non-relativistic quantum mechanics (QM), consisting in the modification of the interaction rate for a short-distance process, in presence of a long-range potential. In the language of scattering theory, the effect is the result of the distortion away from the plain wave approximation of the interacting particles wave-functions, induced by the potential. In this Section we introduce the Sommerfeld effect and discuss its behaviour in the case of Yukawa potential, mainly following [46, 110]. This example displays most of the main features that we will encounter when studying the neutralino/chargino co-annihilation in the pMSSM, and is therefore instructive for a qualitative understanding of the effect.

Consider a free non-relativistic particle, whose only interaction is localized at the origin of the coordinate system and described by an Hamiltonian

$$H_{\text{ann}}(\vec{x}) = U_{\text{ann}} \delta^{(3)}(\vec{x}) . \quad (4.29)$$

The rate $\Gamma^{(0)}$ for the interaction described by H_{ann} is simply proportional to the probability of finding the particle at the origin, encoded in the modulus squared of its wave-function $\psi_E^{(0)}(\vec{x})$. Since the only interaction is localized to a single point, the wave-functions are simple plane waves

$$\psi_E^{(0)}(\vec{x}) = e^{i\vec{k}\cdot\vec{x}} , \quad \text{with eigenvalue } E \equiv \frac{\vec{k}^2}{2m} . \quad (4.30)$$

Introduce now in the system a long-range central potential $V(r)$ that can either attract or repel the particle from the origin. As a result, the wave-function of the particle is distorted from the plane-wave limit and the interaction rate is modified as

$$\Gamma = \frac{|\psi_E(\vec{0})|^2}{|\psi_E^{(0)}(\vec{0})|^2} \Gamma^{(0)} \equiv S \Gamma^{(0)} , \quad (4.31)$$

where we introduced the Sommerfeld factor S , and the wave-function $\psi_E(\vec{x})$ is the solution of the Schrödinger equation

$$\left(-\frac{\nabla^2}{2m} - E + V(r) \right) \psi_E(\vec{x}) = 0 . \quad (4.32)$$

Before focusing on a specific form for the potential, we briefly describe how to compute the solution of the above equation, following the method of [125] (see also [126]).

Due to the central symmetry of the potential, it is convenient to formulate the problem in spherical coordinates. Choosing the reference frame such that the incoming particle is moving along the z axis, the general solution of the equation (4.32) is

$$\psi_E(\vec{x}) = \sum_l A_l \frac{u_l(r)}{r} P_l(\cos \theta) , \quad (4.33)$$

where $P_l(\cos \theta)$ denotes the Legendre polynomials, $u_l(r)$ is the solution of the radial Schrödinger equation

$$\left(-\frac{d^2}{dr^2} + \frac{l(l+1)}{r^2} - mE + mV(r) \right) u_l(r) = 0, \quad (4.34)$$

and the coefficients A_l are fixed by specifying the boundary conditions. The solution does not depend on the azimuthal angle ϕ due to the rotational symmetry along the z axis. The solution for the problem of interest is described by an incoming plane wave propagating along the z axis and an outgoing scattered spherical wave. Assuming that the potential is vanishing faster than $1/r$ for $r \rightarrow \infty$,⁶ the asymptotic form of this solution is

$$\psi_E(\vec{x}) \xrightarrow{r \rightarrow \infty} e^{ikz} + f(\theta) \frac{e^{ikr}}{r}, \quad (4.35)$$

with $k \equiv |\vec{k}| = \sqrt{2mE}$. The radial equation (4.34) has two solutions, one regular at the origin and the other one singular. We are interested in the regular solution, which (again if the potential is falling faster than $1/r$ at large r) has the asymptotic behaviour

$$u_l(r) \xrightarrow{r \rightarrow \infty} n_l \sin \left(kr - \frac{l\pi}{2} + \delta_l \right), \quad (4.36)$$

with constant coefficient n_l and scattering phase δ_l . Inserting the asymptotic behaviour of the radial function (4.36) into the general solution (4.33), and matching with (4.35), we obtain

$$A_l = i^l (2l+1) \frac{e^{i\delta_l}}{n_l k}, \quad (4.37)$$

where we made use of the asymptotic expansion

$$e^{ikz} \xrightarrow{r \rightarrow \infty} \frac{1}{2ikr} \sum_l (2l+1) P_l(\cos \theta) \left(e^{ikr} - (-1)^l e^{-ikr} \right). \quad (4.38)$$

The leading term in the Taylor expansion of $u_l(r)$ around the origin reads

$$u_l(r) \xrightarrow{r \rightarrow 0} \frac{1}{(l+1)!} u_l^{(l+1)}(0) r^{l+1}, \quad (4.39)$$

where $u_l^{(l+1)}(0)$ denotes the $(l+1)^{\text{th}}$ derivative at the origin. Note that, due to the scaling $\sim r^{l+1}$, the contributions from higher partial waves are suppressed. Later on we will see how the partial wave expansion arises when considering the non-relativistic regime of quantum field

⁶Note that the Coulomb potential does not satisfy this condition, and therefore the following asymptotic expression does not hold in this case. However, as explained in [46], a procedure similar to the one described here can still be applied to the Coulomb potential and leads to the same final result for the Sommerfeld factor.

theory, and we will be interested in the first two terms $l = 0, 1$. While the general procedure for any partial wave l is discussed e.g. in [46], for simplicity we consider here the S -wave limit $l = 0$, in which case the result is

$$\psi_E(\vec{0}) = \frac{e^{i\delta_0}}{n_0} \frac{1}{k} \frac{du_0}{dr}(0) . \quad (4.40)$$

Inserting in (4.31) the above result, we relate the Sommerfeld factor S to the solution of the radial equation (4.34) with appropriate boundary conditions to match the asymptotic behaviours (4.36) and (4.39).

In the simple case of Coulomb potential

$$V(r) = -\frac{\alpha}{r} , \quad (4.41)$$

the differential equation can be solved analytically in terms of hypergeometric functions, and the resulting Sommerfeld factor in the S -wave limit is

$$S = \left| \frac{\frac{\pi}{\epsilon_v}}{1 - e^{-\frac{\pi}{\epsilon_v}}} \right| , \quad (4.42)$$

where we introduced the dimensionless parameter ϵ_v

$$\epsilon_v \equiv \frac{v}{\alpha} , \quad (4.43)$$

and v is defined by $E = \frac{1}{2}mv^2$, thus representing the asymptotic velocity of the incoming non-relativistic particle. Note that the Sommerfeld factor approaches 1 for large velocity, in which case the potential interaction does not affect the interaction rate Γ . At small velocity for the attractive Coulomb potential ($\alpha > 0$) the Sommerfeld factor can be expanded as

$$S \simeq \frac{2\pi\alpha}{v} . \quad (4.44)$$

The rate is therefore *enhanced*, the effect being larger for smaller velocity and divergent in the zero-velocity limit (Coulomb singularity). In the repulsive case ($\alpha < 0$) one obtains instead

$$S \simeq e^{-\frac{2\pi\alpha}{v}} , \quad (4.45)$$

namely the exponential *suppression* of the rate Γ due to the need for tunneling through the Coulomb barrier in order to reach the interaction point at the origin.

For more complicated potentials the differential equation has typically⁷ to be solved numerically. In this case it is useful to reformulate the problem by combining the regular and

⁷An important exception is given by the Hulthén potential [127], which reproduces with a good approximation the short- and long-distance behaviour of the Yukawa potential, and can be solved analytically.

the singular solutions. In the radial equation (4.34) there is no single derivative term, and therefore, according to the Abel's theorem, one can construct a conserved (independent on r) Wronskian as

$$W_l = v_l^*(r) \frac{du_l}{dr}(r) - \frac{dv_l^*}{dr}(r) u_l(r) , \quad (4.46)$$

where $v_l(r)$ is the singular solution and the complex conjugate allows for the treatment of complex-valued potentials. The singular solution has asymptotic behaviour

$$v_l(r) \xrightarrow{r \rightarrow 0} \frac{1}{r^l} , \quad (4.47)$$

$$v_l(r) \xrightarrow{r \rightarrow \infty} T_l^* e^{-ikr} , \quad (4.48)$$

which defines the constants T_l . From the asymptotic behaviour of $u_0(r)$ and $v_0(r)$ it follows

$$W_0 \xrightarrow{r \rightarrow 0} \frac{du_0}{dr}(0) , \quad (4.49)$$

$$W_0 \xrightarrow{r \rightarrow \infty} T_0 k n_0 e^{-i\delta_0} . \quad (4.50)$$

Comparing the asymptotic values of the conserved Wronskian at zero and ∞ , we obtain the wave-function at the origin in the S -wave limit (see (4.40))

$$\psi_E(\vec{0}) = T_0 . \quad (4.51)$$

We conclude that the Sommerfeld factor in the S -wave approximation can be obtained by performing the following steps:

1. solve the differential equation (4.34) with $l = 0$ and boundary conditions

$$u_0(r_0) = r_0 , \quad \frac{du_0}{dr}(r_0) = 1 , \quad (4.52)$$

where r_0 is close to zero (e.g. $r_0 = 10^{-7}/mv$) and the normalization is chosen such that $W_0 = 1$;

2. determine the constant T_0 by imposing the condition $W_0 = 1$ for a large value r_∞

$$T_0 = e^{-ikr_\infty} \left(\frac{du_0}{dr}(r_\infty) - ik u_0(r_\infty) \right)^{-1} ; \quad (4.53)$$

3. compute the Sommerfeld factor from the definition (4.31)

$$S = |T_0|^2 . \quad (4.54)$$

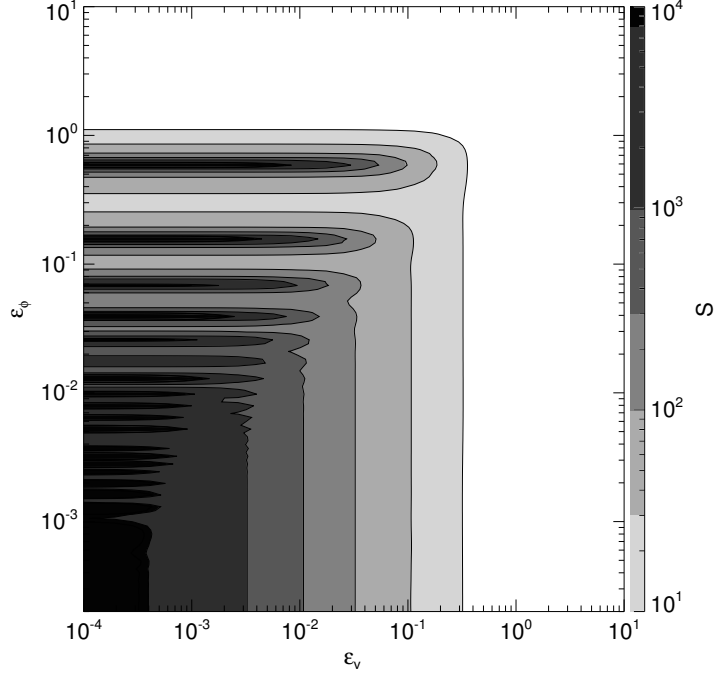


Figure 4.1: Contour plot from [110] of the S -wave Sommerfeld factor for an attractive Yukawa potential as a function of ϵ_v and ϵ_ϕ .

For a detailed study of the Sommerfeld effect from different potentials we refer the reader to [128], while here we briefly review the main properties for a Yukawa potential

$$V(r) = -\frac{\alpha}{r} e^{-m_\phi r} . \quad (4.55)$$

In this case, in addition to ϵ_v , the Sommerfeld factor depends also on the dimensionless parameter

$$\epsilon_\phi \equiv \frac{m_\phi}{\alpha m} , \quad (4.56)$$

which can be thought of as the ratio of the Bohr radius $r_B = 1/\alpha m$ over the characteristic range of the Yukawa potential $1/m_\phi$. The numerical result from [110] for the attractive case is displayed in Fig. 4.1. As in the Coulomb case, the Sommerfeld factor is negligible for large velocity (white region on the right of the plot). Moreover, the same is true when the range of the potential interaction is smaller than the Bohr radius (white region in the upper part of the plot). In the region in which the Sommerfeld factor is larger than one we observe two qualitatively different

behaviours. When the Yukawa mass m_ϕ approaches zero, and in general for $\epsilon_\phi < \epsilon_v$ (lower-right triangle), we recover the $\sim \epsilon_v^{-1}$ behaviour, typical of the Coulomb case. Note however that the finite range determines a saturation of the effect, such that there is no Coulomb singularity. In the opposite regime $\epsilon_\phi > \epsilon_v$, the dependence on the velocity is weak and a resonance pattern is observed (dark horizontal lines of large enhancement extending to relatively high velocity in the upper-left triangle). The highest resonances are due to the formation of zero-energy bound states, another typical feature of finite-range potentials. Smaller, but still relevant resonances are found in the case of loosely-bound states, of small but positive binding energy. Note that, in the neighbourhood of a resonance, the Sommerfeld factor depends strongly on the exact value of ϵ_ϕ . The strong dependence of S on the parameters of the model in presence of resonances is a general feature of the Sommerfeld enhancement, as we will see when studying the neutralino/chargino sector of the pMSSM in Sec. 4.5.

4.3.2 The Sommerfeld enhancement in quantum field theory

In the previous Section we have seen how in non-relativistic QM the presence of a long range potential can have a dramatic effect on the rate for some short-distance interaction. The distortion of the incoming state wave-function induced by the potential can lead to an enhancement of the short-distance rate up to several orders of magnitude. In this Section we consider a simple quantum field theory (QFT) model and study how the Sommerfeld effect arises from the breakdown of the perturbation series in the non-relativistic limit. Consider the simple model described by the Lagrangian

$$\mathcal{L} = \mathcal{L}_Z + \mathcal{L}_\phi + \mathcal{L}_f + \mathcal{L}_{\text{ann}} , \quad (4.57)$$

with

$$\mathcal{L}_Z = -\frac{1}{4}F^{\mu\nu}F_{\mu\nu} + \frac{1}{2}m_Z^2 Z^\mu Z_\nu , \quad (4.58)$$

$$\mathcal{L}_\phi = (D_\mu\phi)^\dagger (D^\mu\phi) - m^2\phi^\dagger\phi , \quad (4.59)$$

where $F_{\mu\nu}$ is the field-strength tensor of the massive vector boson Z , $D_\mu\phi = (\partial_\mu - igZ_\mu)\phi$ the covariant derivative for the complex scalar boson ϕ , \mathcal{L}_f contains the kinetic term of a particle f , that does not interact with Z and may have any spin, and \mathcal{L}_{ann} is an effective interaction term such as

$$\mathcal{L}_{\text{ann}} = \frac{c_{\text{ann}}}{\Lambda}\phi^\dagger\phi\bar{f}f , \quad (4.60)$$

in the case of fermionic f . Assume the following energy hierarchy

$$\Lambda \gtrsim m \gg m_Z, m_f . \quad (4.61)$$

We are interested in the pair-annihilation process $\phi\phi^\dagger \rightarrow f\bar{f}$, in the non-relativistic regime. At leading order, the process is encoded in the effective four-particle vertex contained in \mathcal{L}_{ann} ,

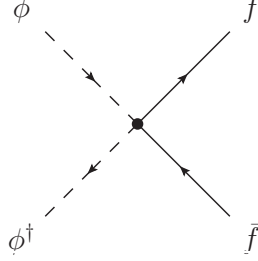


Figure 4.2: The tree-level diagram $i\mathcal{M}_0$, encoding the annihilation process $\phi\phi^\dagger \rightarrow f\bar{f}$.

such that the corresponding rate is⁸

$$\begin{aligned}\Gamma^{(0)} &\equiv \sigma_{\phi\phi^\dagger \rightarrow f\bar{f}} v_{\phi\phi^\dagger} \\ &= \int d\text{LIPS}_{f\bar{f}} \left| \overline{\mathcal{M}}_0^{\text{NR}} \right|^2 ,\end{aligned}\quad (4.62)$$

where

$$d\text{LIPS}_{f\bar{f}} = d\Pi_f d\Pi_{\bar{f}} (2\pi)^4 \delta^{(4)}(p_\phi + p_{\phi^\dagger} - p_f - p_{\bar{f}}) ,\quad (4.63)$$

is the Lorentz-invariant phase-space measure, the diagram $i\mathcal{M}_0$ is shown in Fig. 4.2 and the superscript “NR” is to remind that we adopt the non-relativistic normalization for the states

$$\langle \phi(p') | \phi(p) \rangle = (2\pi)^3 \delta^{(3)}(\vec{p} - \vec{p}') .\quad (4.64)$$

In particular, the different normalization of the NR fields with respect to the usual relativistic one, results in the relation

$$i\mathcal{M}^{\text{NR}} = \frac{1}{\sqrt{2\omega_\phi} \sqrt{2\omega_{\phi^\dagger}}} i\mathcal{M} ,\quad (4.65)$$

such that the rate defined here is equal to the annihilation cross section times velocity as given in (1.35, 1.37).

In this simple model, the only one-loop correction to the annihilation rate consists in the exchange of a Z boson between the two incoming particles, as depicted in Fig. 4.3. For $m_Z = 0$, it is well known that this one-loop diagram is singular in the non-relativistic limit. Its contribution scales as α/v , where $\alpha = g^2/4\pi$ and v is defined in terms of the center-of-mass energy \sqrt{s} as

$$mv^2 = \sqrt{s} - 2m \equiv E ,\quad (4.66)$$

⁸We adopt in the following the notation that was introduced in Sec. 1.4.

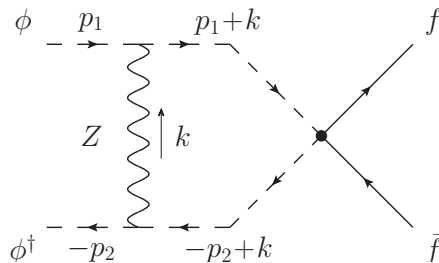


Figure 4.3: The one-loop diagram $i\mathcal{M}_1$, providing the leading radiative correction to the annihilation process. Momenta flow by convention in the direction of the arrows.

such that it corresponds to the velocity of a ϕ particle of energy $\sqrt{s}/2$ in the non-relativistic regime.⁹ This result is in fact not surprising, since it corresponds to the Coulomb singularity that we already encountered in the previous Section. In general, the divergence of loop corrections in a particular kinematic regime implies the breakdown of perturbation theory, and the resummation of a certain class of diagrams is needed to recover a finite result. In fact it can be shown that, in the small-velocity limit $\alpha/v \sim 1$, each n -loop ladder diagram scales as $(\alpha/v)^n$, and its contribution is therefore not suppressed compared to the tree-level. The resummation of the unsuppressed contributions from ladder diagrams to all order is possible and equivalent to the solution of a Schrödinger equation with potential originated by the boson exchange. To see how this works we start by considering the one-loop amplitude, that in unitary gauge¹⁰ reads

$$i\mathcal{M}_1 = \frac{c_{\text{ann}}}{\Lambda} \int \frac{d^4k}{(2\pi)^4} C_Z^\mu(-p_2+k, -p_2) \frac{-i \left(g_{\mu\nu} - \frac{k_\mu k_\nu}{m_Z^2} \right)}{k^2 - m_Z^2} C_Z^\nu(p_1, p_1+k) \times \frac{i}{(p_1+k)^2 - m^2 + i\eta} \frac{i}{(-p_2+k)^2 - m^2 + i\eta}, \quad (4.67)$$

where the coupling factor is

$$C_Z^\mu(p, p') \equiv i g (p + p')^\mu. \quad (4.68)$$

As explained in [129], the leading contribution from the above diagram in the non-relativistic regime comes from the potential region, in which the loop momentum scales as

$$k^0 \sim mv^2, \quad \vec{k} \sim mv. \quad (4.69)$$

⁹For center-of-mass energies much larger than $2m$ the velocity v loses its physical meaning, even becoming larger than 1. In this case it should be just understood as a convenient variable to parametrize \sqrt{s} . Also note that, in the non-relativistic regime, E is twice the kinetic energy of a ϕ particle.

¹⁰The same calculation in R_ξ -gauge can be found in [46], where the cancellation of ξ -dependent terms from the Z propagator against the contribution from the exchange of a Goldstone boson G^0 is explicitly shown.

We can therefore expand systematically the integral in (4.67) for small v , which in this region implies $k^0 \ll \vec{k} \ll m$. The integrand in the first line of (4.67) simplifies to

$$\begin{aligned} -i 4m^2 \tilde{V}(\vec{k}) &\equiv C_Z^\mu(-p_2+k, -p_2) \frac{-i \left(g_{\mu\nu} - \frac{k_\mu k_\nu}{m_Z^2} \right)}{k^2 - m_Z^2} C_Z^\nu(p_1, p_1+k) \\ &\simeq -i 4m^2 \frac{-g^2}{\vec{k}^2 + m_Z^2}. \end{aligned} \quad (4.70)$$

Note that this is independent on k^0 and describes therefore an instantaneous potential. The second line of (4.67) can be simplified by making use of

$$\begin{aligned} (p_1+k)^2 - m^2 + i\eta &= (m + p_1^0 - m + k^0)^2 - (\vec{p}_1 + \vec{k})^2 - m^2 + i\eta \\ &\simeq 2m \left[k^0 + p_1^0 - m - \frac{(\vec{p}_1 + \vec{k})^2}{2m} + i\eta \right], \end{aligned} \quad (4.71)$$

$$(-p_2+k)^2 - m^2 + i\eta \simeq 2m \left[-k^0 + p_2^0 - m - \frac{(-\vec{p}_2 + \vec{k})^2}{2m} + i\eta \right], \quad (4.72)$$

and the integral in k^0 can be solved with the method of residues. Closing the contour on the upper half-plane, thus picking up the pole of (4.72), we obtain

$$\begin{aligned} \frac{i}{4m^2} \mathcal{I}_0(\vec{k}) &\equiv \int \frac{dk^0}{2\pi} \frac{i}{(-p_2+k)^2 - m^2 + i\eta} \frac{i}{(p_1+k)^2 - m^2 + i\eta} \\ &\simeq \frac{i}{4m^2} \frac{1}{p_1^0 + p_2^0 - 2m - \frac{(\vec{p}_1 + \vec{k})^2}{2m} - \frac{(-\vec{p}_2 + \vec{k})^2}{2m}} \\ &\simeq \frac{i}{4m^2} \frac{1}{E - \frac{(\vec{q} + \vec{k})^2}{m}}, \end{aligned} \quad (4.73)$$

where in the last line we introduced the total and relative momenta

$$p \equiv p_1 + p_2, \quad q \equiv \frac{p_1 - p_2}{2}, \quad (4.74)$$

and work in the center-of-mass frame, where $\vec{p} = \vec{0}$, $q^0 = 0$, and $E = \frac{\vec{q}^2}{m}$. Combining the results in (4.70) and (4.73) we can write the one-loop amplitude as

$$\begin{aligned} i\mathcal{M}_1 &= \frac{c_{\text{ann}}}{\Lambda} \int \frac{d^3\vec{k}}{(2\pi)^3} \tilde{V}(\vec{k}) \mathcal{I}_0(\vec{k}) \\ &= i\mathcal{M}_0 \int \frac{d^3\vec{k}}{(2\pi)^3} \frac{-g^2}{\vec{k}^2 + m_Z^2} \frac{1}{E - \frac{(\vec{q} + \vec{k})^2}{m}}. \end{aligned} \quad (4.75)$$

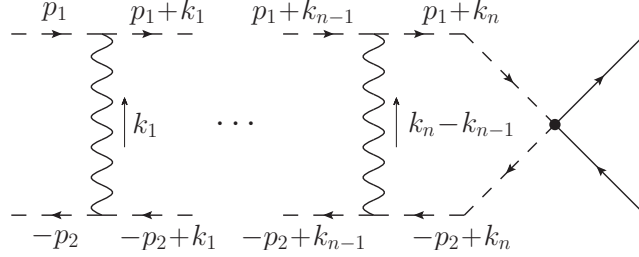


Figure 4.4: The ladder diagram with n exchanged bosons, $i\mathcal{M}_n$.

From the above expression it is now possible to obtain by power counting the anticipated scaling of the one-loop result (see e.g. [129]). For very low mediator mass $m_Z \ll mv$, the scaling of the loop momentum is $\vec{k} \sim mv$, and we immediately obtain $i\mathcal{M}_1 \sim i\mathcal{M}_0 \times \alpha/v$. On the other hand at small velocity $mv \ll m_Z$, the boson mass sets the scale of the loop momentum $\vec{k} \sim m_Z$, and the result is $i\mathcal{M}_1 \sim i\mathcal{M}_0 \times \alpha m/m_Z$. We thus obtained that, in the non-relativistic regime, the one-loop diagram is not suppressed compared to the tree-level, due to the enhancement from the potential region.

Again by power-counting arguments it can be shown that the enhancement from the potential region is present in ladder diagrams to all loop orders, and in no other diagram. The above procedure can be straightforwardly generalized to the n -loop diagram depicted in Fig. 4.4, thus obtaining

$$i\mathcal{M}_n = i\mathcal{M}_0 \int \left[\prod_{i=1}^n \frac{d^3 \vec{k}_i}{(2\pi)^3} \right] \prod_{i=1}^n \tilde{V}(\vec{k}_i - \vec{k}_{i-1}) \mathcal{I}_0(\vec{k}_i), \quad (4.76)$$

where we defined $k_0 \equiv 0$. Writing the tree-level diagram as

$$i\mathcal{M}_0 = \frac{c_{\text{ann}}}{\Lambda} \lim_{E' \rightarrow E} (-1) \left(E' - \frac{\vec{q}^2}{m} \right) \int \frac{d^3 \vec{Q}}{(2\pi)^3} \frac{1}{E' - \frac{\vec{Q}^2}{m}} \left[-(2\pi)^3 \delta^{(3)}(\vec{q} - \vec{Q}) \right], \quad (4.77)$$

we are now ready to perform the resummation

$$\begin{aligned} i\mathcal{M}_{\text{resum}} &\equiv \sum_{n=0}^{\infty} i\mathcal{M}_n \\ &= \frac{c_{\text{ann}}}{\Lambda} \lim_{E' \rightarrow E} (-1) \left(E' - \frac{\vec{q}^2}{m} \right) \int \frac{d^3 \vec{Q}}{(2\pi)^3} \tilde{G}(\vec{q}, \vec{Q}; E'), \end{aligned} \quad (4.78)$$

where we introduced the function $\tilde{G}(\vec{q}, \vec{Q}; E')$ defined as

$$\tilde{G}(\vec{q}, \vec{Q}; E') \equiv \frac{1}{E' - \frac{\vec{q}^2}{m}} \left[-(2\pi)^3 \delta^{(3)}(\vec{q} - \vec{Q}) + iH(\vec{q}, \vec{Q}; E') \frac{1}{E' - \frac{\vec{Q}^2}{m}} \right], \quad (4.79)$$

and

$$H(\vec{q}, \vec{Q}; E') \equiv i \sum_{n=0}^{\infty} \left\{ \int \left[\prod_{i=1}^n \frac{d^3 \vec{k}_i}{(2\pi)^3} \right] \prod_{i=1}^n \tilde{V}(\vec{k}_i - \vec{k}_{i-1}) \mathcal{I}_0(\vec{k}_i) \tilde{V}(\vec{q} - \vec{Q} - \vec{k}_n) \right\} . \quad (4.80)$$

Note that the limiting procedure is required since the function $\tilde{G}(\vec{q}, \vec{Q}; E')$ is singular for $E' = E$. The last step consists in showing that the resummed expression (4.78) is equivalent to the tree-level diagram multiplied by the value at the origin of a wave-function, that can be obtained by solving an appropriate Schrödinger equation. It is easy to verify that the Fourier transform of the function \tilde{G} is the Green function for the Schrödinger equation

$$\left(-\frac{\nabla_{\vec{x}}^2}{2m} - E + V(r) \right) G(\vec{x}, \vec{X}; E) = \delta^{(3)}(\vec{x} - \vec{X}) , \quad (4.81)$$

where from (4.70) we obtain in configuration space the Yukawa potential

$$V(r) = -g^2 \int \frac{d^3 \vec{k}}{(2\pi)^3} e^{i\vec{k} \cdot \vec{x}} \frac{1}{\vec{k}^2 + m_Z^2} = -\frac{\alpha}{r} e^{-m_Z r} . \quad (4.82)$$

In terms of elementary scattering theory we can therefore write

$$\tilde{G}(\vec{q}, \vec{q}'; E') \equiv \langle q | \hat{G}(E') | q' \rangle , \quad (4.83)$$

where $|q\rangle$ denotes the momentum eigenstate of the free Hamiltonian \hat{H}_0

$$\hat{H}_0 |q\rangle = \frac{\vec{q}^2}{m} |q\rangle , \quad (4.84)$$

and the Green operator is defined in terms of the interacting Hamiltonian \hat{H} as

$$\hat{G}(E') \equiv \frac{1}{\hat{H} - E' - i\eta} . \quad (4.85)$$

From the Schrödinger equation for the Green function (4.81), it follows that the eigenfunctions of the interacting problem

$$\left(-\frac{\nabla^2}{2m} - E + V(r) \right) \psi_E(\vec{x}) = 0 , \quad (4.86)$$

can be written (in Fourier space) as

$$\tilde{\psi}_E(\vec{Q}) = \langle Q | \lim_{E' \rightarrow E} \hat{G}(E') \hat{G}_0^{-1}(E') | q \rangle , \quad (4.87)$$

where the free Green operator \widehat{G}_0 is defined as (4.85) but with \widehat{H} replaced by \widehat{H}_0 and satisfies

$$G_0^{-1}(\vec{q}, \vec{q}'; E') = \left(E' - \frac{\vec{q}^2}{m} \right) \delta^{(3)}(\vec{q} - \vec{q}') . \quad (4.88)$$

Replacing the above expressions into (4.78) we can finally conclude

$$i\mathcal{M}_{\text{resum}} = \psi_E^*(\vec{0}) i\mathcal{M}_0 , \quad (4.89)$$

where $\psi_E(\vec{0})$ is the value at the origin of the wave-function solving the Schrödinger equation (4.86). The complex conjugated wave-function appears in the equation above as a result of the convention used for left and right states in the definition of the Green function (4.83). We chose here to follow the convention from [46], to which we refer the reader for the generalization of the calculation presented here to co-annihilation models. From the above result it follows

$$\Gamma = \left| \psi_E(\vec{0}) \right|^2 \Gamma^{(0)} = S \Gamma^{(0)} , \quad (4.90)$$

where the tree-level rate was given in (4.62). This result is what we were looking for, namely the derivation of the Sommerfeld enhancement (4.31) from QFT. The wave-function in the above expression is normalized such that $|\psi_E^{(0)}(\vec{0})|^2 = 1$.

4.3.3 EFT treatment, co-annihilations and higher orders

In the previous Section we studied the annihilation of two non-relativistic particles in a simple scenario, focusing on the effect of multiple exchanges of light vector bosons. The result we obtained is that the resummation of the unsuppressed ladder diagrams is equivalent to the solution of a Schrödinger equation, in which a Yukawa potential is generated by the massive boson exchange. The calculation of the Sommerfeld-enhanced annihilation rate consists of two main ingredients, the short-range perturbative rate $\Gamma^{(0)}$ and the enhancement factor $S = |\psi_E(\vec{0})|^2$, determined by the potential $V(r)$ arising via ladder exchange.

In order to apply the above described procedure to the case of neutralino/chargino co-annihilations in the pMSSM, a number of generalizations have to be taken into account. For the comprehensive study of this scenario we refer the reader to the original papers [44–46], while in this Section we limit ourselves to a schematic presentation of the generalizations listed below:

- the factorization of the short-range annihilation from the ladder exchange, that in the simple example was trivial, can be systematically treated within an effective field theory (EFT) framework;
- in presence of co-annihilation among multiple particle species, the boson exchange in the ladder may change the incoming two-particle state. In this case, all the accessible

co-annihilating pairs have to be taken into account, and therefore both the short-range rate and the potentials are matrices in the space of two-particle states;

- in the calculation of the annihilation amplitude we retained only the leading order terms in the non-relativistic regime. In order to go to the next order, which is relevant if percent-level accuracy is aimed for, a systematic expansion in the EFT has to be performed. For the off-diagonal entries of the annihilation rate, this requires in particular a simultaneous expansion in the mass splitting among different co-annihilating particles. The consistent treatment of the Sommerfeld factor at this order also requires the solution of the Schrödinger equation with $l = 1$ (P -wave).

In the remaining of this Section we describe with explicit examples how the above listed issues can be addressed. The resulting formalism is then applied in the next Section to the neutralino/sfermion co-annihilation, which is a necessary ingredient for the extension to a larger region of the pMSSM parameter space of the formalism developed for the neutralino/chargino sector in [44–46].

The non-relativistic effective field theory

In the simple example studied in Sec. 4.3.2, the pair annihilation (*hard* process) was encoded in an effective term in the Lagrangian, and the final state particles f, \bar{f} were assumed not to interact with the vector boson Z . The factorization of the boson ladder exchange (*soft* process) from the pair-annihilation was therefore automatic. The same result can be consistently obtained for more general theories within an effective field theory (EFT) framework similar to the NRQCD introduced in [130] to study quarkonium annihilation. The factorization exploits the large hierarchy between the characteristic *hard* scale of the annihilation process, the mass m of the annihilating particles, and the *soft* scales $mv^2 \ll mv \ll m$, characteristic of the ladder exchange. Once the high energy modes are integrated out, the resulting effective theory contains only excitations of energy smaller than m . The hard annihilation is encoded into effective (higher dimensional) operators entering the Lagrangian, whose Wilson coefficients can be determined by appropriate matching. In this Section we present how this framework can be applied to the pair annihilation process $\phi\phi^\dagger \rightarrow f\bar{f}$ in the toy model described by the Lagrangian (4.57).

In the non-relativistic regime low-energy modes of a nearly on-shell particle ϕ and its antiparticle are described by two effective fields, φ and φ_c , whose kinetics is encoded in the Lagrangian

$$\mathcal{L}_{\text{kin}} = \varphi^\dagger \left(i\partial_t + \frac{\boldsymbol{\partial}^2}{2m} \right) \varphi + \varphi_c^\dagger \left(i\partial_t + \frac{\boldsymbol{\partial}^2}{2m} \right) \varphi_c, \quad (4.91)$$

where we denote with $\boldsymbol{\partial} \equiv \vec{\partial}$ the 3-vector derivative with respect to the spatial components. Due to the $2 \rightarrow 2$ kinematics, the decay products $f\bar{f}$ have energies of order m , resulting in

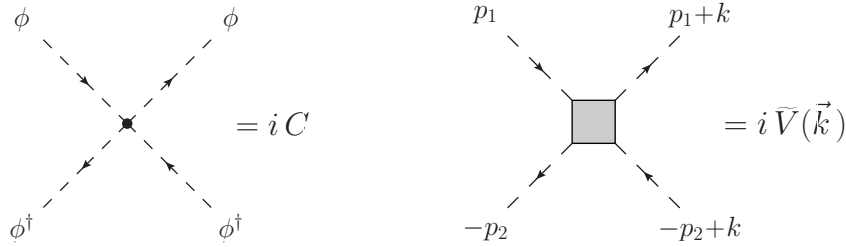


Figure 4.5: Feynman rules for the effective vertices that encode the short-range annihilation (left) and the potential interaction (right).

relativistic velocities for $m_f \ll m$. They are therefore not described within the EFT, and must be integrated out. The pair-annihilation is a *short-distance* process, since its range $1/m$ is much smaller than the characteristic range $1/mv$ or $1/mz$ of the non-relativistic interactions between particles in the EFT. It is therefore consistent to incorporate the pair-annihilation in the EFT by introducing effective local four-particle operators of the form,

$$\delta\mathcal{L}_{\text{ann}} = C \varphi^\dagger \varphi_c^\dagger \varphi \varphi_c, \quad (4.92)$$

where C is a Wilson coefficient. Finally, the instantaneous potential interaction can be encoded into terms of the form

$$\mathcal{L}_{\text{pot}} = - \int d^3\vec{r} \varphi^\dagger(t, \vec{x}) \varphi_c^\dagger(t, \vec{x} + \vec{r}) V(r) \varphi(t, \vec{x}) \varphi_c(t, \vec{x} + \vec{r}), \quad (4.93)$$

where \vec{r} is the spatial three-vector denoting the relative distance in the two-body system. The effective theory is described by the Lagrangian

$$\mathcal{L}_{\text{NREFT}} = \mathcal{L}_{\text{kin}} + \delta\mathcal{L}_{\text{ann}} + \mathcal{L}_{\text{pot}} + \text{higher order terms}, \quad (4.94)$$

and the corresponding Feynman rules are depicted in Fig. 4.5.

The annihilation rate for the process $\phi\phi^\dagger \rightarrow f\bar{f}$ can be related to the imaginary part of the forward scattering amplitude by means of the optical theorem, so we can write

$$\begin{aligned} \Gamma^{(0)} &= 2 \text{Im} \left\{ \langle \phi\phi^\dagger | \int d^4x \delta\mathcal{L}_{\text{ann}} | \phi\phi^\dagger \rangle \right\} \\ &= \widehat{C}, \end{aligned} \quad (4.95)$$

where we defined $\widehat{C} \equiv 2 \text{Im} \{ C \}$, and the states are normalized as in (4.64). Matching with (4.62) we conclude

$$\widehat{C} = \int d\text{LIPS}_{f\bar{f}} |\overline{\mathcal{M}}_0^{\text{NR}}|^2. \quad (4.96)$$

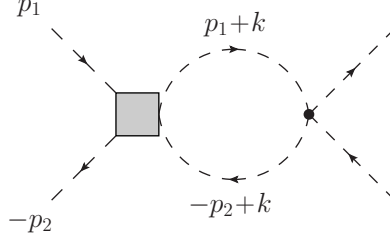


Figure 4.6: The one-loop diagram in Fig. 4.3 as it is given in the effective theory.

Note that this step does not rely on the structure of the tree-level annihilation amplitude and in general $i\mathcal{M}_0$ receives contributions from different s - and t -channel diagrams.

Now we have to consider the loop diagrams obtained by inserting the potential interaction encoded in the Lagrangian term (4.93). It is straightforward to show that the one-loop diagram in Fig. 4.6, computed with propagators as obtained from the kinetic Lagrangian (4.91), is equivalent to the result of the one-loop diagram as given by (4.67). The resummation of the potential interactions to all orders proceeds therefore as in the previous Section.

We conclude that the effective theory described by the Lagrangian (4.94) provides a consistent description of the Sommerfeld enhancement (4.90).

The multichannel co-annihilation

So far we have seen how the Sommerfeld enhancement can be accounted for within an EFT framework in presence of a single annihilation process $\phi\phi^\dagger \rightarrow f\bar{f}$. An important generalization consists in the introduction of additional two-particle states, in which the incoming one can be turned via boson exchange in the ladder. Consider for definiteness the model (4.59), with ϕ promoted to an $SU(2)_L$ doublet $(\phi^+, \phi^0)^T$, and with the consistent introduction of the kinetic and interaction terms of the W boson. In the broken gauge theory the particles ϕ^0 and ϕ^\pm have different masses, which we assume to satisfy

$$m_{\phi^\pm} - m_{\phi^0} \equiv \delta m \ll m_{\phi^0} . \quad (4.97)$$

The kinetic term in the effective theory when we choose the mass of the lightest two-particle state as the cutoff $m \equiv m_{\phi^0}$, reads

$$\mathcal{L}_{\text{kin}} = \varphi_0^\dagger \left(i\partial_t + \frac{\partial^2}{2m} \right) \varphi_0 + \varphi^\dagger \left(i\partial_t - \delta m + \frac{\partial^2}{2m} \right) \varphi + \varphi_c^\dagger \left(i\partial_t - \delta m + \frac{\partial^2}{2m} \right) \varphi_c . \quad (4.98)$$

Note that, since ϕ^0 is identical to its antiparticle, a single non-relativistic scalar field φ_0 is sufficient to describe it. The non-relativistic annihilating pair $\phi^0\phi^0$ can now exchange also

W bosons in the ladder, thus turning into a $\phi^+\phi^-$ pair. This means that, if we denote the two-particle states as

$$[\phi\phi]_1 \equiv \phi^0\phi^0, \quad [\phi\phi]_2 \equiv \phi^+\phi^-, \quad (4.99)$$

then the total annihilation rate for a given state $[\phi\phi]_a$ is obtained from the imaginary part of the forward scattering amplitude for the process

$$[\phi\phi]_a \rightarrow \cdots \rightarrow [\phi\phi]_b \rightarrow f\bar{f} \rightarrow [\phi\phi]_c \rightarrow \cdots \rightarrow [\phi\phi]_a, \quad (4.100)$$

where a sum over the indices b, c is understood. The corresponding diagram is depicted in Fig. 4.7. The potential is therefore a matrix in the space of two-particle states

$$\mathcal{L}_{\text{pot}} = - \sum_{a,b} \int d^3\vec{r} [\varphi\varphi]_a^\dagger(x, \vec{r}) V_{ab}(r) [\varphi\varphi]_b(x, \vec{r}), \quad (4.101)$$

where we adopted the simplified notation $[\varphi\varphi](x, \vec{r}) \equiv \varphi(t, \vec{x})\varphi(t, \vec{x} + \vec{r})$. The contributions to the potential matrix from Z and W exchange, determining respectively the diagonal and off-diagonal entries, can be computed as described in the previous Section. Additionally, the diagonal entry $V_{22}(r)$ contains a constant term $V_{\infty 22} = 2\delta m$, due to the mass-splitting of the $[\phi\phi]_2$ state with respect to the lightest one $[\phi\phi]_1$. An important consequence of the presence of off-diagonal potential terms, is that off-diagonal short-range interactions have to be considered as well

$$\delta\mathcal{L}_{\text{ann}} = \sum_{a,b} n_{ab} C_{ab} [\varphi\varphi]_b^\dagger [\varphi\varphi]_a, \quad (4.102)$$

where n_{ab} is a normalization factor introduced to compensate the symmetry factors arising from the number of identical contractions in annihilating (creating) the initial (final) two-particle state, in case it is built up of two identical particles. In the case considered here it can be written as $n_{ab} = 2^{a+b-4}$.

The matching can be performed by generalizing (4.96) to off-diagonal reactions

$$\begin{aligned} \widehat{C}_{bc} &= \int d\text{LIPS}_{f\bar{f}} \sum_{\text{spin}} \mathcal{M}_0^{\text{NR}} [\phi\phi]_b \rightarrow f\bar{f} \left(\mathcal{M}_0^{\text{NR}} [\phi\phi]_c \rightarrow f\bar{f} \right)^* \\ &\equiv 2 \text{Abs} \left\{ \mathcal{M}_0^{\text{NR}} [\phi\phi]_b \rightarrow f\bar{f} \rightarrow [\phi\phi]_c \right\}, \end{aligned} \quad (4.103)$$

where the second line defines the *absorptive* part of the amplitude in curly brackets. The definition is such that the absorptive part of an amplitude, and of the corresponding Wilson coefficient, coincides with its imaginary part for diagonal reactions (forward scattering). The absorptive part of Wilson coefficients have the property $\widehat{C}_{ba} = \widehat{C}_{ab}^*$. Note that the normalization factor n_{ab} canceled out in the above equation, which is the reason why it was introduced. Finally, we can write the rate for the annihilation $[\phi\phi]_a \rightarrow f\bar{f}$ as

$$\Gamma_{aa} = S_a \Gamma_{aa}^{(0)}, \quad (4.104)$$

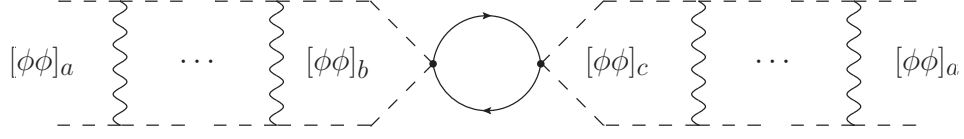


Figure 4.7: The full theory diagram corresponding to the forward scattering amplitude $i\mathcal{M}_{[\phi\phi]_a \rightarrow f\bar{f} \rightarrow [\phi\phi]_a}$. The potential interaction turns the incoming (outgoing) state $[\phi\phi]_a$ into $[\phi\phi]_b$ ($[\phi\phi]_c$), such that the short-range annihilation is given by the off-diagonal amplitude $i\mathcal{M}_0_{[\phi\phi]_b \rightarrow f\bar{f} \rightarrow [\phi\phi]_c}$.

with Sommerfeld factor given by

$$S_a \equiv \sum_{b,c} \frac{(T_0^\dagger)_{ab} \Gamma_{bc}^{(0)} (T_0)_{ca}}{\Gamma_{aa}^{(0)}}, \quad (4.105)$$

where $(T_0)_{ab}$ are the solutions of the coupled set of Schrödinger equations with potentials $V_{ab}(r)$ in the S -wave limit. The above expression is the generalization in presence of co-annihilations of our previous result (4.54). It is important to note that the calculation of the Sommerfeld factor requires the knowledge of the off-diagonal entries of the tree-level annihilation matrix.

The Sommerfeld enhancement in a two-states system similar to the one introduced here has been studied in detail in [126]. For vanishing mass splitting, the enhancement factor S_1 behaves qualitatively as the case of the Yukawa potential described in Sec. 4.3.1, and depends on the two parameters ϵ_v and ϵ_W (corresponding to ϵ_ϕ in Sec. 4.3.1). When introducing the mass splitting, the presence of the additional parameter $\epsilon_\delta \equiv \sqrt{\frac{2\delta m}{\alpha^2 m}}$ results in the following modifications of the enhancement factor.

- The non-resonant, unsaturated enhancement that characterizes the $\epsilon_v \gg \epsilon_W$ regime is enlarged by a factor of ~ 2 .
- For $\epsilon_W > \epsilon_v$, both the positions and the heights of the resonances change. The peaks move to lower values of ϵ_W , are more widely spaced and their height is increased by a factor of ~ 4 . Once again it is worth to stress that, in the resonant region, the value of S is strongly depending on the precise value of the other parameters, and in particular of ϵ_δ .
- The dependence on the velocity of the Sommerfeld factor is no longer monotonic, but a resonant behaviour appears in correspondence of the threshold for on-shell excitation of the heavier state. The enhancement at this resonance may be as much as a factor of ~ 2 larger than at zero velocity.

We conclude this Section with a comment on the products of the annihilation. So far we considered a single final state $f\bar{f}$, but the procedure can be straightforwardly applied to the general case in which more states $X_A X_B$ contribute to the Wilson coefficients. At the one-loop level each contribution from an individual $X_A X_B$ state is free from infrared divergences and can be evaluated separately

$$\widehat{C}_{ab} = \sum_{A,B} 2 \text{Abs} \left\{ \mathcal{M}_0^{\text{NR}} [\phi\phi]_{a \rightarrow X_A X_B \rightarrow [\phi\phi]_b} \right\} . \quad (4.106)$$

We will make use of the above equation when considering the co-annihilation of neutralino/chargino pairs into any pair of SM particles.

The second order in the non-relativistic expansion

So far we worked at the leading order in the non-relativistic expansion. The procedure can be consistently extended to the next-to-next-to-leading order (NNLO), namely including corrections suppressed by a factor of order $\mathcal{O}(v^2)$ to the short-distance annihilation. This requires the introduction of additional operators in the effective Lagrangian and the solution of the Schrödinger equation beyond the S -wave limit.

EFT at $\mathcal{O}(v^2)$ Concerning the EFT we have to introduce all the possible operators at the required order, so

$$\delta\mathcal{L}_{\text{ann}} = \delta\mathcal{L}_{\text{ann}}^{d=6} + \delta\mathcal{L}_{\text{ann}}^{d=8} , \quad (4.107)$$

where the superscript d denote the mass dimension of the corresponding operators. Note that, in the non-relativistic theory, the scalar field has mass dimension $d = 3/2$, as can be seen from the kinetic term in the Lagrangian (4.91). As we have seen in Sec. 4.3.1, the Schrödinger equation from which the Sommerfeld factors are computed is expanded in partial waves. We therefore have to identify the four-particle operators of definite angular momentum configurations. The only allowed configurations for a pair of scalars have $s = 0$ and $j = l$, therefore up to the P -wave we have to consider

$${}^{2s+1}L_j = {}^1S_0, {}^1P_1 . \quad (4.108)$$

In principle, we may consider transitions between different spin and/or orbital angular momentum states in the short-distance annihilation. As explained in [46], this is however not necessary since to compensate the transitions one needs sub-leading non-Yukawa potentials that would introduce additional suppression.

The leading order term $\delta\mathcal{L}_{\text{ann}}^{d=6}$ is given in (4.102), while the NNLO one receives both S -wave and P -wave contributions

$$\delta\mathcal{L}_{\text{ann}}^{d=6} = \sum_{a,b} n_{ab} C_{ab} ({}^1S_0) \mathcal{O}_{ba} ({}^1S_0) , \quad (4.109)$$

$$\delta\mathcal{L}_{\text{ann}}^{d=8} = \sum_{a,b} n_{ab} \frac{1}{M_{ab}^2} [C_{ab}({}^1S_0, \vec{q}^2) \mathcal{O}_{ba}({}^1S_0, \vec{q}^2) + C_{ab}({}^1S_0, \delta m) \mathcal{O}_{ba}({}^1S_0, \delta m) + C_{ab}({}^1P_1) \mathcal{O}_{ba}({}^1P_1)] , \quad (4.110)$$

where

$$M_{11} = 2m , \quad M_{12} = M_{21} = 2m + \delta m , \quad M_{22} = 2m + 2\delta m . \quad (4.111)$$

The normalization factor $1/M_{ab}^2$ has been factored out, so that the NNLO Wilson coefficients have the same mass dimension (-2) as the LO ones. The relevant operators are

$$\mathcal{O}_{ba}({}^1S_0) = [\varphi\varphi]_b^\dagger [\varphi\varphi]_a , \quad (4.112)$$

$$\mathcal{O}_{ba}({}^1S_0, \vec{q}^2) = \frac{1}{2} \left([\varphi\varphi]_b^\dagger [\varphi(-\frac{i}{2} \overleftrightarrow{\partial})^2 \varphi]_a + [\varphi(-\frac{i}{2} \overleftrightarrow{\partial})^2 \varphi]_b^\dagger [\varphi\varphi]_a \right) , \quad (4.113)$$

$$\mathcal{O}_{ba}({}^1S_0, \delta m) = (\delta m_{ab} M_{ab}) [\varphi\varphi]_b^\dagger [\varphi\varphi]_a , \quad (4.114)$$

$$\mathcal{O}_{ba}({}^1P_1) = [\varphi(\frac{i}{2} \overleftrightarrow{\partial})\varphi]_b^\dagger \cdot [\varphi(-\frac{i}{2} \overleftrightarrow{\partial})\varphi]_a , \quad (4.115)$$

where the antisymmetric derivative¹¹ is defined as $f \overleftrightarrow{\partial} g \equiv f(\partial g) - (\partial f)g$, and the mass-splittings

$$\delta m_{11} = \delta m_{22} = 0 , \quad \delta m_{12} = -\delta m_{21} = \frac{\delta m}{2} . \quad (4.116)$$

The need for formally treating the mass differences of the same order as the non-relativistic momenta follows from the energy-conservation relation. To see this, consider the process

$$[\phi(p_1) \phi(p_2)]_a \rightarrow [\phi(p_3) \phi(p_4)]_b , \quad (4.117)$$

in the center-of-mass frame, where the momenta are given by

$$p_1 = (p_1^0, \vec{q}) , \quad p_2 = (p_2^0, -\vec{q}) , \quad p_3 = (p_3^0, -\vec{q}') , \quad p_4 = (p_4^0, \vec{q}') . \quad (4.118)$$

The energy-conservation relation, expanded in the non-relativistic regime, reads

$$M_{ab} - \delta m_{ab} + 2\frac{\vec{q}^2}{M_{ab}} + \dots \stackrel{!}{=} M_{ab} + \delta m_{ab} + 2\frac{\vec{q}'^2}{M_{ab}} + \dots , \quad (4.119)$$

where the dots stands for terms of order \vec{q}^4/M_{ab}^3 or $\vec{q}^2 \delta m_{ab}/M_{ab}^3$ and higher. It follows from (4.119) that energy-conservation in off-diagonal reactions requires mass splittings to be treated formally as quantities of order \vec{q}^2/M_{ab} . We note that the formalism presented in [44] is suited for the more general case of hydrogen-like two-particle states, in which two well-separated mass scales can be introduced.

¹¹In presence of unbroken gauge symmetries the partial derivatives have to be replaced with the covariant one.

The Wilson coefficients are again determined by matching with the EFT with the full theory, performing a systematic expansion in the non-relativistic regime. The result for the tree-level annihilation rate (up to NNLO terms) in the EFT is

$$\begin{aligned}\Gamma_{ab}^{(0)} &= \sum_{wave} \Gamma_{ab}^{(0)}(wave) \\ &= \widehat{C}_{ab}(^1S_0) + \widehat{C}_{ab}(^1S_0, \vec{q}^2) \frac{\vec{q}^2 + \vec{q}'^2}{2M_{ab}^2} + \widehat{C}_{ab}(^1S_0, \delta m) \frac{\delta m_{ab}}{M_{ab}} + \widehat{C}_{ab}(^1P_1) \frac{\vec{q} \cdot \vec{q}'}{M_{ab}^2} .\end{aligned}\quad (4.120)$$

The above expression has to be compared with the result of the calculation in the full theory, performed as described in the following steps:

1. consider an intermediate state $X_A X_B$ and write the amplitudes of the relevant one-loop diagrams for $[\phi\phi]_a \rightarrow X_A X_B \rightarrow [\phi\phi]_b$. Notice that the contributions to the Wilson coefficients are evaluated separately for each $X_A X_B$ state;
2. apply the Cutkosky rules to cut the loop propagators of X_A and X_B , expand the other s - and t -channel propagators in the NR regime, then integrate over the loop momentum;
3. in order to obtain the same coefficient multiplying \vec{q}^2 and \vec{q}'^2 as in (4.120), make use of energy conservation to rewrite

$$\begin{aligned}\vec{q}^2 &= \frac{1}{2}(\vec{q}^2 + \vec{q}'^2) + M_{ab} \delta m_{ab} , \\ \vec{q}'^2 &= \frac{1}{2}(\vec{q}^2 + \vec{q}'^2) - M_{ab} \delta m_{ab} ,\end{aligned}\quad (4.121)$$

which are valid up to higher order terms.

4. the result of the previous steps is an expression of the form of eq. (4.120), from which analytic expressions for the absorptive part of Wilson coefficients in terms the full theory parameters can be extracted.

Sommerfeld enhancement at $\mathcal{O}(v^2)$ The Sommerfeld-enhanced annihilation rate to NNLO in the non-relativistic expansion can then be written as

$$\Gamma_{aa} = \sum_{wave} S_a(wave) \Gamma_{aa}^{(0)}(wave) ,\quad (4.122)$$

where the tree-level rates are given in (4.120) and have to be evaluated at

$$\vec{q}^2 = \vec{q}'^2 = \vec{q} \cdot \vec{q}' = 2\mu_a(\sqrt{s} - M_{aa}) \equiv \vec{q}_a^2 ,\quad (4.123)$$

with reduced mass of the incoming state $[\phi\phi]_a = \phi_i\phi_j$ defined as

$$\mu_a \equiv \frac{m_i m_j}{m_i + m_j} . \quad (4.124)$$

It is convenient to define the Sommerfeld factor associated to a generic Wilson coefficient or combination of Wilson coefficients with the same angular momentum configuration $^{2s+1}L_j$ as

$$S_a \left[\widehat{C} \left(^{2s+1}L_j \right) \right] \equiv \left(\frac{(2l-1)!!}{(k_a)^l} \right)^2 \sum_{b,c} \frac{(T_l^\dagger)_{ab} \widehat{C}_{bc} \left(^{2s+1}L_j \right) (T_l)_{ca}}{\widehat{C}_{aa} \left(^{2s+1}L_j \right)} , \quad (4.125)$$

$$k_a \equiv \sqrt{(M_{aa}v)^2 - M_{aa}V_{\infty aa}} , \quad (4.126)$$

where $V_\infty \equiv \lim_{r \rightarrow \infty} V(r)$ (recall that the potential at infinity is diagonal with entries equal to the mass splittings $V_{aa}(\infty) = \delta m_{1a}$), and the velocity parameter v is defined as

$$mv^2 = \sqrt{s} - 2m . \quad (4.127)$$

The above equation is the generalization of (4.105) to higher partial waves. We refer the reader to [46] for the details of the derivation. Finally, the enhanced rate can be written as

$$\begin{aligned} \Gamma_{aa} = S_a \left[\widehat{C}_h \left(^1S_0 \right) \right] \widehat{C}_{aa} \left(^1S_0 \right) \\ + \frac{\vec{q}_a^2}{M_{aa}^2} \left(S_a \left[\widehat{C}_\kappa \left(^1S_0 \right) \right] \widehat{C}_{aa} \left(^1S_0, \vec{q}^2 \right) + S_a \left[\frac{\widehat{C} \left(^1P_1 \right)}{M^2} \right] \widehat{C}_{aa} \left(^1P_1 \right) \right) , \end{aligned} \quad (4.128)$$

where we defined

$$\widehat{C}_{hab} \left(^1S_0 \right) \equiv \widehat{C}_{ab} \left(^1S_0 \right) + \frac{\delta m_{ab}}{M_{ab}} \widehat{C}_{ab} \left(^1S_0, \delta m \right) , \quad (4.129)$$

$$\widehat{C}_{\kappa ab} \left(^1S_0 \right) \equiv \frac{1}{2M_{ab}^2} \left(\kappa_{ac}^* \widehat{C}_{cb} \left(^1S_0 \right) + \widehat{C}_{ac} \left(^1S_0 \right) \kappa_{cb} \right) . \quad (4.130)$$

In the second line above a sum over the repeated index c is understood and the matrix κ is given by

$$\kappa_{ab} \equiv \vec{q}_a^2 \delta_{ab} + 2\mu_a \sum_i m_{Z_i} g_{iab}^2 , \quad (4.131)$$

where the sum extends to all the bosons exchanged in the potential, and we denote with m_{Z_i} and g_{iab} the mass and coupling constant of the i^{th} boson.

| | Neutral | Single-charged | Double-charged |
|--|---|--|--|
| Spin $\frac{1}{2} \otimes \frac{1}{2}$ | $\chi^0 \chi^0 \rightarrow \chi^0 \chi^0$ | | |
| Spin $\frac{1}{2}$ | | $\chi^0 \tilde{f}^- \rightarrow \chi^0 \tilde{f}^-$ $\chi^0 \tilde{f}^+ \rightarrow \chi^0 \tilde{f}^+$ | |
| Spin 0 | $\tilde{f}^+ \tilde{f}^- \rightarrow \tilde{f}^+ \tilde{f}^-$ | | $\tilde{f}^- \tilde{f}^- \rightarrow \tilde{f}^- \tilde{f}^-$ $\tilde{f}^+ \tilde{f}^+ \rightarrow \tilde{f}^+ \tilde{f}^+$ |

Table 4.3: Collection of the scattering reactions according to electric charge and spin of the two-particle states. Neutralino indices are suppressed, sfermions do not carry any index.

4.3.4 The neutralino/sfermion co-annihilation in the pMSSM

In this Section we apply the EFT formalism for the Sommerfeld enhancement to the co-annihilation in the pMSSM of the neutralinos χ_i^0 with a charged sfermion \tilde{f}^\pm , that can be for example the lightest stau or stop. Previous studies on the dark matter relic density in this scenario and the Sommerfeld enhancement in the relevant channels can be found in [42, 131]. We set the cutoff of the EFT at the scale $m \equiv m_{\chi_1^0}$ and expand each particle mass according to $m_{\tilde{f}^\pm} = m + \delta m_\varphi$ and $m_{\chi_i^0} = m + \delta m_i$, such that the kinetic terms in the Lagrangian read

$$\mathcal{L}_{\text{kin}} = \varphi^\dagger \left(i\partial_t - \delta m_\varphi + \frac{\partial^2}{2m} \right) \varphi + \varphi_c^\dagger \left(i\partial_t - \delta m_\varphi + \frac{\partial^2}{2m} \right) \varphi_c + \sum_{i=1}^{n_0} \xi_i^\dagger \left(i\partial_t - \delta m_i + \frac{\partial^2}{2m} \right) \xi_i, \quad (4.132)$$

where ξ_i is the non-relativistic two-component spinor field describing the low-energy modes of the i^{th} neutralino. Because of the Majorana nature of the neutralino, there is no need for an additional spinor field describing its antiparticle in the non-relativistic theory, as it is the case for Dirac fermions.

We aim at computing the total rate for the annihilation of any two-particle state $[\phi\phi]_a$ into pairs of SM particles and Higgs bosons, where with ϕ we denote here either a fermion (χ_i^0) or a scalar (\tilde{f}^\pm). We therefore consider the one-loop reactions

$$[\phi\phi]_a \rightarrow X_A X_B \rightarrow [\phi\phi]_b, \quad (4.133)$$

where $X_A X_B$ is a generic pair of SM particles or Higgs bosons. The considered scattering reactions, subdivided into three sectors according to the charge of the two-particle states and organized according to the spin of the involved particles, are collected in Table 4.3. The leading-order potentials can be computed as described in Sec. 4.3.2 (See [46]). In the following we consider the short-range annihilations involving four-scalar and two-scalar-two-fermion reactions, while for the annihilation channel involving four fermions we refer the reader to [44, 45].

Four-scalar

The neutral process involving four scalars ($\tilde{f}^+ \tilde{f}^- \rightarrow \tilde{f}^+ \tilde{f}^-$) corresponds to the case we studied in the previous Section with the only two-particle state $ab = 22$. The relevant operators with corresponding Wilson coefficients were defined in (4.109 - 4.115), and in the following we will make the identification $\mathcal{O}^{+-}(\text{wave}) \equiv \mathcal{O}_{22}(\text{wave})$, and same for \hat{C} . The four-particle operators relevant in the double-charged sectors can be easily obtained from the previous expressions by substituting $\varphi \leftrightarrow \varphi_c$ for $\tilde{f}^- \leftrightarrow \tilde{f}^+$.

Two-scalar-two-fermion

Consider now the single-charged sector $\chi_i^0 \tilde{f}^- \rightarrow \chi_j^0 \tilde{f}^-$, described by the four two-particle states

$$[\phi\phi]_a = \chi_a^0 \tilde{f}^- . \quad (4.134)$$

The spin of the involved two-particle states is $s = 1/2$, therefore the possible angular momentum configurations, up to $l = 1$, are

$${}^{2s+1}L_j = {}^2S_{\frac{1}{2}}, {}^2P_{\frac{1}{2}}, {}^2P_{\frac{3}{2}} . \quad (4.135)$$

At leading order $d = 6$ there is only the S -wave contribution

$$\delta\mathcal{L}_{\text{ann}}^{d=6} \supset \sum_{ab} C_{ab}^{0-} \left({}^2S_{\frac{1}{2}} \right) \mathcal{O}_{ba}^{0-} \left({}^2S_{\frac{1}{2}} \right) , \quad (4.136)$$

with operators given by

$$\mathcal{O}_{ba}^{0-} \left({}^2S_{\frac{1}{2}} \right) = \xi_b^\dagger \varphi^\dagger \varphi \xi_a . \quad (4.137)$$

Notice that the other spin- $\frac{1}{2}$ process, $\chi^0 \tilde{f}^+ \rightarrow \chi^0 \tilde{f}^+$, is described by the same operators with the only prescription to substitute $\varphi \rightarrow \varphi_c$.

At the second order both S - and P -wave operators contribute and the annihilation Lagrangian term reads

$$\begin{aligned} \delta\mathcal{L}_{\text{ann}}^{d=8} \supset \sum_{a,b} \frac{1}{M_{ab}^2} & \left[C_{ab}^{0-} \left({}^2S_{\frac{1}{2}}, \vec{q}^2 \right) \mathcal{O}_{ba}^{0-} \left({}^2S_{\frac{1}{2}}, \vec{q}^2 \right) + C_{ab}^{0-} \left({}^2S_{\frac{1}{2}}, \delta m \right) \mathcal{O}_{ba}^{0-} \left({}^2S_{\frac{1}{2}}, \delta m \right) \right. \\ & \left. C_{ab}^{0-} \left({}^2P_{\frac{1}{2}} \right) \mathcal{O}_{ba}^{0-} \left({}^2P_{\frac{1}{2}} \right) + C_{ab}^{0-} \left({}^2P_{\frac{3}{2}} \right) \mathcal{O}_{ba}^{0-} \left({}^2P_{\frac{3}{2}} \right) \right] . \end{aligned} \quad (4.138)$$

The first line contains the NNLO S -wave operators, which are given by

$$\mathcal{O}_{ba}^{0-} \left({}^2S_{\frac{1}{2}}, \vec{q}^2 \right) = \frac{1}{2} \left(\xi_b^\dagger \varphi^\dagger \varphi \left(-\frac{i}{2} \overleftrightarrow{\partial} \right)^2 \xi_a + \xi_b^\dagger \left(-\frac{i}{2} \overleftrightarrow{\partial} \right)^2 \varphi^\dagger \varphi \xi_a \right) , \quad (4.139)$$

$$\mathcal{O}_{ba}^{0-} \left({}^2S_{\frac{1}{2}}, \delta m \right) = (\delta m_{ab} M_{ab}) \xi_b^\dagger \varphi^\dagger \varphi \xi_a, \quad (4.140)$$

where δm_{ab} is the difference between the masses of the outgoing and incoming neutralinos,

$$\delta m_{ab} = \frac{m_{\chi_b^0} - m_{\chi_a^0}}{2}. \quad (4.141)$$

The P -wave operators in the second line are¹²

$$\mathcal{O}_{ba}^{0-} \left({}^2P_{\frac{1}{2}} \right) = \xi_b^\dagger \left(-\frac{i}{2} \overleftrightarrow{\boldsymbol{\partial}} \cdot \boldsymbol{\sigma} \right) \varphi^\dagger \varphi \left(-\frac{i}{2} \overleftrightarrow{\boldsymbol{\partial}} \cdot \boldsymbol{\sigma} \right) \xi_a, \quad (4.143)$$

$$\mathcal{O}_{ba}^{0-} \left({}^2P_{\frac{3}{2}} \right) = 3 \left(\xi_b^\dagger \left(-\frac{i}{2} \overleftrightarrow{\boldsymbol{\partial}} \right) \varphi^\dagger \cdot \varphi \left(-\frac{i}{2} \overleftrightarrow{\boldsymbol{\partial}} \right) \xi_a \right) - \mathcal{O}_{ba}^{0-} \left({}^2P_{\frac{1}{2}} \right), \quad (4.144)$$

where $\boldsymbol{\sigma} \equiv \vec{\sigma}$ denotes the three-vector with components given by the Pauli matrices.

In order to determine the Wilson coefficients we consider the reaction

$$\chi_a^0(p_1) \tilde{f}^-(p_2) \rightarrow \chi_b^0(p_4) \tilde{f}^-(p_3), \quad (4.145)$$

with momenta as in (4.118). The polarized annihilation rate in the EFT up to NNLO terms is given by

$$\begin{aligned} \Gamma_{ab}^{(0)}(\vec{n}) &= \widehat{C} \left({}^2S_{\frac{1}{2}} \right) + \widehat{C} \left({}^2S_{\frac{1}{2}}, \vec{q}^2 \right) \frac{\vec{q}^2 + \vec{q}'^2}{2M_{ab}^2} + \widehat{C} \left({}^2S_{\frac{1}{2}}, \delta m \right) \frac{\delta m_{ab}}{M_{ab}} \\ &+ \left[\widehat{C} \left({}^2P_{\frac{1}{2}} \right) + 2\widehat{C} \left({}^2P_{\frac{3}{2}} \right) \right] \frac{\vec{q} \cdot \vec{q}'}{M_{ab}^2} + \left[\widehat{C} \left({}^2P_{\frac{1}{2}} \right) - \widehat{C} \left({}^2P_{\frac{3}{2}} \right) \right] \frac{i n^k [q, q']^k}{M_{ab}^2}, \end{aligned} \quad (4.146)$$

where for simplicity we omitted the superscript “0–” and the subscript “ ab ” from the Wilson coefficients and we denote $[a, b]^k = \epsilon^{ijk} a^i b^j$. The “spin-polarization vector” of the fermion pair built up with the incoming and the outgoing neutralinos is defined as

$$\vec{n}_{s_i s_j} \equiv \xi_{s_j}^\dagger \boldsymbol{\sigma} \xi_{s_i}. \quad (4.147)$$

Because at the considered order the potential interactions are spin-conserving, the spin-average reduces to the sum over the two equal-spin polarization vectors $\vec{n}_{\uparrow\uparrow} (\downarrow\downarrow) \equiv \pm (0, 0, 1)^T$, and then

¹²The expressions for the P -wave operators can be checked by verifying

$$\langle 0 | \varphi \left(-\frac{i}{2} \overleftrightarrow{\boldsymbol{\partial}} \cdot \boldsymbol{\sigma} \right) \xi_a |^{3/2}, j_z \rangle = \langle 0 | \varphi \left(3 \left(-\frac{i}{2} \overleftrightarrow{\boldsymbol{\partial}} \right) - \left(-\frac{i}{2} \overleftrightarrow{\boldsymbol{\partial}} \cdot \boldsymbol{\sigma} \right) \right) \xi_a |^{1/2}, j_z \rangle = 0 \quad \forall j_z, \quad (4.142)$$

where $|j, j_z\rangle$ with $j = 1/2, 3/2$, represents the component of total angular momentum j of the spin- $\frac{1}{2}$ two-particle state $\chi^0 \tilde{f}^-$ in the $l = 1$ orbital momentum configuration. The decomposition follows from the group representations relation $2 \otimes 3 = 2 \oplus 4$, where 2 (3, 4) represents the spin- $\frac{1}{2}$ ($1, \frac{3}{2}$) representation.

the last term in (4.146) vanishes. Moreover, the leading-order potential interactions do not discriminate among the P -wave states ${}^2P_{\frac{1}{2}}$ and ${}^2P_{\frac{3}{2}}$, so we can perform the spin-average before the matching without loss of relevant information.

To write the full pMSSM result in the form of (4.146), in addition to the steps described in the previous Section, we have to perform a spin-projection of the fermionic chain present in each diagram

$$\bar{u}(p_4) \Gamma u(p_2) = \text{Tr} \{ u(p_2) \bar{u}(p_4) \Gamma \} , \quad (4.148)$$

where Γ denotes the (diagram specific) chain of Dirac matrices arising from vertices and propagators. Writing the spinor as

$$u(p) = \sqrt{\frac{p^0 + m}{2p^0}} \begin{pmatrix} \xi_s \\ \frac{\vec{p} \cdot \vec{\sigma}}{p^0 + m} \xi_s \end{pmatrix} , \quad (4.149)$$

the 4×4 matrix in spinor space $u(p_2) \bar{u}(p_4)$ entering the trace in (4.148) can be expressed in terms of the 2×2 spin matrix $\xi_{s_2} \xi_{s_4}^\dagger$ which can be written as

$$\xi_{s_2} \xi_{s_4}^\dagger = \frac{1}{2} (\delta_{s_2, s_4} + \vec{n}_{s_2, s_4} \cdot \vec{\sigma}) , \quad (4.150)$$

where the spin-polarization vector was defined in (4.147). Finally the spin-averaged annihilation rate is simply

$$\Gamma_{ab}^{(0)} = \frac{1}{2} \sum_{\vec{n}} \Gamma_{ab}^{(0)}(\vec{n}) . \quad (4.151)$$

Results

The results for the absorptive part of Wilson coefficients in the neutralino-sfermion co-annihilation scenario described in this Section are collected in the Appendix B. The coefficients encoding diagonal reactions can be cross-checked by means of the relation

$$\begin{aligned} \Gamma_{aa}^{(0)} &= \sigma_a v_{\text{rel}, a} \\ &\simeq a + b v_{\text{rel}, a}^2 , \end{aligned} \quad (4.152)$$

where we defined $\sigma_a \equiv \sum_{A, B} \sigma_{[\phi\phi]_a \rightarrow X_A X_B}$. The coefficients a and b of the annihilation cross section times relative velocity (r.h.s.) can be extracted numerically for a given spectrum with different publicly available computer codes and the rate at the l.h.s., given in (4.120) and (4.151), can be written in the form $a + b v_{\text{rel}, a}^2$ by using

$$v_{\text{rel}, a} = |\vec{v}_i - \vec{v}_j| \simeq \frac{|\vec{q}_a|}{\mu_a} . \quad (4.153)$$

| VV | VS | SS | $f\bar{f}$ | $\eta\bar{\eta}$ |
|---|--|--|--|--|
| W^+W^- , ZZ , $\gamma\gamma, Z\gamma$ | Zh^0, ZH^0 , $\gamma h^0, \gamma H^0$, ZG^0, ZA^0 , $\gamma G^0, \gamma A^0$, W^+G^-, W^+H^- , W^-G^+, W^-H^+ | h^0h^0, h^0H^0, H^0H^0 , G^0h^0, A^0h^0 G^0H^0, A^0H^0 , G^0G^0, G^0A^0, A^0A^0 G^+G^-, G^+H^- , H^+G^-, H^+H^- | $u^I\bar{u}^I$, $d^I\bar{d}^I$, $e^I\bar{e}^I$, $\nu^I\bar{\nu}^I$ | $\eta^+\bar{\eta}^+$, $\eta^-\bar{\eta}^-$, $\eta^Z\bar{\eta}^Z$ |
| | | | $e^I e^I$ | |

Table 4.4: Particle pairs $X_A X_B$ in the neutral reaction $\tilde{\tau}_1^+ \tilde{\tau}_1^- \rightarrow X_A X_B \rightarrow \tilde{\tau}_1^+ \tilde{\tau}_1^-$ (first line) and in the double-charged one $\tilde{\tau}_1^- \tilde{\tau}_1^- \rightarrow X_A X_B \rightarrow \tilde{\tau}_1^- \tilde{\tau}_1^-$ (last line). The states are organized according to the spin of the two particles with vectors, scalars and fermions denoted with V , S and f respectively. Additionally we denote with η the ghosts. The index I runs over the three fermion generations.

| Vf | fS |
|-------------------------------------|--|
| $W^- \nu^I$, $Ze^I, \gamma e^I$ | $e^I h^0, e^I H^0, e^I G^0, e^I A^0$, $\nu^I H^-, \nu^I G^-$ |

Table 4.5: Particle pairs $X_A X_B$ in the single-charged reaction $\chi_i^0 \tilde{\tau}_1^- \rightarrow X_A X_B \rightarrow \chi_j^0 \tilde{\tau}_1^-$, classified according to their spin as in Table 4.4. The index I runs over the three fermion generations.

We performed this cross-check for a few benchmark models by computing separately the annihilation cross sections for the processes

$$\tilde{\tau}_1 \tilde{\tau}_1 \rightarrow X_A X_B, \quad \chi^0 \tilde{\tau}_1 \rightarrow X_A X_B, \quad (4.154)$$

for all the accessible SM and Higgs two-particle final states $X_A X_B$, listed in Tables 4.4 and 4.5.

Positive-charge processes, corresponding to charge-conjugates of the negatively charged ones listed in the tables, are not explicitly written. Our results have been compared with those obtained numerically with MadGraph (version 1.5.12).¹³ We found agreement at 1% up to permille level for the S -wave term a , and up to a few percent for the P -wave coefficient b .

¹³The coefficients a and b have been obtained by computing with MadGraph the cross section $\sigma_a v_{\text{rel}, a}$ at different velocities and fitting the results with a parabola.

The non-relativistic approximation is reliable for single particle velocities up to $v/c \sim 0.3$, thus confirming that this formalism is well suited to study the pair-annihilation at freeze-out.

The treatment of neutralino/sfermion co-annihilation presented in this Section can be used as a starting point for a further generalization of the formalism for the neutralino/chargino sector [44–46], that is the topic of the next Section.

4.4 The procedure in our code

In this Section we describe the general features of the automated computer program in which we implemented the formalism of [44–46] to compute the Sommerfeld-enhanced relic density of neutralino DM for a generic point in the pMSSM parameter space. We describe here the general characteristics of the code, not limited to the analysis of the wino-like scenario from [47], that we present in the next Section.

4.4.1 General framework and limitations

The program is designed to work within the R -conserving pMSSM with complex parameters as described in Sec. 4.2. The matching of the short-range annihilation matrices and the long-range potentials are computed with Feynman rules following the conventions of [132]. We note that, even though the soft SUSY-breaking universality assumption is not necessary for the calculation of the Sommerfeld-enhanced annihilation cross section, the general framework for the computation of the relic density relies on the assumption of negligible CP violation, see Chapter 1.

The code consists in the automated implementation of the effective theory described in [44–46], whose underlying ideas have been described in the previous Section. This formalism is suitable for an accurate calculation of the Sommerfeld-enhanced relic density including the full set of co-annihilations in the neutralino/chargino sector of the pMSSM. The two-particle states $[\chi\chi]_a$ are denoted by the label $a = 1, \dots, N_{|Q|}$, where $N_{|Q|}$ is the total number of states (channels) for each electric-charge sector, $|Q| = 0, 1, 2$, corresponding to neutral ($\chi^0\chi^0, \chi^+\chi^-$), single-charged ($\chi^0\chi^\pm$) and double-charged ($\chi^\pm\chi^\pm$) sectors. If all four neutralinos and two charginos are considered, in the charge-0 sector the label a runs over states

$$\chi_1^0\chi_1^0, \chi_1^0\chi_2^0, \chi_1^0\chi_3^0, \dots, \chi_3^0\chi_4^0, \chi_4^0\chi_4^0, \chi_1^+\chi_1^-, \chi_1^+\chi_2^-, \chi_2^+\chi_1^-, \chi_2^+\chi_2^-, \quad (4.155)$$

with 14 different states in total, whereas in the charge-1 sector we have 8 channels,

$$\chi_1^0\chi_1^\pm, \chi_1^0\chi_2^\pm, \dots, \chi_4^0\chi_1^\pm, \chi_4^0\chi_2^\pm, \quad (4.156)$$

and just 3 in the charge-2 sector,

$$\chi_1^\pm\chi_1^\pm, \chi_1^\pm\chi_2^\pm, \chi_2^\pm\chi_2^\pm. \quad (4.157)$$

The non-relativistic expansion is performed up to the second order (NNLO), thus retaining terms up to $\mathcal{O}(v^2)$ in the calculation of $\sigma_a v_{\text{rel},a}$. As we have seen, in presence of several co-annihilation channels the non-relativistic expansion is not simply the partial wave one, but higher order momentum dependent corrections and mass splittings have to be considered. The full list of terms is

$$wave \in \underbrace{\{^1S_0, ^3S_1\}}_{\text{LO}}, \underbrace{\{^1P_1, ^3P_j, (^1S_0, q^2), (^3S_1, q^2), (^1S_0, \delta m), (^3S_1, \delta m), (^1S_0, \delta \bar{m}), (^3S_1, \delta \bar{m})\}}_{\text{NNLO}}. \quad (4.158)$$

Even though the program can calculate the neutralino relic density for any choice of the pMSSM parameters, there are a few limitations to be kept in mind:

- the lightest neutralino has to be the LSP;¹⁴
- co-annihilation with sfermions or the gluino are not included.¹⁵ As a result, the effective annihilation cross section as computed by the program may not be accurate for parameter points with light sfermions or gluino in the spectrum. In our analysis we only consider points for which those particles are at least 25% heavier than the LSP;
- resonant s -channel annihilations, occurring for example in the H - and A -funnel regions [139, 140], where the mass of the CP -odd Higgs boson A^0 is approximately twice the LSP mass, spoils the factorization of the cross section upon which our formalism is based. The annihilation process is no longer short-ranged compared to the potential interactions. In order to exclude such a situation, a constraint should be imposed on the masses of the heavy Higgs bosons. In our analysis we use

$$m_{H^0, A^0, H^\pm} \notin \left\{ 1.7 m_{\tilde{\chi}_1^0}, 2.3 m_{\tilde{\chi}_1^0} \right\}. \quad (4.159)$$

A final remark concerns thermal effects due to the fact that, for TeV-scale dark matter particles, the freeze-out happens at temperatures close to the electroweak scale. Thermal corrections to the gauge boson masses, determining the range of the potential, and to the chargino-neutralino mass splitting, that influences the position of the Sommerfeld resonance, may affect the relic density. However it turns out that in the temperature range that is relevant for relic density

¹⁴Since charged or colored particles cannot constitute the observed DM, the only other candidates within the pMSSM are the sneutrinos. Purely left-handed sneutrinos have been indeed studied as DM candidate [133–135], but have been definitively ruled out as a dominant component of DM by direct detection searches [136], due to their large interaction with the Z boson. Augmenting the pMSSM with an additional right-handed superfield is a possible way out [137], but it is beyond the scope of this work.

¹⁵The sfermion co-annihilation case has been discussed in the previous Section, where references to existing studies were given. For a recent analysis of the relic density including gluino co-annihilation see e.g. [138].

calculation of TeV-scale dark matter, those effects can be safely neglected,¹⁶ as described in the Appendix of [47].

4.4.2 Generation of a parameter card from the parameters

The calculation of the annihilation cross section is performed in the physical basis (mass eigenstates). The input for our program is a pMSSM spectrum card in the standard SLHA format, which can be obtained, given a set of input parameters, from several public-available codes. For our analysis we used `FeynHiggs 2.9.5` [141, 142].

4.4.3 Calculation of mass splittings and running couplings

As we have seen in Sec. 4.3 when we studied the Yukawa potential, the Sommerfeld enhancement from a finite-range potential exhibits a resonant pattern. Around those resonances the enhancement can be as large as many orders of magnitude, the actual value depending strongly on the precise values of the model parameters. In this Section we consider two effects that we take into account in order to improve the accuracy of our results, namely the one-loop neutralino/chargino on-shell mass corrections and the running of the electroweak couplings.

A rigorous treatment of Sommerfeld enhancement in neutralino/chargino co-annihilations should refer to the on-shell mass spectrum, instead of the $\overline{\text{DR}}$ -parameters that are computed by the spectrum generators. Moreover, due to the strong dependence of Sommerfeld factors on the mass differences among the pair-annihilating states (in particular $\chi_1^0\chi_1^0$ and $\chi_1^+\chi_1^-$), a sub-GeV precision in the mass determination is required. To achieve such a precision in the heavy scenarios that we are interested in, one-loop corrections to the neutralino and chargino masses have to be taken into account, since they are of the same order of the tree-level splittings induced by electroweak symmetry breaking discussed in Sec. 4.2.1. This is particularly relevant in the pure-wino limit, in which the radiatively induced splitting is given by¹⁷

$$\delta m_{\chi_1^\pm} \simeq \delta m_{\chi^\pm}|_{\text{radiative, pure-wino}} = \frac{1 - c_W}{2} \alpha_2 m_W \approx 158 \text{ MeV} , \quad (4.160)$$

and dominates over the $\mathcal{O}(1 \text{ MeV})$ tree-level splitting. The importance of the one-loop correction relative to the tree-level splitting decreases as the Higgsino or bino component of the lightest neutralino is increased, as discussed in the Appendix of [47].

The parameter renormalization in the MSSM has been studied in [143–147], and we refer the reader to those references for the description of the problem. We follow the on-shell scheme as in e.g. [144], in which the renormalization constants for the parameters M_1 , M_2 and μ

¹⁶A combination of estimates, analytical calculations and numerical checks shows that the thermal modifications of the Sommerfeld effect change the relic density at most in the upper permille range, which is negligible for all practical purposes.

¹⁷The expression refers to the approximation $m_Z \ll m_\chi$ and the numerical value employs the $SU(2)_L$ coupling $\alpha_2(m_\chi) = 0.032810$ at the scale $m_\chi = 2.5 \text{ TeV}$.

are fixed by the requirement that three out of the total six physical masses of the charginos and neutralinos are on-shell, i.e. the tree-level masses coincide with the one-loop renormalized masses. The choice of which masses should be chosen on-shell is non-trivial, as certain choices can lead to unphysical divergences. We follow the NNC scheme discussed in [146,148], in which the on-shell particles are chosen to be the wino-like chargino and two neutralinos, the bino- and one of the Higgsino-like (the closest in mass to the wino-like one). Note that when all three mass parameters are very close ($< 0.1\%$ splittings) a situation may arise in which the ordering of the neutralinos changes after the mass splittings are included. In this case we perform a consistent reordering of the masses and of the mixing matrices. The diagrams determining the mass shifts for the remaining three chargino and neutralino masses are computed by using `FeynArts` [149,150], together with the packages `FormCalc` [151] and `LoopTools` [151], using the model files presented in [152].

Due to the multi-scale nature of the considered problem, the running of the coupling constants has to be consistently treated. In different parts of the calculation the couplings should be taken at a different energy scale Q , in particular $Q = m_Z$ for the potential interactions, $Q = m_{\chi_1^0}$ for the mass splittings in the neutralino/chargino sector and $Q = 2m_{\chi_1^0}$ for the short-range annihilations. We perform the running in the unbroken $SU(2)_L \times U(1)_Y$ theory, since most of the running occurs above the electroweak scale. The starting values of the $SU(2)_L$ and $U(1)_Y$ couplings at $Q = m_Z$ are taken as $\alpha_2(m_Z) = 0.034723$ and $\alpha_1(m_Z) = 0.009986$, respectively. Since the short-range annihilation is evaluated at tree-level, we run the couplings at $Q = 2m_{\chi_1^0}$ with the one-loop renormalization group equation (RGE)

$$\frac{d\alpha_i}{d\log\mu} = -2\beta_{0,i} \frac{\alpha_i^2}{4\pi}. \quad (4.161)$$

The solution is

$$\alpha_i(Q) \simeq \alpha_i(Q_0) \left(1 - \alpha_i(Q_0) \frac{\beta_{0,i}}{4\pi} \log \frac{Q^2}{Q_0^2} \right), \quad (4.162)$$

valid between two scales Q_0 and Q where the leading order beta function $\beta_{0,i}$ is constant. At the required level of accuracy there are no threshold effects to be considered and the LO beta function $\beta_{0,i}$ is given by

$$\beta_{0,i} = \frac{11}{3} \text{Tr} \left[T_A^{(i)2} \right] - \frac{2}{3} \sum_f \text{Tr} \left[T_f^{(i)2} \right] - \frac{1}{3} \sum_s \text{Tr} \left[T_s^{(i)2} \right], \quad (4.163)$$

where $T_R^{(i)}$ are the generators of the group i in the representation R and the three terms correspond respectively to gauge bosons (always in the adjoint representation A), fermions, and scalars. The sums extend only to particles with mass smaller than Q . The energy range

we are interested in can be divided into five regions¹⁸ of constant beta functions,

$$\text{region}[n] = M_n \leq Q < M_{n+1} , \quad (4.164)$$

where, working in the unbroken theory, the masses M_n are taken from the list

$$m_Z, M_A, |M_1|, M_2, |\mu| , \quad (4.165)$$

ordered such that $M_{n+1} > M_n$. The first region extends from m_Z to the smallest between M_A and $m_{\chi_1^0}$, such that the beta functions are those of the Standard Model. Above M_n we have to add to the beta functions of region $[n-1]$ the contribution from the corresponding multiplet, as listed in Table 4.6.¹⁹

| Particles | $\text{Tr} \left[T_A^{(i) 2} \right]$ | | $\sum_f \text{Tr} \left[T_f^{(i) 2} \right]$ | | $\sum_s \text{Tr} \left[T_s^{(i) 2} \right]$ | |
|-------------|--|-----------|---|-----------|---|-----------|
| | $U(1)_Y$ | $SU(2)_L$ | $U(1)_Y$ | $SU(2)_L$ | $U(1)_Y$ | $SU(2)_L$ |
| SM | 0 | 2 | 10 | 6 | 1/2 | 1/2 |
| Φ_2 | 0 | 0 | 0 | 0 | 1/2 | 1/2 |
| \tilde{B} | 0 | 0 | 0 | 0 | 0 | 0 |
| \tilde{W} | 0 | 0 | 0 | 2 | 0 | 0 |
| \tilde{H} | 0 | 0 | 1 | 1 | 0 | 0 |

Table 4.6: Contributions to the $U(1)_Y$ and $SU(2)_L$ beta functions.

4.4.4 Calculation of the annihilation matrices

The SLHA spectrum card with one-loop corrections to the masses in the neutralino/chargino sector and running couplings is the required input for the routine calculating the tree-level annihilation matrices $\Gamma_{ab}^{(0)}(wave)$. The calculation follows the procedure introduced in [44, 45], that we described in the case of sfermion co-annihilation in Sec. 4.3.4. Additionally, we developed an improved prescription for the expansion of s -channel propagators. This modification is needed in order to avoid spurious resonances and is described in the Appendix C.

¹⁸We neglect the contribution to the beta functions from the sfermions. We checked that the error introduced in this way is small: for a 2.5 TeV LSP the total running of α_2 from m_Z up to $2m_{\chi_1^0}$ is around 5-6 %, and the maximum contribution from sfermions (when they are all decoupled at $1.25 m_{\chi_1^0}$) is only 0.4 %.

¹⁹In the decoupling limit $M_A \gg m_Z$ the two Higgs doublets $H_{u,d}$ can be rotated into the mass eigenstates $\Phi_{1,2}$, with $m_{\Phi_1} \simeq m_{h^0}$ and $m_{\Phi_2} \simeq M_A$.

Once the hermiticity property is used to reduce the number of independent entries, each one of the ten annihilation matrices for a given *wave* in (4.158) requires the evaluation of 105, 2×36 and 2×6 distinct entries for neutral, single- and double-charged sectors, respectively, making up a total number of 1890 independent entries. In the *CP*-conserving case, the annihilation matrices of the charged-conjugated sectors, $\chi^0\chi^+$ and $\chi^0\chi^-$, $\chi^+\chi^+$ and $\chi^-\chi^-$, become equal, and the previous number is reduced to 1470. The expressions account for the sum of all $X_A X_B$ exclusive states with $X_{A,B}$ being a SM (including the light Higgs) or a heavy MSSM Higgs, such that the mass of $X_A X_B$ is smaller than $2m_{\chi_1^0}$.²⁰ A complete list of the $X_A X_B$ states can be found in Appendix A of [44].

Despite coming from the product of tree-level amplitudes, the analytic expressions for the Wilson coefficients are very large, which is traced back to the fact that there are several diagrams with different topologies and/or virtual intermediate particles contributing to a given exclusive state, and because of the non-relativistic expansion performed. The numerical evaluation of all matrix entries for a given pMSSM parameter is done using pre-compiled functions within MATHEMATICA, taking in average ~ 300 seconds of CPU time. If only the annihilation matrices necessary for the leading-order cross section, $\widehat{C}_{ab}(^1S_0)$ and $\widehat{C}_{ab}(^3S_1)$, are evaluated, the cost in CPU time reduces to less than 40 seconds per model.

4.4.5 Calculation of the Sommerfeld factors

For a given two-particle state $[\chi\chi]_a \equiv \chi_i\chi_j$ formed out of two neutralino or chargino species, the annihilation rate including long-distance Sommerfeld corrections in their center-of-mass frame, can be parametrized as [46]

$$\begin{aligned} \sigma_a v_{\text{rel}, a} = & S_a \left[\widehat{C}_h(^1S_0) \right] \widehat{C}_{aa}(^1S_0) + S_a \left[\widehat{C}_h(^3S_1) \right] 3 \widehat{C}_{aa}(^3S_1) \\ & + \frac{\vec{q}_a^2}{M_{aa}^2} \left(S_a \left[\widehat{C}_\kappa(^1S_0) \right] \widehat{C}_{aa}(^1S_0, \vec{q}^2) + S_a \left[\widehat{C}_\kappa(^3S_1) \right] 3 \widehat{C}_{aa}(^3S_1, \vec{q}^2) \right. \\ & \left. + S_a \left[\frac{\widehat{C}(^1P_1)}{M^2} \right] \widehat{C}_{aa}(^1P_1) + S_a \left[\frac{\widehat{C}(^3P_J)}{M^2} \right] \widehat{C}_{aa}(^3P_J) \right), \end{aligned} \quad (4.166)$$

up to higher orders in \vec{q}_a , the relative momentum of the particles in the two-particle state. The combinations of Wilson coefficients are defined as

$$\widehat{C}_{hab}(^{2s+1}S_j) \equiv \widehat{C}_{ab}(^{2s+1}S_j) + \frac{\delta m_{ab}}{M_{ab}} \widehat{C}_{ab}(^{2s+1}S_j, \delta m) + \frac{\delta \overline{m}_{ab}}{M_{ab}} \widehat{C}_{ab}(^{2s+1}S_j, \delta \overline{m}) \quad , \quad (4.167)$$

$$\widehat{C}_{ab}(^3P_J) \equiv \frac{1}{3} \widehat{C}_{ab}(^3P_0) + \widehat{C}_{ab}(^3P_1) + \frac{5}{3} \widehat{C}_{ab}(^3P_2) \quad . \quad (4.168)$$

²⁰Strictly speaking, the upper limit on the mass of the $X_A X_B$ state should be M_I , when dealing with the co-annihilation cross section of the two-particle state I . This would require having a different set of annihilation matrices for each co-annihilation channel, which is impractical.

By setting all the Sommerfeld factors to one, (4.166) reproduces the Born annihilation cross section including $\mathcal{O}(v^2)$ terms.

The Sommerfeld factors are computed separately in each sector of two-particle states with different electric charge $0, \pm 1, \pm 2$, by solving the coupled set of Schrödinger equations. In CP -conserving MSSM only the positively charged two-particle states sectors are calculated explicitly, since the corresponding negatively charged ones are identical. The leading-order Yukawa and Coulomb potentials entering the Schrödinger equations are generated by the exchange of electroweak gauge bosons, Higgs bosons and the photon. In the case of Higgs bosons, the potentials are included only when their mass is less than $m_{\chi_1^0}/2$. Due to numerical instabilities arising for large mass splittings, the adopted method of solving the Schrödinger equation is improved compared to the one described in Sec. 4.3.1, as explained in [46]. The instability originates from the presence of kinematically closed channels, which happens generically for small v , defined by

$$E = m_{\chi_1^0} v^2 = \sqrt{s} - 2m_{\chi_1^0} , \quad (4.169)$$

such that $2m_{\chi_1^0} + m_{\chi_1^0} v^2 \ll M_{ab}$.

The large value r_∞ is determined by requiring that the Sommerfeld factor changes by less than 0.3%, when r_∞ is doubled. This accuracy is often difficult to achieve for very small velocity v , or near values, where new two-particle channels with mass above $2m_{\chi_1^0}$ open, especially for $\chi^+ \chi^-$ states which experience the long-range Coulomb interaction. Hence we fix $x_\infty = r_\infty/m_{\chi_1^0} v$ to 20 (50), when $v < 0.03$ (within 0.0002 of a threshold). This can lead to local inaccuracies of several percent. However, we find that the deviation from the exact result is oscillatory, and mostly averages out in the thermal average.

The time needed for the solution of the matrix Schrödinger equation increases rapidly with the number of two-particle states. Heavier states are strongly Boltzmann-suppressed and irrelevant for freeze-out or they are sufficiently off-shell within the ladder diagrams to not contribute substantially to the Sommerfeld effect of the lighter states. It is therefore in general safe to reduce the number of coupled Schrödinger equations by retaining only the two-particle states with mass below $1.2 \times 2m_{\chi_1^0}$. The annihilation rate of two-particle states heavier than this cutoff are included in the total $\langle \sigma_{\text{eff}} v \rangle$ at the Born level. Even with this criterion, the number of contributing two-particle states can be large and the solution very slow. As already mentioned, an approximate treatment of heavier two-particle states that consists in including them only in the last loop near the annihilation vertex (and not in the full ladder exchange) has been developed in [46]. We introduced in the code the possibility to set the maximum number of states N_{exact} to be treated exactly in the Schrödinger equation. The lightest N_{exact} two-particle states are always included in the Schrödinger equation, while any additional state lighter than $1.2 \times 2m_{\chi_1^0}$ is included approximately.

In our analysis we set the number of exact states to four. The restriction is certainly sufficient for models close to the pure-wino case, when the degenerate states are $\chi_1^0 \chi_1^0$, $\chi_1^+ \chi_1^-$ in the neutral sector, and $\chi_1^0 \chi_1^+$, $\chi_1^+ \chi_1^+$ in the charge-1 and and charge-2 sectors, respectively.

When the LSP acquires a substantial Higgsino or bino component, the number of degenerate states increases and may exceed four in the neutral and charge-1 sector. In fact, in strongly mixed wino-Higgsino LSP models, there are typically 10 neutral states falling below the mass cut $1.2 \times 2m_{\chi_1^0}$. An example of such a model, in which all the neutralinos and charginos contribute apart from the bino-like χ_4^0 , has been analyzed in [117]. The relic density results for different choices of N_{exact} show that the effect of the additional heavier states is accurately reproduced by the approximate treatment in the last loop. We further confirmed this by analyzing with $N_{\text{exact}} = 10$ a subset of 1575 model points. The largest difference we find is 4%, but it is below 1% in 96% of the points and most of the time closer to the permille level.

4.4.6 Thermal average and solution of the Boltzmann equation

The central ingredient of the Boltzmann equation is the thermally-averaged effective cross section $\langle \sigma_{\text{eff}} v \rangle$, that we introduced in Chapter 1 and was given in (1.41). By changing the integration variable from the squared center-of-mass energy s to v we can write (1.41) as

$$\langle \sigma_{\text{eff}} v \rangle = \frac{2 m_{\chi_1^0} \sum_a \int_{v_{\text{thr},a}}^{\infty} dv v f(v) (\sigma_a v_{\text{rel},a})(v) K_1\left(\frac{\sqrt{s}}{T}\right)}{T \left(\sum_{i=1}^N m_i^2 K_2\left(\frac{m_i}{T}\right) \right)^2}, \quad (4.170)$$

where the lower extreme of the integration reads

$$v_{\text{thr},a} = \sqrt{\frac{m_i + m_j - 2m_{\chi_1^0}}{m_{\chi_1^0}}}, \quad (4.171)$$

and the function $f(v)$

$$f(v) \equiv \frac{1}{8s} \sqrt{s^2 - 2s(m_i^2 + m_j^2) + (m_i^2 - m_j^2)^2} (s^2 - (m_i^2 - m_j^2)^2), \quad (4.172)$$

where the dependence on v is implicit into s .

The cross sections $\sigma_a v_{\text{rel},a}$ for each two-particle state (4.166) are computed for $\mathcal{O}(50)$ values of the LSP velocity v , chosen adaptively in the range $\{10^{-4}, 10\}$, with more sampling points near threshold and the characteristic velocity near the freeze-out temperature. The results are then interpolated to get the continuous functions $(\sigma_a v_{\text{rel},a})(v)$, which are then integrated over v and summed to get the thermal averaged effective cross section, according to (4.170). This procedure is repeated for around 60 suitably chosen values of $x = m_{\chi_1^0}/T$ between 1 and 10^8 . This table is interpolated and the interpolating function $\langle \sigma_{\text{eff}} v \rangle(x)$ is employed in the Boltzmann equation (1.42), which is integrated as described in Sec. 1.4. The result $Y(x_{\text{max}})$ is the present value of the yield, from which the DM relic density is obtained as in (1.13). The value x_{max} is chosen to be large enough such that the yield is stable.

Given the annihilation matrices, the calculation of all Sommerfeld factors, cross section tables, thermal averages and, finally, the evolution of the Boltzmann equation through freeze-out takes about 400 sec of CPU time, leading to a total computation time (including the evaluation of the annihilation matrices) of somewhat above 10 min per MSSM parameter point.

4.5 Results of our analysis for wino-like dark matter

The well-studied minimal fermion triplet model [111] consists in assuming the DM particle to be the neutral component of an unbroken $SU(2)_L$ fermionic triplet, interacting with the electroweak gauge bosons only. When the Sommerfeld enhancement is considered, this scenario reproduces the observed value for the relic density for $m_{\chi_1^0} \simeq 2.75$ TeV. Even though this parameter point is not located at the peak of the Sommerfeld resonance, the enhancement is still quite large, $\sim 35\%$. This property results in strong constraints from indirect detection [116, 118, 119], since the effect of the Sommerfeld enhancement is even stronger for the present-day cross sections, due to the smaller velocities of DM particles today compared to the freeze-out time.

The minimal triplet scenario is realised within the MSSM in the pure-wino limit, in which $|Z_{12}|^2 \simeq 1$ and the sfermions are decoupled to very high masses, such that contributions to neutralino/chargino co-annihilations from non-gauge interactions are negligible. Due to the afore mentioned properties of the minimal triplet scenario, it is of phenomenological interest to investigate the characteristics of wino-like neutralinos in the MSSM. In particular, the departure from the pure-wino limit can be obtained in different ways: *i*) lowering the sfermion masses, *ii*) introducing co-annihilations with additional nearly degenerate neutralinos/charginos, and *iii*) allowing for Higgsino- and/or bino-admixture of the LSP. A reliable study of the relic density in models exhibiting those features is made possible for the first time by the automated code that we described in the previous Section.

The first phenomenological application of the code²¹ was discussed in [117], which focused on heavy (\sim TeV) wino- and Higgsino-like models, considering in particular a series of pMSSM parameter space points giving the correct relic density according to perturbative calculations and interpolating between these two limiting cases. In agreement with previous investigations, the impact of the Sommerfeld enhancement on the relic density along this “Higgsino-to-wino” trajectory was found to range from a few percent for predominant Higgsino composition, up to $\sim 60\%$ for a wino-like model close to the (loosely) bound state resonance. The total enhancement in the Higgsino-like case is generically smaller than in the wino-like one due to smaller couplings to gauge bosons and larger mass splittings of $\chi_1^0 \chi_1^0$ with heavier (charged) states. Moreover, a strong cancellation between enhancement in the neutral and suppression in the charged sector was found in Higgsino-like scenarios. A light scenario with $m_{\chi_1^0} \sim 500$ GeV was

²¹We note that the analysis in [117] was performed with a previous version of the code compared to the one described here, in which the one-loop mass splittings and the running couplings were not included.

also studied in [117], in which the LSP is bino-like, but the spectrum contains a nearly degenerate wino-like NLSP. In this case the effect of the Sommerfeld enhancement, even though it affects only the co-annihilating heavier wino states, still leads to a $\sim 15\%$ suppression of the relic density.

Even though based on the analysis of a few model points, this study already shows how the complicated structure of the full MSSM allows for obtaining the measured value of the relic abundance over a large region of the parameter space. With this in mind we performed extensive and dedicated scans of the pMSSM parameter space to study the relic density of close-to-wino models exhibiting the three features described above. This lead us to identify phenomenologically viable and potentially testable regions of the parameter space where the Sommerfeld enhancement constitutes the dominant radiative correction. In this Section we review our findings, that have been presented in [47]. We start in Sec. 4.5.1 by describing the adopted choices for the points selection, then we present the results in Sec. 4.5.2.

4.5.1 Scan strategy and constraints

We work within the framework of the pMSSM described in Sec. 4.2. In addition to the soft SUSY-breaking universality assumptions (4.10), we furthermore simplify the sfermion sector by adopting a universal sfermion mass parameter M_{sf} . This simplification does not introduce any nontrivial modification of the DM properties, since at the TeV scale in the close-to-wino limit the dominant contribution to the annihilation cross section involve gauge interactions and gauge universality implies equal contributions from all flavours. Therefore, the main effect of introducing more freedom in the sfermion masses can be estimated by a rescaling of the results presented here.²² We are then left with the following real parameters:

$$\mu, M_1, M_2, M_3, A_f, M_{\text{sf}}, M_A, \tan \beta, \quad (4.173)$$

for $f \in \{u, d, e, c, s, \mu, t, b, \tau\}$. The freedom of field reparametrization allows us to assume the signs of $M_2, M_3, M_{\text{sf}}, M_A$ and $\tan \beta$ to be positive, without loss of generality. The remaining mass parameters μ and M_1 , and the trilinear couplings A_i can either be positive or negative. Within this framework we perform dedicated scans over the parameters, with ranges collected in Table 4.7. The ranges are chosen to be as wide as possible within the theoretically and experimentally allowed windows, according to the limitations of our formalism discussed in Sec. 4.4.1 and to the constraints described in the following Section. The upper bounds correspond to the reach of the decoupling limit, such that no qualitative change in the phenomenology is observed for larger values. The most important parameters are the ones in the first block, and the corresponding ranges reflects the aim at studying the wino-like DM at the TeV scale. The

²²We note however that the accuracy of a simple rescaling is reduced for larger LSP Higgsino fraction, as the coupling of the sfermions with the Higgsino is Yukawa-type, and therefore discriminates the three generations, as well as squarks from sleptons. A more detailed study of the Higgsino-like neutralino LSP is left for a future investigation.

| Parameter | Range |
|-----------------|--------------------------|
| M_2 | 1 – 5 TeV |
| $ M_1 - M_2$ | 0 – 500 GeV or decoupled |
| $ \mu - M_2$ | 0 – 500 GeV or decoupled |
| M_{sf} | 1.25 M_2 – 12 TeV |
| M_A | 0.5 – 10 TeV |
| $\tan\beta$ | 5 – 30 |
| $ A_f $ | 0 – 8 TeV |
| M_3 | decoupled |

Table 4.7: Ranges of pMSSM parameters adopted in the various scans. For the trilinear couplings we denote $f \in \{u, d, e, c, s, \mu, t, b, \tau\}$, while “decoupled” parameters were fixed to a multiple of M_2 (usually 2 or 3, see the descriptions of single scans for details).

lower bound on M_{sf} is set to avoid accidental co-annihilations, as explained in Sec. 4.4.1, while the one on $\tan\beta$ is chosen to ease the satisfying of the constraint on the observed light Higgs boson mass, as we will see below. Concerning M_A we recall the constraint (4.159), that we require to avoid s -channel resonances. The gluino mass M_3 plays no role in our scenario, as we do not consider its co-annihilation. We can therefore safely decouple it to a multiple of the wino mass parameter.

In the remaining of this Section we discuss the implementation of the experimental and theoretical constraints that we imposed to all the points of our scan, and comment on their relevance on limiting the ranges of the MSSM parameters, in particular in the wino-like region. All the involved quantities are computed with the use of `FeynHiggs` and `micrOMEGAs` [59, 153]. As expected, many current collider and flavour constraints do not limit the region of the parameter space where the neutralino LSP is at the TeV scale, nevertheless we include all possibly relevant constraints for completeness.²³ We choose not to include any experimental limits coming from indirect detection or CMB, as these are subject to large systematic uncertainties, the discussion of which goes beyond the scope of our work but should be addressed in the future.

²³We do not discuss in the following additional constraints that are not relevant at all for TeV-scale models, such as the $\mathcal{O}(100\text{ GeV})$ lower bounds on charged sparticles masses from LEP [154], more recent bounds from the ATLAS analysis after LHC Run 1 [155], and the invisible width of the Z boson.

Higgs mass We require that the light Higgs mass m_{h^0} lies within 4% deviation of the measured central value $125.09 \pm 0.21 \pm 0.11$ GeV, from the combination of ATLAS and CMS data [156]. The approximate formula for the Higgs mass at one-loop level reads [157, 158]

$$m_{h^0}^2 \simeq m_Z^2 \cos^2 2\beta + \frac{3}{4\pi^2} \frac{m_t^4}{v^2} \left[\log \frac{M_{\text{sf}}^2}{m_t^2} + \frac{X_t^2}{M_{\text{sf}}^2} \left(1 - \frac{X_t^2}{12 M_{\text{sf}}^2} \right) \right], \quad (4.174)$$

where the stop mixing parameter X_t is related to the top quark trilinear coupling

$$A_t = X_t + \frac{\mu}{\tan \beta}. \quad (4.175)$$

From the above expression for $m_{h^0}^2$ we deduce that the main implication of the Higgs mass constraint is to impose that $\tan \beta \gtrsim 5$, such that $\cos^2 2\beta$ is close to 1 and the tree-level value is maximal. Even when this is case, the loop correction has to be large enough to raise the Higgs mass from m_Z up to $\simeq 125$ GeV. This requires that either the stop masses are a few TeV, or the stop mixing is large. The first condition is often satisfied in the scenarios we consider, and when not the trilinear coupling A_t can easily be chosen such that this constraint is satisfied, without affecting the result for the relic density. In our numerical analysis we adopt the two-loop result for the Higgs mass which we calculate using `FeynHiggs`.²⁴

ρ parameter We require that the Δ_ρ contribution from SUSY to the SM value of the ρ parameter does not exceed two standard deviations from the SM expectation [51]:

$$\rho_0 = 1.0004 \pm 0.00024, \quad \text{therefore} \quad \Delta_\rho < 0.00048. \quad (4.176)$$

Since the SUSY contribution can be large only when there exist large mass splitting in the sfermion $SU(2)$ doublets [160], and in the scenario we consider all the sfermions doublets are taken to be nearly degenerate, it does not have significant impact on our parameter space.

$b \rightarrow s\gamma$ In many MSSM scenarios this branching ratio provides strong constraints, as the contribution from broken SUSY is generically large, while the SM prediction is compatible with measurement. The experimental [161] and SM theory [162] values that we use, with the correspondent uncertainties, are

$$\begin{aligned} \mathcal{B}^{\text{exp}}(\bar{B} \rightarrow X_s \gamma) &= (3.37 \pm 0.23) \times 10^{-4}, \\ \mathcal{B}^{\text{SM}}(\bar{B} \rightarrow X_s \gamma) &= (3.15 \pm 0.23) \times 10^{-4}. \end{aligned}$$

²⁴We note that the resummation of logarithmic corrections arising due to the large hierarchy between the top and the stop masses, not included in `FeynHiggs`, would lead to large corrections beyond $M_{\text{sf}} \simeq 6 - 7$ TeV, such that the allowed 4% window may be slightly below the estimation of the theoretical uncertainties [159]. This has however no impact on our analysis, since the value of A_t can be tuned to reproduce the correct Higgs mass leaving the relic density unaltered.

The SUSY contribution $\Delta\mathcal{B}(\bar{B} \rightarrow X_s\gamma)$ is computed with `FeynHiggs` and the implemented criterion reads

$$\left[\left(\mathcal{B}^{\text{SM}}(\bar{B} \rightarrow X_s\gamma) + \Delta\mathcal{B}(\bar{B} \rightarrow X_s\gamma) \right) - \mathcal{B}^{\text{exp}}(\bar{B} \rightarrow X_s\gamma) \right]^2 < (3\sigma^{\text{exp}})^2 + (\sigma^{\text{SM}})^2 . \quad (4.177)$$

There are three classes of diagrams which contribute to $b \rightarrow s\gamma$ in the MSSM, involving either charged Higgs bosons, charginos or gluinos [163]. The first always interfere constructively with the SM contribution, and decouple as the heavy Higgs mass increases beyond the TeV scale. The chargino contribution can take either sign, depending on the sign of μ and A_t , and also decouples with increasing $|\mu|$ and M_2 . The gluino diagrams also take either sign, but do not decouple as $|\mu|$ increases. Because the gluino does not affect the dark matter phenomenology, the contribution of gluino diagrams can in general be adjusted to compensate the contributions of the charginos and charged Higgses ones. Those cancellations ensures that at the TeV-scale relevant to this study, this constraint does not have a large impact on the available parameter space.

$B_s \rightarrow \mu^+\mu^-$ The correction to $B_s \rightarrow \mu^+\mu^-$ from SUSY should also lie within the errors from the experimental measurement and the SM calculation. To this end, we check whether the result of the calculation in the MSSM [160] is consistent with the combined CMS and LHCb result, $(2.9 \pm 0.7) \times 10^{-9}$ [164]. The three-sigma error on the experimental result is added to the uncertainty on the theoretical result in quadrature, where the updated SM prediction is $(3.56 \pm 0.30) \times 10^{-9}$, using latest values on the B_s^0 lifetime and relative B_s^0 decay width difference [164, 165]. We note that as we consider the wino-like region with masses of the LSP of $\mathcal{O}(\text{TeV})$, and masses of the heavy Higgs bosons also of $\mathcal{O}(\text{TeV})$, this constraint does not have much influence on our parameter space. Another related constraint is of course the branching ratio of $B \rightarrow \tau\nu$, measured precisely at the B-factories [166, 167]. However, we do not consider this constraint as the parameter space of interest in our analysis, in particular the large masses of the charged Higgs bosons and values of $\tan\beta$, do not result in MSSM contributions beyond the combined experimental and theoretical uncertainty [168].

$g_\mu - 2$ We require that the Δa_μ contributions to the muon anomalous magnetic moment $a_\mu = \frac{g_\mu - 2}{2}$ do not exceed the experimental value, but do not insist on explaining the deviation between the SM value and the experimental one.²⁵ The experimental and SM theory values adopted are given by [51],

$$\begin{aligned} a_\mu^{\text{exp}} &= (1165920.91 \pm 0.63) \times 10^{-9} , \\ a_\mu^{\text{SM}} &= (1165918.03 \pm 0.48) \times 10^{-9} , \end{aligned}$$

²⁵The experimentally measured value, if confirmed, would indeed provide strong constraints on the pMSSM spectrum, favouring in particular sub-TeV scale models. A lower bound $m_{\tilde{\mu}_1} \lesssim 1 \text{ TeV}$ on the mass of the light smuon was found under this assumption in [155].

and we require

$$-\sigma^{\text{exp-SM}} < \Delta a_\mu < (a_\mu^{\text{exp}} - a_\mu^{\text{SM}}) + \sigma^{\text{exp-SM}} , \quad (4.178)$$

where for the error on the difference between experimental and SM values we take

$$\sigma^{\text{exp-SM}} = \sqrt{(3\sigma^{\text{exp}})^2 + (\sigma^{\text{SM}})^2} . \quad (4.179)$$

Note that as the SUSY contribution is proportional to $\tan \beta$ and inversely proportional to the square of the masses of the sparticles, it is typically strongly suppressed in the region of interest where M_{sf} lies at the TeV scale.

Direct Detection We require that the DM-nucleon spin-independent cross section σ^{SI} is below twice the 2014 LUX limit [136]. The theoretical prediction of σ^{SI} is obtained using the separate DM cross sections for scattering off a proton and a neutron computed by `micrOMEGAs`, according to

$$\sqrt{\sigma^{\text{SI}}} = \sum_i f_i \left(\frac{Z_i}{A_i} \sqrt{\sigma_p^{\text{SI}}} + \frac{A_i - Z_i}{A_i} \sqrt{\sigma_n^{\text{SI}}} \right) , \quad (4.180)$$

where the sum, with appropriate weights f_i , is over the different atomic species constituting the detector (^{129}Xe in the case of LUX). We require

$$\sigma^{\text{SI}} < 2 \times \left(\frac{\Omega h^2|_{\text{tree}}}{\Omega h^2|_{\text{exp}}} \right) \sigma_{\text{exp}}^{\text{SI}} , \quad (4.181)$$

where $\sigma_{\text{exp}}^{\text{SI}}$ is the LUX result, whose dependence on m_χ has been obtained by interpolating the plot in [136]. The spin-independent cross section is sensitive to the Higgs exchange between the LSP and the quarks of the nucleon. The interaction with the Higgs relies on the LSP having both a gaugino and a Higgsino component, and therefore this constraint is most relevant for the scenarios we study where $|\mu| \sim M_2$. Note that limits on the spin-dependent cross section coming from direct detection experiments and neutrino signals from the Sun are always much weaker than those coming from spin-independent results for our scenarios, and therefore we can safely neglect them.

Finally, in addition to the experimental constraints discussed above, we require theoretical consistency of the electroweak symmetry breaking by studying the scalar potential.

Higgs potential The scalar potential has to be free from charge and/or color breaking minima (CCB). For the potential at the tree level the corresponding criteria read [169, 170]

$$A_t^2 < 3 \left(\cos^2 \beta M_A^2 + \frac{m_Z^2}{2} \cos 2\beta + 2M_{\text{sf}}^2 \right) ,$$

$$A_{b(\tau)}^2 < 3 \left(\sin^2 \beta M_A^2 - \frac{m_Z^2}{2} \cos 2\beta + 2M_{\text{sf}}^2 \right). \quad (4.182)$$

One can always choose the trilinear couplings low enough that CCB constraint is satisfied without changing the neutralino properties.

4.5.2 Results

In this Section we describe the results of the scan presented in [47]. We discuss separately the different ways of departing from the pure-wino scenario, obtained by lowering the sfermion, the Higgsino, or the bino mass parameter. Those three cases refer to dedicated scans, in which for clarity we fixed the marginally relevant parameters to benchmark values. We conclude this Section with a discussion on the residual dependence of the relic density on those parameters.

Impact of sfermions

In the pure-wino scenario the dark matter pair-annihilation proceeds via s -channel exchange of gauge and Higgs bosons only. On the contrary, the annihilation into two SM fermions of wino-like neutralino in the MSSM receives contributions from diagrams with t - and u -channel sfermion exchange. The magnitude of those contributions, which vanish in the sfermion decoupling limit, increases for smaller sfermion masses. The presence of light sfermions in the spectrum also affects directly the neutralino relic density through additional co-annihilations entering the calculation of $\langle \sigma_{\text{eff}} v \rangle$. Finally, an indirect effect comes from the loop corrections to the neutralino and chargino masses.

As we already explained, the sfermion co-annihilation is beyond the scope of this work and we make sure that its effect is negligible for the models we study by considering only points with sfermions more than 25% heavier than the LSP. The indirect effect of modifying the spectrum turns out to be subdominant even close to the Sommerfeld resonance, since the diagrams with sfermions in the loop are suppressed compared to those with gauge bosons due to the large sfermion masses.

The additional t - and u -channel diagrams contributing to the annihilation into SM fermions introduce, on the other hand, large modifications. Because of the helicity suppression of the direct LSP annihilation to fermion pairs, the additional diagrams are particularly relevant for the co-annihilation process (e.g. $\chi_1^+ \chi_1^- \rightarrow f \bar{f}$, $\chi_1^0 \chi_1^\pm \rightarrow f' \bar{f}$), in which they interfere destructively with the s -channel exchange ones [171]. As a result, lowering the sfermion mass parameter M_{sf} while keeping M_2 fixed, leads to a reduction of the effective annihilation cross section. Because of the approximate quadratic dependence of the relic density on the LSP mass (1.19), a smaller cross section requires a smaller $m_{\chi_1^0}$ to keep the relic density constant. This effect can clearly be observed in the left panel of Fig. 4.8, where the contours of constant *perturbative* relic density

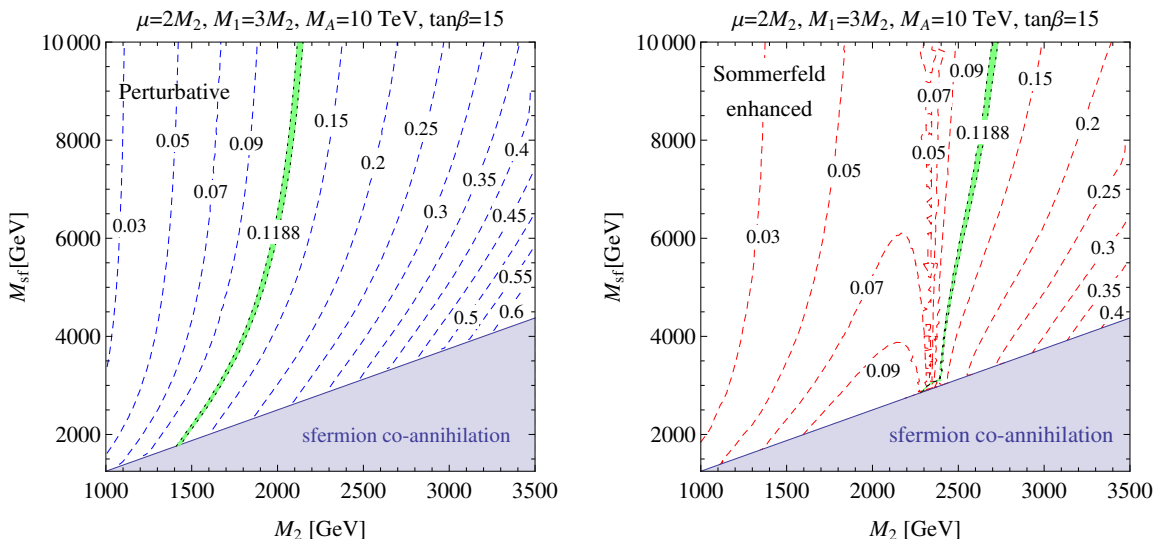


Figure 4.8: The contours of constant relic density: perturbative (left) and Sommerfeld enhanced (right). The green bands show the region within 2σ of the observed dark matter abundance. The blue area indicates region in parameter space where the co-annihilations with sfermions are potentially relevant and which is not studied in this work. Other parameters are as indicated, with $M_3 = 3M_2$ and $A_i = 8$ TeV except for A_t , which is fixed by the measured Higgs mass.

move towards lower values of M_2 ,²⁶ as M_{sf} decreases.²⁷ The approximate quadratic dependence of $\Omega h^2|_{\text{pert}}$ on M_2 also explains why the contours become denser for larger wino mass. In the upper part of the plot, corresponding to large sfermion masses, the contours flatten out as the decoupling limit is approached. We define the pure-wino limit for $M_{\text{sf}} = 20$ TeV, in which case we find that the correct perturbative relic density is obtained for $m_{\chi_1^0} \simeq 2.22$ TeV. It is important to note that, departing from this simple scenario by lowering the sfermion masses, one can obtain the correct perturbative relic abundance over a large range (~ 800 TeV) of LSP masses, going down roughly to values as low as 1.4 TeV.

The situation becomes more involved when the Sommerfeld enhancement is included, as shown in the right panel of Fig. 4.8. The main features that we encountered in the perturbative case are still present, but two important modifications arise. First, as a result of generically

²⁶Note that the x -axis of most of our plots is chosen to be M_2 , which in general lies within a few GeV of $m_{\chi_1^0}$ for the considered models.

²⁷This plot, as well as the remaining two described in this paragraph, are based on a dedicated scan in which we decoupled the bino-like (Higgsino-like) neutralino by setting $M_1 = 3M_2$ ($\mu = 2M_2$), and we fixed $M_3 = 3M_2$, $M_A = 10$ TeV, $\tan \beta = 15$ and $A_i = 8$ TeV (except for A_t , which is instead fixed by the observed Higgs boson mass). The residual dependence on those parameters is discussed in a dedicated paragraph at the end this Section.

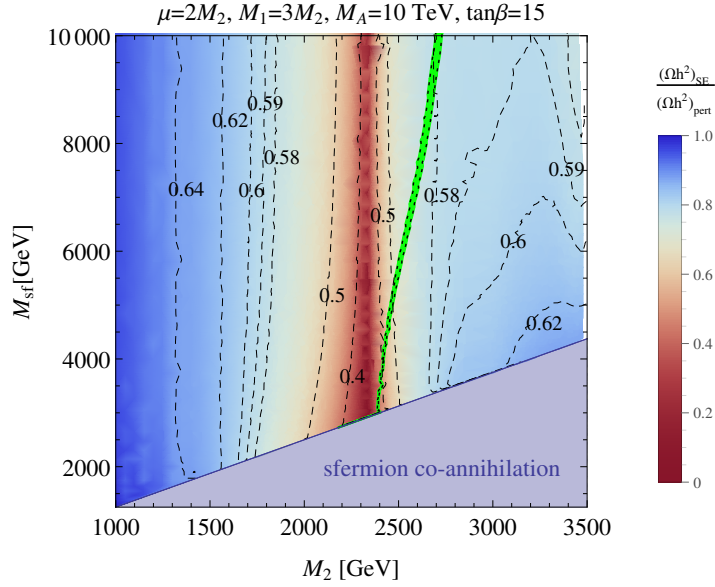


Figure 4.9: The ratio of the relic density including Sommerfeld enhancement to the perturbative result is shown via a density map as well as black dashed contours. The green bands indicate the region within 2σ of the observed dark matter abundance. Other parameters are as indicated, with $M_3 = 3M_2$ and $A_i = 8$ TeV except for A_t , which is fixed by the measured Higgs mass.

larger cross sections, the contours are shifted towards larger values of M_2 . In the pure-wino limit we obtain that the Sommerfeld enhancement pushes the LSP mass giving correct relic abundance from 2.22 TeV up to 2.88 TeV. Lowering the sfermion masses we find wino-like models with the correct abundance and LSP mass down to 2.3 TeV. Second, due to the resonant behaviour of the enhancement, the size of the shift depends in a non-trivial way on the wino mass. The strong dependence of the enhancement factor on the model parameters in the neighbourhood of the resonance is responsible for the high density of contours around $M_2 \simeq 2.3$ –2.4 TeV. In the pure-wino limit the resonance is found at 2.33 TeV, and the relic density is reduced by a factor 3.9, compared to the computation based on the tree-level cross section. The presence of the resonance is most clearly seen in Fig. 4.9, where the impact of the Sommerfeld effect on the relic density is shown, in terms of a density plot with contour lines overlaid. As expected, the reduction of the relic abundance with respect to the perturbative result is generically large in this scenario (above 30%), and it typically grows when increasing the LSP mass, until the resonance is reached. In the resonance region the reduction is nearly an order of magnitude. It is worth stressing that the enhancement is approximately independent on the value of the sfermion masses. This can be easily understood by noting that the largest impact of the Sommerfeld effect comes from its contribution on the $\chi_1^0 \chi_1^0$ annihilation, which does not

depend in any significant way on the nature of the sfermions.

In the following we will see that the generic dependence of the relic density on sfermion masses that we discussed above still holds when one departs from wino-like neutralino by allowing for non-negligible bino- and Higgsino-fractions of the LSP.

Wino-Higgsino co-annihilation

In the previous paragraph we studied the properties of wino-like neutralino models, in which the large hierarchy $M_1, \mu \gg M_2$ results in the decoupling of heavier bino- and Higgsino-like neutralinos. We turn now on to models in which the Higgsino mass parameter is at the same scale as M_2 . As we have seen in Sec. 4.2, the pMSSM spectrum contains in this case three neutralinos and two charginos at nearly the same mass scale. The first obvious implication for the relic density is then the change in relevant number and weights of the co-annihilation channels entering the calculation of $\langle \sigma_{\text{eff}} v \rangle$. Moreover, depending on the difference $|\mu| - M_2$, the wino-Higgsino mixing can be large, resulting in larger Higgsino fraction of the predominantly wino LSP. A second source of change for the relic density arises therefore from the modification of the annihilation cross sections due to the different couplings of the wino and Higgsino component. This effect, which is already present and very well known at the perturbative level, turns out to be even stronger when the Sommerfeld enhancement is considered.

In order to study systematically the departure from the pure-wino scenario when a non-negligible Higgsino component is introduced, we performed a dedicated scan in which we varied μ in the range from $M_2 + 500 \text{ GeV}$, where the Higgsino is decoupled, down to M_2 , where the Higgsino fraction in the LSP reaches 50%.²⁸ To single out the effect of the Higgsino co-annihilation and mixing, we first decouple the sfermions by fixing their common mass parameter to 12 TeV. The results of this analysis are displayed on Figs. 4.10 and 4.11. The impact of lowering the sfermion masses in the mixed wino-Higgsino scenario has then been studied by repeating the same analysis for different values of M_{sf} . The results are displayed on Fig. 4.12.

In Fig. 4.10 the contours of constant relic density are shown in the M_2 vs. $(\mu - M_2)$ plane, in both the perturbative (left) and Sommerfeld enhanced case (right). The left panel closely resembles the corresponding one in Fig. 4.8, meaning that, at the perturbative level, a larger Higgsino fraction suppresses the annihilation cross section. This can be traced back to the smaller coupling to gauge bosons of the Higgsino component, compared to the wino one. Comparing the perturbative result with the full one on the right panel, one observes two main effects: *i*) the contours are shifted to higher masses and exhibit a more pronounced bending for large Higgsino fraction, and *ii*) a resonance is clearly visible for $M_2 \gtrsim 2 \text{ TeV}$. The overall shift of the contours is, again as in the previous paragraph, following from the decrease of the relic density with respect to the perturbative result, due to the Sommerfeld enhancement. It is worth noticing that the shift is smaller for larger Higgsino fraction, resulting in a stronger

²⁸The bino is decoupled with $M_1 = 2M_2$, and the remaining parameters are fixed to their benchmark values as in the previous paragraph.

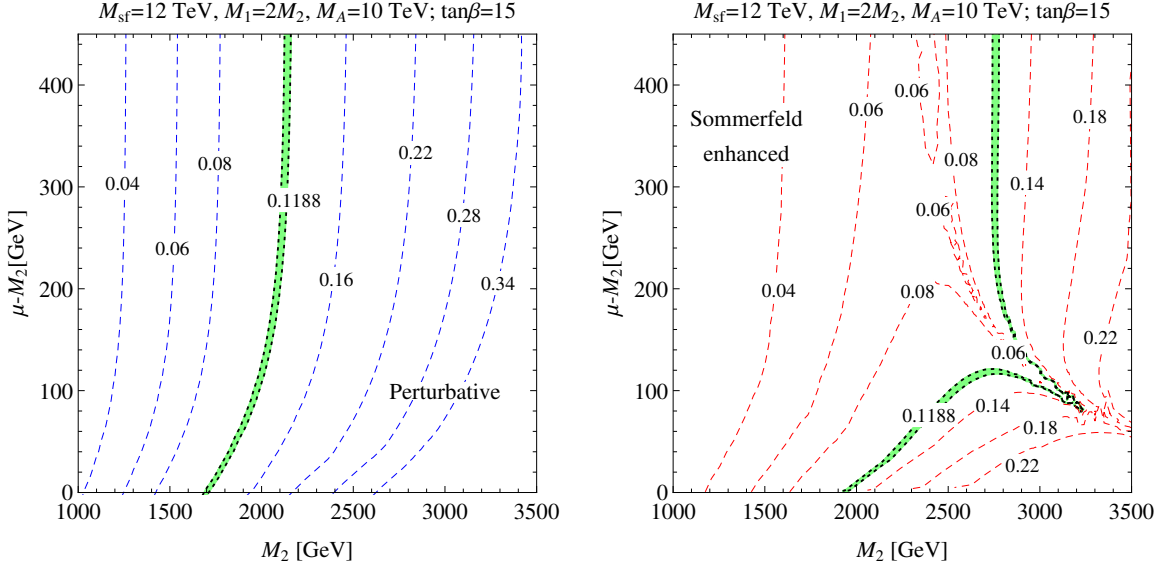


Figure 4.10: Contours of constant relic density are shown for the case of the perturbative (left) and Sommerfeld enhanced (right) calculation. The green bands indicate the region within 2σ of the observed dark matter abundance. Other parameters are as indicated, with $M_3 = 3M_2$ and $A_i = 8$ TeV except for A_t , which is fixed by the measured Higgs mass.

bending of the contours in the lower part of the plot, compared to the perturbative case. This is in agreement with the known fact that the Sommerfeld enhancement is in general smaller for the Higgsino component, mainly due to smaller couplings to gauge bosons and larger mass splitting between the LSP and the lightest chargino. In both plots the contour lines flatten in the upper region, showing that for $\mu - M_2$ larger than ~ 400 GeV the Higgsino effectively decouples and we recover the pure-wino scenario.

The strong suppression of the relic density for resonant annihilation modifies this picture for $M_2 \gtrsim 2$ TeV. The clustering of the contours around the resonance is a manifestation of the strong dependence of the enhancement on the precise values of the parameters. In particular, the actual position of the resonance peak depends on the neutralino composition, as it is most clearly visible in Fig. 4.11, where we show the ratio of the above plots in order to display the impact of the Sommerfeld enhancement over the M_2 vs. $(\mu - M_2)$ plane. We observe that the resonance occurs for heavier LSP as the Higgsino fraction is increased, which is mainly due to the increasing of the mass splitting between the lightest chargino and neutralino (4.24), since the location of the resonance depends on the splitting through $\delta m_{\chi_1^\pm}/m_{\chi_1^0} \alpha_2^2$. The green line, representing points with the correct relic abundance, crosses the resonance around $M_2 \simeq 2.7$ TeV and the resulting deformation reaches nearly 3.3 TeV. This means that the Higgsino co-

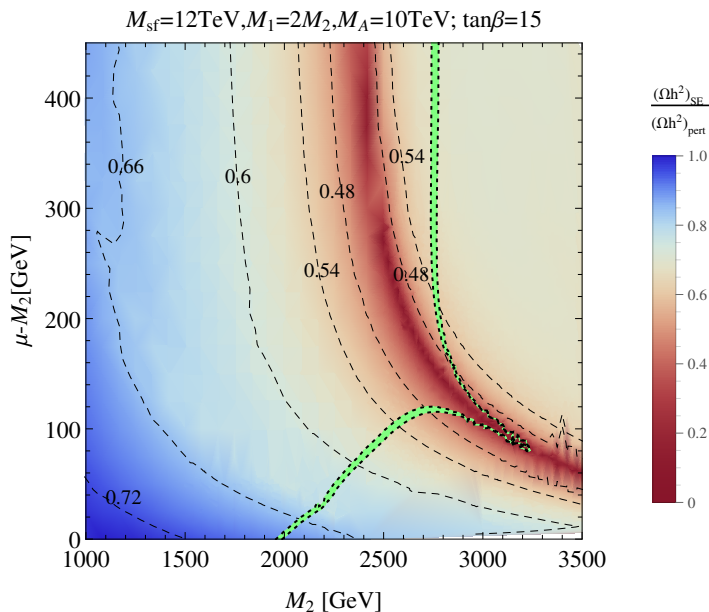


Figure 4.11: The impact of the Sommerfeld enhancement of the relic density shown as a density map as well as via the black dashed contours. The green bands indicate the region within 2σ of the observed dark matter abundance. Other parameters are as indicated, with $M_3 = 3M_2$ and $A_i=8$ TeV except for A_t , which is fixed by the measured Higgs mass.

annihilation allows to obtain the measured relic density for LSP masses up to 20% larger than in the pure-wino scenario. It is worth mentioning that those points, being in very close vicinity to the resonance, are likely to be subjected to strong bounds coming from dark matter indirect detection. So far only the limiting cases of pure-wino and Higgsino have been studied from this perspective with the inclusion of the Sommerfeld effect [111, 172, 173]. A precise analysis of indirect detection constraints on mixed scenarios will be presented in upcoming work [174].²⁹ We also note that, in correspondence of the resonance, for fixed values of $\mu - M_2$ there are three different values of M_2 which give the correct relic density.

The effect of lowering the sfermion masses has been investigated by two additional dedicated scans. The obtained results are summarized in Fig. 4.12, where we compare the contours giving the correct thermal relic density for the three different values of the sfermion mass parameter M_{sf} . We observe that the qualitative behaviour does not change with the introduction of lighter sfermions. Moreover, in agreement with our discussion in the previous paragraph, lowering the sfermion masses results in larger relic density, both for the perturbative and the Sommerfeld-

²⁹The only related works available in the literature [175–177] are considering the Sommerfeld effect in an approximate way and/or without inclusion of recent developments [44–46].

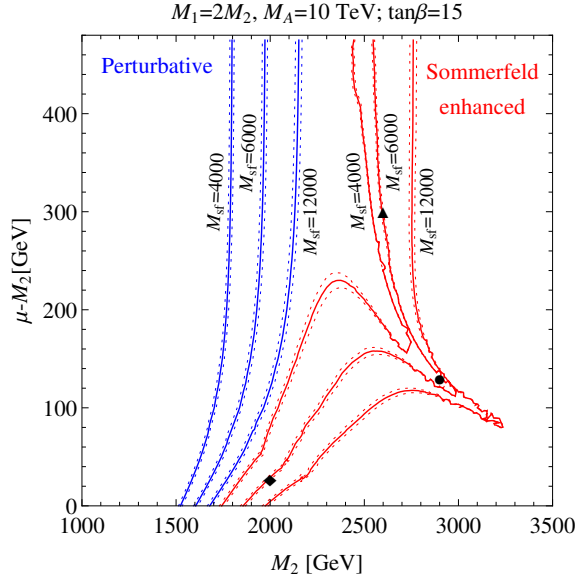


Figure 4.12: Contours providing the correct relic density are shown for the case of the perturbative (blue) and Sommerfeld enhanced (red) calculation for three different values of the common sfermion mass parameter. Other parameters are as indicated, with $M_3 = 3M_2$ and $A_i = 8$ TeV except for A_t , which is fixed by the measured Higgs mass to a different value depending on M_{sf} . The black markers denote the three points studied in Sec. 4.5.2.

enhanced results. As a result, models with dominant wino component but large Higgsino fraction are found giving the correct relic density for masses as low as 1.7 TeV.

Effect of the heavy Higgs bosons

In the analyses presented so far the heavy Higgs bosons have been decoupled by setting the parameter $M_A = 10$ TeV. For smaller values of M_A the heavy Higgs bosons, having positive R-parity, can affect the relic density in the following two ways:

- i.* by contributing to the (co-)annihilation rate via s -channel diagrams, particularly if M_A lies in the vicinity of $2m_{\chi_1^0}$, thereby typically reducing the relic density;
- ii.* by providing additional final states with one heavy Higgs plus one gauge or light Higgs boson, or with two heavy Higgs bosons, if the combined mass of the final state lies below $2m_{\chi_1^0}$, which leads to a reduction in the relic density.

The coupling between a Higgs boson and a pair of neutralinos (and/or charginos) is non-negligible only when one of the two contains a considerable gaugino component and the other

a considerable Higgsino component. The contribution in i . is therefore only relevant in the mixed wino-Higgsino case. As for the point ii ., the heavy Higgs and gauge boson final state is obtained via a s -channel gauge boson, or a t -channel neutralino or chargino. This is again more relevant when the LSP contains some Higgsino admixture, as this also allows the coupling of neutralinos to Z bosons. However, in contrast to the case i ., this contribution does not vanish when the Higgsino decouples, as a co-annihilating chargino and neutralino can annihilate into a heavy Higgs and gauge boson via a s -channel W boson even in the pure-wino limit.

In order to study these issues we performed a dedicated scan in which we varied M_A in the range $\{0.5, 10\}$ TeV. In order to have a substantial wino-Higgsino admixture we fixed $\mu = M_2 + 25$ GeV. The bino and the sfermions are decoupled by choosing $M_1 = 3M_2$ and $M_{\text{sf}} = 12$ TeV respectively, and the remaining parameters are fixed to the benchmark values. The results are displayed in Fig. 4.13, where we show contours of constant relic density in the M_2 vs. M_A plane both at the perturbative level (left) and on taking account of the Sommerfeld effect (right). We note that, as discussed in Sec. 4.4.1, we do not allow values of M_A inside the interval $1.7\text{--}2.3 m_{\chi_1^0}$, where resonant annihilations would occur. This accounts for the excluded region in the middle of the plots. For the perturbative case we note that above this excluded region the lines are approximately vertical, just bending slightly towards higher values of M_2 on approaching this region. Below the excluded area we find that there is a slight shift to the right as the heavy Higgs bosons are accessible in the final state. The difference in M_2 giving the correct relic density is approximately 150 GeV when M_A changes from 10 TeV to 500 GeV. For the Sommerfeld-enhanced case the result is qualitatively similar, however the difference in M_2 giving the correct relic density is around 250 GeV for the same change of M_A .

In Fig. 4.14 we further investigate the effect of the heavy Higgs bosons on the contours showing the correct relic density in the M_2 vs. $(\mu - M_2)$ plane. The blue lines show the perturbative result while the red lines include the Sommerfeld enhancement. We see that on decreasing M_A from 10 TeV to 800 GeV, the shift in the value of M_2 giving the correct density is indeed dependent on the proximity of μ to M_2 , increasing from 50 to 150 GeV in the perturbative case and 100 to 250 GeV in the Sommerfeld-enhanced case. As mentioned earlier, an increased Higgsino admixture allows a stronger coupling to the Higgs and Z bosons in the s -channel (where Z bosons can give rise to heavy Higgs bosons in the final state), increasing the effect of the heavy Higgs boson. Nevertheless when the Higgsino is decoupled a dependence on M_A persists; for the $M_A = 800$ GeV contours co-annihilation via a W boson to a final state containing a heavy Higgs boson and a gauge boson is allowed but not for the $M_A = 10$ TeV contours.

Wino-bino co-annihilation

In this Section we study the effect of allowing for a small bino mass parameter $M_1 \simeq M_2$. We only consider the case $M_1 > 0$ since, as we have seen in Sec. 4.2.1, for $M_1 < 0$ the bino is essentially decoupled. Because the wino-bino mixing proceeds via the off-diagonal term in the

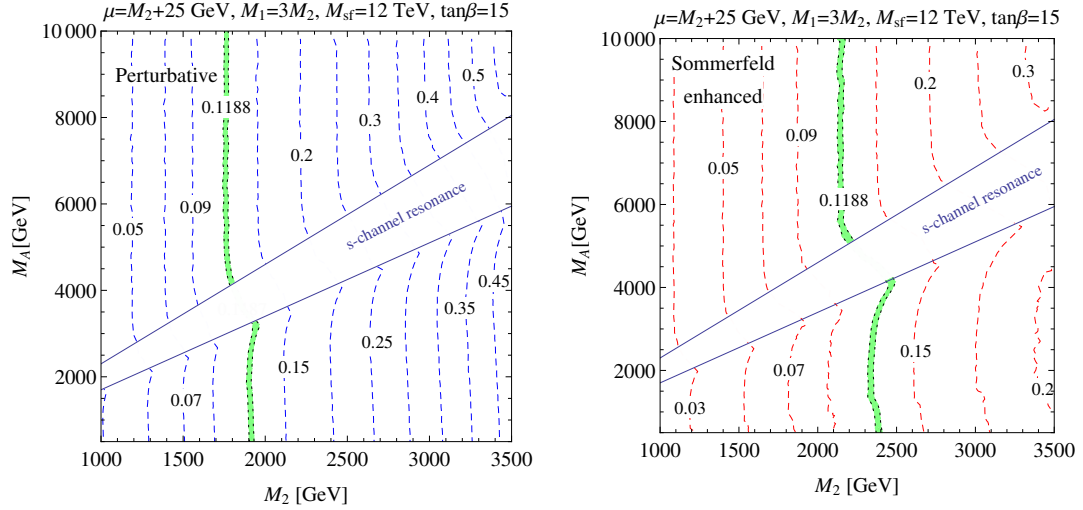


Figure 4.13: Contours of constant relic density are shown for the case of the perturbative (left) and Sommerfeld enhanced (right) calculation. The (green) bands indicate the region within 2σ of the observed dark matter abundance. Other parameters are as indicated, with $A_i = 8$ TeV and X_t is fixed by the measured Higgs mass.

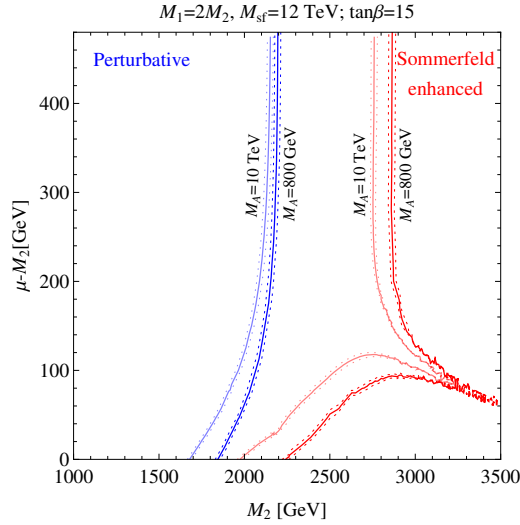


Figure 4.14: Contours providing the correct relic density are shown for the case of the perturbative (blue) and Sommerfeld enhanced (red) calculation for three different values of the heavy Higgs mass M_A . Other parameters are as indicated, with $A_i = 8$ TeV and X_t is fixed by the measured Higgs mass.

Higgsino block of the neutralino mass matrix, to obtain substantial mixing in the decoupled Higgsino scenario a high degeneracy between M_1 and M_2 is required. For example, for $\mu = 2 M_2$ and $\tan \beta = 15$, the mixing is about 1% when $\delta M_1 = 10$ GeV and decreases to 0.1% when $\delta M_1 = 100$ GeV. For smaller values of the Higgsino parameter μ the same wino-bino mixing is obtained at larger splitting $M_1 - M_2$. Furthermore, the mixing is sensitive to $\tan \beta$ and the sign of μ . Due to the larger sensitivity of the results to many parameters, in order to provide a detailed investigation of the wino-bino co-annihilation scenario we proceeded in several steps:

- i.* we study the contours of constant relic density as in the previous paragraphs. For this scan we decouple the Higgsino at $\mu = 2M_2$, fix the sfermion mass to $M_{\text{sf}} = 4$ TeV and the remaining parameters to our benchmark values. The results are displayed on Figs. 4.15 and 4.16;
- ii.* we investigate the impact of the sfermions by repeating the analysis for two different values of M_{sf} and comparing the contours of correct relic density in Fig. 4.17;
- iii.* the impact of $\tan \beta$ and the sign of μ is investigated by performing additional dedicated scans. In all cases we consider decoupled sfermions ($M_{\text{sf}} = 12$ TeV) and the results are displayed on Fig. 4.18;
- iv.* the departure from the decoupled Higgsino case is finally studied by repeating the analysis (again with decoupled sfermions) for four additional values of μ , down to $\mu = 1.1M_1$, see Fig. 4.19.

Contours of constant relic density in the M_2 vs. $(M_1 - M_2)$ plane from the scan described at the point *i.* are displayed in Fig. 4.15, both for the perturbative (left) and Sommerfeld enhanced case (right). Note that the logarithmic scale for the y -axis, chosen due to the very weak mixing between the bino and the wino unless $(M_1 - M_2)$ is very small, changes the appearance of the resonance with respect to the Higgsino case, even though the qualitative behaviour is largely the same. However, for the Sommerfeld enhanced results a difference in the shape also exists due to the different mixing behaviour: the splitting in this case is inversely proportional to the Higgsino parameter μ rather than M_2 , and therefore as maximal mixing is reached the result is independent of M_1 . The strength of the enhancement is studied in Fig. 4.16, where we show the ratio between the relic densities on the right and left panels of Fig. 4.15. The contour with correct relic density for the full calculation including the Sommerfeld enhancement is given by the green line. We observe that the maximal effect of the Sommerfeld enhancement is indeed in the region where the relic density agrees with observation, in particular when the difference between M_1 and M_2 is below approximately 10 GeV. The Sommerfeld enhanced relic density in agreement with that observed is reduced by 70%, compared to the perturbative result. Note that over the entire region covered by the plot the effect of the Sommerfeld enhancement is larger than 30%.

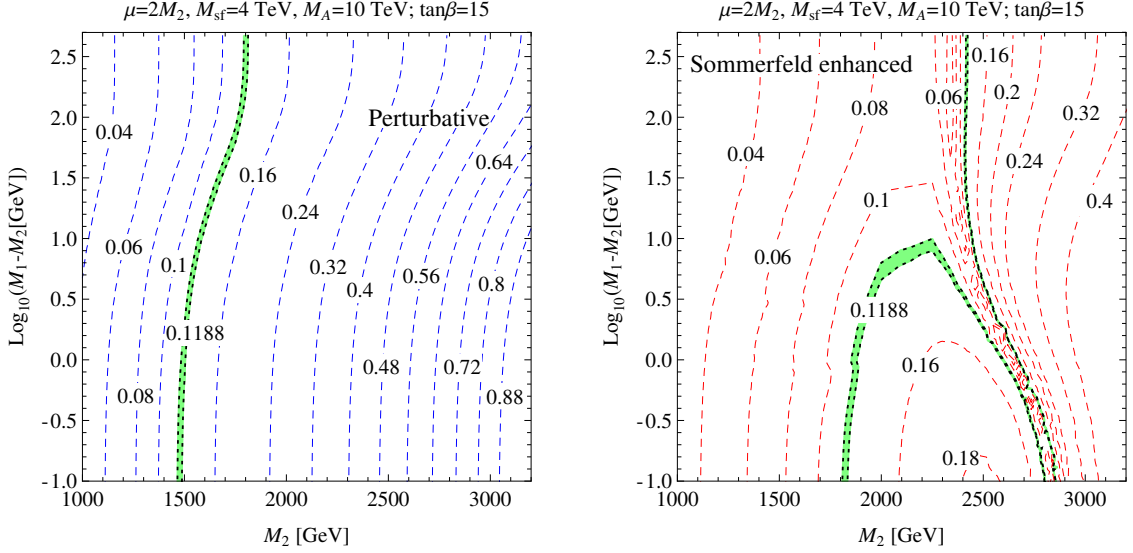


Figure 4.15: Contours of constant relic density are shown for the case of the perturbative (left) and Sommerfeld enhanced (right) calculation. The green bands indicate the region within 2σ of the observed dark matter abundance. Other parameters are as indicated, with $M_3 = 3M_2$ and $A_i=8$ TeV except for A_t , which is fixed by the measured Higgs mass.

As introduced in *ii.*, we show in Fig. 4.17 contours with the correct relic abundance for three choices of the sfermion mass parameter. The results again resemble the Higgsino admixture case, up to differences already commented on. Note in particular that, around the resonance region, the effect of the sfermion masses is less pronounced than elsewhere. For the given benchmark choice of the other parameters, we observe that the lowest mixed wino-bino neutralino mass giving the observed relic density is around 1.8 TeV (for $M_{\text{sf}} = 4$ TeV), which is marginally higher than the wino-Higgsino case. The highest value of 2.9 TeV (for $M_{\text{sf}} = 12$ TeV) is instead lower than the 3.3 TeV we observed in Fig. 4.12.

The dependence of our results on the value of $\tan\beta$ and the sign of μ , that we investigated as introduced in *iii.*, is displayed in Fig. 4.18, where the contour of correct relic density from the previous analysis (solid black line, corresponding to the benchmark choices $\tan\beta = 15$ and $\mu > 0$) is compared to the results of three additional analyses (in all cases we set $M_{\text{sf}} = 12$ TeV). We observe that outside the resonance region the result is not affected by the different choices of the parameters, and the four lines overlap for splittings above a few tens of GeV. On the contrary, large deviations among the different scenarios are seen in the resonant region. The milder effect is obtained when $\tan\beta$ is increased to 30 (dot-dashed red line), showing that a value of 15 is already close to the decoupling limit for $\tan\beta$. Considerably stronger is on the other hand the modification produced by lowering $\tan\beta$ to 5 (dashed blue line), in which case

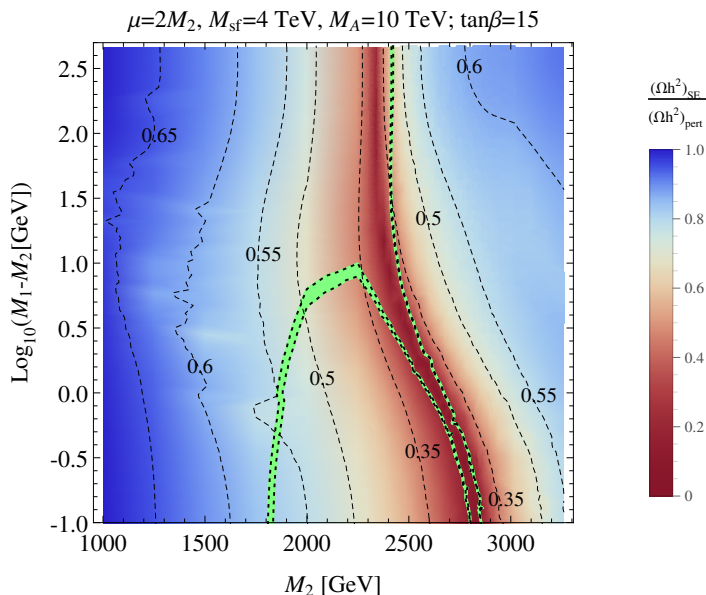


Figure 4.16: The impact of the Sommerfeld enhancement of the relic density shown as a density map as well as via the black dashed contours. The green bands indicate the region within 2σ of the observed dark matter abundance. Other parameters are as indicated, with $M_3 = 3M_2$ and $A_i = 8$ TeV except for A_t , which is fixed by the measured Higgs mass.

the resonance is pushed to higher values of M_2 as a result of the larger mass splitting of the lightest chargino (4.27) and (4.28). Finally, choosing a negative value of μ (dotted green line, with $\tan\beta = 15$ as in the benchmark case), moves the resonance towards smaller values of M_2 , as a result of the reduced mass splitting obtained in this case.

We conclude this paragraph with the results from the investigation on the impact of μ , introduced in *iv.*. The contour of correct relic density is plot in Fig. 4.19, for five different choices of μ , ranging from $2M_1$ (solid black line) down to $1.1M_1$ (solid blue line). The main effect of lowering μ consists in moving the resonance to larger values of the wino mass, again as expected from the increasing of the lightest chargino mass splitting (4.27). We also note that the contour for $\mu = 1.1M_1$ bears a closer resemblance to the wino-Higgsino case (most easily seen in a linear plot, not shown here). Due to the presence of the resonance, it appears that by making an appropriate choice in μ and M_1 the entire region of the plot could be covered, at least for values of M_2 from 2.1 TeV up to 4.2 TeV if not even higher. All these points would be on or around the resonance, having implications for indirect detection.

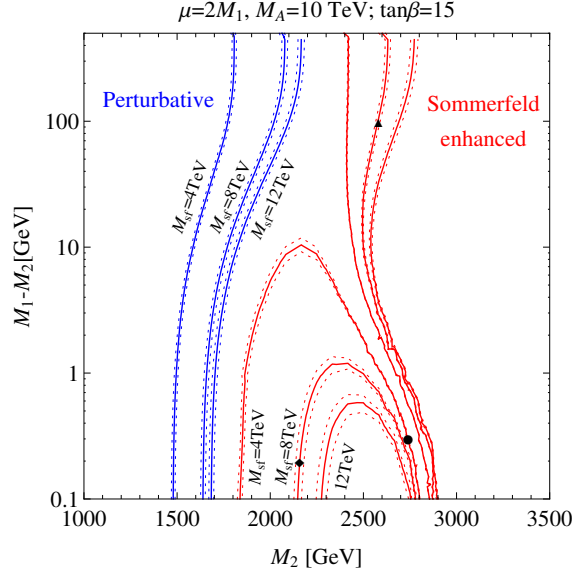


Figure 4.17: Contours of correct relic density: perturbative (blue) and Sommerfeld enhanced (red) are shown for 3 different values of the sfermion mass parameter. Other parameters are as indicated, with $M_3 = 3M_2$ and $A_i = 8$ TeV except for A_t , which is fixed by the measured Higgs mass. The black markers denote the three points studied in Sec. 4.5.2.

Residual dependence on other parameters

In the dedicated scans that we described in the previous paragraphs we focused on the dependence of the wino-like relic density on a few central parameters (e.g. M_2 , μ , M_{sf} and M_A , in the wino-Higgsino scenario), while we fixed the remaining ones to some benchmark values. In this paragraph we justify this choice by examining the sensitivity to the remaining parameters and showing that it is subdominant.

To this end we choose six wino-like points from our previous analysis, three of which contain Higgsino admixtures and three bino admixtures of varying degree. These points are marked (up to signs in μ , M_1) in Figs. 4.12 and 4.17 by a triangle, a circle and a diamond. For each of these points we fix the values of the central parameters and compute the relic density for 1000 different realizations of the remaining parameters with ranges given in Table 4.7 and a uniform random distribution before the constraints are imposed. The results are displayed in Fig. 4.20, as histograms of the % of points in bins of $\Omega h^2 / \langle \Omega h^2 \rangle$, where $\langle \Omega h^2 \rangle$ is the mean value of the relic density, both for the perturbative and the full calculation. The left (right) hand plots from top to bottom corresponds to the points marked in Fig. 4.12 (4.17) by the triangle, circle and diamond respectively, such that the bino (Higgsino) component increases from top to bottom panels.

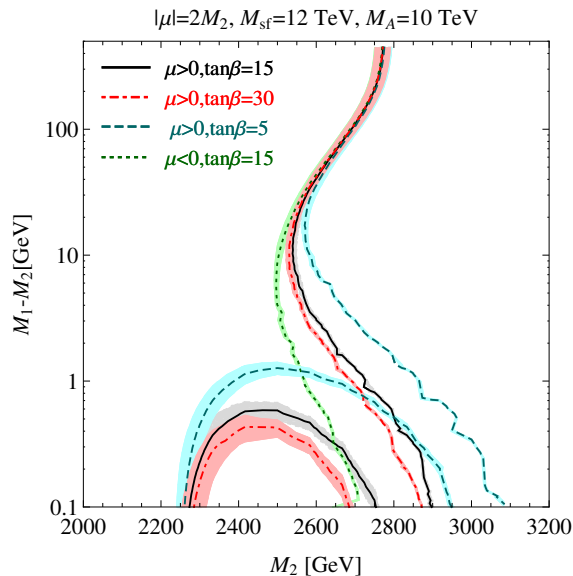


Figure 4.18: The contours of correct relic density for different choices of $\tan\beta$ and the sign of μ . Other parameters are as indicated, with $M_3 = 3M_2$ and $A_i=8$ TeV except for A_t , which is fixed by the measured Higgs mass.

First consider the perturbative result, shown as blue histograms. We see that in all cases the distribution is strongly peaked near the central value. The sensitivity to the other parameters increases with the departure from pure-wino limit (top to bottom panels), but the variations are of order of a few percent at most. The situation changes when considering the Sommerfeld enhanced results, as all the distributions become broader and asymmetric. This occurs because the Sommerfeld effect is sensitive to the values of the neutralino mass, couplings and mass splitting with the chargino, which are (slightly) depending on the remaining MSSM parameters. As we have seen, this effect is expected to be particularly large close to the resonance region. Indeed, the broadening of the full result with respect to the perturbative one is strongest in the middle panels (circle benchmark points, in the vicinity of the resonance) and in the upper left-hand one, which point is not far from the resonance as well. Asymmetry in the distributions is caused by the fact that deviations around central parameters may go towards or away from the resonance, leading to larger or smaller Sommerfeld effect respectively. The bottom line of this analysis is that away from the resonance the residual MSSM parameters have a very mild impact, justifying our choice of central parameters, while in the vicinity of the resonance regions the variation is very significant.

To further study the impact of the residual parameters, we performed two additional scans, consisting of a large number of points (50000 and 90000 for the Higgsino and bino case, respec-

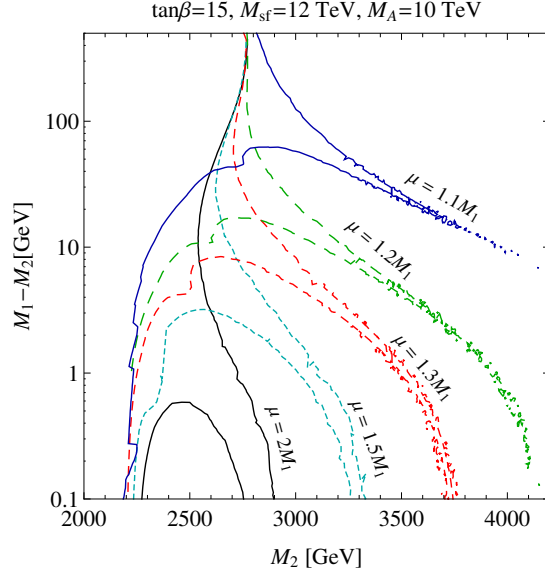


Figure 4.19: Contours of correct relic density for different values of μ . Other parameters are as indicated, with $M_3 = 3M_2$ and $A_i = 8$ TeV except for A_t , which is fixed by the measured Higgs mass.

tively), where we considered the wino mass in the range $M_2 \in \{1, 3.5\}$ TeV. Our choices for the central parameters in the Higgsino case are:

$$\mu \in \{M_2, M_2 + 0.5 \text{ TeV}\}, \quad |M_1| = 2.01M_2, \quad M_{\text{sf}} = 6 \text{ TeV}, \quad (4.183)$$

and in the bino case:

$$|M_1| \in \{M_2, M_2 + 0.1 \text{ TeV}\}, \quad |\mu| = 2M_1, \quad M_{\text{sf}} = 8 \text{ TeV}. \quad (4.184)$$

The other parameters were sampled randomly within the ranges in Table 4.7.³⁰ The results are displayed in Fig. 4.21, where we only show those points where either the perturbative (blue) or the Sommerfeld enhanced (red) relic density lies within 2σ from the central value (1), namely $\Omega h^2 \in \{0.1168, 0.1208\}$. The selected points are overlaid on the relevant contours from Figs. 4.12 and 4.17 for the Higgsino and bino case respectively. For the wino-Higgsino case (upper panel), in order to isolate those points in proximity of the heavy Higgs funnel region and study the effect of the sign of M_1 on the lightest neutralino/chargino mass splitting, we

³⁰In order to make it more likely for the constraint on the observed Higgs mass to be satisfied, we actually replaced A_t by $x_t \equiv x_t/M_{\text{sf}}$ and sampled it in the range $\{0.5, 3\}$. Moreover, we fixed the gluino mass parameter as $M_3 = 2M_2$ and we moved the lower limit for M_A to 1 TeV. As already discussed, both A_t and M_3 have no impact at all on the relic density in the considered scenarios.

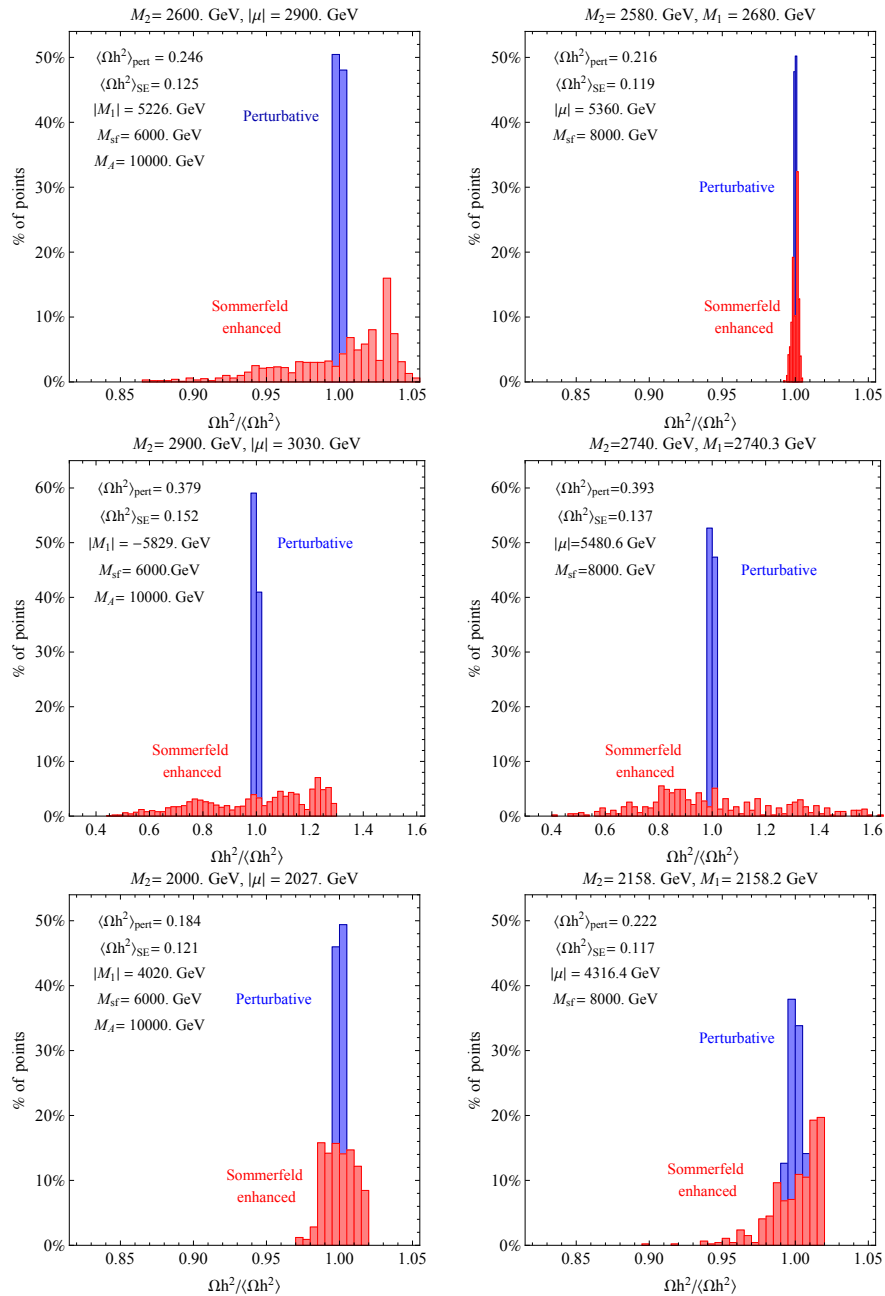


Figure 4.20: Histograms showing the impact of the remaining parameters on the relic density for wino-like LSPs with a varying Higgsino (left) and bino (right) admixtures. The relic density is normalised to the mean for each case respectively.

have divided the points according to whether $2.3m_{\chi_1^0} < M_A < 2.5m_{\chi_1^0}$ (cross), $M_A > 2.5m_{\chi_1^0}$ and $M_1 > 0$ (filled circle) or $M_A > 2.5m_{\chi_1^0}$ and $M_1 < 0$ (open circle). For the wino-bino case (lower panel) we separated the points according to whether $\mu > 0$ (filled circle) or $\mu < 0$ (open circle). The effect of the residual parameters is sub-dominant with respect to e.g. that of the sfermion masses, but both the sign of μ and M_1 are seen to play a role in the resonance region for the wino-bino and wino-Higgsino cases, respectively. This can be understood in terms of the expressions for the mass difference between the lightest chargino and neutralino in Eqs. (4.24), (4.25) and (4.27), (4.28) to which the resonance is sensitive. As the splitting increases the position of the resonance moves towards higher values of $m_{\chi_1^0}$. Whether the heavy Higgs is below, above, or, in particular, close to the excluded window also has a noticeable effect for the case of wino-Higgsino mixing, and this extends beyond the resonance region and holds for the perturbative case as well. This is because for states with larger mixing the coupling to the heavy Higgs is enhanced, and therefore when M_A decreases the s-channel annihilation cross section increases, and one has to go to higher values of M_2 to obtain the correct relic density. This is not relevant for the wino-bino case, where the dependence on the value of M_A is negligible.

To summarise, we find that the assumption that our results of the previous Sections were to a good approximation independent of certain parameters was largely justified. Only for the wino-Higgsino case there is some dependence on the value of M_A , and in the resonance region the sensitivity to these parameters is somewhat enhanced, particularly to the values of $\tan\beta$ and the sign of μ for the case of wino-bino mixing and M_1 for the case of wino-Higgsino mixing.

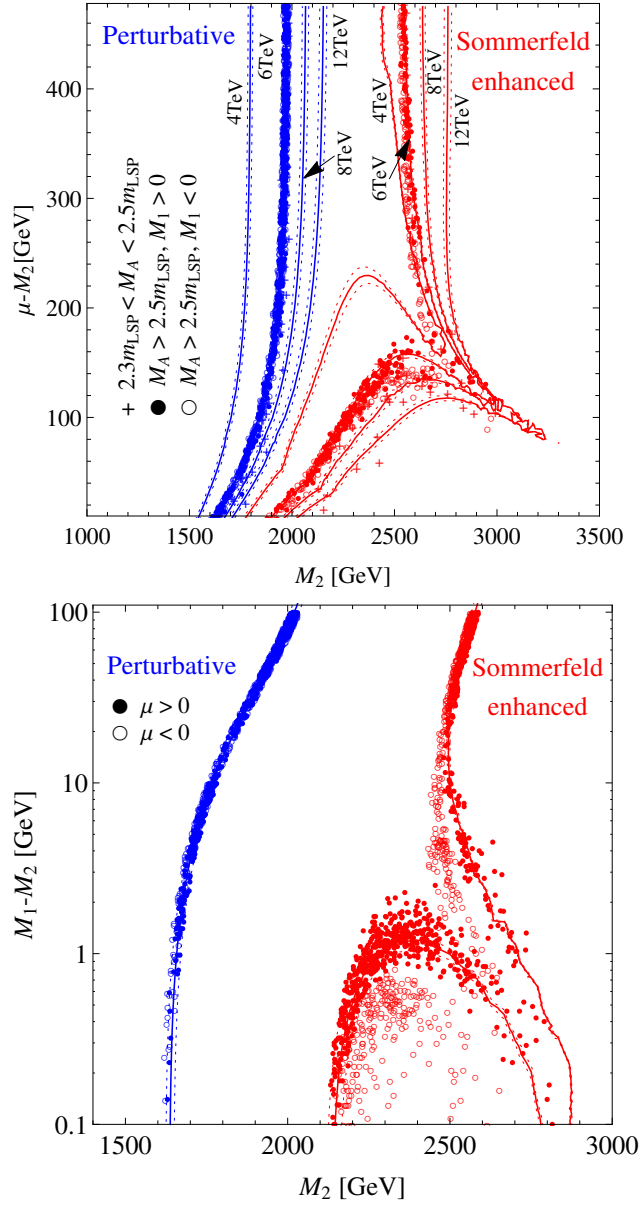


Figure 4.21: Plots showing points satisfying the relic density constraint obtained on varying the parameters $\tan\beta$, M_A and A_f for wino-like LSPs with varying Higgsino (upper) and bino (lower) admixtures. The points are overlaid on contours for fixed values of these parameters and M_{sf} as indicated.

Conclusions

In this thesis we studied radiative corrections to the cross section times velocity for pair-annihilation processes, relevant to determine the dark matter (DM) relic density within the so-called “freeze-out” scenario. We considered in particular two aspects of this problem: *i*) the development of a consistent framework for treating perturbative corrections beyond the leading order (LO), and *ii*) a phenomenological study of the relic density of heavy (TeV-scale) neutralinos in the general minimal supersymmetric standard model (MSSM), including the non-perturbative effect called Sommerfeld enhancement.

The consistent extension of relic density calculations to next-to-leading order (NLO) in perturbation theory is formally a non-trivial task. The standard calculation is based on a semiclassical approach, in which the LO annihilation cross section computed from quantum field theory (QFT) enters the classical Boltzmann equation for the time evolution of the DM number density. The assumptions upon which this formalism relies are not satisfied by the NLO cross section computed with the standard tools for particle physics calculations, defined in the in-out formalism for the scattering of particles in the vacuum (i.e. at zero temperature). As we have shown in [34], a consistent formalism for treating perturbative corrections in relic density calculations can indeed be developed within the closed time-path (CTP) approach to non-equilibrium QFT. Within this framework, on top of the standard zero-temperature NLO corrections, additional temperature-dependent corrections exist. The cancellation of soft and collinear infrared (IR) divergences at finite temperature is not ensured by any theorem, and therefore the finiteness of NLO corrections is not guaranteed. As a first application of our formalism we explicitly performed the calculation of thermal NLO corrections in a realistic “MSSM inspired” toy-model. As expected, the obtained result is IR finite, the cancellation of divergences occurring within each CTP self-energy diagram, in a way similar to the standard $T = 0$ case (for which the finiteness is ensured by the Block-Nordsieck cancellation and Kinoshita-Lee-Nauenberg theorem). The thermal correction is due to the soft interactions of the annihilating pair with the light SM particles of the background plasma, and can be computed most easily within an effective theory approach, similar to the HQET used for non-perturbative corrections in QCD [35]. In the temperature range that is relevant in the context of freeze-out, the leading thermal correction is found to be small compared to the standard $T = 0$ one, as it

is additionally suppressed by the fourth power of the small ratio of the temperature over the DM particle mass.

The experimental accuracy on the determination of DM relic abundance is already at the percent level and more data will come in the near future. The access to more precise calculations can therefore play a relevant role in constraining possible models for new physics. In the context of thermal production in the early Universe (and subsequent freeze-out), a better precision requires in general going beyond the leading order in perturbation theory in the calculation of the co-annihilation cross sections. The result that we obtained in the first part of this work sets the consistent framework for the inclusion of radiative corrections in relic density calculations.

In the second part of the thesis we focused on the Sommerfeld enhancement, a well-known effect in non-relativistic quantum mechanics that leads to large corrections to the rate for a short-range process in presence of a long-range potential interaction. In QFT this effect arises in the non-relativistic regime as a large non-perturbative correction, which computation is equivalent to the resummation of a particular class of diagrams. The Sommerfeld enhanced cross sections can be computed within an effective field theory (EFT) framework, originally developed for the co-annihilation of neutralinos and charginos in the general MSSM. After a pedagogical introduction to this framework, we presented in full detail the relevant calculations for the case of neutralino/sfermion co-annihilation, which can be used to further generalize the original framework. In order to investigate the phenomenological implications of the Sommerfeld enhancement in the MSSM, we implemented in an automated code the computation of the relic density including the full set of neutralino/chargino co-annihilations. The code allowed us to perform for the first time a detailed study of the relic abundance of generic TeV-scale wino-like neutralino models, which depart in various respects from the simple and well studied pure-wino scenario. We studied in particular the impact of lowering the sfermion masses (which are decoupled in pure-wino case), and of adding Higgsino or bino components to the lightest neutralino (LSP). We found many interesting regions of the MSSM parameter space in which the neutralino accounts for the measured DM abundance and the effect of the Sommerfeld enhancement is large (typically $\gtrsim 30\%$) resulting in potentially large indirect detection signatures. Those regions extend over a wide range of LSP masses, from around 1.7 TeV to above 4 TeV.

The study of wino-like scenarios that we presented in the second part of this thesis is the first large-scale application of our automated code. An interesting follow-up consists in a detailed study of indirect detection constraints on the models that we found. Additionally, there are other regions of the MSSM parameter space that can be investigated, such as Higgsino-like scenarios. Even though generically smaller compared to the wino-case examined here, the Sommerfeld effect in those scenarios can still be the largest radiative correction and be of the order $\mathcal{O}(10\%)$.

Appendix A

Matching of the decay width at NLO in the HPET

In this appendix we cross-check the reparametrization invariance relation (3.50) by explicitly computing the coefficient of the kinetic operator in the OPE of the decay width.

Within the matching procedure, the expansion of full theory operators in terms of HPET ones is a process-independent step. We start in Sec. A.1 by presenting this calculation for those bilinear operators that will be needed in Sec. A.2, where the diagram that is relevant for the matching is computed.

A.1 Operator expansion in HPET

The expansion of full theory operators in terms of HPET ones can be performed by replacing the fermion field ψ with the effective one h_v according to the relation (3.17), up to the required order in $1/M$. We consider here the following bilinear operators, that will be relevant for the matching calculation in the next section

$$\bar{\psi} \gamma^\mu iD^\nu \psi = v^\mu \bar{h}_v iD^\nu h_v + \frac{1}{M} \bar{h}_v iD^{(\mu} iD^{\nu)} h_v + \frac{1}{2M} \bar{h}_v eF^{\alpha\nu} \sigma_\alpha^\mu h_v + \mathcal{O}\left(\frac{1}{M^2}\right), \quad (\text{A.1})$$

$$\bar{\psi} \gamma^\mu iD^{(\nu} iD^{\rho)} \psi = v^\mu \bar{h}_v iD^{(\nu} iD^{\rho)} h_v + \mathcal{O}\left(\frac{1}{M}\right). \quad (\text{A.2})$$

Since the only four-vector on which it can depend is the thermal background velocity v , the spin averaged matrix element of the first term in (A.1) can be written as

$$\frac{1}{2} \sum_{\text{spin}} \langle \psi; \Omega_T | v^\mu \bar{h}_v iD^\nu h_v | \psi; \Omega_T \rangle = v^\mu v^\nu A, \quad (\text{A.3})$$

where A is a scalar matrix element to be determined. Contracting both sides with v_ν and using the equation of motion to order $\mathcal{O}(1/M)$ given in (3.16) we get

$$A = -\frac{1}{2M} (M_k + M_m) . \quad (\text{A.4})$$

The second term in (A.1) can be parametrized as

$$\begin{aligned} \frac{1}{2} \sum_s \langle \psi; \Omega_T | \frac{1}{M} \bar{h}_v iD^{(\mu} iD^{\nu)} h_v | \psi; \Omega_T \rangle &= g^{\mu\nu} B_1 + v^\mu v^\nu B_2 \\ &= (g^{\mu\nu} - v^\mu v^\nu) B_1 , \end{aligned} \quad (\text{A.5})$$

where in the second line we used $B_2 = -B_1$, obtained by contracting both sides with v_μ and using the equation of motion at the leading order. Taking the trace we get

$$B_1 = \frac{1}{2M} \frac{2}{3} M_k . \quad (\text{A.6})$$

Finally, for the third term in (A.1) we can write

$$\begin{aligned} \frac{1}{2} \sum_s \langle \psi; \Omega_T | \frac{1}{2M} \bar{h}_v eF^{\alpha\nu} \sigma_\alpha^\mu h_v | \psi; \Omega_T \rangle &= g^{\mu\nu} C_1 + v^\mu v^\nu C_2 \\ &= (g^{\mu\nu} - v^\mu v^\nu) C_1 , \end{aligned} \quad (\text{A.7})$$

where $C_2 = -C_1$ is again obtained by contracting both sides with v_μ and using $\bar{h}_v \sigma_\alpha^\mu v_\mu h_v = 0$. Taking the trace we obtain

$$C_1 = \frac{1}{2M} \frac{2}{3} M_m . \quad (\text{A.8})$$

Combining the above results we conclude

$$\frac{1}{2} \sum_s \langle \psi; \Omega_T | \bar{\psi} \gamma^\mu iD^\nu \psi | \psi; \Omega_T \rangle = \frac{1}{6M} (2g^{\mu\nu} - 5v^\mu v^\nu) (M_k + M_m) + \mathcal{O}\left(\frac{1}{M^2}\right) , \quad (\text{A.9})$$

$$\frac{1}{2} \sum_s \langle \psi; \Omega_T | \bar{\psi} \gamma^\mu iD^{(\nu} iD^{\rho)} \psi | \psi; \Omega_T \rangle = \frac{1}{3} v^\mu (g^{\nu\rho} - v^\nu v^\rho) M_k + \mathcal{O}\left(\frac{1}{M}\right) . \quad (\text{A.10})$$

The above results provide the expansion up to the required order in $1/M$ of the matrix elements of full theory operators in terms of HPET ones.

A.2 Next-to-leading order matching

The Wilson coefficient of the kinetic operator can be determined by expanding the diagram in Fig. 3.5 up to second order in the residual momentum k . We can ignore here the one-photon

diagram, even if it is of the same order, because it contributes only to the magnetic moment operator. The matching condition reads

$$\widehat{C}_1(p) + \left(\frac{\widehat{C}_1(p)}{4M^2} + \widehat{C}_k(p) \right) M_k = 2 \operatorname{Im} \left\{ \frac{1}{2} \sum_{\text{spin}} \langle \psi; \Omega_T | \mathcal{O}(p) | \psi; \Omega_T \rangle \right\}_{p=Mv+k}, \quad (\text{A.11})$$

where on the l.h.s. we used (3.30). On the r.h.s. we expand the denominator $\Delta \equiv (Mv + k - q)^2$ as

$$\frac{1}{\Delta} = \frac{1}{\Delta_0} - \frac{2(Mv - q) \cdot k}{\Delta_0^2} + \left[\frac{4((Mv - q) \cdot k)^2 - k^2}{\Delta_0^3} - \frac{k^2}{\Delta_0^2} \right] + \mathcal{O}\left(\frac{1}{M^3}\right), \quad (\text{A.12})$$

thus obtaining

$$\mathcal{O}^{(1)}(p) = -\frac{i\lambda^2}{2} \int \frac{d^4q}{(2\pi)^4} \frac{1}{q^2 - m_\chi^2} q_\mu \left[-\frac{2(Mv - q)_\nu}{\Delta_0^2} \right] \bar{\psi} \gamma^\mu k^\nu \psi, \quad (\text{A.13})$$

$$\mathcal{O}^{(2)}(p) = -\frac{i\lambda^2}{2} \int \frac{d^4q}{(2\pi)^4} \frac{1}{q^2 - m_\chi^2} q_\mu \left[-\frac{4(Mv - q)_{\nu\rho}}{\Delta_0^3} - \frac{g_{\nu\rho}}{\Delta_0^2} \right] \bar{\psi} \gamma^\mu k^\nu k^\rho \psi, \quad (\text{A.14})$$

where we adopt the shorthand notation $(Mv - q)_{\mu\nu} \equiv (Mv - q)_\mu (Mv - q)_\nu$. The operators appearing in (A.13) and (A.14) have to be written in terms of the HPET fields to the desired order by using (A.9) and (A.10). We neglected the operators containing γ_5 , since their matrix element vanish between unpolarized states. The result is

$$\frac{\widehat{C}_1(p)}{4M^2} + \widehat{C}_k(p) = \frac{1}{2M^2} \frac{\lambda^2}{32\pi} M \left(1 - \frac{m_\chi^4}{M^4} \right), \quad (\text{A.15})$$

from which we conclude

$$\widehat{C}_k = \frac{1}{4M^2} \widehat{C}_1, \quad (\text{A.16})$$

in agreement with the constraint provided by reparametrization invariance.

Appendix B

Wilson coefficients for neutralino/sfermion co-annihilation

In this appendix we describe the structure of the absorptive part of the Wilson coefficients encoding tree-level annihilation rates of sfermion-sfermion and neutralino-sfermion pairs.

We start in Sec. B.1 with the description of how the results can be written in terms of process-dependent coupling factors and universal kinematic factors. While the construction of the coupling factors has been described in detail in [44], we focus here on the kinematic factors for four-scalar and two-scalar-two-fermion reactions. The full analytic expressions are listed in an electronic supplement `kinfactors_scalars.m`, following the nomenclature described in Sec. B.2.

B.1 Decomposition into coupling and kinematics factors

The contributions to Wilson coefficients from exclusive final states $X_A X_B$ can be computed separately, since at the tree-level they are free from infrared divergences. Each of those contributions can be further decomposed into a sum over different Feynman diagrams, which can be organized according to their topology and labeled referring to the spin of the virtual exchanged particles. Each Feynman diagram can be written as the product of a process-dependent coupling factor, depending on the nature of all the involved particles, and a generic kinematic factor. The method of construction of the coupling factors is described in the appendix A.2 of [44], including a practical example. In the following we focus on the kinematic factors, which full analytic expressions are listed in the electronic supplement. We refer to a generic reaction

$$[\phi\phi]_a \rightarrow X_A X_B \rightarrow [\phi\phi]_b , \quad (\text{B.1})$$

where the constituents of the two-particle external states are

$$[\phi\phi]_a = \phi_{e_1} \phi_{e_2} , \quad [\phi\phi]_b = \phi_{e_4} \phi_{e_3} , \quad (\text{B.2})$$

and their masses are parametrized as

$$m \equiv \frac{m_{e_1} + m_{e_4}}{2}, \quad \bar{m} \equiv \frac{m_{e_2} + m_{e_3}}{2}, \quad (\text{B.3})$$

$$\delta m \equiv \frac{m_{e_4} - m_{e_1}}{2}, \quad \delta \bar{m} \equiv \frac{m_{e_3} - m_{e_2}}{2}. \quad (\text{B.4})$$

We further introduce the quantities

$$\Delta_m \equiv \hat{m} - \widehat{\bar{m}}, \quad (\text{B.5})$$

$$\Delta_{AB} \equiv \hat{m}_A^2 - \widehat{\bar{m}}_B^2, \quad (\text{B.6})$$

$$\beta \equiv \sqrt{1 - 2(\hat{m}_A^2 + \widehat{\bar{m}}_B^2) + \Delta_{AB}^2}, \quad (\text{B.7})$$

where $m_{A,B}$ are the masses of the final state particles $X_A X_B$ and the hat denotes the rescaling by the mass $M \equiv m + \bar{m}$

$$\hat{m} \equiv \frac{m}{M}. \quad (\text{B.8})$$

The s -channel propagator at leading order is parametrized by

$$P_i^s = 1 - \hat{m}_i^2, \quad (\text{B.9})$$

while the t - and u -channel

$$P_{iAB} = \hat{m} \widehat{\bar{m}} + \hat{m}_i^2 - \hat{m} \hat{m}_A^2 - \widehat{\bar{m}} \widehat{\bar{m}}_B^2, \quad (\text{B.10})$$

$$P_{iBA} = P_{iAB}|_{A \leftrightarrow B}. \quad (\text{B.11})$$

The generic diagrams for four-scalars and two-scalars-two-fermions reactions are depicted in Figs. B.1 and B.2, respectively. Notice that the presence of the four-scalar vertex introduces three additional topologies compared to the four-fermion case studied in [44, 45]. We refer to these topologies as 2nd- and 3rd-type self-energy and 2nd-type triangle and we denote with E , F and G their contributions. The absorptive part of the Wilson coefficient for the reaction in (B.1) can be written as

$$\begin{aligned} \widehat{C}_{ab}^{X_A X_B}(wave) = & \frac{\pi \alpha_2^2}{M^2} \left(\sum_n \sum_{i_1, i_2} b_{n, i_1 i_2}^{X_A X_B} B_{n, i_1 i_2}^{X_A X_B}(wave) + \sum_{\alpha=1}^2 \sum_{i_1} e_{i_1}^{(\alpha) X_A X_B} E_{i_1}^{(\alpha) X_A X_B}(wave) \right. \\ & + f^{X_A X_B} F^{X_A X_B}(wave) + \sum_{\alpha=1}^4 \sum_n \sum_{i_1, i_2} c_{n, i_1 i_2}^{(\alpha) X_A X_B} C_{n, i_1 i_2}^{(\alpha) X_A X_B}(wave) \\ & \left. + \sum_{\alpha=1}^4 \sum_{i_1} g_{i_1}^{(\alpha) X_A X_B} G_{i_1}^{(\alpha) X_A X_B}(wave) + \sum_{\alpha=1}^4 \sum_n \sum_{i_1, i_2} d_{n, i_1 i_2}^{(\alpha) X_A X_B} D_{n, i_1 i_2}^{(\alpha) X_A X_B}(wave) \right), \quad (\text{B.12}) \end{aligned}$$

where we denote with capital (lowercase) letters the kinematic (coupling) factors. Note that, since they do not depend on the kinematics, the coupling factors are the same for Wilson coefficients with different quantum numbers denoted by *wave*. The indices $i_{1,2}$ label the particles exchanged in the s -, t - and u -channel, α denotes the different generic diagrams that are needed to cover all possible kinematic configurations and n the different coupling structure arising in presence of fermions (n is a character-string of length equal to the number of vertices that involve fermions, which are by convention enumerated from top to bottom and from left to right. The i^{th} character of n indicates the coupling factor of the i^{th} vertex and is equal to r for scalar/vector and q for pseudo-scalar/axial).

The kinematic factors for the LO and NNLO Wilson coefficients are conveniently written by extracting overall prefactors arising from phase-space integration (β) and from the leading-order expansion of s - or t - and u -channel propagators, as follows self-energy:

$$B_{n,i_1i_2}^{X_AX_B}(wave) = \frac{\beta}{(\hat{m}\hat{m})^{2K} P_{i_1}^s P_{i_2}^s} \tilde{B}_{n,i_1i_2}^{X_AX_B}(wave); \quad (\text{B.13})$$

2nd-type self-energy:

$$E_X^{(\alpha)X_AX_B}(wave) = \frac{\beta}{(\hat{m}\hat{m})^K P_X^s} \tilde{E}_X^{(\alpha)X_AX_B}(wave) \quad \alpha = 1, 2;$$

3rd-type self-energy:

$$F^{X_AX_B}(wave) = \beta \tilde{F}^{X_AX_B}(wave);$$

triangle:

$$\begin{aligned} C_{n,i_1X}^{(\alpha)X_AX_B}(wave) &= \frac{\beta}{(\hat{m}\hat{m})^K P_{i_1AB} P_X^s} \tilde{C}_{n,i_1X}^{(\alpha)X_AX_B}(wave) \quad \alpha = 1, 2, \\ C_{n,i_1X}^{(\alpha)X_AX_B}(wave) &= \frac{\beta}{(\hat{m}\hat{m})^K P_{i_1BA} P_X^s} \tilde{C}_{n,i_1X}^{(\alpha)X_AX_B}(wave) \quad \alpha = 3, 4; \end{aligned} \quad (\text{B.14})$$

2nd-type triangles:

$$\begin{aligned} G_{i_1}^{(\alpha)X_AX_B}(wave) &= \frac{\beta}{P_{i_1AB}} \tilde{G}_{i_1}^{(\alpha)X_AX_B}(wave) \quad \alpha = 1, 2, \\ G_{i_1}^{(\alpha)X_AX_B}(wave) &= \frac{\beta}{P_{i_1BA}} \tilde{G}_{i_1}^{(\alpha)X_AX_B}(wave) \quad \alpha = 3, 4; \end{aligned} \quad (\text{B.15})$$

box:

$$D_{n,i_1i_2}^{(1)X_AX_B}(wave) = \frac{\beta}{P_{i_1AB} P_{i_2BA}} \tilde{D}_{n,i_1i_2}^{(1)X_AX_B}(wave),$$

$$\begin{aligned}
D_{n,i_1i_2}^{(2)X_AX_B}(wave) &= \frac{\beta}{P_{i_1AB}P_{i_2AB}} \tilde{D}_{n,i_1i_2}^{(2)X_AX_B}(wave) , \\
D_{n,i_1i_2}^{(3)X_AX_B}(wave) &= \frac{\beta}{P_{i_1BA}P_{i_2AB}} \tilde{D}_{n,i_1i_2}^{(3)X_AX_B}(wave) , \\
D_{n,i_1i_2}^{(4)X_AX_B}(wave) &= \frac{\beta}{P_{i_1BA}P_{i_2BA}} \tilde{D}_{n,i_1i_2}^{(4)X_AX_B}(wave) ;
\end{aligned} \tag{B.16}$$

where $K = 0$, (1) for LO (NNLO) kinematic factors.

B.2 Notation for the kinematic factors in the electronic supplement

The analytic expressions for the kinematic factors needed to construct the absorptive part of the Wilson coefficients up to next-to-next-to-leading order have been stored in the `Mathematica` package attached to this thesis. The notation that is used in this file is summarized in Table B.1. The labels `i1`, `i2` and `X`, denoting s - and t -channel exchanged particles, applies only to the final states for which they can assume different values, explicitly given in the second column of the table. For spin- $\frac{1}{2}$ reactions in the s -channel there is always a fermion (`f`), while for spin-0 reactions the t -channel exchanged particle is always a fermion for $X_AX_B = \mathbf{ff}$, and a scalar (`S`) otherwise. The argument `XAXB` inside the kinematic factors in Table B.1 can be given the values

$$\mathbf{XAXB} = \mathbf{VV, VS, SS, ff, GG, Vf, fS} ,$$

depending on the type of particles in the final state. Notice that the final states `Vf` and `fS` refer to a spin- $\frac{1}{2}$ reaction, while the others a spin-0 reaction. The partial wave configuration *wave* is specified by one of the following strings:

$$wave = \left\{ \begin{array}{l} \text{"1S0", for the leading-order } S\text{-wave} \\ \text{"1P1", for the } P\text{-wave} \\ \text{"1S0,q2", for the two-derivative } S\text{-wave} \end{array} \right\} \text{ for spin-0 reactions ,}$$

$$\left\{ \begin{array}{l} \text{"2S1/2", for the leading-order } S\text{-wave} \\ \text{"2PJ", for the } P\text{-wave} \\ \text{"2S1/2,q2", for the two-derivative } S\text{-wave} \\ \text{"2S1/2,dm", for the mass splitting} \end{array} \right\} \text{ for spin-}\frac{1}{2}\text{ reactions .}$$

The argument `alpha` inside the kinematic factors `Etilde`, `Ctilde`, `Gtilde` and `Dtilde` in Tab. B.1 can get as input

$$\text{alpha} = \begin{cases} 1,2 & \text{for Etilde ,} \\ 1,2,3,4 & \text{for Ctilde, Gtilde, Dtilde .} \end{cases}$$

referring to our enumeration scheme for the respective two 2nd-type self-energies and four triangle, 2nd-type triangle and box topologies. Finally, the equivalence between the mass variables and propagator structures introduced in Sec. B.1 that enter the expressions for the kinematic factors and the corresponding names in the `Mathematica` package are collected in Tab. B.2.

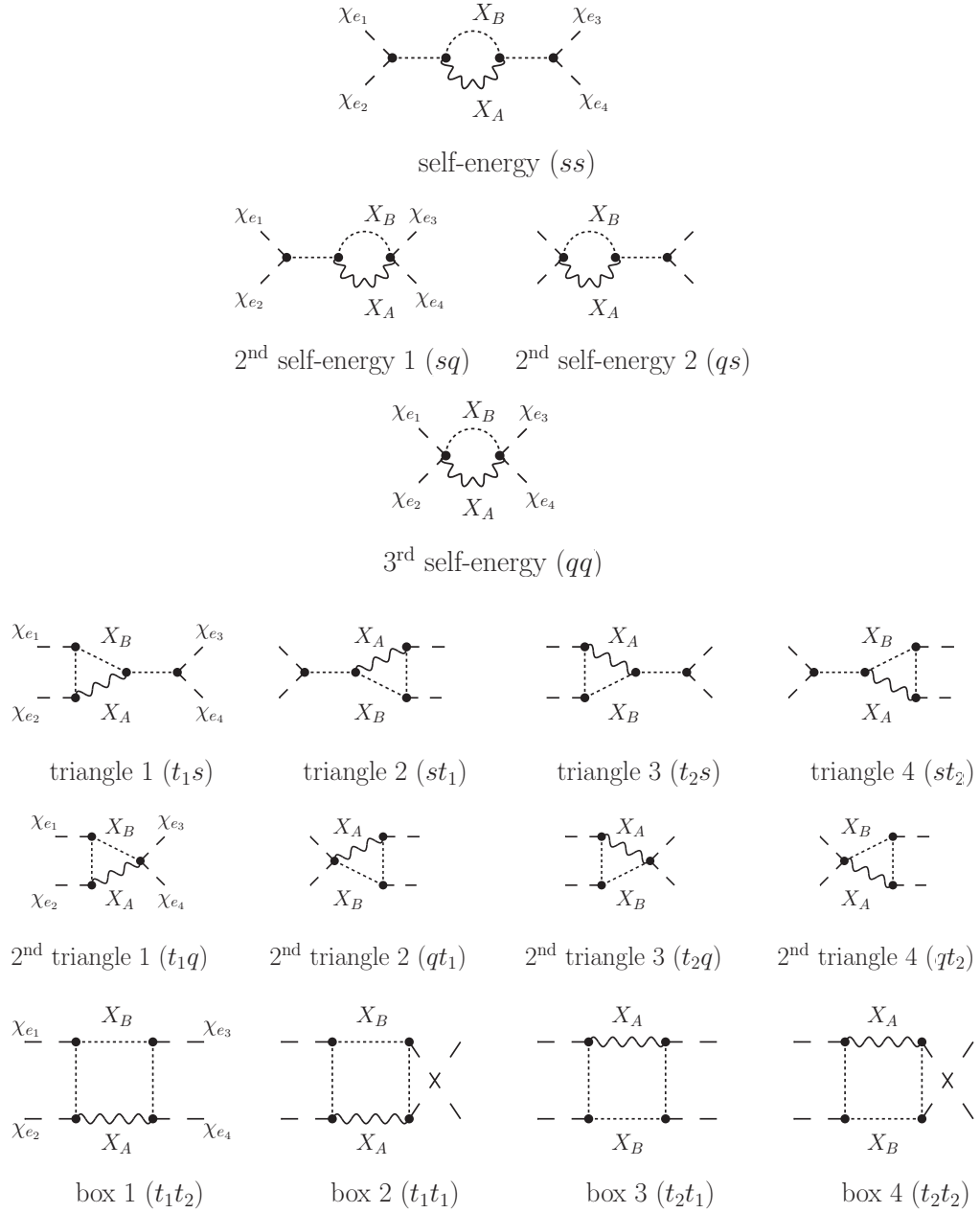


Figure B.1: Generic diagrams that cover all possible kinematic configurations that can arise in a $\tilde{f}\tilde{f} \rightarrow X_A X_B \rightarrow \tilde{f}\tilde{f}$ one-loop amplitude.

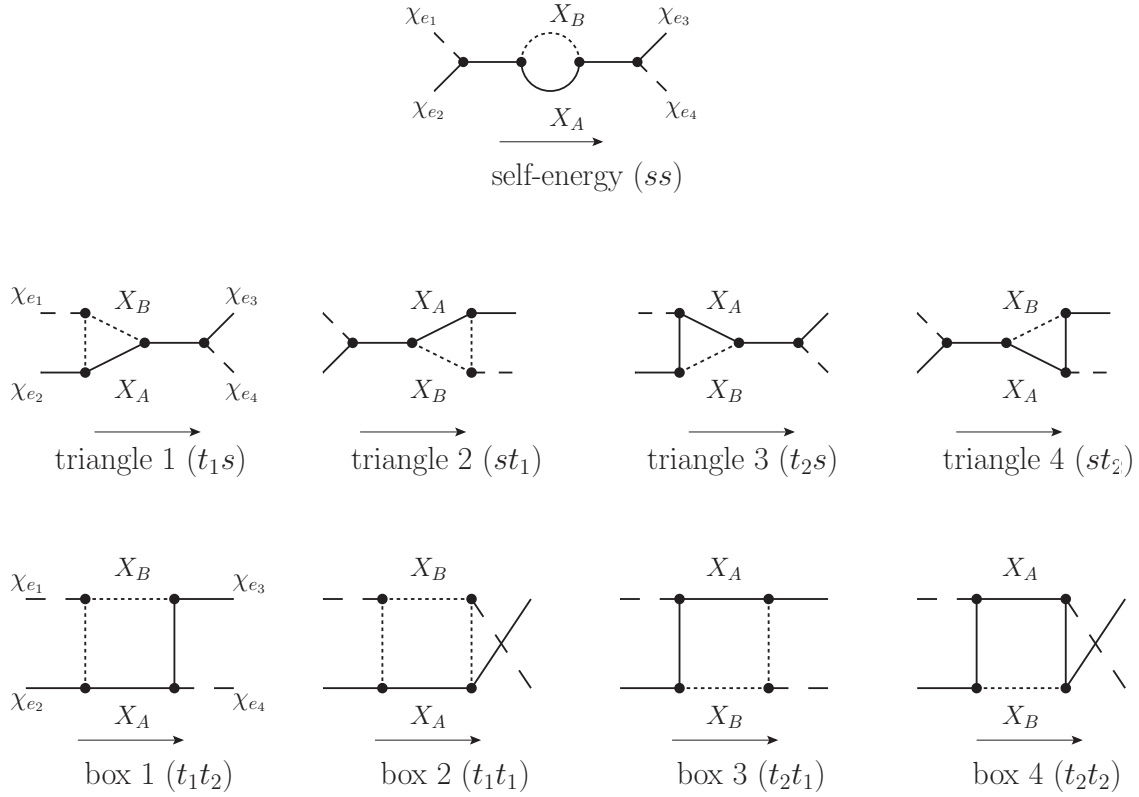


Figure B.2: Generic diagrams that cover all possible kinematic configurations that can arise in a $\tilde{f}\chi^0 \rightarrow X_A X_B \rightarrow \tilde{f}\chi^0$ one-loop amplitude. The arrows denote the conventional choice for the fermion flow [70] (see Sec. 2.3 for the definition of fermion flow).

| Kinematic factor | Name in electronic supplement | Coupling string n ($X_A X_B$) |
|--|---|--|
| $\tilde{B}_{n, i_1 i_2}^{X_A X_B (2s+1) L_J}$ | $\text{Btilde}["(i_1 i_2) X A X B", n, \{2s+1\}^{\wedge} L_J]$ $i_1, i_2 = V, S (X_A X_B = VV, VS, SS, GG, ff)$ | $\left. \begin{array}{l} "rrrr", "qqqq", "rrqq" \\ "qqrr", "rqqr", "qrrq" \\ "rqrq", "qrqr" \\ "rr", "qq" (ff) \end{array} \right\} (Vf, fS)$ |
| $\tilde{E}_X^{(\alpha) X_A X_B (2s+1) L_J}$ | $\text{Etilde}[\text{alpha}, "(X) X A X B", \{2s+1\}^{\wedge} L_J]$ $X = V, S (X_A X_B = VV, VS, SS, GG, ff)$ | |
| $\tilde{F}^{X_A X_B (2s+1) L_J}$ | $\text{Ftilde}["X A X B", \{2s+1\}^{\wedge} L_J]$ | |
| $\tilde{C}_{n, i_1 X}^{(\alpha) X_A X_B (2s+1) L_J}$ | $\text{Ctilde}[\text{alpha}, "(i_1 X) X A X B", n, \{2s+1\}^{\wedge} L_J]$ $i_1 = S, f (X_A X_B = Vf, fS)$ $X = V, S (X_A X_B = VV, VS, SS, GG, ff)$ | $\left. \begin{array}{l} "rrrr", "qqqq", "rrqq" \\ "qqrr", "rqqr", "qrrq" \\ "rqrq", "qrqr" \\ "rrr", "qqr" \\ "rqq", "qrq" \end{array} \right\} (Vf, fS)$ $\left. \begin{array}{l} "rrr", "qqr" \\ "rqq", "qrq" \end{array} \right\} (ff)$ |
| $\tilde{G}_{i_1}^{(\alpha) X_A X_B (2s+1) L_J}$ | $\text{Gtilde}[\text{alpha}, "(i_1) X A X B", \{2s+1\}^{\wedge} L_J]$ $i_1 = S, f (X_A X_B = Vf, fS)$ | |
| $\tilde{D}_{n, i_1 i_2}^{(\alpha) X_A X_B (2s+1) L_J}$ | $\text{Dtilde}[\text{alpha}, "(i_1 i_2) X A X B", n, \{2s+1\}^{\wedge} L_J]$ $i_1 = S, f (X_A X_B = Vf, fS)$ | $\left. \begin{array}{l} "rrrr", "qqqq", "rrqq" \\ "qqrr", "rqqr", "qrrq" \\ "rqrq", "qrqr" \end{array} \right\} (Vf, fS, ff)$ |

Table B.1: Notation for the kinematic factors used in the `Mathematica` package.

| Quantity | Name in electronic supplement |
|--------------------------------|-------------------------------|
| $\hat{m}_{i_1}, \hat{m}_{i_2}$ | mi1, mi2 |
| \hat{m}_A, \hat{m}_B | mA, mB |
| \hat{m}_W | mWr |
| Δ_m | Dm |
| Δ_{AB} | DAB |
| $P_{i_1}^s, P_{i_2}^s$ | Psi1, Psi2 |
| P_X^s | PsX |
| $P_{i_1 AB}, P_{i_2 AB}$ | Pti1[A,B], Pti2[A,B] |

Table B.2: Equivalence between the variables in the kinematic factors introduced in Sec. B.1 and the corresponding names in the `Mathematica` package.

Appendix C

Improved non-relativistic expansion of s -channel propagators

In Sec. 4.3.3 we have seen that for the calculation of the annihilation matrices a non-relativistic expansion of the full theory diagrams is performed, in which the mass splittings among different channels are formally of order $\mathcal{O}(v^2)$. In particular, a diagram with an s -channel exchange of a particle of mass m_i is proportional to the propagator¹

$$\begin{aligned} \frac{1}{s - m_i^2} &= \frac{1}{(\sqrt{s} - M + M)^2 - m_i^2} \\ &\simeq \frac{1}{M^2 - m_i^2} \left(1 - \frac{2M(\sqrt{s} - M)}{M^2 - m_i^2} + \dots \right) \end{aligned} \quad (\text{C.1})$$

$$\simeq \frac{1}{M^2 P_i^s} - \frac{2}{M^3 (P_i^s)^2} \left(\frac{\vec{q}^2}{2\mu} - 2\delta m - 2\delta\bar{m} \right), \quad (\text{C.2})$$

where we used the expansion

$$(\sqrt{s} - M) \simeq \frac{\vec{q}^2}{2\mu} - 2\delta m - 2\delta\bar{m}, \quad (\text{C.3})$$

and in the last line we introduced the quantity

$$P_i^s = 1 - \frac{m_i}{M}. \quad (\text{C.4})$$

In the code, according to the expansion (C.2), s -channel propagators appear in the annihilation matrices $\Gamma_{ab}^{(0)}(\text{wave})$ as

$$\frac{1}{M^2 P_i^s} \quad \text{for } \text{wave} \in \{({}^1S_0), ({}^3S_1), ({}^1P_1), ({}^3P_j)\}$$

¹In this subsection we adopt the notation from [44, 45] for M , μ , δm , and $\delta\bar{m}$, see Appendix B.

and terms in the $\mathcal{O}(v^2)$ waves where the NNLO part of some other quantity (e.g. a t -channel propagator) is taken ,

$$-\frac{1}{\mu M^3(P_i^s)^2}$$

for terms in $wave \in \{({}^1S_0, q^2), ({}^3S_1, q^2)\}$

in which every other quantity is taken at LO ,

$$\frac{4}{M^3(P_i^s)^2}$$

for terms in $wave \in \{({}^1S_0, \delta m), ({}^3S_1, \delta m), ({}^1S_0, \delta \bar{m}), ({}^3S_1, \delta \bar{m})\}$

in which every other quantity is taken at LO .

The propagator (C.2) is resonant for $M \simeq m_i$, and the condition (4.159) ensures that such a resonance is never hit in the $\chi_1^0 \chi_1^0 \rightarrow \chi_1^0 \chi_1^0$ case, when $M = 4m_{\chi_1^0}$, and in nearly degenerate channels. However, when we include heavier states in the last loop, the denominator P_i^s may still become very small. These resonances are spurious since we are interested in the non-relativistic regime for the external (light) states, such that the center-of-mass energy is in the range

$$\sqrt{s} \in \left\{ 2m_{\chi_1^0}, 2m_{\chi_1^0} + T_{\text{f.o.}} \right\}, \quad (\text{C.5})$$

and the original propagator $(s - m_i^2)^{-1}$ is therefore not resonant whenever (4.159) holds. Such spurious resonances can be avoided by replacing the non-relativistic expansion (C.2) with

$$\begin{aligned} \frac{1}{s - m_i^2} &= \frac{1}{(\sqrt{s} - 2m_{\chi_1^0} + 2m_{\chi_1^0})^2 - m_i^2} \\ &\simeq \frac{1}{4m_{\chi_1^0}^2 - m_i^2} \left(1 - \frac{4m_{\chi_1^0}(\sqrt{s} - 2m_{\chi_1^0})}{4m_{\chi_1^0}^2 - m_i^2} + \dots \right), \end{aligned} \quad (\text{C.6})$$

that is formally equivalent up to higher order terms. In order to achieve this form for the propagator starting from our expression (C.1), we expand it further in $(M - 2m_{\chi_1^0})$

$$(\text{C.1}) \simeq \frac{1}{4m_{\chi_1^0}^2 - m_i^2} \left(1 - \frac{4m_{\chi_1^0}(M - 2m_{\chi_1^0})}{4m_{\chi_1^0}^2 - m_i^2} - \frac{2M(\sqrt{s} - M)}{4m_{\chi_1^0}^2 - m_i^2} + \dots \right) \quad (\text{C.7})$$

$$\simeq \frac{1}{4m_{\chi_1^0}^2 - m_i^2} - \frac{4m_{\chi_1^0}(M - 2m_{\chi_1^0})}{(4m_{\chi_1^0}^2 - m_i^2)^2} - \frac{2M}{(4m_{\chi_1^0}^2 - m_i^2)^2} \left(\frac{\vec{q}^2}{2\mu} - 2\delta m - 2\delta \bar{m} \right). \quad (\text{C.8})$$

Note that, multiplying by $2m_{\chi_1^0}/M$ the last term in brackets in (C.7), we get exactly (C.6), and that the multiplication factor is formally equal to 1, up to higher order terms.

Due to the structure of the code explained above, the implementation of the new expansion (C.6) has to rely on an *ad hoc* substitution rule for the quantity P_i^s . In order to reproduce

(C.8) we apply various replacements of P_i^s in the different terms, according to

$$P_i^s \rightarrow \frac{1}{M^2} \left[\frac{1}{4m_{\chi_1^0}^2 - m_i^2} - \frac{4m_{\chi_1^0}(M - 2m_{\chi_1^0})}{(4m_{\chi_1^0}^2 - m_i^2)^2} \right]^{-1} \quad \text{in LO annihilation matrices,}$$

(C.9)

$$\left\{ \begin{array}{l} P_i^s \rightarrow \frac{1}{M^2} \left[\frac{1}{4m_{\chi_1^0}^2 - m_i^2} \right]^{-1} \\ (P_i^s)^2 \rightarrow \left(\frac{M}{2m_{\chi_1^0}} \right) \left(\frac{1}{M^2} \left[\frac{1}{4m_{\chi_1^0}^2 - m_i^2} \right]^{-1} \right)^2 \end{array} \right. \quad \text{in NNLO annihilation matrices.}$$

(C.10)

The substitutions in NNLO matrices are done in two steps: first the $(P_i^s)^2$ are replaced, reproducing properly the last term in (C.7), then the remaining P_i^s , present in terms where the s -channel propagator appears at LO, are replaced with the LO expression. This complication is necessary to avoid the introduction of formally higher order terms, that could be spuriously large when heavy channels are considered. For the same reason in self-energy contributions, where two different s -channel propagators P_i^s and P_j^s appear, the replacement (C.9) is actually implemented as a replacement for the product $P_i^s P_j^s$, in which the $\mathcal{O}(v^4)$ term is consistently dropped.

Bibliography

- [1] F. Zwicky. Die Rotverschiebung von extragalaktischen Nebeln. *Helv.Phys.Acta*, 6:110–127, 1933.
- [2] F. Zwicky. On the Masses of Nebulae and of Clusters of Nebulae. *Astrophys.J.*, 86:217–246, 1937.
- [3] V. C. Rubin and J. Ford, W. Kent. Rotation of the Andromeda Nebula from a Spectroscopic Survey of Emission Regions. *Astrophys.J.*, 159:379–403, 1970.
- [4] J. P. Ostriker and P. J. E. Peebles. *Astrophys.J.*, 186:467, 1973.
- [5] J. P. Ostriker, P. J. E. Peebles, and A. Yahil. *Astrophys.J.*, 193:L10, 1974.
- [6] J. Einasto, E. Saar, A. Kaasik, and A. D. Chernin. *Nature*, 252:111, 1974.
- [7] E. van Uitert, H. Hoekstra, T. Schrabback, D. G. Gilbank, M. D. Gladders, et al. Constraints on the shapes of galaxy dark matter haloes from weak gravitational lensing. *Astron.Astrophys.*, 545:A71, 2012, 1206.4304.
- [8] L. A. Moustakas and R. B. Metcalf. Detecting dark matter substructure spectroscopically in strong gravitational lenses. *Mon.Not.Roy.Astron.Soc.*, 339:607, 2003, astro-ph/0206176.
- [9] D. Clowe, M. Bradac, A. H. Gonzalez, M. Markevitch, S. W. Randall, et al. A direct empirical proof of the existence of dark matter. *Astrophys.J.*, 648:L109–L113, 2006, astro-ph/0608407.
- [10] P. A. R. Ade et al. Planck 2015 results. XIII. Cosmological parameters. 2015, 1502.01589.
- [11] G. B. Gelmini. TASI 2014 Lectures: The Hunt for Dark Matter. 2015, 1502.01320.
- [12] M. Milgrom. A Modification of the Newtonian dynamics as a possible alternative to the hidden mass hypothesis. *Astrophys.J.*, 270:365–370, 1983.

- [13] J. D. Bekenstein. Relativistic gravitation theory for the MOND paradigm. *Phys.Rev.*, D70:083509, 2004, astro-ph/0403694.
- [14] B. Famaey and S. McGaugh. Modified Newtonian Dynamics (MOND): Observational Phenomenology and Relativistic Extensions. *Living Rev.Rel.*, 15:10, 2012, 1112.3960.
- [15] B. J. Carr and S. Hawking. Black holes in the early Universe. *Mon.Not.Roy.Astron.Soc.*, 168:399–415, 1974.
- [16] D. M. Jacobs, G. D. Starkman, and B. W. Lynn. Macro Dark Matter. *Mon.Not.Roy.Astron.Soc.*, 2014, 1410.2236.
- [17] L. Chuzhoy and E. W. Kolb. Reopening the window on charged dark matter. *JCAP*, 0907:014, 2009, 0809.0436.
- [18] J. Fan, A. Katz, L. Randall, and M. Reece. Double-Disk Dark Matter. *Phys.Dark Univ.*, 2:139–156, 2013, 1303.1521.
- [19] K. Griest, A. M. Cieplak, and M. J. Lehner. Experimental Limits on Primordial Black Hole Dark Matter from the First 2 yr of Kepler Data. *Astrophys.J.*, 786:158, 2014.
- [20] W. Hu, R. Barkana, and A. Gruzinov. Cold and fuzzy dark matter. *Phys.Rev.Lett.*, 85:1158–1161, 2000, astro-ph/0003365.
- [21] S. Hannestad. What is the lowest possible reheating temperature? *Phys.Rev.*, D70:043506, 2004, astro-ph/0403291.
- [22] G. Gelmini and P. Gondolo. DM Production Mechanisms. 2010, 1009.3690.
- [23] E. W. Kolb and M. S. Turner. THE EARLY UNIVERSE. REPRINTS. 1988.
- [24] S. Dodelson. Modern cosmology. 2003.
- [25] P. Gondolo and G. Gelmini. *Nucl. Phys.*, B360:145, 1991.
- [26] N. Baro, F. Boudjema, and A. Semenov. Full one-loop corrections to the relic density in the MSSM: A Few examples. *Phys.Lett.*, B660:550–560, 2008, 0710.1821.
- [27] N. Baro, F. Boudjema, G. Chalons, and S. Hao. Relic density at one-loop with gauge boson pair production. *Phys.Rev.*, D81:015005, 2010, 0910.3293.
- [28] B. Herrmann, M. Klasen, and K. Kovarik. Neutralino Annihilation into Massive Quarks with SUSY-QCD Corrections. *Phys.Rev.*, D79:061701, 2009, 0901.0481.

- [29] B. Herrmann, M. Klasen, and K. Kovarik. SUSY-QCD effects on neutralino dark matter annihilation beyond scalar or gaugino mass unification. *Phys.Rev.*, D80:085025, 2009, 0907.0030.
- [30] J. Harz, B. Herrmann, M. Klasen, K. Kovarik, and Q. L. Boulc'h. Neutralino-stop coannihilation into electroweak gauge and Higgs bosons at one loop. *Phys.Rev.*, D87(5):054031, 2013, 1212.5241.
- [31] A. Chatterjee, M. Drees, and S. Kulkarni. Radiative Corrections to the Neutralino Dark Matter Relic Density - an Effective Coupling Approach. 2012, 1209.2328.
- [32] P. Ciafaloni, D. Comelli, A. De Simone, E. Morgante, A. Riotto, et al. The Role of Electroweak Corrections for the Dark Matter Relic Abundance. *JCAP*, 1310:031, 2013, 1305.6391.
- [33] B. Herrmann, M. Klasen, K. Kovarik, M. Meinecke, and P. Steppeler. One-loop corrections to gaugino (co)annihilation into quarks in the MSSM. *Phys.Rev.*, D89(11):114012, 2014, 1404.2931.
- [34] M. Beneke, F. Dighera, and A. Hryczuk. Relic density computations at NLO: infrared finiteness and thermal correction. *JHEP*, 1410:45, 2014, 1409.3049.
- [35] M. Beneke, F. Dighera, and A. Hryczuk. Finite-temperature modification of heavy particle decay and dark matter annihilation. 2016, 1607.03910.
- [36] S. P. Martin. A Supersymmetry primer. *Adv.Ser.Direct.High Energy Phys.*, 21:1–153, 2010, hep-ph/9709356.
- [37] A. Sommerfeld. Über die Beugung und Bremsung der Elektronen. *Annalen der Physik*, 403:257, 1931.
- [38] J. Hisano, S. Matsumoto, M. M. Nojiri, and O. Saito. Non-perturbative effect on dark matter annihilation and gamma ray signature from galactic center. *Phys.Rev.*, D71:063528, 2005, hep-ph/0412403.
- [39] J. Hisano, S. Matsumoto, M. Nagai, O. Saito, and M. Senami. Non-perturbative effect on thermal relic abundance of dark matter. *Phys.Lett.*, B646:34–38, 2007, hep-ph/0610249.
- [40] M. Drees, J. Kim, and K. Nagao. Potentially Large One-loop Corrections to WIMP Annihilation. *Phys.Rev.*, D81:105004, 2010, 0911.3795.
- [41] A. Hryczuk, R. Iengo, and P. Ullio. Relic densities including Sommerfeld enhancements in the MSSM. *JHEP*, 1103:069, 2011, 1010.2172.

- [42] A. Hryczuk. The Sommerfeld enhancement for scalar particles and application to sfermion co-annihilation regions. *Phys. Lett.*, B699:271–275, 2011, 1102.4295.
- [43] A. Hryczuk and R. Iengo. The one-loop and Sommerfeld electroweak corrections to the Wino dark matter annihilation. *JHEP*, 01:163, 2012, 1111.2916. [Erratum: *JHEP*06,137(2012)].
- [44] M. Beneke, C. Hellmann, and P. Ruiz-Femenia. Non-relativistic pair annihilation of nearly mass degenerate neutralinos and charginos I. General framework and S-wave annihilation. *JHEP*, 03:148, 2013, 1210.7928. [Erratum: *JHEP*10,224(2013)].
- [45] C. Hellmann and P. Ruiz-Femenia. Non-relativistic pair annihilation of nearly mass degenerate neutralinos and charginos II. P-wave and next-to-next-to-leading order S-wave coefficients. *JHEP*, 1308:084, 2013, 1303.0200.
- [46] M. Beneke, C. Hellmann, and P. Ruiz-Femenia. Non-relativistic pair annihilation of nearly mass degenerate neutralinos and charginos III. Computation of the Sommerfeld enhancements. *JHEP*, 05:115, 2015, 1411.6924.
- [47] M. Beneke, A. Bharucha, F. Dighera, C. Hellmann, A. Hryczuk, S. Recksiegel, and P. Ruiz-Femenia. Relic density of wino-like dark matter in the MSSM. *JHEP*, 03:119, 2016, 1601.04718.
- [48] G. Bertone, D. Hooper, and J. Silk. Particle dark matter: Evidence, candidates and constraints. *Phys.Rept.*, 405:279–390, 2005, hep-ph/0404175.
- [49] S. Profumo. TASI 2012 Lectures on Astrophysical Probes of Dark Matter. 2013, 1301.0952.
- [50] B. D. Fields. The Primordial Lithium Problem. *Annual Review of Nuclear and Particle Science*, 61:47–68, November 2011, 1203.3551.
- [51] K. Olive et al. Review of Particle Physics. *Chin.Phys.*, C38:090001, 2014.
- [52] P. Ade et al. Planck 2013 results. XVI. Cosmological parameters. *Astron.Astrophys.*, 571:A16, 2014, 1303.5076.
- [53] K. Griest and M. Kamionkowski. Unitarity Limits on the Mass and Radius of Dark Matter Particles. *Phys.Rev.Lett.*, 64:615, 1990.
- [54] B. W. Lee and S. Weinberg. Cosmological Lower Bound on Heavy Neutrino Masses. *Phys.Rev.Lett.*, 39:165–168, 1977.
- [55] K. Petraki and R. R. Volkas. Review of asymmetric dark matter. *Int. J. Mod. Phys.*, A28:1330028, 2013, 1305.4939.

- [56] J. Edsjo and P. Gondolo. Neutralino relic density including coannihilations. *Phys.Rev.*, D56:1879–1894, 1997, hep-ph/9704361.
- [57] M. Hindmarsh and O. Philipsen. WIMP dark matter and the QCD equation of state. *Phys.Rev.*, D71:087302, 2005, hep-ph/0501232.
- [58] P. Gondolo, J. Edsjo, P. Ullio, L. Bergstrom, M. Schelke, et al. DarkSUSY: Computing supersymmetric dark matter properties numerically. *JCAP*, 0407:008, 2004, astro-ph/0406204.
- [59] G. Belanger, F. Boudjema, P. Brun, A. Pukhov, S. Rosier-Lees, et al. Indirect search for dark matter with micrOMEGAs2.4. *Comput.Phys.Commun.*, 182:842–856, 2011, 1004.1092.
- [60] T. Prokopec, M. G. Schmidt, and S. Weinstock. Transport equations for chiral fermions to order \hbar and electroweak baryogenesis. Part 1. *Annals Phys.*, 314:208–265, 2004, hep-ph/0312110.
- [61] J. S. Schwinger. Brownian motion of a quantum oscillator. *J.Math.Phys.*, 2:407–432, 1961.
- [62] L. Keldysh. Diagram technique for nonequilibrium processes. *Zh.Eksp.Teor.Fiz.*, 47:1515–1527, 1964.
- [63] K.-c. Chou, Z.-b. Su, B.-l. Hao, and L. Yu. Equilibrium and Nonequilibrium Formalisms Made Unified. *Phys.Rept.*, 118:1, 1985.
- [64] A. Das. Finite temperature field theory. 1997.
- [65] R. Kubo. *J. Phys. Soc. Japan*, 12:570, 1957.
- [66] P. Martin and J. S. Schwinger. *Phys. Rev.*, 115:1342, 1959.
- [67] E. Calzetta and B. Hu. Nonequilibrium Quantum Fields: Closed Time Path Effective Action, Wigner Function and Boltzmann Equation. *Phys.Rev.*, D37:2878, 1988.
- [68] J. M. Cornwall, R. Jackiw, and E. Tomboulis. Effective Action for Composite Operators. *Phys.Rev.*, D10:2428–2445, 1974.
- [69] G. Baym and L. P. Kadanoff. Conservation Laws and Correlation Functions. *Phys.Rev.*, 124:287–299, 1961.
- [70] A. Denner, H. Eck, O. Hahn, and J. Kublbeck. Feynman rules for fermion number violating interactions. *Nucl.Phys.*, B387:467–484, 1992.

- [71] F. Boudjema, G. Drieu La Rochelle, and S. Kulkarni. One-loop corrections, uncertainties and approximations in neutralino annihilations: Examples. *Phys. Rev.*, D84:116001, 2011, 1108.4291.
- [72] N. Baro, F. Boudjema, and A. Semenov. Automatised full one-loop renormalisation of the MSSM. I. The Higgs sector, the issue of $\tan(\beta)$ and gauge invariance. *Phys.Rev.*, D78:115003, 2008, 0807.4668.
- [73] N. Baro and F. Boudjema. Automatised full one-loop renormalisation of the MSSM II: The chargino-neutralino sector, the sfermion sector and some applications. *Phys.Rev.*, D80:076010, 2009, 0906.1665.
- [74] <http://code.sloops.free.fr/index.php>.
- [75] B. Herrmann and M. Klasen. SUSY-QCD Corrections to Dark Matter Annihilation in the Higgs Funnel. *Phys.Rev.*, D76:117704, 2007, 0709.0043.
- [76] <http://dmnlo.hepforge.org>.
- [77] F. Bloch and A. Nordsieck. Note on the Radiation Field of the electron. *Phys.Rev.*, 52:54–59, 1937.
- [78] T. Kinoshita. Mass singularities of Feynman amplitudes. *J.Math.Phys.*, 3:650–677, 1962.
- [79] T. Lee and M. Nauenberg. Degenerate Systems and Mass Singularities. *Phys.Rev.*, 133:B1549–B1562, 1964.
- [80] A. Czarnecki, M. Kamionkowski, S. K. Lee, and K. Melnikov. Charged Particle Decay at Finite Temperature. *Phys.Rev.*, D85:025018, 2012, 1110.2171.
- [81] D. Besak and D. Bodeker. Thermal production of ultrarelativistic right-handed neutrinos: Complete leading-order results. *JCAP*, 1203:029, 2012, 1202.1288.
- [82] A. Anisimov, D. Besak, and D. Bodeker. Thermal production of relativistic Majorana neutrinos: Strong enhancement by multiple soft scattering. *JCAP*, 1103:042, 2011, 1012.3784.
- [83] A. Salvio, P. Lodone, and A. Strumia. Towards leptogenesis at NLO: the right-handed neutrino interaction rate. *JHEP*, 1108:116, 2011, 1106.2814.
- [84] M. Laine and Y. Schroder. Thermal right-handed neutrino production rate in the non-relativistic regime. *JHEP*, 1202:068, 2012, 1112.1205.
- [85] B. Garbrecht, F. Glowna, and M. Herranen. Right-Handed Neutrino Production at Finite Temperature: Radiative Corrections, Soft and Collinear Divergences. *JHEP*, 1304:099, 2013, 1302.0743.

- [86] T. Altherr, P. Aurenche, and T. Becherrawy. On Infrared and Mass Singularities of Perturbative QCD in a Quark - Gluon Plasma. *Nucl.Phys.*, B315:436, 1989.
- [87] H. A. Weldon. Bloch-Nordsieck cancellation of infrared divergences at finite temperature. *Phys.Rev.*, D44:3955–3963, 1991.
- [88] H. A. Weldon. Cancellation of infrared divergences in thermal QED. *Nucl.Phys.*, A566:581C–584C, 1994, hep-ph/9308249.
- [89] D. Indumathi. Cancellation of infrared divergences at finite temperature. *Annals Phys.*, 263:310–339, 1998, hep-ph/9607206.
- [90] P. Ciafaloni, M. Cirelli, D. Comelli, A. De Simone, A. Riotto, et al. On the Importance of Electroweak Corrections for Majorana Dark Matter Indirect Detection. *JCAP*, 1106:018, 2011, 1104.2996.
- [91] T. Altherr and P. Aurenche. Finite Temperature QCD Corrections to Lepton Pair Formation in a Quark - Gluon Plasma. *Z.Phys.*, C45:99, 1989.
- [92] J. F. Donoghue and B. R. Holstein. Renormalization and Radiative Corrections at Finite Temperature. *Phys.Rev.*, D28:340, 1983.
- [93] A. G. Grozin. Introduction to effective field theories. 1. Heisenberg-Euler effective theory, decoupling of heavy flavours. In *Helmholtz International School - Workshop on Calculations for Modern and Future Colliders (CALC 2009) Dubna, Russia, July 10-20, 2009*, 2009, 0908.4392.
- [94] A. G. Grozin. Introduction to effective field theories. 3. Bloch–Nordsieck effective theory, HQET. 2013, 1305.4245.
- [95] N. Isgur and M. B. Wise. Weak Decays of Heavy Mesons in the Static Quark Approximation. *Phys.Lett.*, B232:113–117, 1989.
- [96] N. Isgur and M. B. Wise. WEAK TRANSITION FORM-FACTORS BETWEEN HEAVY MESONS. *Phys. Lett.*, B237:527–530, 1990.
- [97] B. Grinstein. The Static Quark Effective Theory. *Nucl. Phys.*, B339:253–268, 1990.
- [98] H. Georgi. An Effective Field Theory for Heavy Quarks at Low-energies. *Phys. Lett.*, B240:447–450, 1990.
- [99] K. Kopp and T. Okui. Effective Field Theory for a Heavy Majorana Fermion. *Phys.Rev.*, D84:093007, 2011, 1108.2702.

- [100] S. Biondini, N. Brambilla, M. A. Escobedo, and A. Vairo. An effective field theory for non-relativistic Majorana neutrinos. *JHEP*, 1312:028, 2013, 1307.7680.
- [101] T. Mannel, W. Roberts, and Z. Ryzak. A Derivation of the heavy quark effective Lagrangian from QCD. *Nucl. Phys.*, B368:204–220, 1992.
- [102] M. E. Luke and A. V. Manohar. Reparametrization invariance constraints on heavy particle effective field theories. *Phys.Lett.*, B286:348–354, 1992, hep-ph/9205228.
- [103] B. Blok, L. Koyrakh, M. A. Shifman, and A. I. Vainshtein. Differential distributions in semileptonic decays of the heavy flavors in QCD. *Phys. Rev.*, D49:3356, 1994, hep-ph/9307247. [Erratum: *Phys. Rev.*D50,3572(1994)].
- [104] A. V. Manohar and M. B. Wise. Inclusive semileptonic B and polarized Lambda(b) decays from QCD. *Phys. Rev.*, D49:1310–1329, 1994, hep-ph/9308246.
- [105] S. Caron-Huot. Asymptotics of thermal spectral functions. *Phys.Rev.*, D79:125009, 2009, 0903.3958.
- [106] A. Fowlie, K. Kowalska, L. Roszkowski, E. M. Sessolo, and Y.-L. S. Tsai. Dark matter and collider signatures of the MSSM. *Phys. Rev.*, D88:055012, 2013, 1306.1567.
- [107] M. Cahill-Rowley, R. Cotta, A. Drlica-Wagner, S. Funk, J. Hewett, A. Ismail, T. Rizzo, and M. Wood. Complementarity of dark matter searches in the phenomenological MSSM. *Phys. Rev.*, D91(5):055011, 2015, 1405.6716.
- [108] E. A. Bagnaschi et al. Supersymmetric Dark Matter after LHC Run 1. *Eur. Phys. J.*, C75(10):500, 2015, 1508.01173.
- [109] K. J. de Vries et al. The pMSSM10 after LHC Run 1. *Eur. Phys. J.*, C75(9):422, 2015, 1504.03260.
- [110] N. Arkani-Hamed, D. P. Finkbeiner, T. R. Slatyer, and N. Weiner. A Theory of Dark Matter. *Phys. Rev.*, D79:015014, 2009, 0810.0713.
- [111] M. Cirelli, A. Strumia, and M. Tamburini. Cosmology and Astrophysics of Minimal Dark Matter. *Nucl. Phys.*, B787:152–175, 2007, 0706.4071.
- [112] M. Cirelli and J. M. Cline. Can multistate dark matter annihilation explain the high-energy cosmic ray lepton anomalies? *Phys. Rev.*, D82:023503, 2010, 1005.1779.
- [113] D. P. Finkbeiner, L. Goodenough, T. R. Slatyer, M. Vogelsberger, and N. Weiner. Consistent Scenarios for Cosmic-Ray Excesses from Sommerfeld-Enhanced Dark Matter Annihilation. *JCAP*, 1105:002, 2011, 1011.3082.

- [114] M. Drees and J. Gu. Enhanced One-Loop Corrections to WIMP Annihilation and their Thermal Relic Density in the Coannihilation Region. *Phys.Rev.*, D87(6):063524, 2013, 1301.1350.
- [115] J. Chen and Y.-F. Zhou. The 130 GeV gamma-ray line and Sommerfeld enhancements. *JCAP*, 1304:017, 2013, 1301.5778.
- [116] A. Hryczuk, I. Cholis, R. Iengo, M. Tavakoli, and P. Ullio. Indirect Detection Analysis: Wino Dark Matter Case Study. *JCAP*, 1407:031, 2014, 1401.6212.
- [117] M. Beneke, C. Hellmann, and P. Ruiz-Femenia. Heavy neutralino relic abundance with Sommerfeld enhancements - a study of pMSSM scenarios. *JHEP*, 03:162, 2015, 1411.6930.
- [118] J. Fan and M. Reece. In Wino Veritas? Indirect Searches Shed Light on Neutralino Dark Matter. *JHEP*, 1310:124, 2013, 1307.4400.
- [119] T. Cohen, M. Lisanti, A. Pierce, and T. R. Slatyer. Wino Dark Matter Under Siege. *JCAP*, 1310:061, 2013, 1307.4082.
- [120] S. Weinberg. Implications of Dynamical Symmetry Breaking. *Phys. Rev.*, D13:974–996, 1976.
- [121] G. 't Hooft. Symmetry Breaking Through Bell-Jackiw Anomalies. *Phys. Rev. Lett.*, 37:8–11, 1976.
- [122] S. Dimopoulos and D. W. Sutter. The Supersymmetric flavor problem. *Nucl. Phys.*, B452:496–512, 1995, hep-ph/9504415.
- [123] G. R. Dvali, G. F. Giudice, and A. Pomarol. The Mu problem in theories with gauge mediated supersymmetry breaking. *Nucl. Phys.*, B478:31–45, 1996, hep-ph/9603238.
- [124] S. Y. Choi, J. Kalinowski, G. A. Moortgat-Pick, and P. M. Zerwas. Analysis of the neutralino system in supersymmetric theories. *Eur. Phys. J.*, C22:563–579, 2001, hep-ph/0108117. [Addendum: *Eur. Phys. J.*C23,769(2002)].
- [125] R. Iengo. Sommerfeld enhancement: General results from field theory diagrams. *JHEP*, 05:024, 2009, 0902.0688.
- [126] T. R. Slatyer. The Sommerfeld enhancement for dark matter with an excited state. *JCAP*, 1002:028, 2010, 0910.5713.
- [127] S. Cassel. Sommerfeld factor for arbitrary partial wave processes. *J. Phys.*, G37:105009, 2010, 0903.5307.

- [128] C. Hellmann. *Sommerfeld corrections in neutralino dark matter pair-annihilations and relic abundance in the general MSSM*. PhD thesis, Technische Universität München, 2015, <http://mediatum.ub.tum.de/node?id=1234004>.
- [129] M. Beneke and V. A. Smirnov. Asymptotic expansion of Feynman integrals near threshold. *Nucl. Phys.*, B522:321–344, 1998, hep-ph/9711391.
- [130] G. T. Bodwin, E. Braaten, and G. P. Lepage. Rigorous QCD analysis of inclusive annihilation and production of heavy quarkonium. *Phys. Rev.*, D51:1125–1171, 1995, hep-ph/9407339. [Erratum: *Phys. Rev.*D55,5853(1997)].
- [131] J. Edsjo, M. Schelke, P. Ullio, and P. Gondolo. Accurate relic densities with neutralino, chargino and sfermion coannihilations in mSUGRA. *JCAP*, 0304:001, 2003, hep-ph/0301106.
- [132] J. Rosiek. Complete set of Feynman rules for the MSSM: Erratum. 1995, hep-ph/9511250.
- [133] L. E. Ibanez. The Scalar Neutrinos as the Lightest Supersymmetric Particles and Cosmology. *Phys. Lett.*, B137:160, 1984.
- [134] J. S. Hagelin, G. L. Kane, and S. Raby. Perhaps Scalar Neutrinos Are the Lightest Supersymmetric Partners. *Nucl. Phys.*, B241:638, 1984.
- [135] T. Falk, K. A. Olive, and M. Srednicki. Heavy sneutrinos as dark matter. *Phys. Lett.*, B339:248–251, 1994, hep-ph/9409270.
- [136] D. S. Akerib et al. First results from the LUX dark matter experiment at the Sanford Underground Research Facility. *Phys. Rev. Lett.*, 112:091303, 2014, 1310.8214.
- [137] N. Arkani-Hamed, L. J. Hall, H. Murayama, D. Tucker-Smith, and N. Weiner. Small neutrino masses from supersymmetry breaking. *Phys. Rev.*, D64:115011, 2001, hep-ph/0006312.
- [138] K. Harigaya, K. Kaneta, and S. Matsumoto. Gaugino coannihilations. *Phys. Rev.*, D89(11):115021, 2014, 1403.0715.
- [139] M. Drees and M. M. Nojiri. The Neutralino relic density in minimal $N = 1$ supergravity. *Phys. Rev.*, D47:376–408, 1993, hep-ph/9207234.
- [140] P. Nath and R. L. Arnowitt. Predictions in SU(5) supergravity grand unification with proton stability and relic density constraints. *Phys. Rev. Lett.*, 70:3696–3699, 1993, hep-ph/9302318.

- [141] S. Heinemeyer, W. Hollik, and G. Weiglein. FeynHiggs: A Program for the calculation of the masses of the neutral CP even Higgs bosons in the MSSM. *Comput. Phys. Commun.*, 124:76–89, 2000, hep-ph/9812320.
- [142] G. Degrossi, S. Heinemeyer, W. Hollik, P. Slavich, and G. Weiglein. Towards high precision predictions for the MSSM Higgs sector. *Eur. Phys. J.*, C28:133–143, 2003, hep-ph/0212020.
- [143] T. Fritzsche and W. Hollik. Complete one loop corrections to the mass spectrum of charginos and neutralinos in the MSSM. *Eur. Phys. J.*, C24:619–629, 2002, hep-ph/0203159.
- [144] A. Fowler and G. Weiglein. Precise Predictions for Higgs Production in Neutralino Decays in the Complex MSSM. *JHEP*, 1001:108, 2010, 0909.5165.
- [145] A. Fowler. *Precise Predictions for Higgs Production in Neutralino Decays in the Complex MSSM*. PhD thesis, Durham University, 2010, http://etheses.dur.ac.uk/449/1/Thesis_AFowler.pdf.
- [146] A. Bharucha, A. Fowler, G. Moortgat-Pick, and G. Weiglein. Consistent on shell renormalisation of electroweakinos in the complex MSSM: LHC and LC predictions. 2012, 1211.3134.
- [147] A. Bharucha, S. Heinemeyer, F. von der Pahlen, and C. Schappacher. Neutralino Decays in the Complex MSSM at One-Loop: a Comparison of On-Shell Renormalization Schemes. 2012, 1208.4106.
- [148] A. Chatterjee, M. Drees, S. Kulkarni, and Q. Xu. On the On-Shell Renormalization of the Chargino and Neutralino Masses in the MSSM. 2011, 1107.5218.
- [149] T. Hahn. Generating Feynman diagrams and amplitudes with FeynArts 3. *Comput.Phys.Comm.*, 140:418–431, 2001, hep-ph/0012260.
- [150] T. Hahn and C. Schappacher. The Implementation of the minimal supersymmetric standard model in FeynArts and FormCalc. *Comput.Phys.Comm.*, 143:54–68, 2002, hep-ph/0105349.
- [151] T. Hahn and M. Perez-Victoria. Automatized one loop calculations in four-dimensions and D-dimensions. *Comput.Phys.Comm.*, 118:153–165, 1999, hep-ph/9807565.
- [152] T. Fritzsche, T. Hahn, S. Heinemeyer, H. Rzehak, and C. Schappacher. The Implementation of the Renormalized Complex MSSM in FeynArts and FormCalc. 2013, 1309.1692.

- [153] G. Belanger, F. Boudjema, A. Pukhov, and A. Semenov. micrOMEGAs 3: A program for calculating dark matter observables. *Comput.Phys.Commun.*, 185:960–985, 2014, 1305.0237.
- [154] The LEP SUSY Working Group and the ALEPH, DELPHI, L3 and OPAL experiments, note LEPSUSYWG/01-03.1. <http://lepsusy.web.cern.ch/lepsusy>.
- [155] G. Aad et al. Summary of the ATLAS experiment’s sensitivity to supersymmetry after LHC Run 1 - interpreted in the phenomenological MSSM. 2015, 1508.06608.
- [156] G. Aad et al. Combined Measurement of the Higgs Boson Mass in pp Collisions at $\sqrt{s} = 7$ and 8 TeV with the ATLAS and CMS Experiments. 2015, 1503.07589.
- [157] M. Carena, J. Espinosa, M. Quiros, and C. Wagner. Analytical expressions for radiatively corrected Higgs masses and couplings in the MSSM. *Phys.Lett.*, B355:209–221, 1995, hep-ph/9504316.
- [158] H. E. Haber, R. Hempfling, and A. H. Hoang. Approximating the radiatively corrected Higgs mass in the minimal supersymmetric model. *Z.Phys.*, C75:539–554, 1997, hep-ph/9609331.
- [159] T. Hahn, S. Heinemeyer, W. Hollik, H. Rzehak, and G. Weiglein. High-Precision Predictions for the Light CP -Even Higgs Boson Mass of the Minimal Supersymmetric Standard Model. *Phys. Rev. Lett.*, 112(14):141801, 2014, 1312.4937.
- [160] S. Heinemeyer, W. Hollik, and G. Weiglein. Electroweak precision observables in the minimal supersymmetric standard model. *Phys. Rept.*, 425:265–368, 2006, hep-ph/0412214.
- [161] S. Stone. *Plenary talk at the International Conference on High Energy Physics (ICHEP 2012), Melbourne, Australia, July 4-11th, 2012.*
- [162] M. Misiak and M. Steinhauser. NNLO QCD corrections to the anti-B \rightarrow X(s) gamma matrix elements using interpolation in $m(c)$. *Nucl.Phys.*, B764:62–82, 2007, hep-ph/0609241.
- [163] M. Wick and W. Altmannshofer. A Reconsideration of the b \rightarrow s gamma Decay in the Minimal Flavor Violating MSSM. *AIP Conf.Proc.*, 1078:348–353, 2009, 0810.2874.
- [164] CMS and L. Collaborations. Combination of results on the rare decays $B_{(s)}^0 \rightarrow \mu^+ \mu^-$ from the CMS and LHCb experiments. 2013.
- [165] A. J. Buras, J. Girrbach, D. Guadagnoli, and G. Isidori. On the Standard Model prediction for BR(Bs,d to mu+ mu-). *Eur. Phys. J.*, C72:2172, 2012, 1208.0934.

- [166] J. P. Lees et al. Evidence of $B^+ \rightarrow \tau^+ \nu$ decays with hadronic B tags. *Phys. Rev.*, D88(3):031102, 2013, 1207.0698.
- [167] I. Adachi et al. Evidence for $B^- \rightarrow \tau^- \bar{\nu}_\tau$ with a Hadronic Tagging Method Using the Full Data Sample of Belle. *Phys. Rev. Lett.*, 110(13):131801, 2013, 1208.4678.
- [168] W. Altmannshofer, M. Carena, N. R. Shah, and F. Yu. Indirect Probes of the MSSM after the Higgs Discovery. *JHEP*, 01:160, 2013, 1211.1976.
- [169] J. Frere, D. Jones, and S. Raby. Fermion Masses and Induction of the Weak Scale by Supergravity. *Nucl.Phys.*, B222:11, 1983.
- [170] M. Claudson, L. J. Hall, and I. Hinchliffe. Low-Energy Supergravity: False Vacua and Vacuous Predictions. *Nucl.Phys.*, B228:501, 1983.
- [171] H. Baer, A. Mustafayev, E.-K. Park, and S. Profumo. Mixed wino dark matter: Consequences for direct, indirect and collider detection. *JHEP*, 07:046, 2005, hep-ph/0505227.
- [172] J. Hisano, S. Matsumoto, and M. M. Nojiri. Explosive dark matter annihilation. *Phys.Rev.Lett.*, 92:031303, 2004, hep-ph/0307216.
- [173] J. Hisano, S. Matsumoto, O. Saito, and M. Senami. Heavy wino-like neutralino dark matter annihilation into antiparticles. *Phys.Rev.*, D73:055004, 2006, hep-ph/0511118.
- [174] M. Beneke, A. Bharucha, A. Hryczuk, S. Recksiegel, and P. Ruiz-Femenia. In preparation.
- [175] L. Roszkowski, E. M. Sessolo, and A. J. Williams. Prospects for dark matter searches in the pMSSM. *JHEP*, 02:014, 2015, 1411.5214.
- [176] M. E. Cabrera-Catalan, S. Ando, C. Weniger, and F. Zandanel. Indirect and direct detection prospect for TeV dark matter in the nine parameter MSSM. *Phys. Rev.*, D92(3):035018, 2015, 1503.00599.
- [177] J. Bramante, N. Desai, P. Fox, A. Martin, B. Ostdiek, and T. Plehn. Towards the Final Word on Neutralino Dark Matter. 2015, 1510.03460.

List of publications

- [1] M. Beneke, F. Dighera and A. Hryczuck. *Relic density computations at NLO: infrared finiteness and thermal corrections*. Published on JHEP, 10(2014)045. arXiv: 1409.3049.
- [2] M. Beneke, A. Bharucha, F. Dighera, C. Hellmann, A. Hryczuck, S. Recksiegel, and P. Ruiz-Femenia. *Relic density of wino-like dark matter in the MSSM*. Published on JHEP, 03(2016)119. arXiv: 1601.04718.
- [3] M. Beneke, F. Dighera and A. Hryczuck. *Finite-temperature modification of heavy particle decay and dark matter annihilation*. Submitted to JHEP. arXiv: 1607.03910.

Acknowledgments

I am particularly grateful to my advisor Martin Beneke for having inspired and supported with his experience my research work over the last years.

Furthermore, I sincerely wish to thank Andrzej Hryczuk, *in primis* for everything he taught me during our collaboration, and for the patience and care dedicated to reading and commenting on this manuscript.